

Exploring Lunar Geochemistry beyond the Procellarum KREEP Terrane: Insights from Basaltic and Brecciated Meteorites

A thesis submitted in partial fulfilment of
the requirements for the degree of

Doctor of Philosophy

by

Yash Srivastava

(Roll No. 18330027)

Under the supervision of

Dr. Amit Basu Sarbadhikari

Associate Professor

Planetary Sciences Division

Physical Research Laboratory, Ahmedabad



Discipline of Earth Sciences

Indian Institute of Technology Gandhinagar, India

2023

This Thesis is dedicated to

My father, who keeps on guiding me from heaven

*My Mother and Brother, who had been pillars of my strength
throughout this journey*

Declaration

I declare here that this thesis report represents my own ideas in my own words and I have included others' ideas with appropriate citations from original sources. I also declare that I have followed all principles of academic honesty and integrity and have not misrepresented or fabricated or falsified any idea/fact/source/data in my submission. I understand that any violation of the above can cause disciplinary action by the Institute and can also evoke penal action from the sources which have thus not been properly cited or from whom proper permission has not been taken when needed.

Date: March 04, 2024

Yash Srivastava
(Roll No.: 18330027)



Discipline of Earth Sciences

Indian Institute of Technology, Gandhinagar

Gandhinagar, Gujarat-382355

CERTIFICATE

It is certified that the work contained in the thesis titled “**Exploring Lunar Geochemistry beyond the Procellarum KREEP Terrane: Insights from Basaltic and Brecciated Meteorites**” by **Yash Srivastava** (Roll no: 18330027), has been carried out under my supervision and that this work has not been submitted elsewhere for a degree.

Dr. Amit Basu Sarbadhikari
(Thesis Supervisor)
Associate Professor
Planetary Sciences Division
Physical Research Laboratory,
Ahmedabad, India

Date: March 04, 2024

Acknowledgments

As I sit here writing this section of my thesis, I am filled with a sense of fulfillment as the moment I have eagerly awaited, my Ph.D. submission, finally comes to life. This journey has been a whirlwind of emotions, encompassing both moments of profound joy and deep sorrow. I am overwhelmed with gratitude as I reflect upon the individuals who have provided unwavering motivation and support throughout this remarkable endeavour, whether directly or indirectly. I consider myself incredibly fortunate to have been surrounded by an inspiring professional and social network, which has culminated in the creation of the ensuing document and the milestone it represents. In the forthcoming paragraphs, I will highlight the pivotal elements that have not only shaped my career but have also had a profoundly positive impact on my life.

In spite of the limited availability of dedicated courses in Planetary Sciences, my fascination with the subject has persisted since my undergraduate years. Within this fascination, two individuals have played the role of torchbearers in my academic journey: *Dr. Shyama Narendranath* and *Dr. Amit Basu Sarbadhikari*. During my undergraduate studies, I had the fortunate opportunity to collaborate with them as part of an internship project between ISRO and PRL. Their unwavering support, both on a personal and professional level, has empowered me to explore the depths of this subject. I wish to express my deepest gratitude to *Dr. Sarbadhikari*, who is also my PhD supervisor, to give me freedom to work on new ideas and always show encouragement towards learning new things. It is through his invaluable suggestions and constructive comments that I have been able to accomplish this work successfully.

There are several other people without their support the completion of my PhD was not possible. I express my sincere gratitude to my Doctoral Studies Committee members, *Prof. Jyotiranjana S Ray*, *Dr. Dwijesh Ray* and *Dr. Vineet Goswami*, who always supported and guided during the progress of my thesis by providing constructive remarks and swift responses to my urgency in obtaining their feedback. My external collaborators, *Drs. Akira Yamaguchi*, *Teresa Ubide*, *Atsushi Takenouchi*, *T Vijay Kumar* and *E.V.S.S.K. Babu* are thanked kindly for their contributions and insight during the completion of each project. Specifically, I thank *Prof. James Day*, Professor

at Scripps Institution of Oceanography, UC San Diego, for numerous conversations incredible insights, guidance, and patience. I am also thankful to the Academic Committee members for their insightful comments and encouragement during my research period. I would like to make a notable mention to *Mr. Viswesh* who has been available at all times during any administrative help. I also express my sincere thanks to all the faculties and staff members especially of the Planetary Sciences Division for their assistance in the form of academic and administrative guidance.

I am very grateful to the Director, *Prof. Anil Bhardwaj*; Dean, *Prof. D. Pallamraju*; PSDN Chairman, *Prof. Varun Sheel*; Deputy Head, *Prof. Debabrata Banerjee* and Head of Academic Services, *Dr. Bhushit Vaishnav* for their constant support and assistance during my Ph.D. tenure to complete the thesis work. I thank the people from accounts, purchase, library, administration, canteen, CMD, dispensary, transport, and housekeeping sections for all the help they have provided me during my Ph.D. tenure. I am also thankful to the Computer Center staff, namely *Jigar sir, Tejas sir, Mishra Ji, Vaibhav Bhai*, and others for their extended help regarding computational problems. I deeply appreciate their support for providing me with a smooth computational facility at all times. I would also like to thank office colleagues *Ms Garima Arora, Mr Anirban Ghosh (Dada), Mr. Avadh Rautela* and *Mr Vikram Goyal* for creating a enjoyable office space and providing important academic and administrative guidance.

The inspiration, support, and collaboration that I have received from my group members exceed the confines of any acknowledgment. Nonetheless, I would like to extend my sincere gratitude to all my group members for their invaluable assistance during my Ph.D. journey. In particular, I am deeply grateful to *Dr. Alka Rani*, my remarkable senior, and *Ms. Varsha M. Nair*, my talented junior, for their exceptional suggestions, insightful discussions, and unwavering support that have been instrumental in sustaining me throughout this expedition. I have gained invaluable knowledge from their contributions. Lastly, I would like to express my heartfelt appreciation to *Dr. Shashikiran Ganesh* and his research group, including *Dr. Archita Rai, Dr. Aravind K, Dr. Namita Uppal* and, *Mr. Goldy Ahuja*, for strengthening my astronomy background and fostering a delightful and harmonious working environment.

Doing a PhD also requires a side hobby which oftentimes help in reducing the work stress. In this regard, I take a moment to appreciate my incredible extracurricular partners *Sandeep, Naval, Vikas, Dayanand, Sunil, and Yogesh* (probably all Drs. till the time of this thesis publication) with whom I learned several life skills such as Swimming and Driving. Apart from extracurriculars, food outings and home cooking has been another important aspect and this could not be as memorable as it is, without the company of *Deepak, Akanksha, Monika, Pranav* and *Anju*. I would like to express my heartfelt thanks to *Dr. Namita Uppal*, for always being there for discussing academic and personal matters. Your handwork and dedication has been an inspiration for me throughout this journey. Additionally, I am thankful to all my seniors and juniors as they have been a constant source of inspiration and learning. I would like to express my heartfelt appreciation to all friends outside PRL, *Mayank, Ashu, Shubham* and *Ashish*, who were always there like a family.

I am deeply in debt to my family, who have been my pillar of strength throughout my whole journey. Their boundless love, support, and constant encouragement have been instrumental in helping me overcome the countless challenges I encountered along the way. I am forever obliged to my parents, my guiding lights, for their sacrifices and unconditional love and for providing me with an environment where I could thrive and pursue my dreams. I am grateful to my elder brother, *Harsh Srivastava*, for his constant support, encouragement, and inspiration, which always motivated me to move forward in my life.

To all those who have contributed in big or small ways, I am sincerely grateful. Your collective impact has left an unforgettable imprint on my academic and personal growth

Yash

Abstract

Moon is not merely cherished by scientists but humankind. Our view of the Moon has undergone a significant transformation, most of which started during the Apollo Era. Sample return missions such as Apollo, Luna, and the recent Chang'E 5 have provided an invaluable understanding of the chemical and thermal evolution of the Moon. Although these missions sampled a plethora of lithologies on the Moon, all of them were brought from regions with unusually high abundances of incompatible elements (such as K, REEs, P) within or adjacent to the Procellarum KREEP Terrane (PKT). Consequently, our understanding of the Moon is somewhat biased due to this restricted sampling. This study focuses on lunar meteorites, which offer access to unexplored regions of the Moon. Using the lunar meteorites, we aim to understand two important processes that have shaped the Moon throughout its geological history, i.e., Volcanism and Meteoritic impacts.

In this thesis work, I first target to understand the magmatic processes that carried the information about the mantle sources and the incipient secondary basaltic crust formation away from the PKT on the Moon. Over the past four decades, the conceptual framework of the lunar magma ocean (LMO) model has served as the dominant paradigm for interpreting all lunar data. The mantle source of mare basalts was suggested to form by variable degrees of mixing of cumulates crystallized from the lunar magma ocean, with melting assisted by mixing of radioactive element-rich layer known as urKREEP. However, some lunar basalts are devoid of these urKREEP signatures. We studied unbrecciated lunar meteorite A-881757, which is free from urKREEP component, along with paired samples Y-793169, MIL 05035, MET 01210 (together as YAMM). These samples, based on their Sr-Nd isotopic characteristics classify into a relatively new basaltic rock type termed as KREEP-free (source) basalts. The applied petrological modelling suggests these older (4.3-3.9 Ga) KREEP-free (source) basalts were generated through low degree partial melting of a shallow pyroxene-rich mantle, distinct from later (3.8-3.3 Ga) KREEP-bearing Apollo mare basalts, suggesting a fundamental change in lunar melting processes. This study provides insights into the early thermo-chemical evolution of the Moon, and highlights

the importance of KREEP-free (source) basalts in understanding the partial melt mechanisms at the lunar interior.

The geological history of the Moon, since its formation, is imprinted on its surface. Lunar brecciated meteorites serve as valuable proxies for investigating the compositional variations across the lunar crust beyond the Procellarum KREEP Terrane (PKT) regions. Thus, this study focuses on examination of three lunar regolith breccia meteorites, Yamato (Y)-981031, Y-983885, and Y-86032, in order to gain insights into the compositional diversity within the lunar primary and secondary crustal components. The mineralogical and petrological examination of these samples suggest their derivation from the regions outside PKT. Furthermore, both basaltic and brecciated meteorites are employed to study the impactor inputs into the lunar crust (\pm mantle) to gauge the interaction of the airless lunar surface with the dynamic solar system environment. The studied meteorites A-881757, Y-981031, Y-983885 and Y-86032 have potentially been launched away from the PKT, and therefore provide new insights into the meteoroid impacts and volcanism that have shaped the previously unexplored lunar surface. Highly siderophile elements (HSEs: Re, Os, Ir, Ru, Pt, and Pd), and Re-Os isotopes are utilized to examine the variation of HSE composition in the lunar crust and mantle from a non-PKT perspective. The Re-Os isotope systematics and HSE abundance in A-881757 yield valuable insights into the abundance of these elements in the KREEP-free (source) lunar mantle, while the brecciated lunar meteorites offer constraints on the HSE abundance at the lunar crust. The inter-elemental HSE ratio of lunar regolith breccia Y-86032 implies late accretion of an ordinary chondrite-type impactor, while Y-981031 and Y-983885 show fractional crystallization and metal segregation within impact melt sheets, resembling the HSE enrichment observed in terrestrial impact settings. Collectively, findings presented in this thesis expand our knowledge to the Moon's geological processes and provide a more comprehensive understanding of its complex evolution history.

Keywords: Moon, Procellarum KREEP Terrane, Lunar Meteorites, Lunar Volcanism, KREEP-free (source) basalts, Lunar Breccia, Lunar mantle, Lunar Crust, Highly siderophile elements, Late Accretion.

Contents

Acknowledgments	ix
Abstract	xiii
List of Figures	xix
List of Tables	xxv
Abbreviations	xxvii
Chapter 1 Introduction	1
1.1 Lunar Exploration.....	1
1.1.1 Pre-Apollo Era.....	1
1.1.2 Apollo Era	3
1.1.3 Post Apollo Era	4
1.2 Lunar Formation	6
1.2.1 Theories of lunar formation in Pre-Apollo Era	6
1.2.2 Theories regarding Origin of the Moon	6
1.3 Early state of the Moon	9
1.4 Lunar terranes and associated lithologies	13
1.4.1 Lunar Terranes	14
1.4.2 Lunar lithologies	15
1.5 Objectives of the thesis.....	19
1.6 Thesis organization.....	21
Chapter 2 Analytical Methods	23
2.1 Electron Microscopy.....	23
2.1.1 Fundamental principles	23
2.1.2 Sample Preparation	24
2.1.3 Scanning Electron Microscopy (SEM)	25
2.1.4 Electron Probe Microanalysis (EPMA).....	26
2.2 Mass spectrometry	28
2.2.1 Fundamental principle.....	29

2.2.2	High resolution Inductively coupled Plasma Mass Spectrometer (HR-ICPMS)	32
2.2.3	Thermal Ionization Mass Spectrometer	34
2.3	Measurement Protocols	36
2.3.1	Analytical procedure for bulk major and trace element analysis	36
2.3.2	Analytical procedure for in-situ trace element analysis	37
2.3.3	Analytical procedure for Re-Os isotope and highly siderophile element abundance measurements	38

Chapter 3 Understanding KREEP-free (source) volcanism on the Moon using Lunar basaltic meteorites

3.1	Introduction	47
3.2	Sample Description.....	51
3.3	Methods	52
3.3.1	Scanning electron microscope analysis	52
3.3.2	Electron probe microanalysis	53
3.3.3	Inductively coupled plasma mass spectrometry.....	53
3.3.4	Mantle melting model	55
3.3.5	Construction of P-T path for YAMM basalts.....	57
3.3.6	Estimation of pressure (P) and temperature (T)	58
3.3.7	Estimation of mantle potential temperature	60
3.3.8	Estimation of surface heat flow	61
3.4	Results	62
3.4.1	Petrography and Mineral chemistry of A-881757.....	63
3.4.2	Cooling and shock history of A-881757	74
3.4.3	Petrography and mineral chemistry of other KREEP-free (source) basalts	75
3.4.4	Estimation of parental melt and source composition	78
3.4.5	Parent melt composition of Apollo mare basalts	84
3.4.6	Feasibility of REE modelling and choosing mineral modes of mantle source	86
3.4.7	Reconciliation of estimated pressure (P) and temperature (T) for KREEP-free (source) samples	90
3.4.8	Formation P-T of Apollo mare basalts	92
3.5	Discussion.....	93
3.5.1	Origin of symplectites and pre-symplectite composition.....	93
3.5.2	Formation conditions of pyroxene sector zoning in A-881757	94

3.5.3	Crystallization history of A-881757 and other YAMM meteorites ...	98
3.5.4	Petrogenetic model for A-881775	101
3.5.5	Mantle potential temperature and surface heat flux	107
3.5.6	A possible melting mechanism for KREEP-free (source) basalts....	109
3.5.7	Conclusions and implications for ancient volcanism on the Moon .	111

Chapter 4 Insights to lunar crustal diversity from lunar regolith breccia meteorites Y-981031, Y-983885 and Y-86032..... 135

4.1	Introduction	135
4.2	Sample Description.....	137
4.3	Methods	139
4.3.1	Petrography	139
4.3.2	In situ mineral composition.....	140
4.3.3	In situ trace element composition.....	140
4.3.4	Bulk major and trace element composition.....	141
4.4	Lunar Origin	142
4.5	Petrography and Mineral Chemistry Results.....	143
4.5.1	Sample Y-981031.....	143
4.5.2	Sample Y-983885.....	151
4.5.3	Sample Y-86032.....	155
4.6	Bulk Composition.....	159
4.7	Identifying Potential Source Regions of Y-981031, Y-983885 and Y-86032 from the lunar surface	162
4.7.1	Evidence from bulk rock chemistry, impact melts, and mare basalts 163	
4.7.2	Evidence from remote sensing datasets	164
4.8	Summary and Conclusion.....	180

Chapter 5 Abundance of Highly Siderophile Elements in the Lunar Mantle and Crust from meteorites 183

5.1	Introduction	183
5.1.1	Lunar Mantle	185
5.1.2	Lunar exterior	191
5.2	Samples.....	193
5.3	Analytical Methods.....	194
5.4	Results	195
5.4.1	Composition of metal grains	196

5.4.2	Rhenium-osmium (Re-Os) isotope systematics and highly siderophile element (HSE) abundances	197
5.5	Discussion.....	201
5.5.1	Origin of metal grains in unbrecciated basalt A-881757 and regolith breccia Y-981031 and Y-983885	201
5.5.2	Post-crystallization disturbances and origin of HSE in YAMM basalts 202	
5.5.3	Osmium isotope and HSE abundance in the KREEP-free (source) mantle 205	
5.5.4	HSE compositions of lunar regolith breccia meteorites and composition of late accreted materials beyond PKT	207
5.5.5	What we learn new about the lunar HSE inventory	214
Chapter 6 Summary and Future Work		217
6.1	Introduction	217
6.2	Understanding KREEP-free (source) volcanism on the Moon using Lunar basaltic meteorites.....	219
6.3	Lunar crustal diversity as observed from the lunar regolith breccia meteorites Y-981031, Y-983885 and Y-86032	220
6.4	Understanding the highly siderophile elements abundance in Lunar mantle and crust from Lunar meteorites	222
6.5	Potential Future Work	223
Bibliography		225
List of Publications		255
Recognition/awards.....		256
Research in news.....		256

List of Figures

Figure 1.1 The first documented map of the Moon by William Gilbert printed in his <i>De mundo nostro sublunari philosophia nova physiologia</i>	2
Figure 1.2 Images of the Moon taken during Pre-Apollo Era.	3
Figure 1.3 Lunar Sample Mission timelines covering Apollo and Post Apollo era missions along with some recent future missions.	5
Figure 1.4 Lunar magma ocean crystallization and formation of primary crust of the Moon.	10
Figure 1.5 An example showing complementary rare earth element (REE) pattern of lunar anorthosites (60025) and mare basalts (12022).	11
Figure 1.6 Thorium map of the Moon highlighting the regions of the PKT (Procellarum KREEP Terrane), Feldspathic highlands Terrane (FHT) and South Pole-Aietkin basin Terrane (SPAT).	13
Figure 1.7 A discriminant plot of Mg# ($Mg/Mg+Fe$) in mafic minerals (olivine and pyroxene) versus An# ($Ca/Ca+Na+K$) in plagioclase for the lunar crustal lithologies.	16
Figure 2.1 The effect of bombardment of accelerated and focused electron beam over the sample. The interaction that are primarily utilized in this study are backscattered electrons, secondary electrons and characteristic X-rays.	24
Figure 2.2 Backscattered electron image (BSE) showing compositional information as a function of the contrast.	25
Figure 2.3 X-ray map of Ca and Mg for Sample Y-981031 highlighting the abundance of elements throughout the section.	28
Figure 2.4 Primary components of a Mass Spectrometer.	29
Figure 2.5 Schematic diagram of ICP torch.	30
Figure 2.6 The trajectory of the ions through the quadrupole is actually very complex the figure shows a simplified schematic.	31
Figure 2.7 Schematic of electron multiplier ion beam detector.	31
Figure 2.8 Schematic of energy filtering in the electrostatic sector. Only ions with energy (V) follows a trajectory through the sector exit slits.	32
Figure 2.9 The trajectories of two ion beams in a 60° magnetic sector, Note that the mass of m_1 is greater than the mass of m_2	34

Figure 2.10 Two filaments in thermal ionization mass spectrometry.....	35
Figure 3.1 Bulk major-element composition comparison among A-881757, YAMM and other lunar basalts..	48
Figure 3.2 Sm-Nd and Rb-Sr source isotopic characteristics of YAMM meteorites and other lunar basalts..	50
Figure 3.3 BSE (left panel) and X-ray composite (right panel) images of studied sections A-881757, 88a (a) and 88b (b) (area ~0.55 cm ²)..	52
Figure 3.4 Source composition deduced from trace element modeling for YAMM and other KREEP-free (source) basalts	56
Figure 3.5 Formation temperature (<i>T</i>), pressure (<i>P</i>) and surface heat flow of KREEP-free (source) basalts compared to other lunar lithologies	59
Figure 3.6 BSE images of A-881757 highlighting pervasive effects of melt vein (a-b)	62
Figure 3.7 Pyroxene and Spinel mineral compositions for A-881757.....	63
Figure 3.8 CI-normalized rare earth element patterns for A-881757 pyroxenes (a), plagioclase (b) and symplectites (c).....	64
Figure 3.9 X-ray (a) and BSE (b-d) images showing pyroxene, plagioclase and late crystallizing phases in A-881757.....	65
Figure 3.10 Electron microprobe transects across sector zoned pyroxenes in A-881757.....	66
Figure 3.11 The minor and trace element variation in sector zoned pyroxenes (a-e) in A-881757 along X-X' transect shown in Figure 3.9a	67
Figure 3.12 Comparison of enrichment of minor, trace along with some major elements in Ca-rich sector relative to Ca-poor sector of sector zoned pyroxenes of A-881757 and Mt. Etna lavas.	68
Figure 3.13 Symplectites with different texture and their compositional relations.	70
Figure 3.14 Fayalite, Fe-augite and silica symplectites in A-881757 showing three different textures.	71
Figure 3.15 Preservation of shock features at various scales in A-881757.	73
Figure 3.16 Measured REE abundance of A-881757 compared with other YAMM , lunar meteorites and selected Apollo mare basalts.	76
Figure 3.17 The calculated degree of melting for YAMM and other KREEP-free (source) rocks compared to Apollo mare basalts using trace element modeling.....	77

Figure 3.18 Calculated $^{87}\text{Rb}/^{86}\text{Sr}$ versus $^{147}\text{Sm}/^{144}\text{Nd}$ for source regions of Apollo mare basalts and meteorites.	79
Figure 3.19 Plot of Mg# of the bulk rock versus Mg# of the olivine and pyroxene in different KREEP-free (source) rocks.	80
Figure 3.20 Plot showing partial melting relation of YAMM meteorites and primitive nature of MIL 05035.	88
Figure 3.21 The site-specific variation of elements along traverse in A-881757 sector zoned pyroxenes (a-d).	95
Figure 3.22 Plot of Al-(2Ti+Cr) for sector zoned pyroxenes along AA' (Figure 3.9a) showing affinity toward Ca-rich and Fe-poor sectors.	96
Figure 3.23 The site-specific variation of elements along traverse in terrestrial sector zoned pyroxenes, in both tholeiitic (a) and alkaline (b) clinopyroxene.	99
Figure 3.24 Crystallization model calculations using the MELTS algorithm.	100
Figure 3.25 Calculated phase diagram of A-881757 with stable phase saturation curves, highlighting equilibrium phase assemblages at different P - T conditions along with modal isopleths.	103
Figure 3.26 Calculated phase diagram of A-881757 with stable phase saturation curves, indicating equilibrium phase assemblages at different P - T conditions along with modal isopleths.	106
Figure 3.27 Al-Ti geobarometer in clinopyroxene of KREEP-free (source) basalts.	107
Figure 4.1 Backscattered electron images of the polished thick sections of Y-981031, Y-983885 and Y-86032.	137
Figure 4.2 Combined Ca-Mg-Fe X-ray images of studied regolith breccia meteorites.	139
Figure 4.3 Fe/Mn ratio in the olivine (a) and pyroxene (b) of studied meteorites confirming their lunar origin.	141
Figure 4.4 Backscattered electron image of sample Y-981031 showing variety of clasts present in the sample.	142
Figure 4.5 Backscattered electron images of clasts and components in Y-981031.	144
Figure 4.6 Pyroxene chemistry from selected clasts in sample Y-981031.	145
Figure 4.7 Compositional evolution trend of pyroxene in Y-981031.	146
Figure 4.8 REE composition of minerals of clast B1.	147

Figure 4.9 Trace elemental abundance in breccia and impact melt clast of Y-981031 measured using broad (55-60 μm) laser beam over the clasts.	149
Figure 4.10 Chondrite normalized REE composition of mineral fragments in Y-981031.....	150
Figure 4.11 Crystalline impact melt clast (IMB), basaltic clasts (BB) and feldspathic clasts (FC) in lunar regolith breccia meteorite Y-983885..	152
Figure 4.12 Compositional variation in pyroxenes basalt within lithic clasts pyroxene and as isolated pyroxenes mineral fragments (yellow circles) in Y983885.	152
Figure 4.13 Trace elemental variation in (a) pyroxene mineral fragments and (b) bulk composition of crystalline impact melt clast IMB_3 of Y-983885 measured using broad beam of $\sim 55 \mu\text{m}$ showing REE rich composition.	153
Figure 4.14 Compositional evolution trend of pyroxenes in Y-983885.	154
Figure 4.15 Lithologies of sample Y-86032 seen under optical camera (left panel) and microscope (right panel).	155
Figure 4.16 Backscattered electron images of Y-86032 marking granulitic breccia (GB1 (left) and GB2 (right)), and lithologies identified in optical images (Dark grey, white, grey and light-grey lithology).	156
Figure 4.17 Compositional variation observed in isolated pyroxene grains (marked as red) of Y-86032.....	157
Figure 4.18 Plot of An# $[(\text{Ca}/\text{Ca}+\text{Na}+\text{K}) \times 100]$ in plagioclase mineral fragments (plotted over axes) and clasts versus Mg# $[\text{Mg}/(\text{Mg}+\text{Fe}) \times 100]$ in olivine and pyroxene mineral fragments (plotted over axes) and clasts of the studied lunar breccias.	158
Figure 4.19 Bulk rock chemistry of the studied rock compared with Lunar samples and meteorites.	159
Figure 4.20 Bulk rare earth element (REE) abundances of lunar meteorite Y981031, Y-983885, Y-86032 and clast B1.	160
Figure 4.21 Sc/Sm versus Eu/Sm measured in the bulk rock and clasts of studied samples compared with Apollo ancient magmatics (High Mg suites and High Alkali suites), Apollo mare basalts, lunar meteorites and Apollo impact melt breccias (IMB, marked as “+”).	161
Figure 4.22 Fe-TiO ₂ -Th filtered possible source locations of the studied samples..	165
Figure 4.23 Identification of lunar regolith with similar composition to the studied meteorites.....	167

Figure 5.1 Highly Siderophile Elements (except monoisotopic Rh and Au) abundance in different planetary bodies	184
Figure 5.2 Comparison of Ir composition of lunar mare lithologies, highland lithologies and breccias.....	185
Figure 5.3 The HSE pattern in lunar pristine rocks..	186
Figure 5.4 MgO (wt.%) versus Os (ng/g) for lunar mare basalts, FAN and MGS rocks shown along with terrestrial lavas.....	187
Figure 5.5 (a) U versus W concentrations in lunar basalts from Apollo 11, 12, 15,17 along with YAMM basalts and other lunar meteorites.....	191
Figure 5.6 Backscattered electron images of metal grains in the studied samples... ..	196
Figure 5.7 The HSE pattern for A-881757 and MIL 05035 compared with previously analyzed Apollo basalts and lunar meteorites.....	197
Figure 5.8 $^{187}\text{Re}/^{188}\text{Os}$ versus $^{187}\text{Os}/^{188}\text{Os}$ for YAMM basalts compared with mare basalts.....	198
Figure 5.9 Carbonaceous Ivuna (CI) normalized highly siderophile (HSE) abundances for studied regolith breccia meteorites.....	199
Figure 5.10 Plots of $^{187}\text{Os}/^{188}\text{Os}$ versus a) Ru/Ir b) Pd/Ir and c) Pt/Ir for studied regolith breccia meteorites,	200
Figure 5.11 Ni/Co ratios in metal grains of the studied samples (marked as colored stars) compared with lunar mare basalts, MGS, impact melt breccias, iron meteorites and chondrites.	201
Figure 5.12 Sulfide fractionation model for YAMM basalts using sulfide-silicate partition coefficient from (Blue) Righter et al. (2005) and (Orange) Mungall and Brenan, (2014).	204
Figure 5.13 Binary mixing between KREEP and pristine lunar crust. 1-10% KREEP is need to recreate the composition observed in the studies rocks.	207
Figure 5.14 Modelled HSE/Ir ratios within an impact melt pool.....	209
Figure 5.15 Bulk HSE/Ir ratios of the studied samples and other lunar impact rocks..	210
Figure 5.16 Modelled HSE/Ir ratios for solid metal-liquid metal fractionation within an impact melt pool.....	212

List of Tables

Table 2.1 The list of elements and their corresponding measuring crystal and standards used in EPMA.	27
Table 2.2 Steps for purification of reagents and observations.	42
Table 3.1 Representative electron microprobe analyses of minerals in A-881757, 88a&b.....	113
Table 3.2 Bulk rock chemistry of A-881757 and other associated lunar rocks.	118
Table 3.3 Representative minor and trace analysis of pyroxenes, plagioclase, symplectites and olivine in A-881757	122
Table 3.4 The mineral REE partition coefficients used in model calculations.	128
Table 3.5 Estimated trace element compositions of the YAMM basalts, Kalahari 009, NWA 032, LAP basalts and Luna 24 ferrobasalts. The assumed source mineralogy for each meteorite and melting model are described in Methods, respectively.	129
Table 3.6 Estimated formation P-T, mantle potential temperature and heat flow for A-881757 and other KREEP-free (source) basalts.	132
Table 3.7 Average modal abundances (Vol.%) of major silicate phases in Asuka-881757 and other YAMM basalts.....	133
Table 3.8 Reconstructed bulk compositions of symplectites in A-881757 (88a & 88b).	134
Table 4.1 Bulk rock chemistry of sample Y-981031, Y-983885, Y-86032 and clast B1.	168
Table 4.2 Quantitative EPMA data for silicate, oxide, and other accessory phases in Y-981031.....	170
Table 4.3 Major element composition of impact melt basalts, basalts and granulite clast in sample Y-983885.....	174
Table 4.4 EPMA composition of minerals in Y-86032	175
Table 4.5 Trace elemental composition of mineral in clast B1.....	176
Table 4.6 Trace elemental composition of minerals and clast (analyzed as broad beam) in Y-983885.	178
Table 4.7 Compositional ranges and textures of representative lithic clasts studied in this thesis.....	179
Table 5.1 Re-Os isotope and highly siderophile element concentration in Y-86032, Y-981031, and Y-983885.....	216

Abbreviations

BSE: Backscatter Electron

BSE: Bulk Silicate Earth

BSM: Bulk Silicate Moon

CRE: Cosmic Ray Exposure

EDS: Energy dispersive X-ray Spectroscopy

EPMA: Electron probe microanalysis

FAN: Ferroan Anorthosite

FHT: Feldspathic Highlands Terrane

HSE: Highly siderophile elements

IMB: Impact melt breccia

ITE: Incompatible trace elements

KREEP: Potassium (K), rare earth elements (REE), and phosphorous (P)

LHB: Late Heavy Bombardment

LMO: Lunar Magma Ocean

MORB: Mid Oceanic Ridge Basalts

NASA: National Aeronautics and Space Administration

PKT: Procellarum KREEP Terrane

PPB: Parts per billion

PPM: Parts per million

PPT: Parts per trillion

REE: Rare earth elements

SCSS: Sulfide concentration and sulfide saturation

SE: Secondary electron

SEM: Secondary electron microscope

SPAT: South-Pole Aietkin Basin Terrane

WDS: Wavelength dispersive Spectrometry

XRF: X-ray fluorescence

Chapter 1

Introduction

Moon is not merely cherished by scientists, but humankind. Every ancient civilisation had a close connection with this celestial body and have utilized it for variety of purposes such as timekeeping, navigation or agriculture. Many cultures have crafted stories and legends around the Moon, relating it with deities, creation myths, and celestial events. The cycle of waxing and waning of the Moon is often associated with themes of birth, growth, transformation, literature, and religious rituals. Lunar exploration has always been a shared endeavour for humanity that goes far beyond the boundaries of nations. It is a common quest for knowledge and discovery. Although, Moon is quite different in external appearance than our home Earth, but both planetary bodies have a shared origin. The airless and lifeless Moon offers an advantage to study the geological processes that have affected both Earth and Moon (other terrestrial planets as well) since their formation, which is otherwise obliterated by complex geological process on Earth such as plate tectonics.

1.1 Lunar Exploration

1.1.1 Pre-Apollo Era

The interest in the Moon or particularly the Earth-Moon system has started before 17th century. Most interestingly, it is widely known that the systematic studies of the lunar surface were paved by Galileo and his telescope. However, it has been argued

recently that some observational programs have dates back to pre-telescopic age (Włodarczyk, 2019). Much of such effort was started by William Gilbert (1544-1603), the queen's physician into his work titled as *De mundo nostro sublunari philosophia nova* (*A new philosophy of our sublunary world*) (Pumfrey, 2011) (**Figure 1.1**). Later, Gresham in his *Astrostrereon* tried to convince that the Moon is built much like Earth and other celestial bodies. The naked eye observations by Gresham and parallel studies by Kepler and Galileo between (1604-1606) suggest Moon to have mountains, valleys

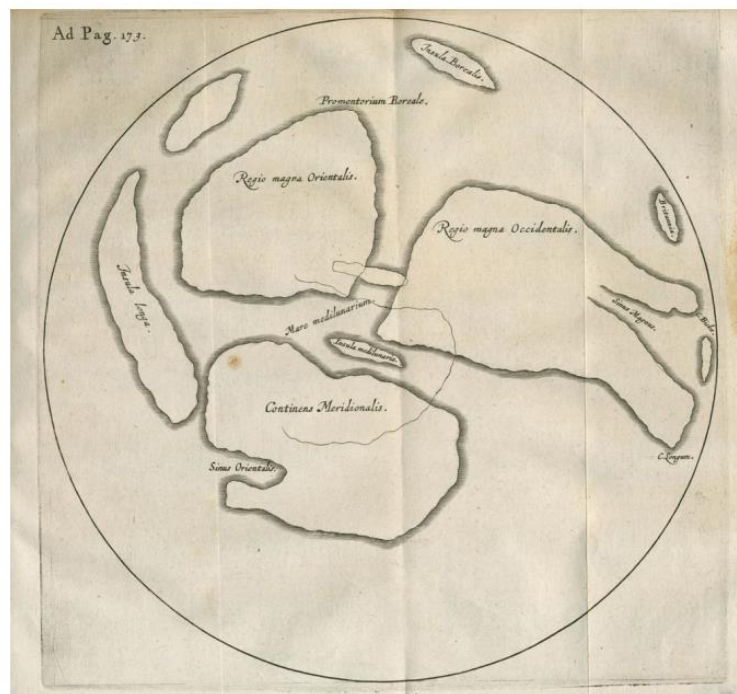


Figure 1.1 The first documented map of the Moon by William Gilbert printed in his *De mundo nostro sublunari philosophia nova physiologia*. Source: Courtesy of the Museum of Planetary Mapping.

and craters. The dark spots were named as “Maria” which in Latin translates to sea. While the highlands were understood as “Mountains” of the Moon. The observation of shadow cast by the Sun on the Moon’s surface made by Galileo to propose the heliocentric model, supporting the fact that the Moon orbits the Earth, which in turn, orbits the Sun. it was Despite having interest since millennia, yet it is only in relatively modern times that we have been able to visit this body. The first touch to the Moon was made by Soviet spacecraft Luna 1 in January, 1959, followed by Luna 3 in same

year photographing the far side of the Moon (**Figure 1.2**). After several failures, Ranger 7 was the first US spacecraft which succeeded in sending back pictures of Mare Nubium in July 1964 (**Figure 1.3**). The much closer look of the Lunar surface came from Luna 9, which was also first soft-landing robotic spacecraft, which was later followed by Surveyor 1. It was realized from these missions that lunar surface to be powdery dirt strewn with a few rocks. Surveyor 1 also collected soil properties including its chemical composition showing similarity to terrestrial basalts. All of these missions collected important information mainly through high resolution images which were later utilized to plan landing sites for Apollo missions to follow.

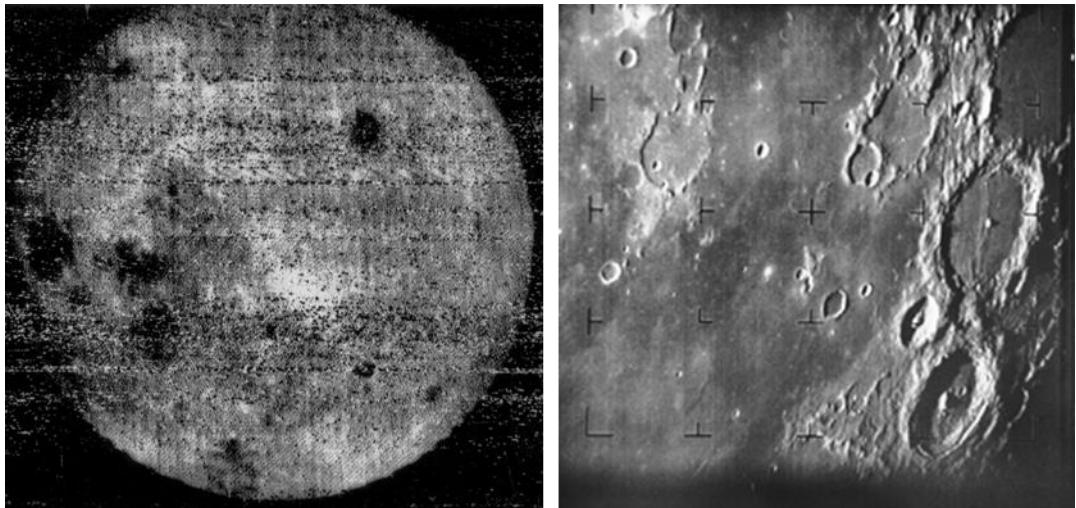


Figure 1.2 Images of the Moon taken during Pre-Apollo Era. **a)** The first image returned by Luna 3 showed the far side of the Moon was very different from the near side, most noticeably in its lack of lunar maria (the dark areas). **b)** The first image of the Moon taken by US Spacecraft Ranger 7. Source: NASA NSSDC Image Catalog.

1.1.2 Apollo Era

Our view of the Moon has undergone significant transformation and most of it has started from the Apollo Era. The Apollo era lasted from 1969 to 1972, which had six manned sample return missions to the Moon. Each Apollo mission (11, 12, 14, 16 and 17) landed on the near side of the Moon and brought back ~382 kg of samples constituting rocks, soils and core samples (NASA, 2016). The Soviet Luna robotic

missions, Luna 16, Luna 20 and Luna 24, between 1970 and 1976, brought ~0.3 Kg of lunar soils back to Earth (NASA, 2005). These samples have provided invaluable understanding of Lunar formation and evolution. These missions also confirmed the absence of significant atmosphere on the Moon. The absence of atmosphere on the Moon exposes its surface to solar radiation and micrometeorite bombardments causing charging of dust. The dust charging also affected the equipment onboard the Apollo missions (NASA, 2005). The surface of the Moon is understood to be dominated by two rock types, basalt and anorthosite. It was realized that the surface of the Moon was blanketed with lunar regolith, consisting of fragmented rocks, soils and fine dust of thickness ranging from few meters in the Mare regions to few tens of meters in highland regions. The missions also deployed seismometers on the lunar surface which later recorded moonquakes, suggesting the presence of tectonic activity. Laboratory sample analysis of the returned Apollo samples led to conclusions such as (i) the Moon is bone dry (Hartmann et al., 1986), (ii) the presence of anorthosite suggestive of the fact that the Moon started as a molten ball (Lunar Magma Ocean) (Smith et al., 1970; Wood et al., 1970), (iii) lunar surface holds record of billion years of solar system evolution and therefore special among all the planetary bodies.

1.1.3 Post Apollo Era

The Luna 24 was last mission of the Space race between Soviet Union and USA. This was followed by hiatus of lunar missions until Japan sent a Lunar Orbiter Hiten (Muses-A) in 1990. There were two important missions by USA in 1990s, the Clementine (1994) and the Lunar Prospector (1998) which provided global chemical and mineralogical variations maps of the Lunar surface. In the next decade, several other countries joined the space race like Europe SMART-1 (2003), China Chang'E 1 (2007) and India Chandrayaan-I (2008). All these missions provide important results, some of them revolutionized our standing of the Moon. Japan in 2007 launched its second mission Kaguya to the Moon and this was followed by Lunar Crater Observation and Sensing Satellite (LCROSS) mission by USA which also touches the Moon after

1976 via an impact probe. The next decade of the 21st century saw more missions towards lunar exploration. It started with China’s Chang’E 2 mission and later two important missions, the Gravity Recovery and Interior Laboratory (GRAIL) in 2011, and the Lunar Atmosphere and Dust Environment Explorer (LADEE) in 2013 were launched by USA. GRAIL mission provided lunar gravity maps and LADEE studied the exosphere and lunar dust. China’s mission Chang’E 3 was the launched in 2013 which landed a rover on the Moon to study the surface properties (Crawford and Joy, 2014). This was first rover landed in 40 years, since Luna 21. Chang’E 4 mission landed another rover in 2018 and it was the first landing on the farside of the Moon. Chandrayaan II mission which included a Lunar orbiter, lander and rover launched in 2019. Although just before the landing, contact was lost with the lander and it crash-landed. However, the orbiter is still working and providing excellent science results (Basu, 2019). China with its Chang’E 5 was the first sample return mission of 21st century and the mission brought back 1.731 kg of sample from Mons Rumker (Xu et al., 2021).

The several missions to the Moon are in planning and deploying stages. With Chandrayaan III about to launch and NASA Artemis is going back to the Moon in its Artemis 3, there is so much excitement and potential in our coming future (Figure 1.3; Srivastava and Basu Sarbadhikari, 2020).

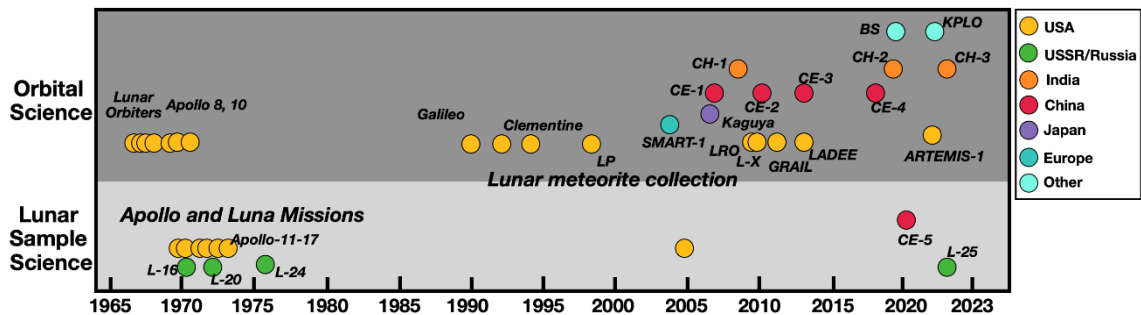


Figure 1.3 Lunar Sample Mission timelines covering Apollo and Post Apollo era missions along with some recent future missions.

1.2 Lunar Formation

1.2.1 Theories of lunar formation in Pre-Apollo Era

The theories regarding the lunar formation in the Pre-Apollo era were largely speculative. The first documented attempt to explain the Moon's by Descartes in his *Le Monde*, published in 1644. It describes the universe where the Solar System bodies formed with each independent body producing vortices and trailing objects of its own and in this grander scheme of the Universe, the Moon was formed as an object within the Earth's vortices. The next major hypothesis of the Lunar formation was proposed by George Darwin, son of Charles Darwin. In series of papers written in 1879, he describes the formation of the Moon as "fission" of the Moon from a rapidly spinning Earth (Houston, 2022). It was not until the 1950's that interest in formation of the Moon began. In Harold Urey's *World System*, written in 1952. He proposed that the formation of the Solar system was started as a Presolar interstellar dust cloud. The Moon, and other planets, were the "survivors" of the fractionation and collisional process. The scientific understanding of the Harold Urey and his interesting in lunar exploration was instrumental in the early years of lunar exploration by NASA. Lunar Science changed significantly after the advent of space missions to the Moon.

1.2.2 Theories regarding Origin of the Moon

The theory explaining the scenario of the lunar formation is required to explain the Moon's physical, dynamical, chemical and internal thermal states (Ahrens, 2020). Any (successful) scenario to model the Moon's origins must satisfy (Barr, 2016) (i) a planet of roughly Earth's mass $M_E = 5.98 \times 10^{24}$ kg, and a Moon of Mass $M_L = 7.3 \times 10^{22}$ g; (ii) an angular momentum of $L_{EM} = 3.5 \times 10^{34}$ kg m² s⁻¹ within the system; (iii) a Moon with ~8% iron (by mass); (iv) stable isotope ratios similar to the terrestrial mantle, including a degree of volatile depletion; and (v) a magma ocean initially 200–300 km thick. Of note is that the Moon is anomalously large relative to the size of the

Earth and contains the bulk of the total angular momentum of the system (MacDonald, 1966).

Four major theories have come forward and out of all, the Giant Impact Theory has stood the test of time. Before going into the Giant Impact Theory let us look into other three alternative hypotheses. Three alternative lunar formation scenarios were i) Capture ii) Fission and iii) Co-accretion.

Capture hypotheses was proposed in 1952 by Harold Urey and later intricacies were added by Mitler (1975). This hypothesis suggest that the Moon was captured by the Earth and circularized in a stable orbit (Urey and Korff, 1952; Mitler, 1975). Asphaug, (2014) states the favorability of Earth decelerating a planetoid, to the point of capturing of (partial or complete) body into stable orbit. Opik (1972) proposed that proto-Moon approached the Earth in a parabolic orbit, if this body passes the Earth with a perigee within a Roche distance, then it would have broken to the point where the inner half would be captured rejecting the other portions. The captured pieces would then revolve around in a highly eccentric orbit which get circularized by subsequent collisions. Lastly mild collisions would eventually make the pieces coalesce (Mitler, 1975; Ahrens, 2020). This mechanism does not require any disruptive process and any special configuration of Earth-*proto-Moon* or loss of angular momentum. Capture type mechanism as noted by Mitler, (1975) can explain the extensive cratering on the Moon, Similar ages of Earth and Moon. This hypothesis however, struggles to explain the similarities in isotopic compositions between the Moon and Earth. It also requires highly specific conditions for successful capture, making it less likely than other hypotheses.

Fission hypothesis was first proposed in Pre-Apollo era by Darwin in 1879. This theory suggests that the Moon was once a part of the Earth and separated from it due to centrifugal forces caused by Earth's rapid rotation. According to this hypothesis, the early Earth was spinning so rapidly that a portion of its mantle and crust broke away and formed the Moon. Čuk and Stewart, (2012) proposed a variant of this theory where first spin-up of Earth cause disruption and fission of mantle is triggered by smaller energetic Theia-type impactor planetoids and finally, orbital evolution of the Earth-

Moon system loses half of its angular momentum to reach present day configuration. The positives of this theory are to explain the similar direction of the Moon's rotation as the Earth, circular orbit of the Moon around Earth, settling of core can predict the observed specific gravity of the Moon (Wise, 1963). It also explains the fundamental difference in the near versus far side of the Moon where far side of the Moon contains lighter primitive Earth materials and nearside would have heavier mantle constituents. However, the Fission Hypothesis faces challenges in explaining the Moon's angular momentum, its distinct isotopic compositions, and the lack of a significant iron core (Asphaug, 2014).

Co-accretion hypothesis suggest the Earth and the Moon co-accreted as binary pairs. and this idea was refined by Morishima and Watanabe, (2001) in context of the waning solar nebula. Morishima and Watanabe (2001) proposed two scenarios, first where the Moon starts as a small embryo and grew in a swarm of planetesimals with low velocity dispersion and the angular momentum was essentially supplied to planetary spinning. The second scenario describes the Moon formed by a giant impact occurring during Earth's accretion which supplied enough angular momentum as a large as the present Earth-Moon system. The combined scenario is the basis of present and the most favored Giant-Impact theory. Co-accretion hypothesis is not favored on the ground that it requires Earth and Moon to grow together in a solar nebula. The age of the Moon considering scenario should be same as the age of solar system, which is not observed. It also faces challenges in explaining the Moon's angular momentum, if not associated with a giant impact.

Giant Impact theory is currently the leading theory for the origin of the Moon (Hartmann and Davis, 1975; Cameron and Ward, 1976; Wood, 1986). This involves a collision between proto-Earth and Mars sized body during waning stages of planetary accretion (Canup and Asphaug, 2001; Canup, 2004). According to Canup (2004), in few hundred to thousand years after the fateful impact, the material within the disk and silicate vapor atmosphere condenses. Some of the post impact material that spreads beyond the Earth's Roche limit, where gravitational tidal forces are small enough to allow accretion of the Moon (Ida et al., 1997; Kokubo et al., 2000; Asphaug, 2014;

Barr, 2016). The Mars size object is named as “Theia”. The lunar petrological, geological and results from the remote sensing mission indicate a regional scale melting of the Moon (Shearer and Borg, 2006; Shearer et al., 2006). The giant impact model suggests the collision has an impact angle of $\sim 45^\circ$ in a captured orbit and it swings by a second time for a high-angular momentum merger (Asphaug, 2014). The large-scale collision would deliver the enthalpy for global melting by accretion and shock. However, the details of the collisions and the environment just after it is poorly constrained. Some recent workers have argued the possibility of two energetic impacts to form the Moon (Rufu et al., 2017). The giant impact model could also explain the isotopic similarities in several ways i) the Moon is largely made of terrestrial mantle materials; ii) the giant collision caused the isotopic equilibration between two bodies or iii) the Earth and the impactor (Theia) formed in isotopically similar reservoirs. All the numerical simulation till now, suggest the Moon must have formed largely from the impactor.

According to Asphaug, (2014), the final and the standard model of the giant impact is, to some extent a variant of Capture, Fission, and Co-accretion. It is “Capture” because Moon forms predominantly from the Theia. It is also “Fission”, except that it is the impactor which is fissioned by grazing and merging collision to the Earth. There is “Co-accretion”, if Theia derives from the same isotopic reservoir as Earth. All the recent models of giant impact are a response to isotopic crisis and there are several combinations of potentially viable scenarios. As new data and evidence emerge, our understanding may evolve, potentially leading to refinements or even a shift in the prevailing explanation of the Moon's origin. Ongoing missions, such as NASA's Artemis program, aim to gather more data and samples from the Moon, which will contribute to further refining our understanding of its formation.

1.3 Early state of the Moon

It is the results from the returned lunar samples that models of Moon formation could be developed. The samples from the Apollo 11 missions led to belief that the

Moon might have had a large scale melting during its formation (Smith et al., 1970; Wood et al., 1970). This global melting of the Moon might have resulted from the giant impact (e.g., Hartmann and Davis, 1975; Cameron and Ward, 1976; Pritchard and Stevenson, 2000; Canup and Asphaug, 2001; Canup, 2004, 2012; Ćuk and Stewart, 2012). The Moon formed from the resulting disk of debris consisting of molten and vaporized silicate material leading to a body in partially or completely molten state. This molten stage, also referred as the Lunar Magma Ocean (LMO) stage or “magmasphere” {Citation}.

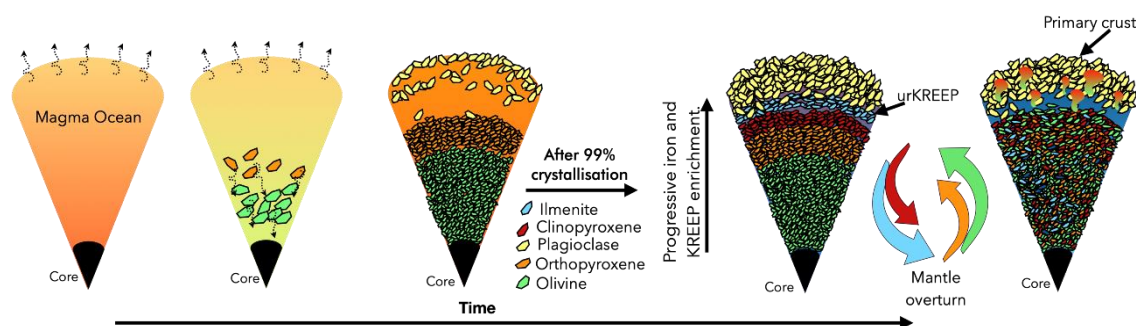


Figure 1.4 Lunar magma ocean crystallization and formation of primary crust of the Moon. Modified after Gross and Joy, (2016) and Borg and Carlson, (2023).

LMO model was proposed by two groups from Harvard and Chicago, independently. Both, Wood et al., (1970) and Smith et al., (1970) recognized that a concentration mechanism was required to accumulate plagioclase rich anorthosite in the lunar crust. Both the group proposed a common mechanism suggesting that the anorthositic crust on the Moon is the result of fractionation and subsequent flotation of anorthosite on a denser Fe-rich magma layer, which might have covered the entire Moon (**Figure 1.4**). The LMO crystallization model is based upon variety of geochemical evidences. The first strong evidence of the LMO is widespread presence of anorthosites and antiquity of the lunar crustal rocks such as ferroan anorthosites (4.29-4.57 Ga; Carlson and Lugmair, 1981; Shih et al., 1993; Alibert et al., 1994; Borg et al., 1999, 2011, 2015; Norman et al., 2003; Carlson et al., 2014; Boyet et al., 2015). The next line of evidence comes from the complimentary geochemistry of crust and mantle (**Figure 1.5**). The striking expression is observed in the REE profiles of the lunar rock suites, ferroan anorthosites have a light REE-enriched profile with pronounced positive Eu-anomaly while the mare basalts typically have light REE

depleted and ubiquitously negative Eu anomalies (Papike et al., 1998; Elardo, 2016). The third strong line of evidence of the global magma ocean comes from the existence of KREEP lithologies. The KREEP was first identified in Apollo 12 samples by Meyer and Hubbard, (1970). The mere existence of KREEP and its broad distribution on the lunar nearside offer strong support to lunar magma ocean hypothesis (Jolliff et al., 2000).

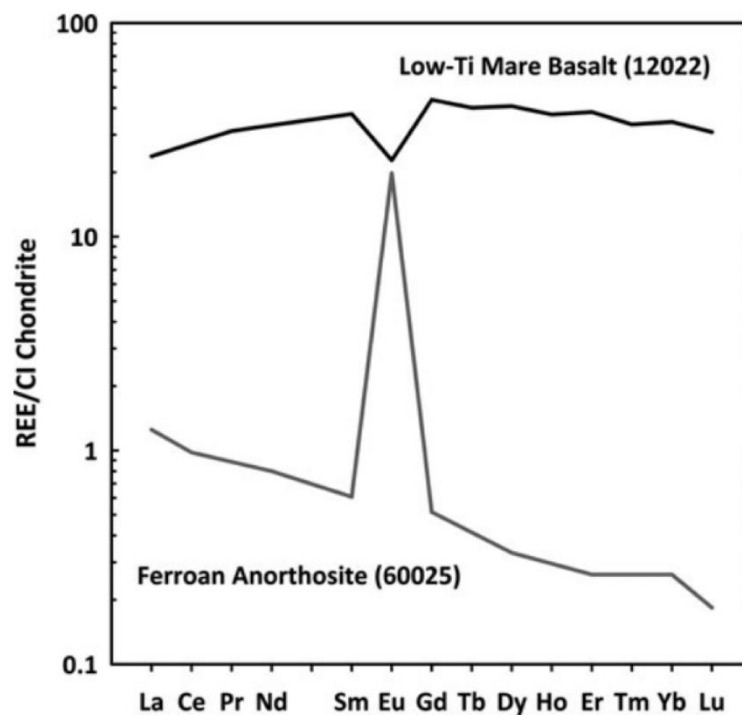


Figure 1.5 An example showing complementary rare earth element (REE) pattern of lunar anorthosites (60025) and mare basalts (12022). cf. Elardo, (2016) and references therein.

LMO model suggest that the composition of the Moon (or Bulk Silicate Moon) to either be earth like and refractory element enriched (e.g., Morgan et al., 1978; Taylor, 1982; Lognonné et al., 2003; Taylor et al., 2006) or similar to bulk composition of terrestrial upper mantle with volatile element depletion (e.g., Ringwood et al., 1987; Jones and Delano, 1989; O'Neill, 1991; Warren et al., 2005; Longhi, 2006; Taylor and Wieczorek, 2014). The cooling of this magma ocean resulted in geochemical differentiation of the Moon and separation of anorthositic flotation crust (e.g., Smith et al., 1970; Wood et al., 1970; Taylor and Jakes, 1974; Warren and Wasson, 1979; Snyder

et al., 1992; Shearer and Papike, 1999; Shearer et al., 2006; Elardo et al., 2011; Elkins-Tanton et al., 2011; Rapp and Draper, 2018; Johnson et al., 2021). Numerous models of evolution and crystallization of the LMO has been attempted to explain various geochemical, geophysical and geological observations of the Moon. During the LMO crystallization, the early stages were dominated by Mg-rich olivine (Taylor and Jakes, 1974; Taylor, 1982; Snyder et al., 1992; Elardo et al., 2011; Johnson et al., 2021), which is predicted from a mantle of peridotitic composition. After nearly ~40-50% crystallization of the LMO, initially low-Ca pyroxene and later high-Ca pyroxenes became stable in the crystallization sequence. These olivine-pyroxene rich cumulates are thought to be the source regions of the mare basalts and picritic glasses (e.g., Longhi, 1992; Shearer and Papike, 1999; Hess, 2000; Shearer et al., 2006). Plagioclase becomes stable at ~70-80% of LMO solidification. As the plagioclase crystals are lower in density when compared to the Fe-rich LMO liquid, they became buoyant and floated to form the lunar crust (e.g., Smith et al., 1970; Wood et al., 1970; Taylor and Jakes, 1974; Taylor, 1982; Warren, 1985). As the LMO reaches ~99% crystallization, the residual liquid crystallized Fe-Ti rich minerals and became highly enriched in geochemically incompatible elements such as potassium (K), the rare earth elements (REE), and phosphorous (P), among other incompatible elements such as thorium. This residual layer has been termed as urKREEP (e.g., Warren and Wasson, 1979; Warren, 1985, 1989; Shearer et al., 2006). This urKREEP layer and Fe-Ti-rich layer reside below the plagioclase rich crust and above Mg-rich mafic cumulates. This ilmenite and KREEP rich layer being denser than the underlying layer created a gravitational instability (Solomon and Longhi, 1977; Elkins-Tanton et al., 2011). This instability is believed to cause overturn of the lunar mantle where Fe-Ti and KREEP rich layer sank down and Mg-rich olivine and pyroxene rich cumulates rose. This overturn hybridized the lunar mantle chemistry and gave rise to various lunar rock types as seen in the analyzed samples. It is also suggested that this overturn might also be responsible for lunar magmatism, generation of magnesian and alkali suite rocks (Shearer and Papike, 2005; Elardo et al., 2011; Shearer et al., 2015; Borg and Carlson, 2023).

Some of the details regarding the LMO model such as the extent and depth of the LMO, the global or local nature of mantle overturn still remains to be understood and

requires further scrutiny. Additionally, though the LMO explains many of the observed characteristics of the Moon quite well but still it fails to explain some observed facts such as compositional asymmetry of the lunar near side and far side. Answers to such questions will require more and more sample analysis and the resulted datasets to verify and test the model and constraints key traits like timing, duration and scale of the LMO.

1.4 Lunar terranes and associated lithologies

The lunar surface has visible differences in the composition which can be seen through our naked eye. The dark terranes or mare regions are formed by the basaltic volcanic rocks including lava flows and pyroclastic deposits. The more reflective (seen as bright white) lunar highlands are mainly formed by anorthositic rocks and

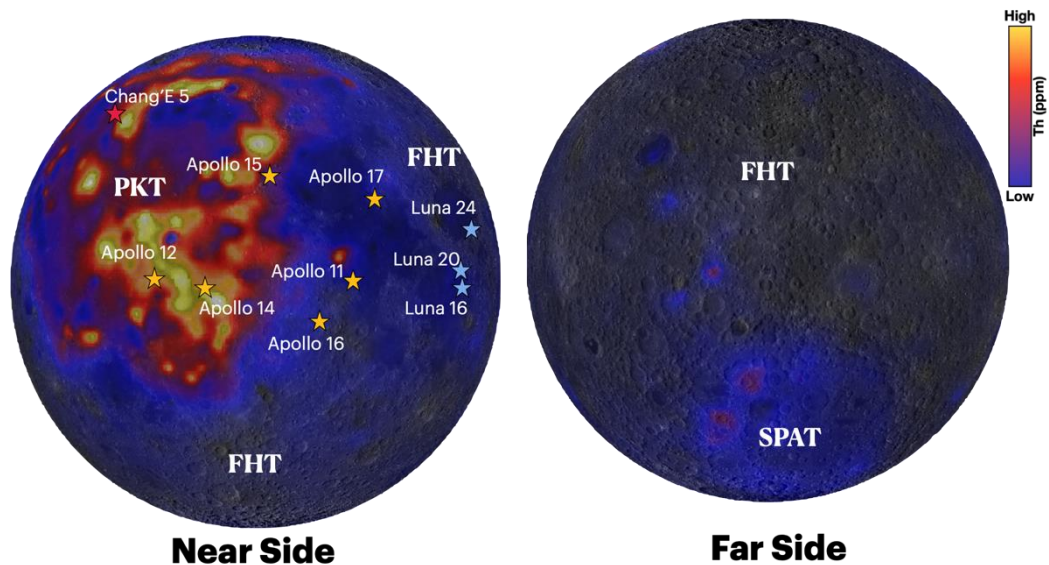


Figure 1.6 Thorium map of the Moon highlighting the regions of the PKT (Procellarum KREEP Terrane), Feldspathic highlands Terrane (FHT) and South Pole-Aietkin basin Terrane (SPAT). Modified after Jolliff et al., (2000).

plagioclase-rich magnesian suite rocks including norites, troctolites, Mg-suite dunites and some newly discovered rare rocks such as Mg-spinel anorthosites. Alkali suite rocks and KREEP basalts are uncommon and found among the Apollo 12, 14, 15 and 17 samples. Apart for detailed compositional analyses through samples, the global geochemical variation on the lunar surface has been observed from gamma-ray spectrometers onboard USA's Lunar Prospector and Japanese Kaguya mission.

1.4.1 Lunar Terranes

Using the gamma-ray datasets, Jolliff et al. (2000) divided the lunar surface into three geochemically distinct terranes. These terranes are the Procellarum KREEP Terrane (PKT), the Feldspathic Highlands Terrane (FHT) and South-Pole Aitken Terrane (SPAT) (**Figure 1.6**; e.g., Haskin et al., 2000; Wieczorek and Phillips, 2000). The largest and the most extensive terrane is Feldspathic Highland Terranes which covers ~60-65% of the lunar surface and is composed primarily of ancient anorthositic rocks called as ferroan anorthosite suite. This terrane can also be characterized by low crustal Th abundance (1-3 ppm). Most of the basaltic flows in this terrane are of ~3.8-3.2 Ga in age and have low to moderate TiO₂ (<6 wt. %) (Shearer et al., 2006). The PKT regions covering ~10-16% of the lunar surface and is characterized by high concentration of Th (4-13 ppm). This terrane has largely composed of mare basalts having ages from ~4.2 – 1.0 Ga in the Oceanus Procellarum and Mare Imbrium regions. The high abundance of the heat-producing elements within this region are likely the cause of the extensive magmatic productivity (Shearer and Borg, 2006). South-Pole Aietkin terrane is marked on the basis of high average FeO concentration relative to typical non-mare lunar crust (7-14 wt. %; Lucey et al., 1998). The SPAT is dominated by impact melt rocks consisting of amalgamation of mantle olivine-pyroxenes with highland anorthosites. The Th abundance in this terrane have elevated concentration ranging up to 10 ppm in some locations but have overall sparse distribution. With an approximate diameter of 2600km, it is the largest impact basin in the Solar System (Spudis et al., 1994). This SPA basin forming impact event is believed to occur rarely in the lunar history and undoubtedly had a great affect in lunar thermo-chemical evolution. Recent studies have associated the SPA basin impact to the primary reason for the lunar nearside - farside asymmetry (Zhang et al., 2022; Jones et al., 2022).

1.4.2 Lunar lithologies

The three terranes described in previous subsection composed of different proportions lunar lithologies which can be broadly divided into three groups: highland lithologies, mare volcanics and impact related lithologies. Among Highland rocks are the pristine lunar rocks including ferroan anorthosite suite (FAS), magnesian suit (Mg-suite), alkali (Warren, 1993). Mare Volcanics contains rocks that are products of mare volcanism and are typically classed as mare basalts and pyroclastic glasses. With continuous meteoritic impacts, the preexisting lithologies get modified to form rocks (breccias, impact melts rocks) and soils (lunar regolith).

1.4.2.1 Highland rocks: primary crust building

The highland rocks account for more than 90% volume of the lunar crust can be categorized into FAS, Mg-suites, and Alkali suites (Head, 1976). These rocks are all ancient (>3.8 Ga) and therefore have been largely modified by meteoritic bombardment. The samples which are uncontaminated or least contaminated by the impactors are termed as pristine samples. The determination degree of pristineness of the samples is key to differentiate and understand the geochemical difference that are caused by internal and external processes. The signatures such as presence of impact melts, increased siderophile elements, phase homogeneity and reset in radiometric ages can be used to assess the degree of pristineness.

Ferroan anorthosite suites contains rocks with very high modal abundance of Ca-plagioclase (anorthite) with minor amount of mafic minerals such as olivine, pyroxenes (e.g., Wieczorek et al., 2006). The FAN suite has age range from 4.29-4.57 Ga and these lithologies are thought to be result of large-scale plagioclase separation from the LMO (Shearer et al., 2006; Borg and Carlson, 2023). Magnesian suites rocks, on the other hand, are lithologies that are grouped together due to their overall high Mg# in olivine and pyroxene (**Figure 1.7**). This suite contains coarse grained plutonic rocks with varying modal mineralogy ranging from dunites (>90 vol. % olivine), troctolites (predominantly olivine and plagioclase), norites and

gabbronorites (predominantly pyroxene and plagioclase), and spinel-bearing troctolites (Shearer et al., 2015). Both FAS and Mg suite is believed to represent the first stage of lunar crust building as both FAS and Mg suite show ancient ages (Borg and Carlson, 2023). Several models have been attempted to explain the petrogenesis of Mg suite rocks. An unusual trait of the Mg suite rocks is bulk composition with the high Mg# (indicating a primitive origin from mafic cumulate) but with high concentration of REEs (implying a more evolved origin). Despite several available models, a further scrutiny is required to completely understand the Mg-suite formation. Alkali suites, on the other hand, have lower Mg# than Mg-suite and lesser anorthite content that FAS (**Figure 1.7**). These suites contain lithologies such as granites, quartz monzodiorites, alkali anorthosites, felsite and alkali gabbronorites which are enriched in alkali elements (e.g., Na, K) (Taylor, 2009).

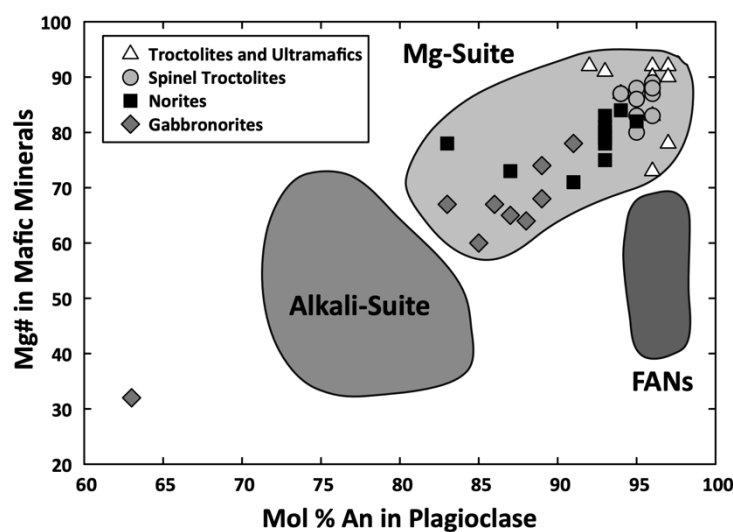


Figure 1.7 A discriminant plot of Mg# ($Mg/Mg+Fe$) in mafic minerals (olivine and pyroxene) versus An# ($Ca/Ca+Na+K$) in plagioclase for the lunar crustal lithologies. cf. Shearer et al. (2015).

1.4.2.2 Mare Volcanics: secondary crust building

The second stage of crustal building on the Moon occurred in the form of basaltic volcanism mainly concentrated in the PKT regions. These basaltic regions cover ~17% of the Moon surface. The volcanism on the Moon seems to start ~4.3 Ga,

peaked in 3.8-3.2 Ga and lasted at least till ~1 Ga. The mare volcanics consists of rock types such as mare basalts, KREEP-basalts and pyroclastic deposits (Head, 1976; Head and Wilson, 1992).

Mare basalts have flooded ancient impact basins and dominates the lunar nearside. They exhibit wide compositional array usually classified on the basis of their bulk TiO_2 (high Ti >6wt.%; low Ti 1-6 wt. %; very low-Ti <1 wt.%), Al_2O_3 (high Al >11 wt.%; low Al <11wt.% Al) and K_2O (high K > 0.2 wt.% and low K < 0.2 wt.%) contents (Neal and Taylor, 1992). The mare basalts are sub-classified based on their modal proportion of minerals such as olivine, pyroxene, plagioclase and ilmenite. They also contain minor phases such as apatite, baddeleyite, tranquillityite, merrillite, K-feldspar, ulvöspinel, armalcolite and residual glass. Mare basalts are sourced from the lunar mantle and the compositional diversity observed is often because of the heterogeneity in their source regions (Grove and Krawczynski, 2009). The experimental studies of the mare basalts suggest their derivation via low degree (< 10%) partial melting of olivine rich lunar mantle at a depth ~250 km below the lunar surface. The duration of volcanism, its source composition and mechanism of mare basalt generation has been a focus of research over the past decades. Pyroclastic deposits on the surface of moon are the result of effusive fire fountain eruptions that later formed large deposits of glass beads on the lunar surface. These glass bead comes in array of colors with color corresponding to their TiO_2 contents, which ranges from green (VLT glasses), to yellow, orange and red with increasing TiO_2 contents and eventually black (Grove and Krawczynski, 2009). These samples are ultramafic with high MgO (>35 wt. %) and are suggested to have been equilibrated at depth >400 km and temperature ~1450 °C (Shirley and Wasson, 1981; Delano, 1986; Longhi, 1992, 1993; Elkins-Tanton et al., 2002). The compositional diversity in these glasses also highlights the heterogeneity in the lunar mantle.

KREEP basalts are volcanic rocks enriched in incompatible trace elements and believed to have close relation to urKREEP layer of the lunar magma ocean. There are very few such rocks in our sample collection. Apollo 15 KREEP basalts show ages from 3.82 to 3.86 Ga (Shearer and Papike, 1999) and thought to have genetic

relationship with the alkali suite which also extends up to an age of 4.39 Ga. Warren (1988) proposed that extreme fractional crystallization of the source with mixture of Mg-suite parental melts and urKREEP can also produce KREEP basalts. The petrogenesis of the KREEP basalt are however, still debated.

1.4.2.3 Impact related lithologies: modification of lunar crust

The impact related lithologies are result of impact modification of the lunar surface over time. Impacts of varied sizes and composition have churned the lunar surface to create lunar regolith, impact melts and breccias. The impact related lithologies are mixtures of various endogenous lithologies and sometimes contains other impact related lithologies (like impact melt breccia clast in brecciated rocks). The top few hundred meters to kilometers of the lunar surface is covered in lunar soils or regolith, created through continuous rain of micrometeorites that progressively churn the lunar surface into fine powders. This regolith can either have composition similar to bedrock or could also contains material that are transported by the larger impacts in secondary crater rays (Pieters et al., 1985; Wentworth et al., 1994).

Besides the fine regolith, another product of impact cratering are impact breccias. They contain lithic clasts of various endogenous lithologies and mineral fragments all welded together in fine grained matrix as a result of heat from impact events. They are compositionally diverse across whole Moon and usually thought to represent the average crustal composition of their source. The clasts and mineral fragments within can be essentially used to understand the lunar crustal diversity. Several new lithologies have been identified in lunar regolith breccias and soil fragments (Zeng et al., 2018, 2023). Impact melt rocks are another suite of lithologies that are produced by energetic impact events (Melosh, 1989). Larger impact produces large amount of impact melts and many a times, blend very small amount of target material. The abundance of the highly siderophile elements in the impact melt rocks and breccias can be used to trace the nature and composition of impactor (Day et al.,

2007; Walker, 2009; Fischer-Gödde and Becker, 2012; Gleißner and Becker, 2017, 2019; McIntosh et al., 2020).

1.5 Objectives of the thesis

Over the past 60 years, extensive research has been carried out to decipher the history of the Moon. Despite numerous discoveries, evolving theories, and successive generations of scientists dedicating their careers to lunar studies, numerous queries persist regarding lunar volcanism and impact bombardment. This thesis aims to address a some of those unresolved questions.

Due to the fact that a significant portion of our knowledge regarding the Moon is derived from samples gathered at or adjacent to the Procellarum KREEP Terrane (PKT), this limits us to have a comprehensive knowledge of the Moon (Shearer and Borg, 2006). Therefore, returning samples from unexplored regions, such as the South Pole Aitken Terrane (SPAT) and Feldspathic Highland Terrane (FHT) of the Moon, are amongst the top priorities for future missions. This thesis investigates the geochemical evolution of the Moon using samples not limited to the Procellarum KREEP terrane (PKT). Here, I am using lunar meteorites as proxies for understanding regions of the Moon that have not been sampled by sample return missions. Using samples from non-PKT regions, this work aims to understand two important processes that have shaped the Moon, i.e., Volcanism and Meteoritic impacts.

Understanding the formation of different varieties of lunar basalts is key to constrain the models of early thermo-chemical evolution of the Moon. Some lunar basalts especially in our sample collection are suggested to be unrelated to the KREEP reservoir. Lunar meteorite samples such as NWA 032, LAP basalts as well as recently returned basaltic samples from Chang'E 5 show absence of KREEP in their source (Borg et al., 2009; Elardo et al., 2014; Tian et al., 2021). An important consequence of the lunar magma ocean is the lunar mantle overturn which enables the mixing of denser urKREEP layer with less dense mafic cumulates. It is understood that the mixing of radioactive element rich KREEP layer with the source of the lunar basalts provide the

heat essential for melting the mantle source lithologies and generation of mare basalts. Therefore, understanding the petrogenesis of KREEP-free (source) basalts, which have no to minimal KREEP in their source, is important to constrain the LMO models and test the traditional mechanism of mare basalt generation.

Furthermore, despite several types of lithologies discussed previously, lunar surface especially outside PKT regions contains numerous unidentified lithologies. The PKT region encompassing only 16% of the Moon and detailed investigation of lunar soils and breccia outside the PKT terrane might reveal lithologies that are previously unexplored or underrepresented. Lunar regolith breccia meteorites can offer us insight into mineralogy and geochemistry of the unexplored regions. Discovering new lunar lithologies or finding an underrepresented lithology will help us in constraining the thermal and geochemical evolution of the Moon.

All the samples on the Moon, including those that are part of this study are once part of lunar surface which is exposed to continuously impact bombardments. Samples such as impact melt rock records such interactions and therefore may provide information related to nature and composition of impactors. Several recent studies have utilized the highly siderophile elements to constrain the nature and composition of impactors. These elements are an excellent tracer of core-mantle differentiation and subsequent late accretion. Most of our present understanding of the highly siderophile elements is biased by the samples from the PKT (Apollo 12, 14, 15, Chang'E 5) and its adjacent (Apollo 11, 16, 17, Luna 16, 20 and 24) regions, having a relatively high abundance of incompatible trace elements. It is therefore important to better constrain the abundance of highly siderophile elements of the lunar mantle and crust using the samples from the non-PKT regions. Such constraints on the HSE abundance are crucial in understanding the lunar mantle differentiation, and examine the nature and composition of late accreting materials.

The primary goals of this thesis are described below

1. To understand the petrogenesis of KREEP-free (source) basalts, their magmatic settings and formation pressure-temperature (P-T) conditions.

2. To deduce the mantle source composition of KREEP-free (source) basalts and Apollo mare basalt parental melts and discuss their possible generation mechanism in the lunar settings.
3. To study lithological diversity in the lunar crust and discuss the compositional variation between them. Later use compositional information of individual clasts to understand their formation in the context of LMO.
4. To better constrain the concentration of HSE in the Bulk Silicate Moon and infer the nature and composition of impactors (if any) from their abundance and Re-Os isotopic composition.

1.6 Thesis organization

The thesis is organized into six chapters

In Chapter 1, the evolving understanding of lunar science is described, tracing its trajectory from the pre-Apollo era to the present while discussing unanswered questions targeted in this thesis. It sets a stage by discussing motivation and primary research objectives of this work. In Chapter 2, the experimental/analytical methods used in this study, their operational principles, and runtime conditions are highlighted. The protocols governing each measurement are also discussed in detail. Chapter 3 is dedicated to exploring the petrogenesis of unbrecciated lunar meteorite A-881757 and its associated clan members. The aim is to assess the magmatic evolution of the Moon through the lens of KREEP-free (source) basalts. It explores the mantle source compositions for KREEP-free (source) basalts and Apollo mare basalts, estimating their formation P-T. A discussion is also engaged in regarding lunar basalt generation and the role of the radioactive element-rich KREEP layer in mantle melting. In Chapter 4, the compositional heterogeneity of the lunar crust is delved into, detailing the mineralogy and petrology of three compositionally distinct lunar regolith breccia meteorites. Attempts are made to understand the possible source regions of these meteorites, while providing a detailed compositional characterization of the basaltic

clasts within them. In Chapter 5, the highly siderophile element (HSE) abundance and Re-Os isotopic composition of the studied meteorite samples are presented. Detailed petrography is conducted on each sample to identify signs of impactors, and the metal Ni/Co ratio is utilized to distinguish between external and internal processes. Moreover, the highly siderophile element and Re-Os isotopic data are interpreted based on petrographic findings, aiming to understand the BSM HSE composition and the contribution from late accreted materials. Chapter 6 summarizes the primary outcomes and conclusions derived from the studies presented in this thesis. Additionally, insights into potential future projects that could be pursued are offered.

Chapter 2

Analytical Methods

This chapter describes the methodology used for sample preparation, identification of textures and lithologies and their characterization. Each analytical technique with their underlying principle, capabilities and their operating procedure is detailed throughout this chapter. The steps related to the sample preparation methods for each analysis is also outlined in each discussion. The latter part of this chapter highlights a detailed discussion regarding each measurement protocol applied in this thesis.

2.1 Electron Microscopy

This analytical technique is one of the first methods of non-destructive analysis used to study the rock samples. In contrast to optical microscopy, this technique which utilize a beam of electrons with much shorter wavelengths (in picometers) to achieve a significantly high-resolution analysis. This technique differs from all other techniques in a way that it involves excitation and subsequent chemical analysis of a selected regions with area as small as few microns on the sample surface.

2.1.1 Fundamental principles

When a focused beam (up to 1 nm diameter) of high energy electrons (accelerating voltage 5 – 30 keV) is bombarded over a solid sample surface, the

interaction between this primary electron beam and the sample causes several phenomena yielding derivative electrons and x-rays (**Figure 2.1**). The interaction depth and volume, which can range from $1\mu\text{m}$ to 0.1nm allows variety of measurements to be made on the samples.

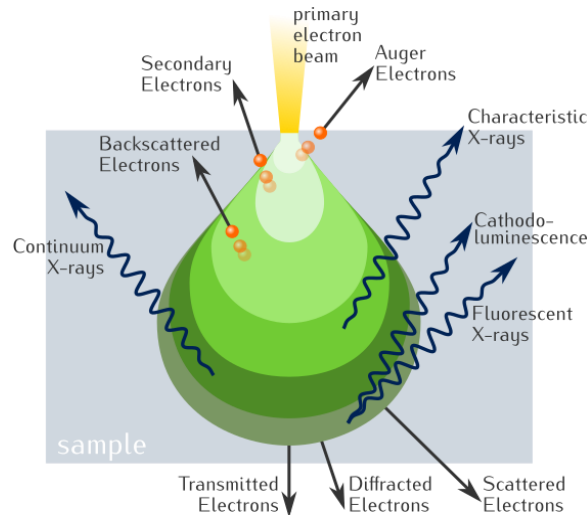


Figure 2.1 The effect of bombardment of accelerated and focused electron beam over the sample. The interaction that are primarily utilized in this study are backscattered electrons, secondary electrons and characteristic X-rays. Image credits: Ponor, CC-BY-SA.

2.1.2 Sample Preparation

The Lunar meteorite samples in this study were provided by National Institute of Polar Research (NIPR), Japan. The polished sections (approx. 2.5×2.5 mm surface) were made from small chips of meteorites. In this process, the chips were first mounted over resin block and each resin block were then polished in number of stages. The first stage polishing is performed using 6-micron diamond paste with *Hifin* diamond-based extender oil over a polishing cloth attached to an automated polishing machine *Buehler Automet 250*. Next the sample was polished over 3-micron, 1-micron and 0.25-micron diamond paste for 40-60 minutes in each size. Lastly, the samples polished over 0.05-micron alumina paste for final finishing. During the entire process the polishing quality was monitored using optical microscope. The polished section was then clean

ultrasonically using ethanol or isopropanol for ~ 5 minutes to remove the excess material and fluids from the samples. Each polished sample was then coated with appropriate thickness of either gold (< 10 nm) or carbon (~20 nm) for further analysis under electron beam.

2.1.3 Scanning Electron Microscopy (SEM)

The SEM is a high-resolution imaging technique which primarily uses secondary electron signals emitted when electron beam hits the sample surface. In this study, this technique has been utilized for petrographic examination of the samples. The SEM instrument, sometimes also consists of backscattered electron (BSE) detectors and therefore can also be utilized for BSE imaging. The BSE images are grayscale images and usually correlated with the number of backscattered electrons obtained from the sample surface. The larger atoms (with greater atomic number, Z) because of their

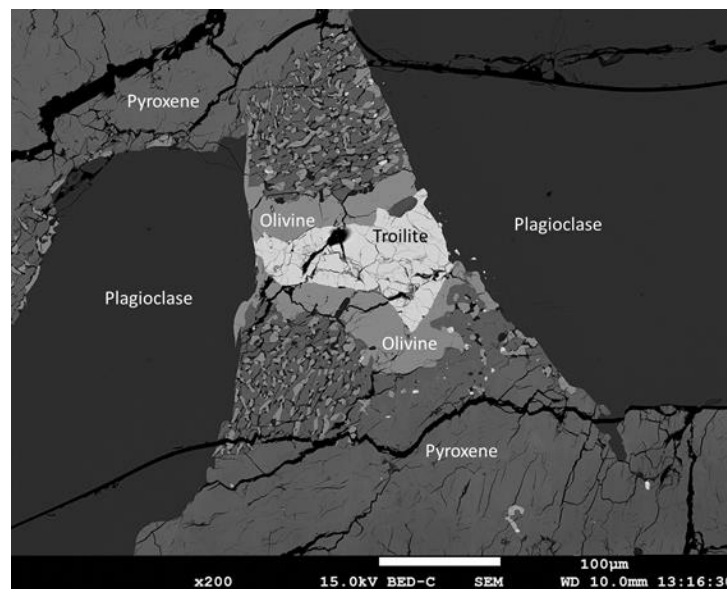


Figure 2.2 Backscattered electron image (BSE) showing compositional information as a function of the contrast. The mineral composed of lighter elements such as plagioclase (Si, Al) looks darker when compared to mineral composed of heavier elements such as troilite.

larger cross-sectional area have high probability of backscattering. Consequently, the number of backscattered electrons received by the BSE detector is directly proportional

to the mean atomic number of the chosen region (**Figure 2.2**). The regions containing heavier elements like Fe or Ti, would appear brighter when compared to regions composed of lighter elements like Si or Al.

This study makes extensive use of high-resolution BSE images of the lunar meteorites obtained using *JEOL JSM-7100F* Field Emission Scanning Electron Microscope (FE-SEM) at NIPR, Japan and backscattered and secondary electron detectors integrated to *JEOL JXA 8530F* Field Emission Electron Probe Micro Analyzer (FE-EPMA) at Physical Research Laboratory, Ahmedabad.

2.1.4 Electron Probe Microanalysis (EPMA)

In the electron probe microanalysis, the electron beam is arranged such that it strikes the sample at right angle to its surface and the incident beam of electrons then displaces inner shell electrons from the atoms it interacts. Further in order to fill the vacancy of the displaced electrons, an electron from the outer shell comes down to inner shell. During this transition, the energy is lost in the form of X-rays and the wavelength of this X-rays are characteristic of the target atom (element). The characteristic X-rays generated from the samples are detected using either wavelength dispersive (WDS) or energy dispersive (EDS) spectrometers. The WDS has an advantage over EDS in having high precision ($\pm 1\%$), better spectral resolution of $\sim 1\mu\text{m}$ and low elemental detection limit ~ 10 ppm, is therefore more preferred for quantitative analysis. Unlike SEM, the EPMA instrument is also fitted with optical microscope and a CCD camera to identify the region of interest. In this study the EPMA is used to determine the chemical composition of individuals minerals present within the sample.

The Wavelength Dispersive Spectrometer is used to measure the wavelength of emitted x-rays from the sample. The dispersion of x-rays is related to their wavelength by Bragg's equation: $n\lambda = 2d\sin(\theta)$, where n is the diffraction order, λ is the wavelength, d is the interatomic/lattice spacing, and θ is the angle of diffraction. *JEOL JXA 8530F* Field Emission Electron Probe Micro Analyzer (FE-EPMA) at National Institute of Polar Research, Japan and Physical Research Laboratory, Ahmedabad, India is utilized

for the analysis. Both the instruments are fitted with five WDS multi-crystal spectrometers, each distinct crystal has a fixed lattice plane spacing which diffracts specific x-rays generated within a sample. Only the x-rays that encountered the crystals at a Bragg's angle and satisfy the Bragg's equation are diffracted and exit at angle equal to the incident x-ray beam to reach the detector. The analytical crystals move to specific angles with respect to sample and the detector such that only one particular element can be selected on one crystal at a time. Therefore, all the crystals have to be selected efficiently, in a sequential manner, to analyze different elements. One crystal, however cannot satisfy the Bragg's Law for full spectrum of wavelength emitted by the elements in the periodic table. To serve this purpose, the EPMA is usually associated with multiple standard analyzing crystals. The EPMA at PRL is equipped with pseudo crystals LDE1, thallium acid phthalate (TAP), pentaerythritol (PET) and lithium fluoride (LIF) and large crystals varieties such as TAPL, PETL and LIFL. The elements and their preferred crystal are given in **Table 2.1**.

Table 2.1 The list of elements and their corresponding measuring crystal and standards used in EPMA.

Elements	Preferred Crystals	Standards
Si, Al, Mg	TAP	Diopside (Si, Mg), Olivine (Si, Mg), Plagioclase (Al)
Na	TAPL	Plagioclase (Na), Jadeite (Na)
Ca, Ti and K	PETJ or PETL	Plagioclase (Ca) Diopside (Ca), Rutile (Ti), Sanidine (K), Orthoclase (K)
Fe, Mn, Cr	LIF or LIFL	Magnetite (Fe), Fe- metal (Fe), Rhodonite (Mn), Cr-oxide (Cr)

In order to obtain precise and high quality EPMA, a combination of natural and synthetic reference standards is used for calibration and is measured periodically within each analytical session to ensure data quality. The reference standards also allow to convert the X-ray counts per second into element concentration for an unknown sample.

In addition to the quantitative analysis, the WDS and EDS spectrometer are also used to generate x-ray elemental maps of the whole section and some specific regions of interest. X-ray mapping involves rastering over the sample with simultaneously measuring the variation in the x-ray intensity using either WDS or EDS. The resulting image show the variation of single element over a region, which can be further combined to generate a more informative false color image (**Figure 2.3**).

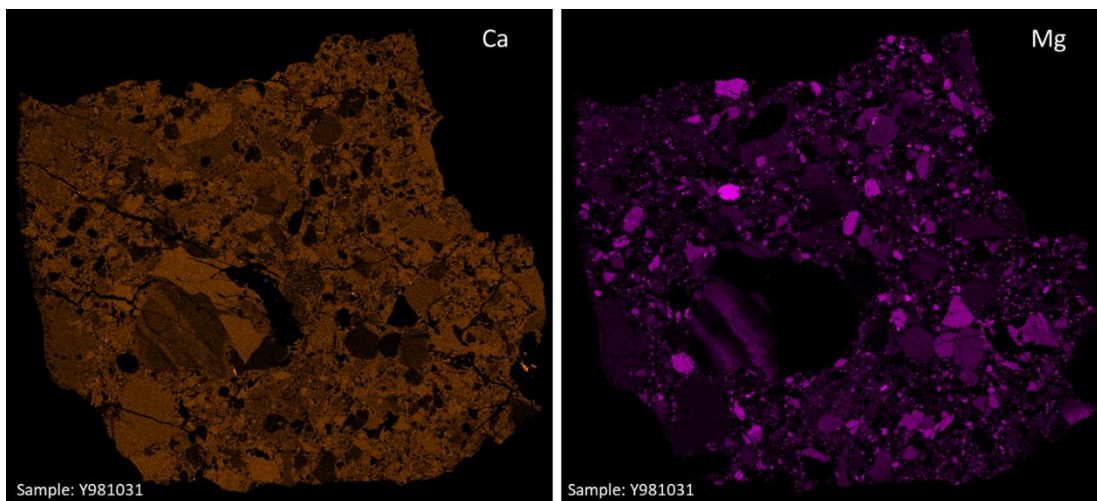


Figure 2.3 X-ray map of Ca and Mg for Sample Y-981031 highlighting the abundance of elements throughout the section.

2.2 Mass spectrometry

The mass spectrometry has always been at an unequalled position among analytical methods due to its high sensitivity, very low detection limits and diversity in applications. Following Thomson's Nobel Prize-winning experiment in 1897, during which he discovered the electron and determined its mass-to-charge ratio, a multitude of mass spectrometers have been developed, adhering to its foundational principles (Potts, 1992).

This thesis utilizes the mass spectrometry technique to measure bulk chemical composition of the samples including the abundance of highly siderophile elements (using Quadrupole- Inductively Coupled Plasma Mass Spectrometer), in-situ trace element composition of different mineral phase present in the sample (using Laser Ablation Inductively Coupled Plasma Mass Spectrometer) and Re-Os isotopic composition of the bulk samples (using Thermal Ionization Mass Spectrometer). The principles and working of the above-mentioned instrument are briefly described below and the results are present in the following chapters of the thesis.

2.2.1 Fundamental principle

The mass spectrometer ionizes the sample compounds and then separates them according to their specific mass to charge ratio (m/z), and further records the relative abundance of each ion. Each mass spectrometer consists of four essential components (Figure 2.4):

- i. Sample inlet: *introduction of sample in either liquid, or gas form*
- ii. Ion source: *for ionizing the samples*
- iii. Mass analyser: *for separating ions corresponding to their mass to charge (m/z) ratio*
- iv. Detector: *to count the ions separated by the mass analyser*

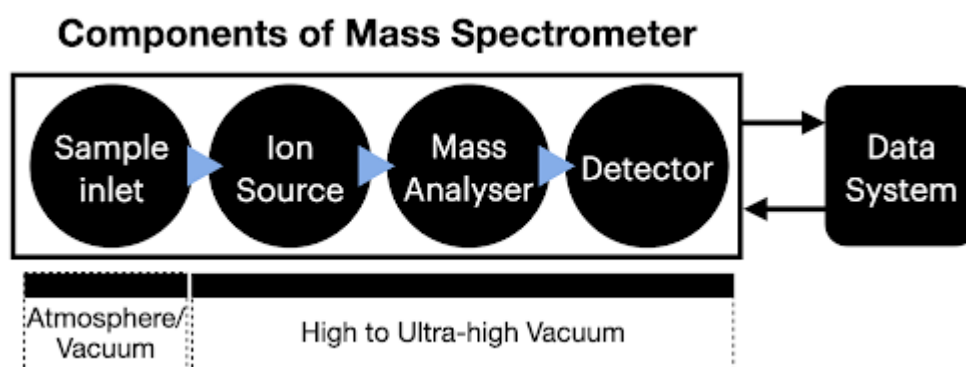


Figure 2.4 Primary components of a Mass Spectrometer.

2.2.1.1 Quadrupole Inductively Coupled Plasma Mass Spectrometer (Q-ICPMS)

This instrument measures the bulk elemental composition of samples as well as in-situ trace elemental composition of the associated mineral phases in the samples. Ion source and mass analyser in this machine makes it different from other mass spectrometer. The ionization of atoms is attained using Argon-plasma which is generated by directing the energy from the radio frequency generator to the Argon (Ar) gas. The coupling is performed by producing a magnetic field, by passing a high frequency electric current through an induction coil. The coil further generates a rapidly oscillating magnetic field oriented in vertical plane of the coil. The ionization of the flowing Ar gas is initiated by a spark from Tesla coil. The resulting ions and the

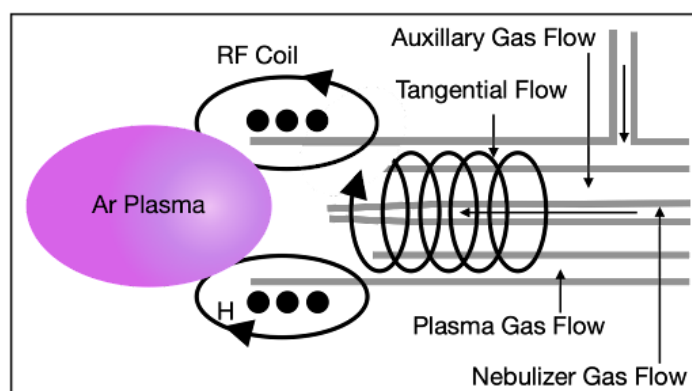


Figure 2.5 Schematic diagram of ICP torch.

electrons further interact with the fluctuating magnet field in the coil and ionize more argon atoms by collision excitation. All this process happens within seconds and a stable steady state is achieved having temperature around 6000 K – 10,000 K (**Figure 2.5**).

The ions are further passed through quadrupole mass analyser. This instrument employs two pair of rods aligned with high accuracy and connected electrically. Each pair of rods is operated at equally opposite charged dc voltage. The DC voltage is superimposed with radiofrequency (RF) such that there is phase difference of 180 between two pairs (**Figure 2.6**). When ions are accelerated through the ICP, a relatively low gradient (a few volts) cause them to flow along axis of the quadrupole. In between the quadrupole, the ions are influenced by varying combination of RF and DC fields

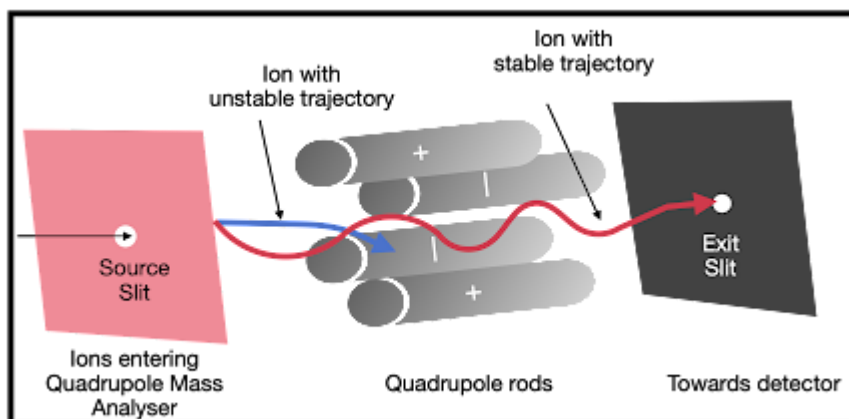


Figure 2.6 The trajectory of the ions through the quadrupole is actually very complex - the figure shows a simplified schematic.

which imparts them a complex sinusoidal motion. The magnitude of the motion is dependent on the applied AC and DC fields, and the mass-to-charge ratio of the individual ions. For a fixed set of AC and DC fields, there exists a unique mass-to-charge ratio which will satisfy the resonance requirement of the particular ion to be transmitted through the quadrupole. While other ions entering the quadrupole oscillate with frequencies which eventually let them strike a quadrupole rod or pumped away by the vacuum system. The quadrupole has an advantage that it allows to choose a trade-off between high resolution ($V_{DC}/V_{AC} \sim 0.168$) and large signal ($V_{DC}/V_{AC} < 0.168$). The resolution of the quadrupole mass filters can be improved at design stage of the

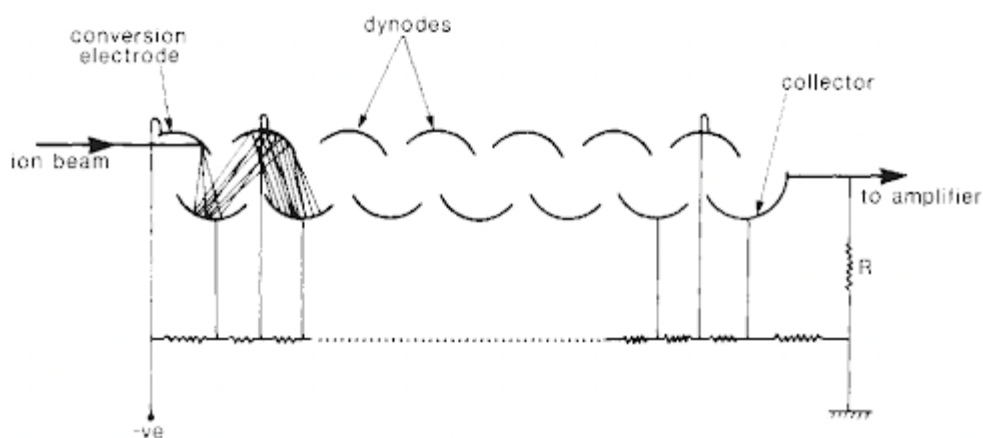


Figure 2.7 Schematic of electron multiplier ion beam detector. Source: Potts, P.J., 1992; Beynon and Benton, 1982)

instrument such as increasing the length of the rod (trade off will be the lowering of the signal).

As the ions are separated by quadrupole mass filter, the ions pass through a slit towards the detector assembly. An electron multiplier detector is used for detection of ions that are allowed to pass through the quadrupole. The electrode of the detector is composed of either Beryllium/Copper or Silver/Magnesium alloys that optimizes the yield of secondary electrons when its surface is bombarded by ions. The generated secondary ions are further passed through chain of dynodes (typically 10-20), giving overall internal signal gain of 2^n (n = number of dynodes) and multiplication factors in the range of 10^5 - 10^7 can readily be achieved. To collect the signal, a Faraday cup is placed at the end of electron multiplier assembly (**Figure 2.7**).

2.2.2 High resolution Inductively coupled Plasma Mass Spectrometer (HR-ICPMS)

This instrument has improved capability over Q-ICPMS in separating spectral interferences and produce clean elemental spectra enabling accurate measurement of isotopic signals. This mass spectrometer is different from the Q-ICPMS in its mass

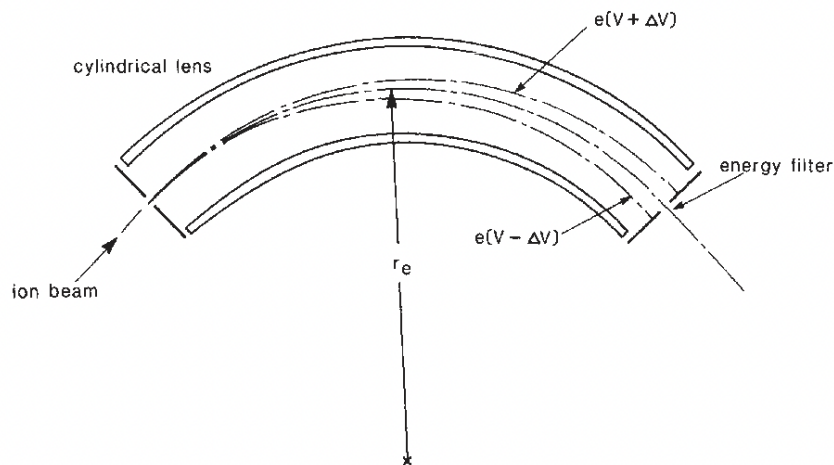


Figure 2.8 Schematic of energy filtering in the electrostatic sector. Only ions with energy (V) follows a trajectory through the sector exit slits. Source: Potts, P.J., (1992); White, (1968).

analyzer assembly. This instrument uses two dispersion elements for ion separation, i) an Electrostatic sector which filters the ions based on its energy allowing to pass a monogenetic beam of ions towards next dispersion elements, a magnetic sector. In the electrostatic sector, centrifugal force due to the kinetic energy of the ion beam entering the sector is balanced by centripetal force generated by electrostatic plates:

$$\frac{mv^2}{r} = \frac{Ee}{d} \quad (2.1)$$

$$r = \frac{Ee}{dmv^2} = \frac{2Ee}{d(KE)} \quad (2.2)$$

where, m is the mass of ion, v is its velocity, r is the mean radius between two curved plates, E is the voltage between the electrostatic plates, d is the distance between the plates and e is the charge in the ion.

The radius of deflection of the ion beam depends on the electrostatic field strength (E/d) and the kinetic energy (KE) of the ions entering the field, but not on the mass of the ion. E/d can be adjusted so that the electrostatic sector passes ions with same kinetic energy irrespective of their masses while ions of different kinetic energies do not pass the exit slit (**Figure 2.8**). As the focused ion reaches the magnetic sector, it is subjected to a magnetic field which further deflects the ions. The ions entering the magnetic field experiences centrifugal force ($\frac{mv^2}{r}$) due to its kinetic energy which is exactly balanced by magnetic centripetal force.

$$r = \frac{1}{H} \sqrt{\frac{2Vm}{e}} \quad (2.3)$$

or,

$$\frac{m}{e} = \frac{H^2 r^2}{2V} \quad (2.4)$$

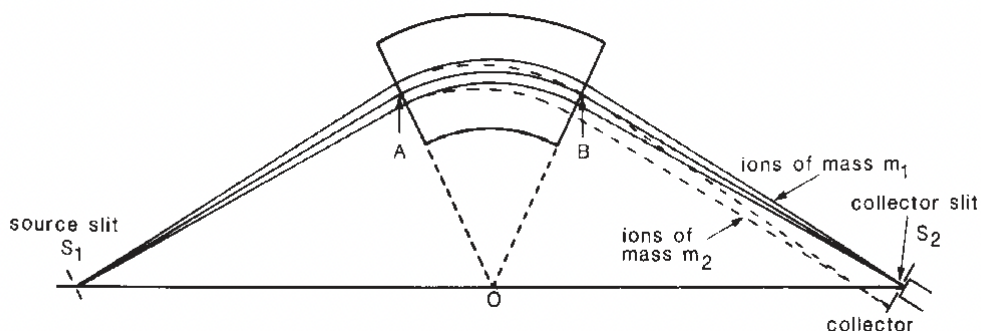


Figure 2.9 The trajectories of two ion beams in a 60° magnetic sector, Note that the mass of m_1 is greater than the mass of m_2 . Source: Litzow and Spalding, (1973)

The angle at which ion beam enters the magnetic sector, the total flight path all of the parameters is controlled by instrument design. Therefore, mass to charge ratio observed at slits is controlled by the field strength of magnets (H) and the accelerating potential (V).

2.2.3 Thermal Ionization Mass Spectrometer

This mass spectrometry is a technique, chiefly developed to accurately measure the isotopic ratio of elements such as Rb-Sr, Sm-Nd, U-Th-Pb, Re-Os etc. This instrument differs from all the previous ones in its ion source characteristics. An extensive chemical separation methodology is required before the analysis (section 2.3.3) to avoid isobaric interferences. After the chemical separation, samples in solution are deposited as small (μL) drops on to a metal filament and then heated to evaporate the solvent leading to deposition of sample residue suitable for analysis (**Figure 2.10**).

The filament is mounted in the sample turret of the mass spectrometer in a high vacuum. Further, the sample is ionized by heating the filament by passing electric

current until the required temperature is achieved. The proportion of ions (+ve) relative to neutral ions emitted from the heating filament is given by Langmuir-Saha equation:

$$\frac{n^+}{n^0} \propto \exp \left[\frac{e(W-IP)}{kT} \right] \quad (2.5)$$

Where n is the element in positive (n^+) and neutral (n^0) configuration, e is the electronic charge, W is the work function, k is the Boltzmann constant, IP is the ionization potential of the isotope and T is the filament temperature.

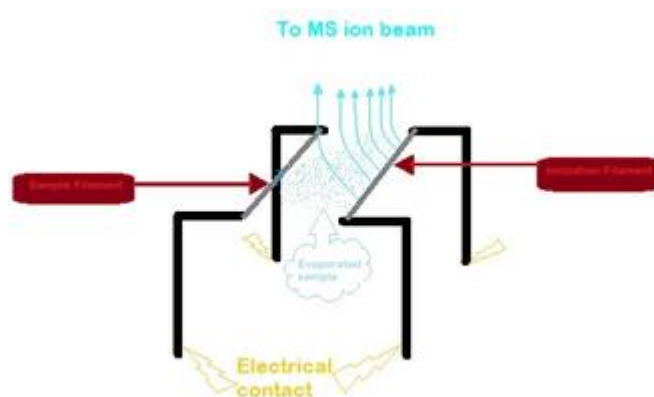


Figure 2.10 Two filaments in thermal ionization mass spectrometry. Source: Wikipedia.

Negative ions can also be produced and measured using similar techniques, which offer the advantage of ionizing a variety of elements with high ionization potentials as negative atomic or oxide species, such as Re-Os. Similar, Langmuir-Saha equation can be used to describe the ratio of ions to neutral species produced. The production of negative ions (n^-) is dependent on the electron affinity of the sample (EA), as well as the temperature (T) and work function (W) of the filament.

$$\frac{n^-}{n^0} \propto \exp \left[\frac{e(EA-W)}{kT} \right] \quad (2.6)$$

Due to the physical evaporation of the samples this technique requires mass fractionation correction in order to account for the effect that lighter isotopes are more volatile than the heavier isotopes. Most important advantage of the thermal ionization is that the energy spread of ions emitted from a filament source is very small ~ 0.2 eV, which helps in achieving high mass resolution. Furthermore, since the filament

ionization is a surface phenomenon, the mass spectra obtained are essentially interferences free.

2.3 Measurement Protocols

2.3.1 Analytical procedure for bulk major and trace element analysis

In the case of bulk measurement, Q-ICPMS is run in the solution mode. The chunk meteorite samples are finely powdered manually using agate mortar and pestle under a clean lab fume hood. The finely grounded powder is then digested under acid mixture of HNO₃ : HCl : HF in the fixed ratio of 3 mL : 1 mL : 0.5 mL. The acid-treated sample mixture is then digested using microwave digestion system at 220 °C for 45-50 minutes. All the acid digestion and dilution were performed using either a double distilled (Teflon and Quartz distilled) acid or ultra-pure acid. A well digested samples takes on a clear solution while undigested or partially digested sample show some residue. The digested samples are further diluted in either Milli Q water or 2% HNO₃ to prepare solution with elemental concentration within the sensitivity of the instrument.

In case of trace elements, samples were diluted with various concentrations like M, M/2, M/4, and M/40, where M is the original concentration of trace elements in the samples. All the samples were run as sample-standard bracketing in standard analysis mode in ICP-MS, where standards are analysed before and after the sample to account for any instrument related drift if present. The major elements were also measured from same aliquots but at higher dilution. For major elements measurement, samples were diluted to M/100, M/200, M/400, and M/4000 and measured in Kinetic Energy Discrimination (KED) mode to selectively attenuate all polyatomic interferences based on their size. KED works on the principle that all polyatomic ions are larger than analyte ions of the same mass, so they collide with the cell gas more often as they pass through

the cell, emerging with lower residual energy. Silicon (Si) is not measured during the analyses and is expressed as differences from the rest of the measured major elements. The errors in the Si abundance of the samples are assumed to be similar to the deviation in the Si abundance observed in the standards. In some of the analysis, Indium doping is also performed to monitor the drift and inter-element corrections. The obtained data is handled using Iolite software.

The instrument *ThermoScientific iCAP-Q* housed at Physical Research Laboratory, Ahmedabad and at Scripps Isotope Geochemistry Laboratory (SIGL), Scripps Institution of Oceanography, were used for the bulk major and trace element analysis. The standards are chosen based on sample type and the details are described in the following chapters where bulk major and trace elements data and results are discussed.

2.3.2 Analytical procedure for in-situ trace element analysis

The trace elemental abundance of minerals such as pyroxene, olivine, and plagioclase were obtained using Laser Ablation Inductively Coupled Plasma Mass Spectrometer (LA- ICPMS). LA-ICPMS uses a powerful nanosecond-pulsed laser beam to remove material from the sample surface. The laser beam falling on the sample surface cause heating, evaporation and ionization of sample materials, a phenomenon known as Laser ablation. The ablated particles are then carried via a constant flow of helium/argon gas to ICPMS, where it is subsequently ionized, separated according to their mass-to-charge ratio. The thick sections used for EPMA analysis can directly be used in LA-ICPMS and this makes this instrument extremely versatile. The area as small as 10-20 μm can be analyzed in LA-ICPMS.

The sample coatings were removed and then inserted in the LA-ICPMS sample chamber. The analyses were performed in both spot and line modes. Spot analyses were made using a 50 μm spot at a 10 Hz repetition rate, with 150 shots per spot while line analyses (1-2 mm long) were made using a 50 μm beam diameter, at 10 $\mu\text{m s}^{-1}$, and 20 Hz repetition rate. Isotope peaks were collected in low-resolution mode ($R\sim 400$) with

triple-mode detection. The measured isotopes were ^{29}Si , ^{31}P , ^{44}Ca , ^{45}Sc , ^{71}Ga , ^{74}Ge , ^{85}Rb , ^{88}Sr , ^{89}Y , ^{90}Zr , ^{93}Nb , ^{138}Ba , ^{139}La , ^{140}Ce , ^{141}Pr , ^{145}Nd , ^{147}Sm , ^{151}Eu , ^{158}Gd , ^{159}Tb , ^{164}Dy , ^{165}Ho , ^{166}Er , ^{169}Tm , ^{174}Yb , ^{175}Lu , ^{180}Hf , ^{181}Ta , ^{208}Pb , ^{232}Th , and ^{238}U . All peaks were acquired by peak jumping between peak tops with a 10% mass window and 50-100 milliseconds of acquisition time on the peak top. Elemental abundances were calculated using relative sensitivity factors (RSFs) obtained from USGS glass BHVO-2G and from NIST SRM 610 glass reference material. SiO_2 concentrations determined by EPMA were used as internal standard. $^{232}\text{Th}^{16}\text{O}/^{232}\text{Th}$ ratios were tuned to ~0.4-0.7%.

This study utilizes LA-HR-ICPMS instrument at National Institute of Polar Research (NIPR), Japan and LA-ICPMS instrument at Physical Research Laboratory, Ahmedabad, India and National Geophysical Research Institute, Hyderabad, India. The NIPR and PRL uses the same 213 nm laser procured from CETAC, Model: LSX-213 while NGRI uses 193 nm laser procured from New Wave Research. The results and specific run condition of the instruments are mentioned in detail in the following chapters.

2.3.3 Analytical procedure for Re-Os isotope and highly siderophile element abundance measurements

2.3.3.1 Isotope dilution (ID)

Over past 15 years, the advances in sample preparation, chemical separation and instrumentation have made precise determination of highly siderophile elements and Os isotopes possible. The highly siderophile elements are measured using traditional Isotope Dilution (ID) methods, where finely grounded sample powders are equilibrated with precisely known quantities of an isotopically enriched tracer solution. Thus, by knowing the isotopic composition of spike and measuring the isotopic composition of the spike-sample mixture, the concentration of any element having at least two naturally occurring isotopes can be calculated with great precision. However, some mono-

isotopic elements (Be, I, Cs, Th and Pa) can be analysed with ID using synthetically prepared radio-isotopic spikes.

Samples are typically digested in Carius tubes (CT) or using High pressure Asher (HPA).

Two main drawbacks of this methods are:

i) Amount of sample that can be effectively digested without having nugget-effect (irregular distribution of minor or trace accessory phases rich in HSE) in the CT is relatively small (<3 g). This limitation can be overcome in case of basalts with fine flouring and careful homogenization of large samples.

ii) As these are silicate rocks, the potential for incomplete digestion is there. The normal standard acid digestion mixture sometimes ineffective in breaking most silicates. The silicate breakdown usually requires HF treatment but as HF is strong acid it can also affect the quartz/borosilicate CT by etching its side-walls hence contributing to the overall blank. Despite this, several studies have shown that making few modifications in standard acid digestion, one can avoid such problem especially in case of basaltic samples.

Consider an element with spike isotope SI and reference isotope RI in sample-spike mixture. Concentration of the element in a given sample can be expressed as

$$SI = SI_{sa} + SI_{sp}, \text{ and } RI = RI_{sa} + RI_{sp}$$

$$\left(\frac{SI}{RI}\right)_{mix} = \frac{(SI_{sa} + SI_{sp})}{(RI_{sa} + RI_{sp})} \quad (2.7)$$

where SI and RI are spike and reference isotopes while subscript sa, and sp, refers to sample and spike in the mixture, respectively.

The equation can be further rewritten as

$$\left(\frac{SI}{RI}\right)_{mix} = \frac{\left(\left(\frac{SI}{RI}\right)_{sa} RI_{sa} + \left(\frac{SI}{RI}\right)_{sp} RI_{sp}\right)}{RI_{sa} + RI_{sp}} \quad (2.8)$$

$$\frac{RI_{sa}}{RI_{sp}} = \frac{\left(\frac{SI}{RI}\right)_{mix} - \left(\frac{SI}{RI}\right)_{sp}}{\left(\frac{SI}{RI}\right)_{sa} - \left(\frac{SI}{RI}\right)_{mix}} \quad (2.9)$$

The RI can be calculated as,

$$RI_{sa} = \frac{wt_{.sa} \times conc_{.sa} \times abun.(RI)_{sa} \times N_A}{atwt(element_{sa})} \quad (2.10)$$

Similarly,

$$RI_{sp} = \frac{wt_{.sp} \times conc_{.sp} \times abun.(RI)_{sp} \times N_A}{atwt(element_{sp})} \quad (2.11)$$

where, wt . is the weight of sample(sa)/spike(sp), $conc$. is the concentration of the elements (g/g) in sample/spike, $abun.(RI)$ is the abundance of reference isotope in the sample/spike, $atwt(element)$ is the atomic weight of the element and N_A is Avogadro's number.

Rearranging,

$$conc_{.sa} = \frac{\left(\frac{SI}{RI}\right)_{mix} - \left(\frac{SI}{RI}\right)_{sp}}{\left(\frac{SI}{RI}\right)_{sa} - \left(\frac{SI}{RI}\right)_{mix}} = \frac{wt_{.sp} \times conc_{.sp} \times abun.(RI)_{sp} \times atwt(element_{sa})}{wt_{.sa} \times conc_{.sa} \times abun.(RI)_{sa} \times atwt(element_{sp})} \quad (2.12)$$

Hence, the concentration of an element in a sample can be calculated from the measurement of isotopic composition of sample-spike mixture, atomic weight of spike and sample and measured sample-spike weight and concentration of the spike.

2.3.3.2 Calculation for choosing appropriate amount of spike

There exists a ratio of the sample-spike mixture $\left(\frac{SI}{RI}\right)_{mix}$ for which uncertainty on an element concentration determined by isotope dilution is minimum. This ratio is termed as optimum sample-spike mixture. This is mathematically expressed as a geometric mean of the sample and spike isotopic concentration (Webster, 1960).

$$\left(\frac{SI}{RI}\right)_{mix}^{opt} = \sqrt{\left(\frac{SI}{RI}\right)_{sa} \times \left(\frac{SI}{RI}\right)_{sp}} \quad (2.13)$$

The uncertainty of the determined element concentration is equal to the measurement uncertainty on the ratio $\left(\frac{SI}{RI}\right)_{mix}^{opt} \times EMF$, where EMF is the error magnification factor. At the optimum sample-spike mixture, isotopic concentration can be equated as

$$EMF_{min} = \frac{\left| \left(\frac{SI}{RI}\right)_{sa} - \left(\frac{SI}{RI}\right)_{sp} \right|}{\left(\sqrt{\left(\frac{SI}{RI}\right)_{sa}} - \sqrt{\left(\frac{SI}{RI}\right)_{sp}} \right)^2} \quad (2.14)$$

Normally, EMF and optimum spike-sample mixture is function of purity of the spike and the value of $\left(\frac{SI}{RI}\right)_{sp}$. As the value of optimum isotopic concentration of spike-sample mixture increases, the value of Error magnification factor decreases. Therefore, purer spike allows us more flexibility for spike sampling as then the ratio will be less dependent on accurately estimating the sample concentration before the measurement.

For this study, I procured the sample spike for isotopically enriched (^{99}Ru , ^{106}Pd , ^{185}Re , ^{190}Os , ^{191}Ir , ^{194}Pt) from Oak Ridge National Laboratory.

2.3.3.3 Sample Homogenization

Agate mortar and pestle are used to finely ground the samples. The maximum grit size of the samples was 0.0016 mm. This step is very important to avoid nugget effect. The elements tend to form discrete mineral phases which are inert in nature and also chemically resistant. Fine flouring also ensures complete digestion of the sample.

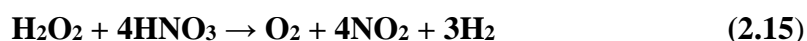
Table 2.2 Steps for purification of reagents and observations.

Experiment	Observations	Inferences
Mix 50ml HNO ₃ + 12ml H ₂ O ₂ in a precleaned 400ml tall quartz beaker and keep it undisturbed in a fume hood.	The reaction initiates a fine bubble stream.	Bubbling step
A vigorous eruption step occurs in same beaker.	Pale brown to yellow solution with no bubbling further.	Eruption step
The solution is gently heated on the hot plate	Colourless solution is observed	Boiling step, NO ₂ is volatilized.

2.3.3.4 Purification of Reagents

HNO₃ purification:

Re-Os content is very low in most geological samples. It is very important to treat HNO₃ with H₂O₂ to remove any Osmium, if present. As it gives background procedural Os blanks.



The total reaction time is approximately 150 minutes and HNO₃ treated with H₂O₂ is further distilled first in Quartz then in Teflon vials at 353 K (**Table 2.2**).

HCl distillation:

HCl is distilled first in quartz then in Teflon vials.

2.3.3.5 Steps of Acid Digestion

- Place 2 g of sample powder + appropriate spike (calculation in Appendix II) + pre-cooled 3.33 ml HCl in a 20 cm long Carius tube.
- Cool the Carius tube in a mixture of ethanol and dry ice up to 283 K, and then add 6.67 ml of 16 M HNO₃ just before sealing the tube.
- Seal the tube with oxygen-propane torch and then place into a steel jacket for heating (Cohen and Waters, 1996; Ishikawa et al., 2014).
- Digest the mixture in an oven for >72 hours at ~543K temperature (Day et al., 2016).
- After the samples are digested cool them at Room Temperature with further cooling in methanol-water mixture up to 283K to prevent any loss of volatile OsO₄ on opening (Cohen and Waters, 1996).
- Carefully open the tube by breaking the narrow neck.
- Cool the digested samples at Room Temperature with further cooling in methanol-water mixture up to 10 °C to prevent any loss of volatile OsO₄ on opening.
- The digested solution is ready for further procedures.
- The same procedure is to be followed in 50 ml High-Pressure Asher digestion vessels for >5 hours at 320 °C temperature. HPA vessels are suitable for HF attack as the glassy-carbon vessels do not etch into the solution. HF desilicification process is required for the effective digestion of silicates.

2.3.3.6 Os Separation

- Transfer the digested liquid into 30 ml Teflon vials by using 4 ml of MQ water for rinsing the inner wall of the tubes.
- Centrifuge the contents in 50 ml centrifugation tubes and transfer the supernatant into a 20 ml test-tube for solvent extraction.
- The remaining slurry is to be used further for HF desilicification and anion exchange.

- Now add 3 ml CCl_4 into it 'a' shake and then centrifuge again (Cohen and Waters, 1996).
- Collect the organic phase into a 15 ml Teflon vial.
- Repeat the same with 3 ml and 2 ml CCl_4 . (CHCl_3 can also be used instead of CCl_4 but CHCl_3 dissolves better in aqueous phase) (Meisel et al., 2001)
- Add conc. HBr 5 ml to the organic liquid collected; shake for few minutes and allow it to settle overnight. Separate the upper layer of HBr containing the reduced Os by pipette and transfer it to a Teflon vial. Heat the contents to 70°C for few hours (overnight) so that OsO_4 reduces to OsBr_6^{2-} .
- Evaporate the HBr till it dries.

Or

- Add conc. HBr to the collected organic solution, tighten the vials and heat the vials overnight at 353 K (to reduce Os (VIII) to Os (IV) which is more soluble in the aqueous phase).
- Discard the organic phase and dry the HBr. (Meisel et al., 2001)

2.3.3.7 Microdistillation of Os

- Transfer the Os to the cap of a 5 mL Teflon conical beaker, covered with in a solution of CrO_3 in 6 mol/L H_2SO_4 . Place a small drop of HBr (20 μL) in conical tip of the beaker.
- Cap the beaker in a upside down position and heat it up to 80°C for 2-3 hr on hot plate. Here, Os is oxidized by the Cr solution, gets volatilized and trapped into the HBr.
- Dry the solution of Os in HBr up to 1-2 μL and is ready for mass spectrometry analysis.

2.3.3.8 HF De-silicification

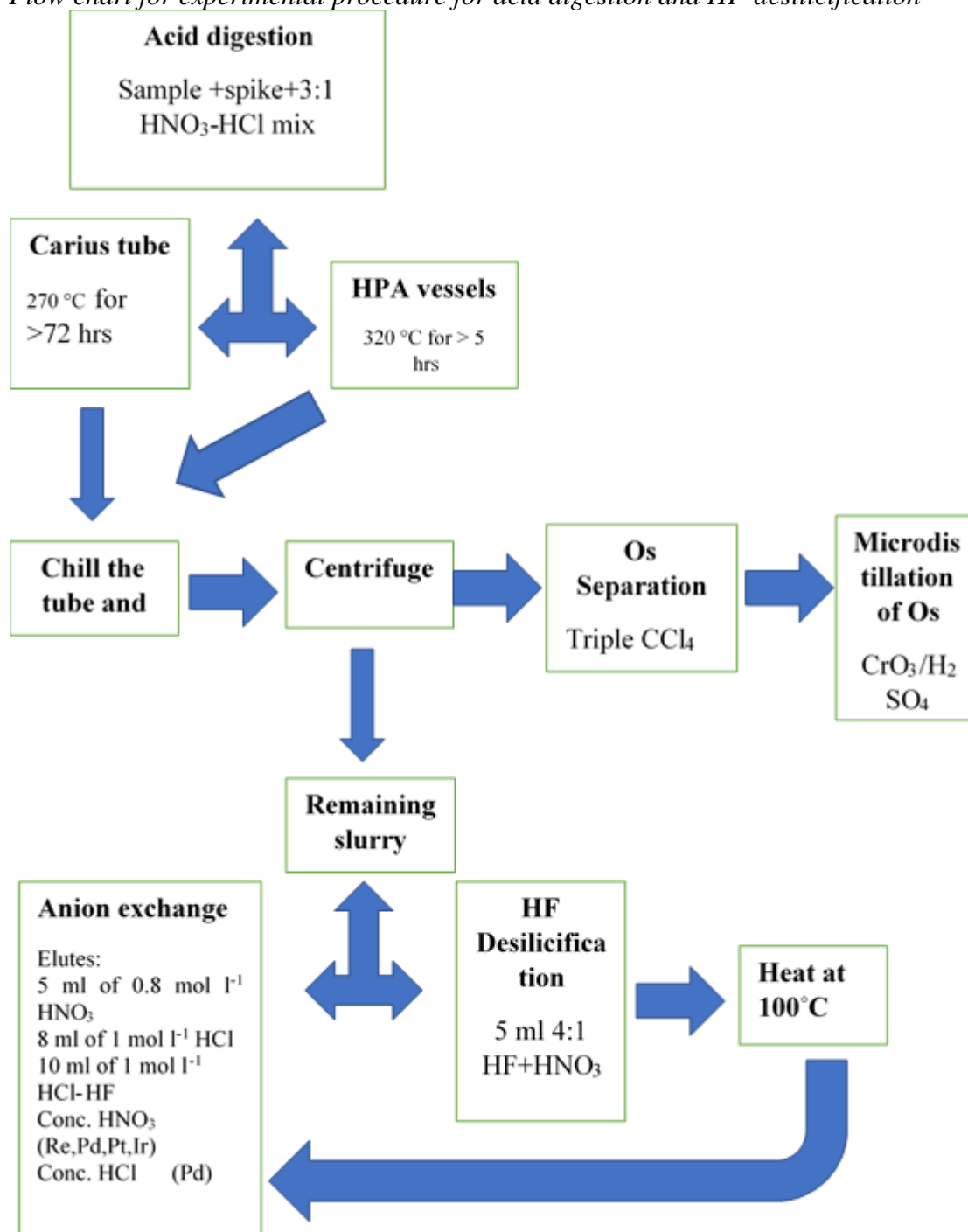
- Vigorously shake the slurry (b) to ensure homogenization.
- Divide the slurry in 2 parts (b1 and b2) and transfer 50% of the aliquot in clean Teflon beaker and dry it.

- Add 5 ml 4:1 mixture of HF-HNO₃ (4 ml HF + 1 ml HNO₃) slowly but continuously in the aliquot (b1).
- Heat it for 6 hours at 100°C temperature on hot plate. The aliquots will get completely dissolved. This forms a fluoride cake.
- Add drops of concentrated HCl until the fluoride cake dissolves and a clear solution is obtained.
- Follow the anion exchange procedures (Day et al., 2016)

2.3.3.9 Anion Exchange Chromatography

- Clean the columns by soaking in 6 N HCl.
- Load AG1-X8 (100-200) (1 ml) anion exchange resin into standard Polypropylene columns with 2 ml resin capacity and a 10-ml reservoir.
- Clean the resin with 20ml of warm (80°C) 12 N HNO₃ and wash with water.
- Elute with 30 ml chlorinated water.
- Dry the aliquoted slurry (b2) add 1ml 20% HCl dry again and equilibrate it with 10 ml 3% HCl
- Load the above solution onto different columns:
 - 5 ml of 0.8 mol l-1 HNO₃
 - 8 ml of 1 mol l-1 HCl (potential interfering elements)
 - 10 ml of 1 mol l-1 HCl-HF (Pearson and Woodland, 2000)
 - Conc. HNO₃ (elutes Re, Ru, Pt, Pd)
 - Conc. HCl (elutes Pd) (Day et al., 2016)
- Repeat the same anion exchange procedure for HF de-silicification solution.
- Collect the respective elutes in different vials, which are ready for mass spectrometric analysis.

Flow chart for experimental procedure for acid digestion and HF-desilicification



Chapter 3

Understanding KREEP-free (source) volcanism on the Moon using Lunar basaltic meteorites

3.1 Introduction

Lunar mare basalts are the primary materials used to study the magmatic and thermal evolution of the Moon. Mare basalts have been obtained by the Apollo, Luna and Chang'E 5 sample return missions, and have crystallization ages from 4.3 to 2.0 billion years (Ga; Taylor et al., 1983; Li et al., 2021), with the vast majority of samples having crystallization ages of between 3.8 and 3.2 Ga (Nyquist and Shih, 1992). Remote sensing observations based on crater counting statistics indicate the presence of younger (~1.2 Ga) exposed mare basaltic flows (Hiesinger et al., 2003; 2010), which however have not been recovered.

Signatures of ancient volcanism (≥ 3.8 Ga) on the lunar surface which are obscured by crater and basin impact ejecta during the era of large impact basin formation are designated as cryptomare (Head and Wilson, 1992; Whitten and Head, 2015a). However, the record of this ancient volcanism is scarce, with only few samples, including some Apollo 14 basaltic clasts, exhibiting old ages (~4.2 Ga; Taylor et al., 1983; Dasch et al., 1987). Additionally, basaltic breccia meteorites Kalahari 009 and

Miller Range (MIL) 13317 have clasts of ~4.3 Ga (Terada et al., 2007; Curran et al., 2019). An important suite of meteorites is the unbrecciated YAMM basalts (Yamato-793169, Asuka-881757, Miller Range 05035 and Meteorite Hills 01210), with ~3.9 Ga crystallization ages (Arai et al., 2010; Srivastava et al., 2022). The YAMM meteorites are basaltic rocks having similarities in textural, chemical and isotopic signatures (Arai et al., 2010) and are devoid of any early potassium (K), rare earth elements (REE) and phosphorous (P), or KREEP signatures. This contrasts with some of returned lunar basalts, which were collected from regions at or near to the Procellarum KREEP Terrane (PKT). For these reasons, understanding of ancient volcanism on the Moon is relatively limited and spatially restricted relative to sampling locations from the Apollo, Luna and Chang'E 5 missions.

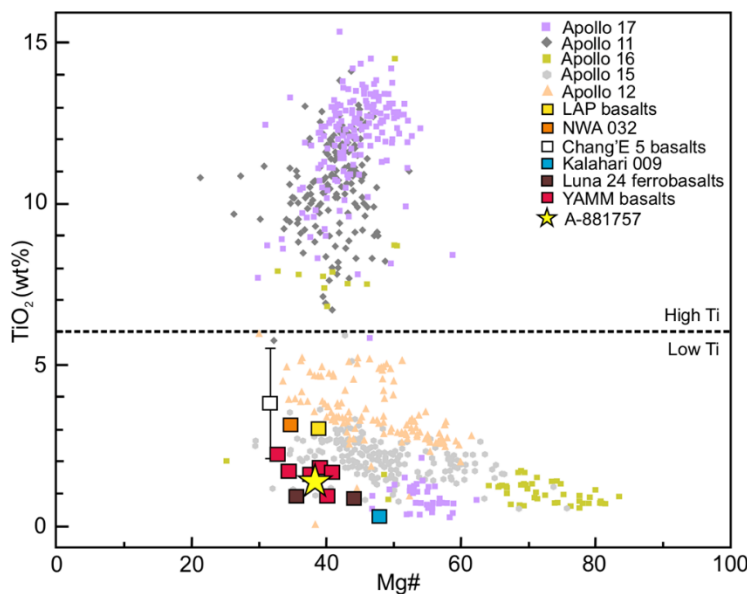


Figure 3.1 Bulk major-element composition comparison among A-881757, YAMM and other lunar basalts. TiO_2 plotted against bulk Mg# (molar $\text{Mg}/(\text{Mg}+\text{Fe})\times 100$), showing YAMM basalts are the low-Ti and most Fe-rich variety. Compositions of Apollo basalts are taken from the ApolloBasalt DB(v2) database (Cone et al., 2020).

At present, it is well understood that the returned Apollo mare basalts contain variable quantities of KREEP (potassium, rare earth element and phosphorus) component mixed into their mantle source(s), possibly from mantle overturn after extensive lunar magma ocean (LMO) crystallization (Neal and Taylor, 1992), widely known as ‘urKREEP’ (Warren and Wasson, 1979). The ‘KREEPy-ness’ of some

returned mare basalts are also supported by observed high abundances of other incompatible trace elements (ITE). A complementary argument to urKREEP addition is that some lunar basalts are of KREEP-free (source) origin with ITE enrichment resulting purely through simple magmatic processes such as low-degree melting of depleted lunar mantle followed by extensive fractional crystallization; a mechanism distinct from urKREEP addition (Borg et al., 2009; Elardo et al., 2014; Hallis et al., 2014; Tian et al., 2021; He et al., 2022). A KREEP-free mantle sources (KREEP-free (source) basalts) are considered to have (i) low initial $^{87}\text{Sr}/^{86}\text{Sr}$ (≤ 0.700) and high $^{143}\text{Nd}/^{144}\text{Nd}$, in contrast to KREEP-rich returned mare materials, which have high initial $^{87}\text{Sr}/^{86}\text{Sr}$ (> 0.701) and low $^{143}\text{Nd}/^{144}\text{Nd}$; (ii) should not have undergone significant fractionation and their bulk composition is close to their parental melt composition; (iii) There was no involvement to very minimal involvement of urKREEP in the origin of the samples. Their incompatible element enrichment, if present, can be explained through simple magmatic processes such as low-degree partial melting of depleted lunar mantle, similar to the results of Borg et al., (2009), Elardo et al., (2014), Hallis et al., (2014), Tian et al., (2021) and He et al., (2022). Recent studies of the returned Chang'E 5 (CE-5) basalts have also suggested, based on radiogenic isotope systematics (Rb-Sr, Sm-Nd and U-Pb) and REE modeling, that CE-5 basalts (~ 2.0 Ga) only possess a marginal quantity of early KREEP material (referred to as urKREEP) in their source (Tian et al., 2021; Hu et al., 2021; He et al., 2022). Previously identified KREEP-free (source) lunar basalts (NWA 032: Borg et al., 2009; LaPaz (LAP) basalts: Elardo et al., 2014; Chang'E 5 basalts: Tian et al., 2021) are typically low in TiO_2 (0.45–5.70 wt.%) and are Fe-rich (Mg# 32-49; **Figure 3.1**), with characteristically low initial $^{87}\text{Sr}/^{86}\text{Sr}$ (0.699-0.700) and positive ϵ_{Nd} (+0.8 to +7.0) indicating mantle source depletion (**Figure 3.2**). From here onwards, we refer to all these rocks (YAMM basalts, NWA 032, LAP basalts, Chang'E 5 basalts as KREEP-free (source) basalts.

In this chapter, I investigate the petrogenesis of the 'YAMM' (Y-793169, A-881757, MIL 05035, MET 01210) lunar meteorites, with special emphasis on Asuka-881757 (A-881757) to understand ancient KREEP-free (source) volcanism. Major, minor and trace element abundance data for ~ 3.9 Ga KREEP-free (source) lunar meteorite Asuka-881757 (A-881757) were integrated to provide constraints on ancient

KREEP-free volcanism possibly buried in the form of cryptomare (Arai et al., 2010). Furthermore, a near complete preservation of mm-scale hourglass sector zoning is seen in clinopyroxene grains of A-881757, and their possible formation mechanisms in terms of lunar magmatic setting is discussed.

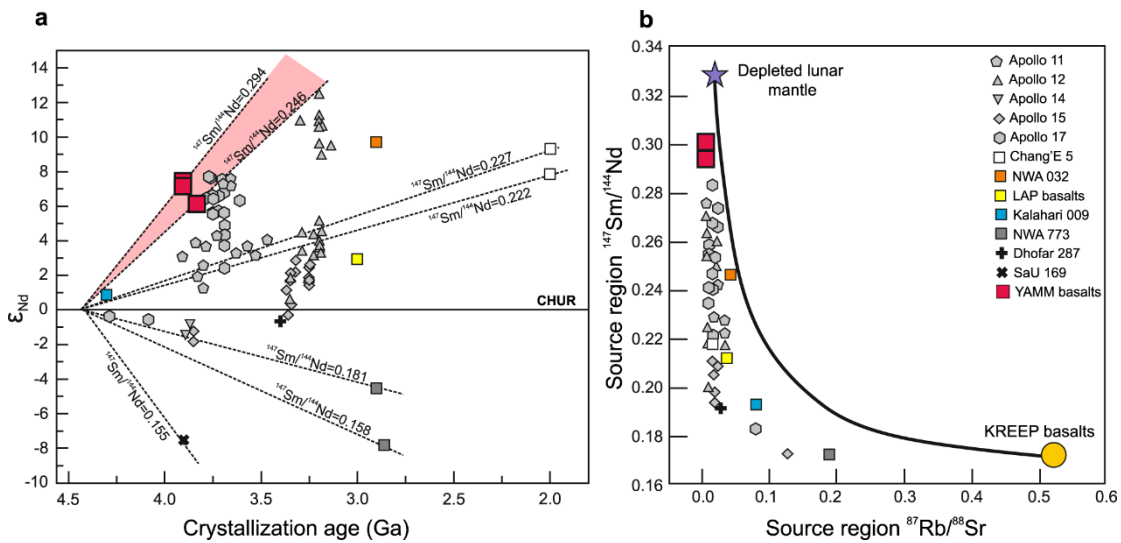


Figure 3.2 Sm-Nd and Rb-Sr source isotopic characteristics of YAMM meteorites and other lunar basalts. a) Plot of age (Ga, billion years) against ϵ_{Nd} composition showing the depleted nature of YAMM meteorites in comparison to other lunar meteorites and Apollo mare basalts. $\epsilon_{Nd}(t) = ((^{143}Nd/^{144}Nd)_{sample}(t)/(^{143}Nd/^{144}Nd)_{CHUR}-1) \times 10,000$, where $(^{143}Nd/^{144}Nd)_{sample}(t)$ and $(^{143}Nd/^{144}Nd)_{CHUR}$ are the Nd isotopic compositions of sample and Chondritic Uniform Reservoir (CHUR) at time (t) of crystallization of the rock, respectively. b) Calculated present day values of $^{147}Sm/^{144}Nd$ plotted against the present day $^{87}Rb/^{86}Sr$ for the source regions of YAMM and other lunar mare basalts (cf. Elardo et al., 2014) using a model where the Moon differentiates at 4558 Ma with an initial $^{87}Sr/^{86}Sr$ of LUNI=0.69903 (Nyquist, 1977). The $^{147}Sm/^{144}Nd$ of basalt source regions are calculated assuming a two-stage model where the Moon follows a chondritic path until differentiation occurs at 4.42 Ga, at which time mare basalt source regions were formed. Data Sources: YAMM meteorites (A-881757, (Misawa et al., 1993); Y-793169, (Torigoye-Kita et al., 1995); MIL 05035, (Nyquist et al., 2007), Kalahari 009 (Sokol et al., 2008), Chang'E 5 basalts (Tian et al., 2021) and other Apollo mare basalts and meteorites (Elardo et al., (2015) and references therein).

I further perform major and trace element modelling to understand the parental melt compositions of A-881757 (YAMM basalts) and other related samples. Equilibrium thermodynamic models and clinopyroxene thermobarometry were utilized to understand the P - T conditions of crystallization of A-881757 in the context of ancient

KREEP-free (source) basalt magmatism on the Moon. The mantle potential temperature and associated heat flow is also calculated to evaluate the early thermal and chemical state of the lunar interior. For methodological consistency and comparison, this chapter also looks into major rock types (Apollo low-Ti, intermediate-Ti and high-Ti basalts) in the Apollo sample suites and discuss them in section 3.4.5 and results are present in **Table 3.6**. The discussion made hereafter compares the studied lunar basaltic meteorites (with KREEP-free (source) origin) and selected parental melt compositions in Apollo sample suites. The chosen rocks in the Apollo sample suites were previously suggest to be parental melt compositions by other studies such as Hallis et al, (2014).

3.2 Sample Description

The Antarctic lunar meteorite A-881757 was found in the Nansen Icefield, near Asuka Station, during the Japanese Antarctica Research Expedition 20 (JARE-20) on December 20, 1989. The main mass is $8.0 \times 8.0 \times 5.8$ cm in size and 442.12 g in weight (Yanai, 1991). The sample is a coarse, holocrystalline (grains more than 5 mm in length), unbrecciated mare basalt with pyroxene and plagioclase as primary constituents (**Figure 3.3**). The meteorite, along with other YAMM (Y-793169, MIL 05035 and MET 01210), is older (~ 3.9 Ga) than most other known mare basalts. These basaltic meteorites are likely launch-paired as suggested by their similar mineral assemblages, pyroxene crystallization trends, REE abundances, crystallization ages (~ 3.8 - 3.9 Ga; Misawa et al., 1993; Torigoye-Kita et al., 1995; Nyquist et al., 2007), and low U/Pb, Rb/Sr, and high Sm/Nd (Arai et al., 2010). The YAMM meteorites crystallization ages broadly coincide with the putative “late heavy bombardment” (LHB) (Bottke and Norman, 2017) that pre-dates Apollo (~ 3.8 - 3.1 Ga) and Chang’E 5 (~ 2.0 Ga) mare basalts. The YAMM meteorites are Fe-rich (Mg# 32-41; **Figure 3.1**) with low bulk REE and other ITE (e.g., 0.48 ppm Th). The low Rb/Sr ($^{87}\text{Sr}/^{86}\text{Sr}_i=0.69908$ - 0.69910), high Sm/Nd ($\epsilon_{\text{Nd}}=+7.2$ to $+7.4$), and unusually low U-Pb ($\mu=9$ - 20) of their sources suggest a KREEP-free source distinct from some of KREEP-rich PKT (Jolliff et al., 2000) basalts (**Figure 3.2**).

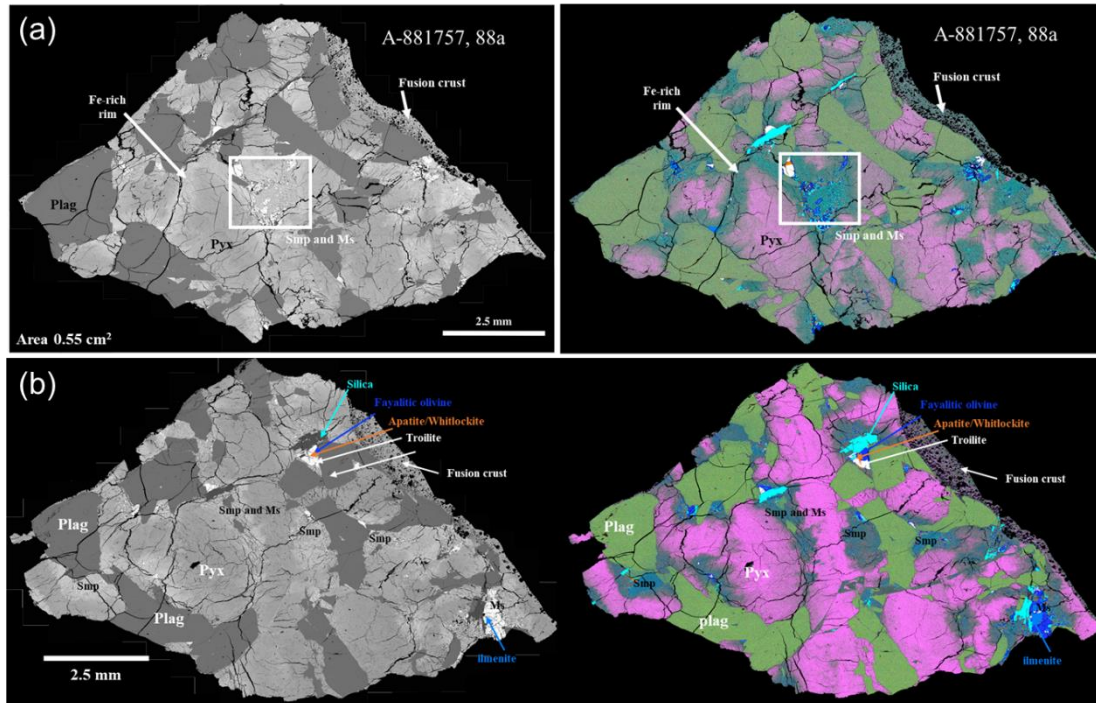


Figure 3.3 BSE (left panel) and X-ray composite (right panel) images of studied sections A-881757, 88a (a) and 88b (b) (area ~ 0.55 cm²). Coarse pyroxene and plagioclase along with symplectite and mesostasis (white box) in A-881757. Combined X-ray image highlights the compositional variation within pyroxenes and late-phase mineral assemblage. Abbreviations used are Pyx: Pyroxene; Plag: Plagioclase; Smp: Symplectites; Ms: Mesostasis. Composite image is made using freely available Image J software (<https://imagej.nih.gov/ij/download.html>). The merged colors are selected as Green-Al, Blue-Fe, Magenta- Mg, Cyan-Si, Yellow-P, Red-Ca, and Gray-Ti.

3.3 Methods

Two thick-sections of A-881757 (88a and 88b) provided by the National Institute of Polar Research (NIPR), Japan were studied. Backscattered electron (BSE) images were obtained to explore textural relationships.

3.3.1 Scanning electron microscope analysis

Analysis was performed on the polished thick sections of A-881757. Detailed imaging of the sections was carried out on a JEOL JSM-7100F field emission scanning electron microscope (FE-SEM) equipped with an energy dispersive spectrometer

(Oxford AZtec Energy) at the NIPR. The sections were coated with carbon. Acceleration voltage was 15 kV. Back-scattered electron (BSE) and X-ray mapping were taken (**Figure 3.3**). The X-ray images obtained for different elements were merged together using AZtec energy software, for the combined elemental X-ray image.

3.3.2 Electron probe microanalysis

Major and minor-element compositions of minerals were determined using JEOL JXA-8530F electron probe micro-analyzers (EPMA) at the NIPR. Olivine, chromite, ilmenite, troilite, and Fe-metals were analyzed with a beam current of 30 nA by a focused beam, plagioclase (maskelynite) with a current of 10 nA by a focused beam, and phosphates with a beam current of 5 nA by a broad beam (~5 μm in diameter), all at 15 kV. Data were reduced using a ZAF correction procedure. The typical counting time for all elements in minerals except phosphates was 30 s except for Na. The counting time for phosphates was 20 s except for F (5 s). The Si, Mg, Fe, Mn, Ca, Na, P, and Al were analyzed using PET, PETH, LIF, LIFH, and LDE spectrometer crystals. The standards used for elements are natural and synthetic materials. The results are given in **Table 3.1**.

3.3.3 Inductively coupled plasma mass spectrometry

3.3.3.1 Bulk major and trace element analysis

Given the coarseness of constituent primary mineral phases in A-881757 and the limited masses typically available for study, a single reported analysis may not be truly representative of the average bulk composition of the sample. In this study, for obtaining a representative bulk chemical composition for A-881757, homogenization

of a substantial amount of the sample (0.71 g) was achieved for a texturally and mineralogically representative sample to avoid sampling bias.

Analytical procedures were undertaken at the Scripps Isotope Geochemistry Laboratory (SIGL) and Physical Research Laboratory (PRL). For major and trace element abundances, a ~50 mg aliquot of homogenized sample powder was digested in Teflon-distilled concentrated HF (4 mL) and HNO₃ (1 mL) for >72 hrs on a hotplate at 150°C, along with total procedural blanks and terrestrial basalt and andesite standards (BHVO-2, AGV-2). Samples were sequentially dried and taken up in concentrated HNO₃ to destroy fluorides, followed by doping with indium to monitor instrumental drift during analysis, and then diluted to a factor of 50,000 for major-element determination and 5000 for trace-element determination. Major-element abundances were obtained using a ThermoScientific iCAP Qc quadrupole inductively coupled plasma mass spectrometer (ICP-MS) in low resolution mode. For major-elements, Si was derived by difference. The reproducibility of other elements measured on BHVO-2 reference material was better than 3%, except Na₂O (7.1%). The results are provided in **Table 3.2**.

3.3.3.2 In-situ trace element analysis

Trace element abundance analysis of pyroxene, plagioclase and symplectites was conducted by laser ablation inductively coupled plasma mass spectrometry (LA-ICP-MS) at the NIPR using a CETAC LSX-213 laser ablation system coupled to a Thermo Element XR Mass spectrometer with line and spot analysis modes. Line analyses (1-2 mm long) were made using a 50 µm beam diameter, at 10 µm s⁻¹, and 20 Hz repetition rate. Spot analyses were made using a 50 µm spot at a 10 Hz repetition rate, with 150 shots per spot. Isotope peaks were collected in low-resolution mode (R~400) with triple-mode detection. The measured isotopes were ²⁹Si, ³¹P, ⁴⁴Ca, ⁴⁵Sc, ⁷¹Ga, ⁷⁴Ge, ⁸⁵Rb, ⁸⁸Sr, ⁸⁹Y, ⁹⁰Zr, ⁹³Nb, ¹³⁸Ba, ¹³⁹La, ¹⁴⁰Ce, ¹⁴¹Pr, ¹⁴⁵Nd, ¹⁴⁷Sm, ¹⁵¹Eu, ¹⁵⁸Gd, ¹⁵⁹Tb, ¹⁶⁴Dy, ¹⁶⁵Ho, ¹⁶⁶Er, ¹⁶⁹Tm, ¹⁷⁴Yb, ¹⁷⁵Lu, ¹⁸⁰Hf, ¹⁸¹Ta, ²⁰⁸Pb, ²³²Th, and ²³⁸U. All peaks were acquired by peak jumping between peak tops with a 10% mass window and 50-100 milliseconds of acquisition time on the peak top. Elemental abundances were

calculated using relative sensitivity factors (RSFs) obtained from USGS glass BHVO-2G and from NIST SRM 610 glass reference material (Jochum et al., 2011). SiO₂ concentrations determined by EPMA were used as internal standard. ²³²Th/¹⁶O/²³²Th ratios were tuned to ~0.4-0.7%. The limit of detection was defined as 3 times the standard deviation of background signal. The reproducibility of standards during each analytical session was better than <5% (RSD) for all the minor and trace elements in minerals. In the case of Fayalite-Hedenbergite-Silica symplectites, reproducibility of minor and trace elements was better than 10%. For all analytical sessions, accuracy was better than 20%. The results are provided in **Table 3.3**.

3.3.4 Mantle melting model

The batch and fractional melting to calculate the REE concentrations in the parental melts to ascertain the petrological history of the samples, assuming that each mineral phase melts in proportion to its modal abundance in the source i.e., modal melting scenario. In most cases, the bulk rock composition was taken as a parental melt composition for the reasons discussed in Section 3.3.6. Assuming the parental melt compositions represent the primary melt and no major process had occurred to significantly change the REE composition between source partial melting and parental melts, the degree of partial melting that likely occurred to generate each rock was estimated. The chemical modelling, similar to Snyder et al. (1992) and Hallis et al. (2014), was applied assuming an initial LMO source REE composition of 3 × chondrite REE composition, using the rationale of Hughes et al. (1989). With the advancement of LMO crystallization, equilibrium crystallization gave way to fractional crystallization at about 50-70 PCS (Snyder et al., 1992; Shearer and Papike, 1999; Elardo et al., 2014; Rapp and Draper, 2018; Johnson et al., 2021). Plagioclase appeared on the liquidus just after ~75 PCS in the modelling, similar to experimental and thermodynamic modelling results (Rapp and Draper, 2018; Johnson et al., 2021). Given that the YAMM, Kalahari 009 meteorites and Luna 24 ferrobasalts are the low-Ti varieties with low REE abundance and had slight negative to positive Eu anomaly, the

best fit was obtained by assuming a modal mineralogy close to 75-80 PCS LMO

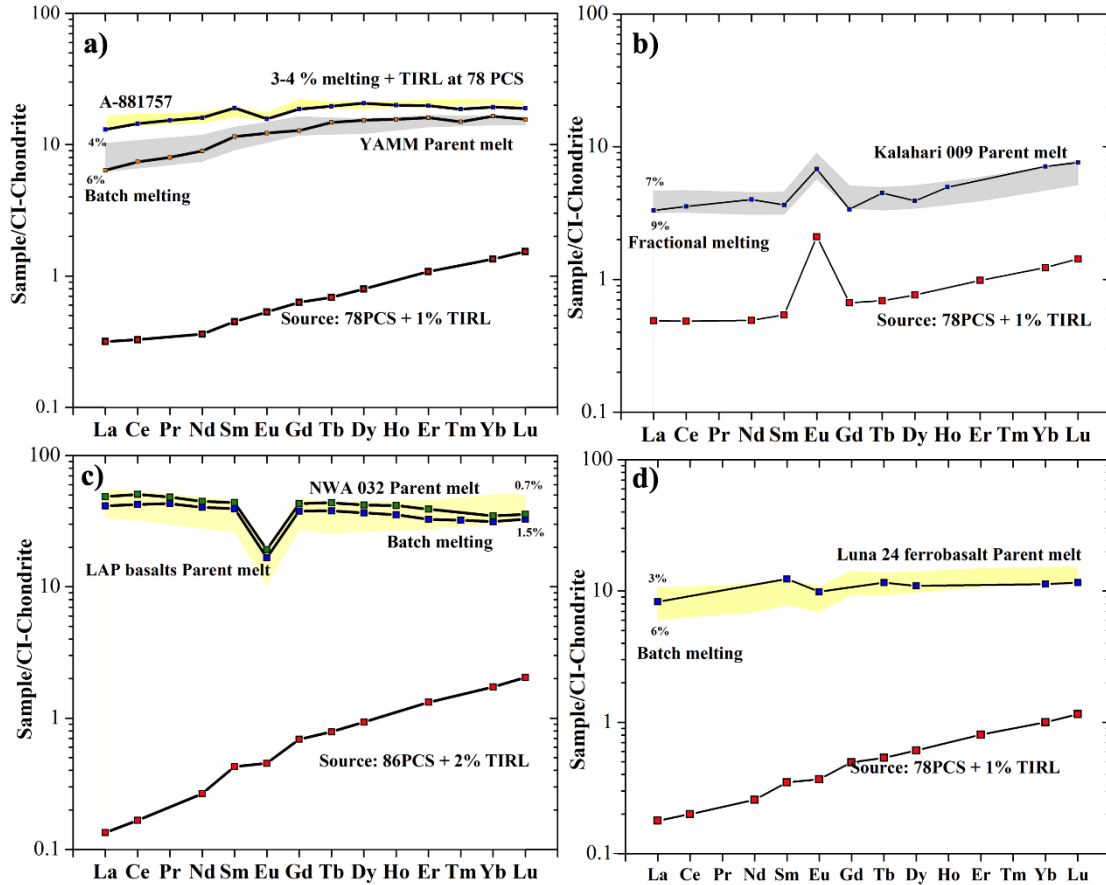


Figure 3.4 Source composition deduced from trace element modeling for YAMM and other KREEP-free (source) basalts. a) Grey area denotes the melt produced by 4-6% partial melting of the mantle source (78 PCS + 2 TIRL; PCS: percent crystallized solid; TIRL: trapped instantaneous residual liquid). Mineral modes in the source are assumed to be 40 vol. % olivine, 40 vol. % orthopyroxene, 19 vol. % pigeonite, and ~1 vol. % plagioclase. A-881757 similarly can be produced by 3-4% partial melting with presence of trapped liquid at 78 PCS. b) Grey area denotes the melt produced by 7-9% partial melting of mantle source at 78 PCS + 1% TIRL with assumed modal mineralogy of 52 vol. % olivine, 23 vol.% orthopyroxene, 17 vol. % pigeonite, and ~8 vol. % plagioclase. c) Yellow area highlights the melt produced by very low (0.7–1.5%) partial melting of mantle source (86 PCS + 2% TIRL) with assumed mineral mode of 52 vol. % olivine, 23 vol. % orthopyroxene, 23 vol. % pigeonite, and 2 vol.% augite for NWA 032 and 52 vol. % olivine, 23 vol. % orthopyroxene, 23 vol. % pigeonite, ~1 vol. % augite and ~1 vol. % plagioclase for LaPaz Icefield (LAP) basalts. d) yellow area indicates the melt produced by 3-6% partial melting of mantle source (78 PCS + 1% TIRL) with assumed mineralogy of 48 vol. % olivine, 23 vol. % orthopyroxene, 23 vol. % pigeonite, 3 vol. % augite and 3 vol. % plagioclase. The additional details are described in Sections 3.3, 3.4.3 and **Table 3.5**.

crystallization with addition of 1-2 % TIRL (**Figure 3.4** and **Table 3.4**). While for NWA 032 and LAP basalts, the estimated model mineralogy was obtained at 86 PCS with the addition of 1-2 % TIRL (**Figure 3.4** and **Table 3.4**). All deduced source modal mineralogy shows a dominance of clinopyroxene (pigeonite) over early formed olivine and orthopyroxene with small amount of plagioclase (Sections 3.4.3, 3.4.5) suggesting that KREEP-free (source) basalts were sourced from a pyroxene-rich mantle. The individual source mineralogy of the studied samples and their feasibility is discussed in Section 3.4.3 and 3.4.5. The REE partition coefficients for olivine (McKay, 1986), orthopyroxene (Yao et al., 2012), augite (Yao et al., 2012), pigeonite (McKay et al., 1991) and plagioclase (Phinney and Morrison, 1990), are shown in **Table 3.5**.

Batch and fractional melting are two end member processes and in nature partial melting can be a combination of the two. Batch melting is calculated using the equation: $C_L/C_0 = 1/(D_0 + F \times (1 - D_0))$, while fractional melting is calculated using equation: $C_L/C_0 = (1/D_0) \times (1 - F)^{(\frac{1}{D_0} - 1)}$, where C_L is the weight concentration of a trace element in the melt, C_0 is the weight concentration of a trace element in the original cumulate source, F is the weight fraction of melt produced and D_0 is the bulk distribution coefficient of the original solid material. The bulk distribution coefficient is calculated by multiplying each mineral partition coefficient with the fraction of that mineral in the source.

3.3.5 Construction of P-T path for YAMM basalts

The MELTS algorithm version 1.2.0 (Ghiorso and Sack, 1995; Asimow and Ghiorso, 1998) was utilized to model fractional crystallization of A-881757 and the other YAMM members. Previous studies have shown that these phase diagrams are capable of providing model melting and crystallization calculations for comparison with petrographic observations during terrestrial (e.g., Asimow and Longhi 2004; Smith and Asimow 2005), martian (e.g., Liu et al., 2013; Basu Sarbadhikari et al., 2016, 2017) and lunar (e.g., Day et al., 2006b; Fagan et al., 2014; Arai and Maruyama, 2017; Elardo and Astudillo Manoslava, 2021) partial melting processes. All MELTS models

were run at 1 bar pressure and fO_2 buffered by Fe–FeO (IW; log unit -1), fractionating solids at 5 °C intervals from liquidus temperatures. The starting whole rock composition of YAMM basalts in the model was taken from **Table 3.2**.

The pMELTS calculation was also applied using the alphaMELTS program to construct phase diagrams and to calculate the formation of A-881757 as a function of pressure (P) and temperature (T). A set of saturation curves in the P – T diagram along the appearance of each phase were traced in phase diagram mode. The model is based on phase equilibrium calculations and uses an internally consistent thermodynamic dataset (Asimow and Ghiorso, 1998). Phase diagram calculations further allow the modes and composition of the mineral and melt phases to be tracked through P – T space, which along with the aid of petrographic observations can yield the P – T path of evolution of A-881757 and other associated meteorites. Isoleth lines in the P – T phase diagram for pyroxene and plagioclase composition were plotted at a regularly-spaced grid of control points using the “ptpath” mode of alphaMELTS, with contours drawn manually by tracing the output. Isoleth contours were plotted for molar Mg/(Mg+Fe) [X_{Mg}] of clinopyroxene and olivine, molar Ca/(Ca+Fe+Mg) [X_{wo}] of clinopyroxene, and molar Ca/(Ca+Na+K) [X_{An}] of plagioclase within a range of pressure (12.0–0.001 kbar), temperature (1500–1000 °C), and fixed fO_2 (IW-1.0) conditions. Additionally, the total melt fraction lines (X_{total}) were also outlined at regular intervals.

3.3.6 Estimation of pressure (P) and temperature (T)

I applied two methods to estimate the pressure and temperature condition of the studied rocks. First, the pMELTS model calculations. The pMELTS mode (Smith and Asimow, 2005) of program alphaMELTS, which is based on equilibrium phase diagram calculations and uses an internally consistent thermodynamic data set (e.g., Ghiorso et al., 2002; Asimow and Longhi, 2004), was used to calculate formation T and P of A-881757, other YAMM and non-KREEP basalts. Since A-881757 and other YAMM meteorites are not extensive fractionation products and rather represent parental melt composition from their mantle source, an equilibrium batch crystallization is more

suitable than the fractionation process (*see section 3.4.4*). Therefore, the equilibrium phase diagram calculation method may infer actual P – T conditions.

Second, thermobarometry techniques was used. With no signs of extensive fractional crystallization, the composition of the most Mg-rich minerals (high Mg#) were considered to be in equilibrium with the parental melt and were chosen for the thermobarometric calculations (*see section 3.4.4*). The primary and the first crystallization phase in A-881757 and other YAMM meteorites is clinopyroxene. clinopyroxene-liquid (Putirka, 2008), clinopyroxene-only (Putirka, 2016; Wang et al., 2021) thermobarometry and olivine-liquid (Beattie, 1993) thermometry were used to estimate the formation pressure and temperature of the YAMM basalts and other

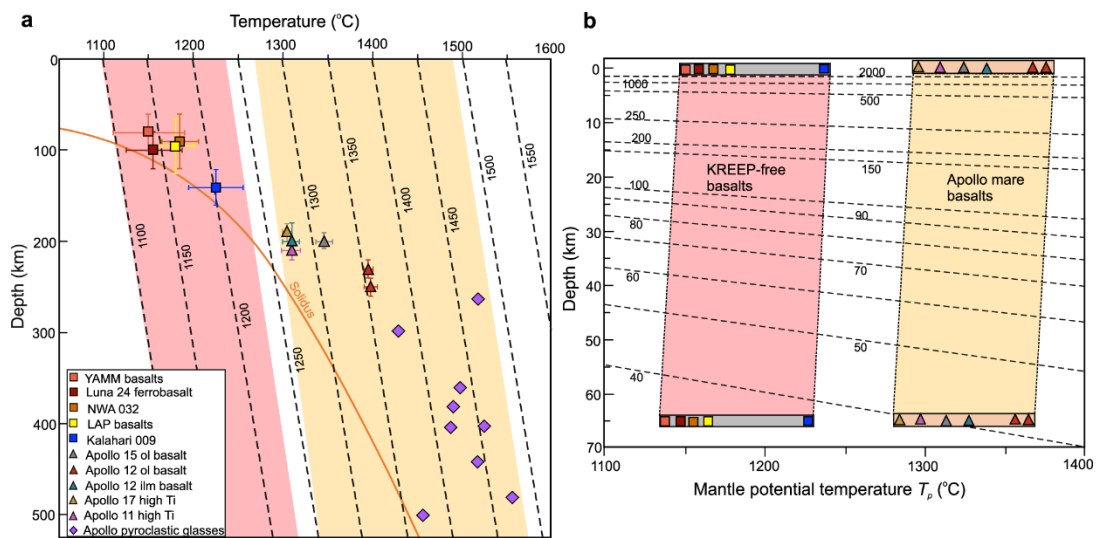


Figure 3.5 Formation temperature (T), pressure (P) and surface heat flow of KREEP-free (source) basalts compared to other lunar lithologies. a) The KREEP-free (source) basalts (red field) show lower formation P – T (see Methods and Supplementary Data 4) than Apollo mare basalts and pyroclastic glasses (orange field). Mantle potential temperatures (T_p) in °C, are shown as dashed lines. The estimates of P – T for pyroclastic glasses are multiple saturation point data and are adopted from Elardo et al. (2015), Elkins-Tanton et al. (2004) and references therein. The P – T for the KREEP-free (source) and Apollo mare basalts are obtained from pMELTS and thermobarometry. Solidus curve is drawn based on Elkins-Tanton et al., (2004, 2011). b) Surface heat flow is calculated assuming variable depth (0–65 km) of magma stalling. For a constant assumed depth, KREEP-free (source) basalts show lower estimated heat flow (shown as dashed lines in mW/m^2) than Apollo mare basalts (Methods and Supplementary Data 4). Lunar pressure–depth relationship is from ref. (Elkins-Tanton et al., 2011).

studied rocks. The list of thermobarometers along with the standard error of estimate (SEE) associated with each are compiled in Putirka (2008). In the case of a sample with olivine on their liquidus, olivine-liquid thermometry was performed using liquid (whole rock) composition (Beattie, 1993). This model is preferred over others because of its insensitivity to the fO_2 and the lowest SEE of $\pm 44^\circ\text{C}$. For calculations, a range of pressures estimated from phase diagram mode pMELTS, as well as clinopyroxene thermobarometers were considered.

For YAMM meteorites which lack olivine, clinopyroxene-liquid and clinopyroxene-only thermobarometry was applied. Equation 30 (for P) and 34 (for T) from Putirka, (2008) for clinopyroxene-liquid thermobarometry was used. The SEE for the pressure and temperature are ± 3.6 kbar and $\pm 45^\circ\text{C}$, respectively. The obtained results for the clinopyroxene-liquid thermobarometry are affected by volatile (Na) loss due to the open furnace nature of earlier experiments leading to systematically high P - T estimates (Tormey et al., 1987). Clinopyroxene-only thermobarometers, however, obviate this problem. Equations 32a (for P) and 32d (for T) from Putirka, (2008), and equations 1 (for P) and 2 (for T) from ref. (Wang et al., 2021) were utilized for clinopyroxene-only thermobarometry. The given SEE for the equations 32a and 32d is ± 3.1 kbar and $\pm 58^\circ\text{C}$, respectively. Wang et al. (2021) provided a new clinopyroxene-only thermobarometer, which is applicable to most basaltic-andesitic compositions and is insensitive to the fugacity conditions (*Fig. 8* of Wang et al., 2021) with $\pm 36.6^\circ\text{C}$ and ± 1.66 kbar SEE. Further, the range of pressure and temperature obtained from both the methods in Section 3.4.3 and **Table 3.6** were compared. The result is plotted in **Figure 3.5a**.

3.3.7 Estimation of mantle potential temperature

The estimated pressure and temperature of formation of the YAMM basalts allow us to place further constraints on the mantle potential temperature for the Moon and its plausible evolution, following the approach of Filiberto and Dasgupta (2011,

2015). The calculation was performed first by evaluating the percentage of melt fraction needed to produce the primary magma composition from trace element modelling (Section 3.4.3). Further, to calculate the mantle potential temperature, T_p , of the lunar mantle, the average pressure and temperature of the bulk Moon composition was corrected to zero pressure using a lunar mantle adiabatic gradient of 0.17 K/km (Elkins-Tanton et al., 2004). The effect of latent heat of fusion on the temperature was normalized using the expression $\Delta T_{fus} = F \left(\frac{H_{fus}}{C_p} \right)$, where F is the melt fraction; H_{fus} ($6 \times 10^5 \text{ J K}^{-1}\text{kg}^{-1}$; Laneuville et al., 2013) is the heat of fusion; and C_p ($1000 \text{ J K}^{-1}\text{kg}^{-1}$; Laneuville et al., 2013) is the heat capacity at a constant pressure. Finally, using the formula:

$$T_p = T_{avg_eq} + \Delta T_{fus} - \Delta T_{lg} \quad (3.1)$$

where T_{avg_eq} is the average equilibrium (formation) temperature; ΔT_{fus} is the latent heat of fusion; and ΔT_{lg} is the lunar temperature gradient correction for adiabatic cooling, mantle potential temperatures were estimated.

3.3.8 Estimation of surface heat flow

The thermal boundary layer structure of a terrestrial body mainly comprises of two parts; in the upper part (crust and upper mantle), heat is transported by conduction while convection dominates in the lower part (lower mantle), also called the convective boundary layer. In a steady state scenario and in the absence of heat-producing elements, heat flow is supposed to be constant in the conductive crust, suggesting a relatively constant temperature gradient for constant thermal conductivity. The calculated steady state heat flux at the base of the lithosphere may directly represent the surface heat flux (assuming no contribution of heat sources in crust and lithospheric mantle). Therefore, in the absence of heat-producing elements, the heat flow is calculated using the relationship between the depth and the mantle potential temperature (Jaupart and Mareschal, 2015). The steady state equation:

$$Q = k_{crust} \left(\frac{T_p - T_s}{d} \right), \quad (3.2)$$

where Q is the heat flow at the surface; k_{crust} is the thermal conductivity of lunar crust; T_p is the mantle potential temperature; T_s is the surface temperature; and d is the depth of the conductive (crust) - convective (mantle) boundary layer that is the thickness of crust. Considering the persisting uncertainty in the lunar thermal boundary layer structure and its rheological properties, I took a simplistic case where I calculated the heat flow assuming a constant thermal conductivity of crust, $k_{crust} \sim 2.0 \text{ W m}^{-1} \text{ K}^{-1}$ (Maurice et al., 2020) and variable thickness of conductive boundary layer (0-60 km), consistent with the GRAIL observations (Wieczorek et al., 2013). The variable crustal thickness allows us to compare the thermal condition during the placement of the non-KREEP basalts and Apollo mare basalts, independent to their age and source location (**Figure 3.5b**). Heat flow values are reported for varying depth in **Table 3.6**.

3.4 Results

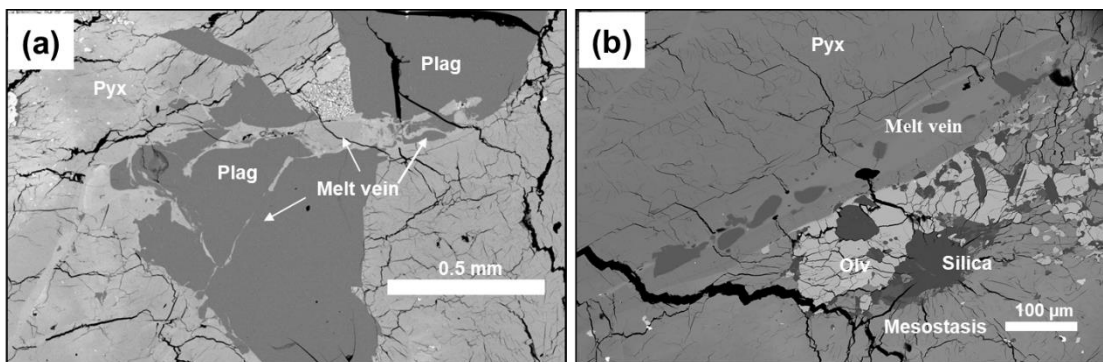


Figure 3.6 BSE images of A-881757 highlighting pervasive effects of melt vein (a-b). (a) A melt vein along plagioclase and pyroxene. (b) A melt vein also found close to mesostasis and pyroxene with some plagioclase grains occurring within them.

3.4.1 Petrography and Mineral chemistry of A-881757

Meteorite A-881757 is comprised of relatively large grains of pyroxene (2-8 mm; ~ 53 vol. %) and plagioclase (1-3 mm; ~ 33 vol. %) along with discrete patches occupied by late phases (symplectites and mesostasis) (**Figure 3.3** and **Table 3.7**). Symplectites (~ 8 vol. %) occur throughout the sections studied, with fayalite, pyroxene and silica as major constituents. The mesostasis phase (~ 6 vol. %) include fayalite (~2 vol. %), troilite (FeS; 0.5-1 vol. %), ilmenite (FeTiO₃; 1 vol%), silica phases (~1 vol.%), a P-rich phase (<1 vol.%), K-feldspar (<<1 vol. %), and spinel (~1 vol%). Fractures are

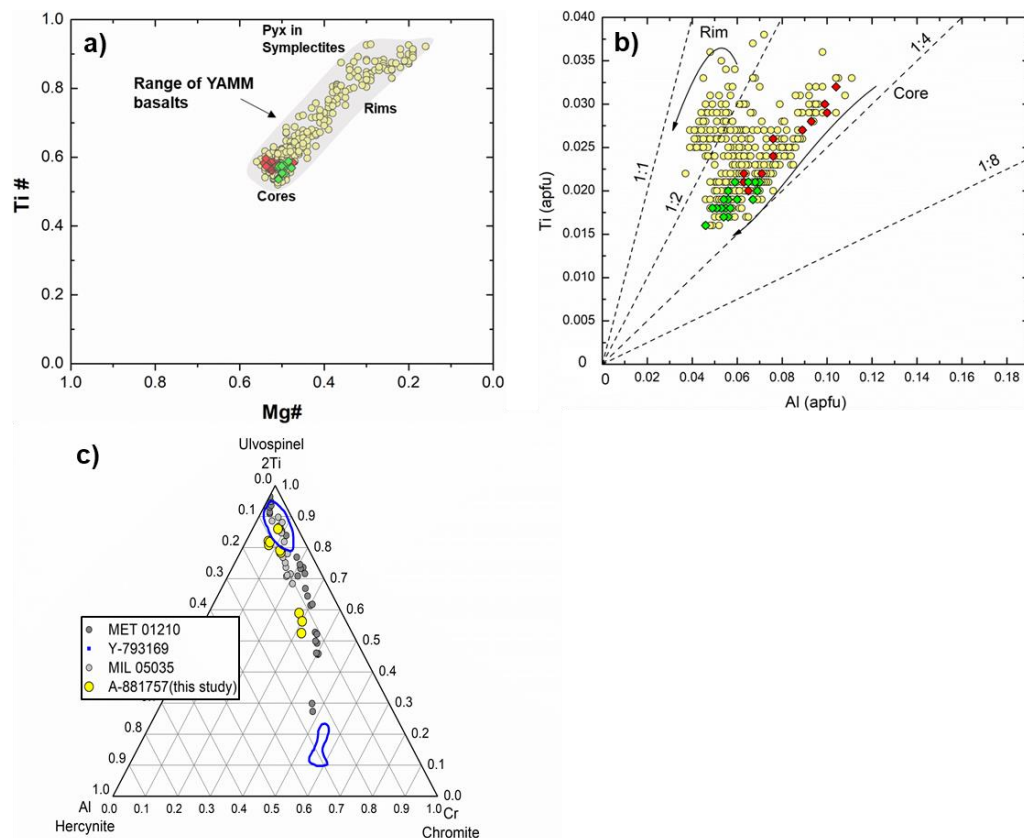


Figure 3.7 Pyroxene and Spinel mineral compositions for A-881757. (a) a plot of Ti# (Ti/(Ti+Cr)) versus Mg# (Mg/(Mg+Fe)) showing progressive Fe-enrichment observed in A-881757 pyroxenes. Grey area indicates results from other YAMM basalts: MIL 05035, MET 01210 and Y-793169. (b) Ti–Al systematics of pyroxenes illustrating path of crystallization trends. The ratio shows a shift from $\frac{1}{4}$ to $\frac{1}{2}$ suggesting an increase in Ti content. The red and green data points corresponds to sector zoned pyroxenes. (c) Compositions of ulvöspinel grains in A-881757, in comparison with ulvöspinel in MIL 05035 from Joy et al. (2008) and Liu et al. (2009), in MET 01210 from Day et al. (2006a), and Y-793169 in Warren and Kallemeyn, (1993).

observed throughout the sample with cracks surrounding individual grains and narrower fractures cross cutting grains, particularly of pyroxene. A highly vesicular fusion crust also exists (**Figure 3.3**). Melt veins (perhaps shock-induced) are present in both the sections (**Figure 3.6a**). The melt veins, which contains different phases within a glassy matrix, have formed from melting of plagioclase grains (**Figure 3.6b**).

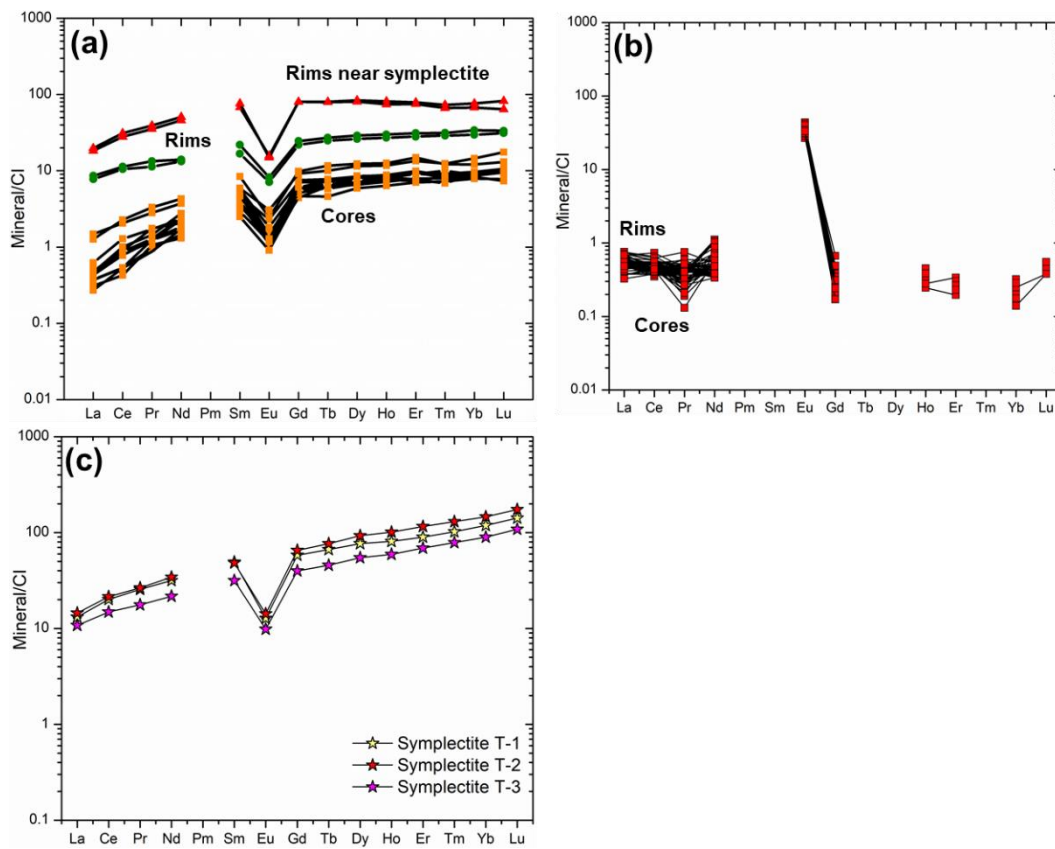


Figure 3.8 CI-normalized rare earth element patterns for A-881757 pyroxenes (a), plagioclase (b) and symplectites (c). Representative data of these minerals are provided in Table 4. CI chondrite normalization from McDonough and Sun (1995).

3.4.1.1 Pyroxenes

Pyroxene is the most abundant phase (53 vol. %) and is surrounded by plagioclase. The pyroxene grains are coarser than most previously reported mare basalt pyroxenes and show fine exsolution (~1 μm) features. Pyroxene grains in A-881757 cover a wide spectrum of compositions from augite to pigeonite. Iron content increases from core to rim for all clinopyroxenes (**Table 3.1**). Almost all pyroxenes progressively

grade outwards into a late Fe-rich phase assemblage of symplectites and mesostasis (**Figure 3.3**). The Fe/Mn ratios of the primary pyroxenes (~58) follow a typical lunar trend (Papike et al., 2003). The Mg# (molar $\text{Mg}^{2+}/[\text{Fe}^{2+} + \text{Mg}^{2+}]$) value of the most Mg-rich cores are 58% for augite and 55% for pigeonite. The Mg# and Ti# (molar $\text{Ti}/[\text{Ti} + \text{Cr}]$) correlations of pyroxenes has been previously interpreted to illustrate the effect of melt fractionation and simultaneous crystallization of different phases (**Figure 3.7a**; Bence and Papike, 1972). These results are in agreement with previous analyses of A-881757 by Yanai (1991) and Takeda et al. (1993), as well as of MIL 05035 (Liu et al., 2009). The increasing Ti# with decreasing Mg# is consistent with a typical lunar

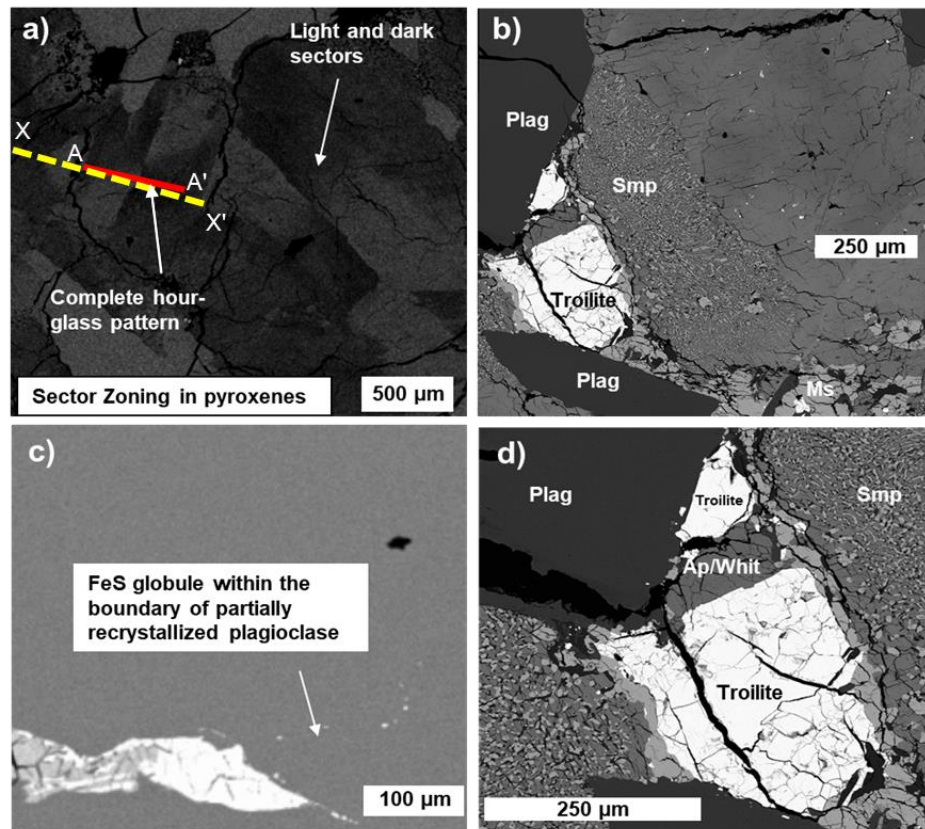


Figure 3.9 X-ray (a) and BSE (b-d) images showing pyroxene, plagioclase and late crystallizing phases in A-881757. (a) Ca X-ray image showing complex zoning in A-881757 where near-complete hour-glass sector zoning is preserved within pyroxene grains. The red line marked as A-A' is transect for EPMA analysis and yellow dashed line marked transect of LA-ICPMS measurement. (b) Plagioclase embedded within the late stage phases. (c) Maskelynitized plagioclase with trains of FeS globules lining the grain boundary or sealed fractures. (d) BSE images of late-crystallizing mineral assemblages in A-881757.

basalt fractionation trend (**Figure 3.7a**; Bence and Papike, 1992), where the slope value abruptly changes at $Mg\#=0.3$, indicating initiation of crystallization of Ti-bearing phases, such as ilmenite and ulvöspinel. A plot of molar Ti versus Al (**Figure 3.7b**) suggests that pyroxenes crystallized over an extended temperature interval. The changing Ti/Al reflects the onset of plagioclase crystallization, simultaneous with pyroxene crystallization (Day et al., 2006a). Chondrite-normalized clinopyroxene rare earth element (REE) abundances in A-881757 shows sub-parallel patterns, convex upward profiles, and increasing abundances with increasing Fe substitution (**Figure 3.8**). All pyroxenes have lower concentrations of the light-REE (LREE) relative to the heavy-REE (HREE) ($[La/Lu]_N=0.02-0.31$) and negative Eu-anomalies with Eu/Eu^* from 0.20-0.41 (**Table 3.3**).

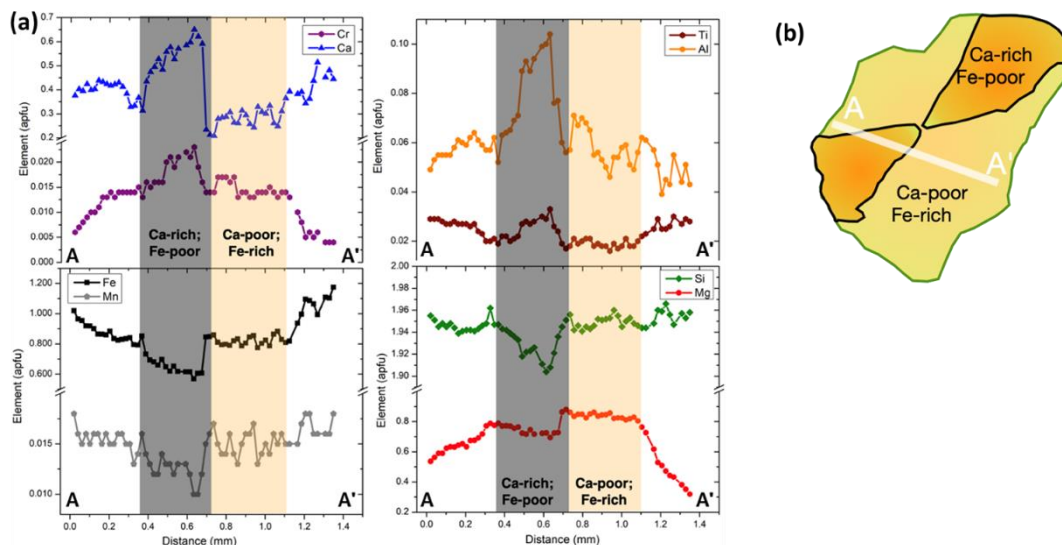


Figure 3.10 Electron microprobe transects across sector zoned pyroxenes in A-881757. The location of transects (A-A') is marked in **Figure 3.9a**. Electron microprobe transects across sector zoned pyroxenes in A-881757. (a) The Ca-rich and Fe-poor zones in the sector are marked by gray background while Ca-poor and Fe-rich sectors are marked by orange. Both ends (white regions) in the transect are Fe-rich rims. The increase in Ca content is correlated with increase in Al, Cr, Ti and decrease in Si, Mg, Fe and Mn. (b) a schematic showing the hour-glass sector zoning in A-881757.

The A-881757 pyroxenes show extensive compositional zoning which is visible in X-ray maps (particularly Ca) of the studied sections (**Figure 3.9a**). A typical hourglass pattern of sector zoning is visible in some pyroxene grains of both the sections and EMP traverses clearly resolve different sectors in these pyroxenes

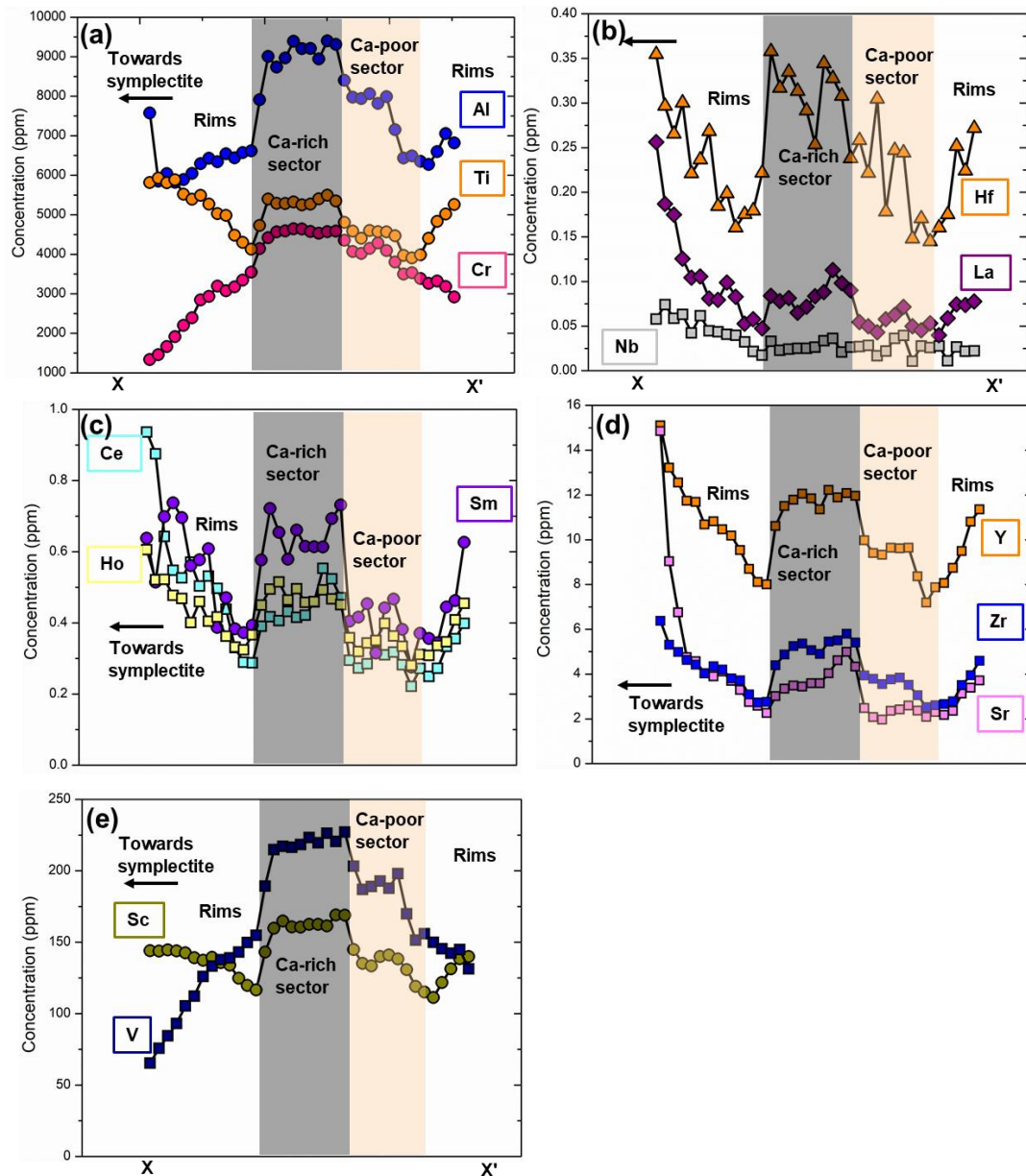


Figure 3.11 The minor and trace element variation in sector zoned pyroxenes (a-e) in A-881757 along X-X' transect shown in **Figure 3.9a**. The compositional variation among sectors can be easily resolved in most of the trace elements. The partitioning pattern of High field strength elements (HFSE) and rare earth elements (REE) show similarity with Al partitioning in tetrahedral (T) sites suggesting a strong correlation in between them.

(Figures 3.9a, 3.10). Hargraves et al. (1970), Hollister and Hargraves (1970) and Boyd and Smith (1971) reported sector zoning in pyroxene phenocrysts from Apollo 11 (10047, 10058 and 10062) and Apollo 12 (12021) mare basalt samples. Although a complex zoning pattern has been previously reported for unbrecciated lunar basalt meteorite MIL 05035 (Liu et al., 2009), clear indication for sector zoning has not been observed. Here, I present the a near complete preservation of mm-scale hour-glass

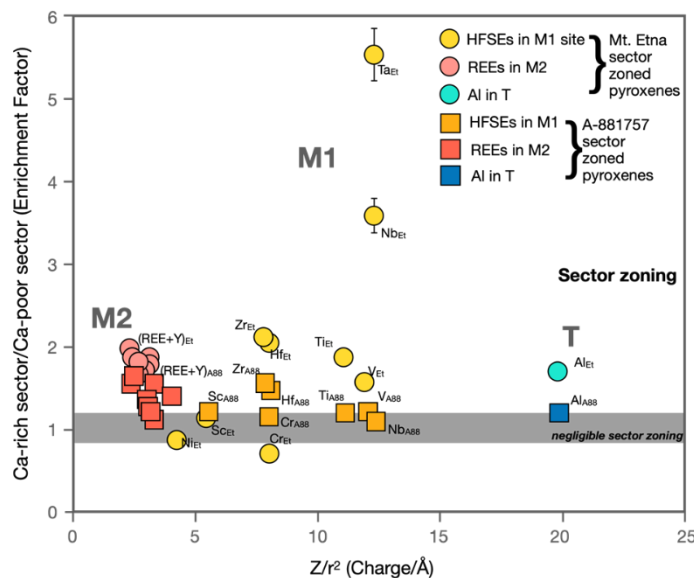


Figure 3.12 Comparison of enrichment of minor, trace along with some major elements in Ca-rich sector relative to Ca-poor sector of sector zoned pyroxenes of A-881757 and Mt. Etna lavas, plotted as a function of ionic potential (ratio of the charge of the cation expressed as Z and the square of the radius of cation r in IV-fold (Tetrahedral, T), VI-fold (Octahedral, M1) and VII-fold (Octahedral, M2) coordination). The plot is after Shimizu, (1981) and Ubide et al., (2019b). The radii values were taken from Shannon, (1976) and data for Mt. Etna pyroxenes were taken from Ubide et al. (2019b). The ionic radius for Aluminum (Al^{3+}) is considered for tetrahedral coordination. The enrichment factor corresponding to Mt. Etna pyroxenes is high when compared to A-881757 pyroxenes. Uncertainties in enrichment factor is calculated as error propagation of the LA-ICPMS data show values which to be smaller than symbols. The data for A-881757 sector zoned pyroxenes is taken along the transect X-X'. Abbreviations: A88- A-881757 sector zoned pyroxenes, Et- Mt Etna sector zoned pyroxenes.

sector zoning in A-881757 basaltic lunar meteorite, and discuss its possible origin and prevailing magmatic environment.

3.4.1.2 Compositional variations across sector zoned pyroxenes

Complex sectors in pyroxene grains occur within the core of the clinopyroxenes from both sections studied (**Figure 3.9a**), but the hour-glass pattern is mostly obliterated by the presence of crystal twins and pervasive residual melt, except in a few grains. Where preserved, hour-glass zoning defines sharp compositional variations. Traverses (as shown in **Figure 3.9a**) along a 1.35 mm segment crossing over the sector zone boundaries in an example clinopyroxene grain show the variations in chemical profiles of the elements Ca, Fe, Mg, Ti, Al, Si, Mn and Cr (**Figure 3.10**). A depletion trend of Si (1.95 to 1.90 apfu), Fe (0.87 to 0.62 apfu), Mg (0.86 to 0.73 apfu) and Mn (0.016 to 0.010 apfu), and an enrichment trend of Ca (0.23 to 0.59 apfu), Al (0.057 to 0.104 apfu), Ti (0.018 to 0.032 apfu) and Cr (0.013 to 0.023 apfu) are evident from Ca-poor sector to Ca-rich sectors. Calcium and Fe abundances show complementary enrichment and depletion with sharp changes in concentration. The observed change for Si is comparatively gradual from the Ca-poor sector to the Ca-rich sector. (**Figure 3.10**). The clinopyroxene sector zoning in A-881757 can be generalized by the equation: $[\text{Si}^{4+} + \text{Mg}^{2+} + \text{Fe}^{2+} + \text{Mn}^{2+}] \rightleftharpoons [\text{Ti}^{4+} + \text{Al}^{3+} + \text{Ca}^{2+} + \text{Cr}^{3+}]$.

In addition to major elements, trace elements analysis along the similar traverse using LA-ICP-MS shows resolvable variations between the sectors (**Table 3.3 and Figure 3.11**). The sector partitioning pattern of incompatible elements, including High Field Strength Elements (HFSE) and REE show remarkable similarity to the Al in Tetrahedral sites and Fe in octahedral sites pattern. Concentrations of highly charged cations such as REE³⁺, Y³⁺, Zr⁴⁺, Hf⁴⁺, and V⁴⁺ in the Ca-rich sector are 1.5-1.7 times greater than concentration in the Ca-poor sector (**Figure 3.12**). Elements Sc, V, Ti and Cr show even lower (~1.2 times) variation between Ca-rich and Ca-poor sector.

3.4.1.3 Plagioclase

Plagioclase (~ 1-3 mm) is the second most abundant phase (33 vol. %) and most grains are maskelynitized. The characteristic lath-shaped form is preserved in the smaller plagioclase grains. Small plagioclase grains are also seen embedded between mesostasis and symplectites (**Figure 3.9b**). A few plagioclase grains show signs of recrystallisation, surrounded by FeS globules (<1 μm diameter) (**Figure 3.9c**). Plagioclase grains have retained their relict compositional igneous zoning even after maskelynitization. The zoning in maskelynite grains range from An₉₆ core to An₈₇ rim (**Table 3.1**). Rims in close contact with the late crystallising phases are An₇₅. The REE concentrations show CI-chondrite normalized patterns typical for lunar plagioclases ([La/Yb]_N = 0.05-0.29) with a strong positive Eu anomaly and a slightly LREE-enriched slope (**Table 3.3** and **Figure 3.8**).

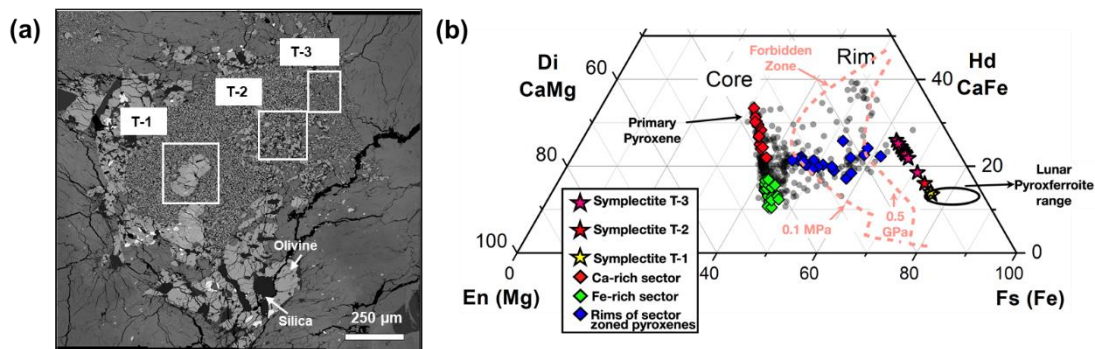


Figure 3.13 Symplectites with different texture and their compositional relations. (a) BSE image showing occurrence of all three symplectites together. (b) Pre-symplectites compositions calculated by reconstruction. Compositional variations within different textural symplectites. The red, blue and green points show composition of sector zoned pyroxenes.

3.4.1.4 Symplectites

Symplectites (6-8 vol. %) occur throughout the studied sections and are usually found associated with the Fe-rich rim of pyroxenes. Fayalite, Fe-rich pyroxene, and silica are the main constituents of symplectites. They are characterized by a small vermicular intergrown fayalite, pyroxene and silica assemblage. In some symplectites close to primary pyroxenes, silica occurs as elongated assemblages at the interface

between the fayalite and Fe-rich pyroxenes, similar to previous observations in A-881757 and its pair MIL 05035 (e.g., Oba and Kobayashi, 2001; Liu et al., 2009). Similar pyroxene dominated symplectites have been observed in some Apollo 11 and 12 high-Fe basalts. High-Mg lunar samples such as mare basalt 15555, dunite 72415 and troctolite 76535 lack pyroxene symplectites; instead, these samples contain distinct symplectites in the vicinity of primary olivine (Bell et al., 1975; Griffiths et al., 2014). In A-881757, most of the symplectites are closely associated with mesostasis phases. Texturally, three sets of symplectites were differentiated (**Figures 3.13, 3.14**). Type-1 symplectites occur close to mesostasis as dense networks of small ($< 10 \mu\text{m}$ sized grains) vermicular intergrown assemblages of fayalite, Fe-rich pyroxene and silica and are fine grained compared to the other symplectites. Type-2 symplectites ($\sim 30 \mu\text{m}$ sized grains) are coarser than the type-1 variety and occur adjacent to the rims of

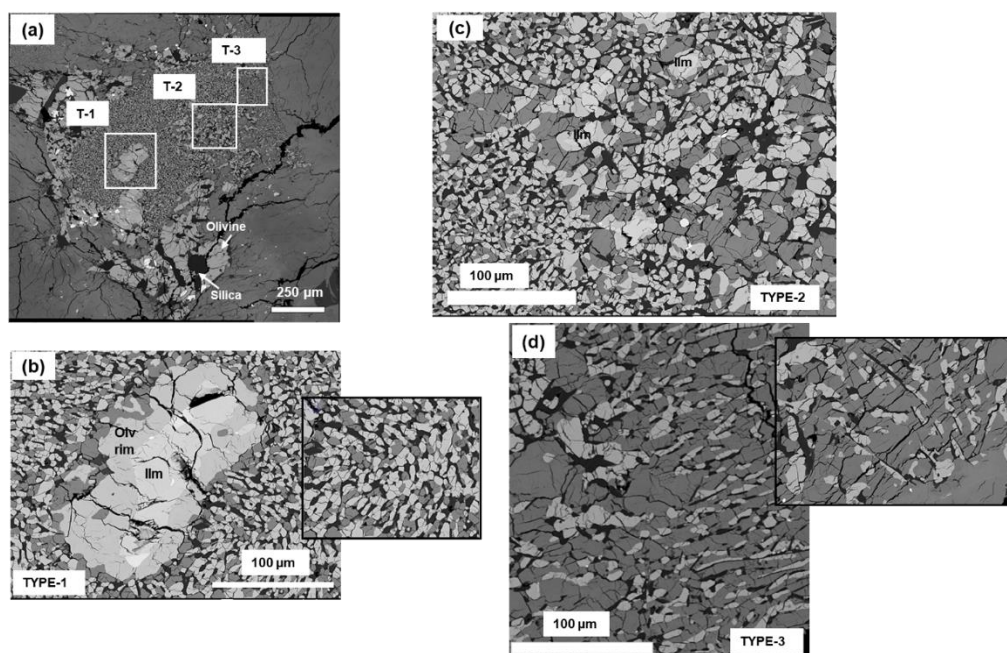


Figure 3.14 Fayalite, Fe-augite and silica symplectites in A-881757 showing three different textures. (a) BSE image showing occurrence of all three symplectites together. (b) Zoomed in Type-1 symplectite with smallest grain size ($< 10 \mu\text{m}$) occurring as a dense network of olivine, pyroxene and silica. They also host ilmenites rimmed by olivine. (c) Zoomed in Type-2 symplectite with $30 \mu\text{m}$ grains lie adjacent to the rims of megacryst pyroxenes. (d) Zoomed in Type-3 symplectite occurs close to fracture and has the coarsest pyroxenes, up to $50 \mu\text{m}$. The symplectites with post fracture marking and micro-faults suggesting formation prior to the fractures.

pyroxenes. Type-3 symplectites occur close to the fractures and consist of most coarse-grained (up to 50 μm sized grains) fayalite, Fe-rich pyroxene and silica than the other two types. Texturally, type-3 symplectites occur in-between type-1 mesostasis and type-2 fractures, indicating a gradational occurrence of the symplectite types. Mineralogically, type-1 and type-3 symplectites host ilmenite grains rimmed by fayalite (**Figures 3.14a, 3.14b**). The measured REE abundance for symplectites in A-881757 have a distinct negative Eu anomaly ($\text{Eu}/\text{Eu}^* = 0.19 - 0.40$) and an increasing HREE profile ($[\text{La}/\text{Lu}]_{\text{N}} = 0.22 - 0.30$) (**Table 3.4** and **Figure 3.8**). These patterns indicate that a consistent compositional evolution of the primary pyroxenes exist even after their breakdown, and the symplectite intergrowths have retained their precursor pyroxene (but evolved Fe-rich) compositions.

3.4.1.5 Oxides and sulfides

Ilmenite grains are usually found sharing their boundaries either with spinel or the rims (20-40 μm thick) of fayalite (**Figure 3.14a**). Their shape varies from elongated subhedral crystals to smaller anhedral aggregates within the late phase assembly. Fayalitic rims surrounding the ilmenite grains have also been reported in Luna 24 samples, suggesting extreme crystal fractionation during silicate liquid immiscibility (Lu et al., 1989).

Spinel crystals occur infrequently as irregular, interstitial grains ($<200 \mu\text{m}$) and are commonly intergrown with ilmenite. Some spinel grains are also rimmed by fayalitic (Fa) olivine of thickness 20-90 μm . Spinel shows a compositional range within the chromite-ulvöspinel solid solution ($2\text{Ti}_{52-85}, \text{Al}_{6-15}, \text{Cr}_{7-32}$) (**Figure 3.7c**).

Troilites (FeS) occur as aggregates of subrounded grains with size ranging from 20 μm (present within the pyroxene rims) to $\sim 300 \mu\text{m}$ (**Figure 3.9d**). They also occur as 1-2 μm globules inside the maskelynitized plagioclase grains (**Figure 3.9c**). In both the studied sections of A-881757, anhedral Fe-Ni metal grains are present: one adjacent to a fracture, sharing boundaries with pyroxene and anhedral troilite; and another associated with ilmenite and spinels.

3.4.1.6 Mesostasis

Mesostasis phases include fine-grained fayalite, troilite (FeS), ilmenite (FeTiO₃), silica, spinel, P-rich phase, and K-feldspar. Texturally, mesostasis occurs along pervasive wide fracture planes. Fayalite (Fo₈₋₁₀) and silica dominate among the mesostasis phases. They occur as a typical ‘swiss-cheese’ textures suggesting that these fayalite grains crystallised at the extreme end-stage of crystallisation, close to the boundary of silicate liquid immiscibility (Taylor et al., 1971; Anand et al., 2003). Silica occurs either as elongated laths (<2 mm length) or as small anhedral (<200 μm diameter) aggregate grains within the mesostasis (**Figure 3.9b**).

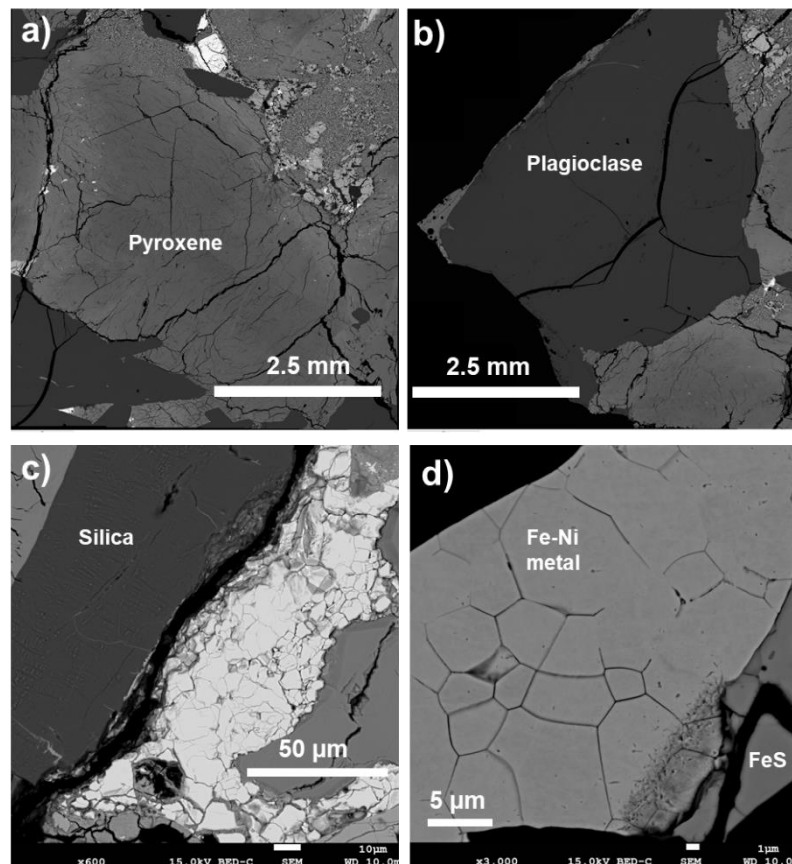


Figure 3.15 Preservation of shock features at various scales in A-881757. (a) Pyroxene with fractures running all along grains. (b) Maskelynitized plagioclase with wide fractures. (c) silica grains showing planar deformations. (d) Fe-Ni metal grains showing polygonal cracks.

Accessory P-rich phases rarely occur in the mesostasis and their grain size varies from 20 to 200 μm (**Figure 3.9d**). A small baddeleyite crystal ($\sim 1 \mu\text{m}$ diameter) was identified within the mesostasis. Similar observations of mesostasis phases are common in low Mg# lunar rocks (e.g., 12063 and 10003), in which mesostasis formed from the immediate host phases (Pernet-Fisher et al., 2014; Potts et al., 2016).

3.4.2 Cooling and shock history of A-881757

The cooling rate of A-881757 was estimated by measuring the width of pyroxene and plagioclase grains, utilizing the experimental study of Grove and Walker (1977) and Grove (1978). The cooling rates obtained from the width of pyroxene grains ($\sim 1.0\text{--}2.0 \text{ mm}$) and plagioclase grains ($\sim 0.5\text{--}1.5 \text{ mm}$) range from $\sim 0.06\text{--}0.2 \text{ }^\circ\text{C/hr}$ and $\sim 0.06\text{--}0.3 \text{ }^\circ\text{C/hr}$, respectively (**Figure 3.9**). The cooling rate of A-881757 is consistent with the results for MIL 05035, $\sim 0.07 \text{ }^\circ\text{C/hr}$ for plagioclase and $\sim 0.2\text{--}0.4 \text{ }^\circ\text{C/hr}$ for pyroxene grains (Joy et al., 2008; Liu et al., 2009). When compared to the other lunar meteorite samples such as the La Paz basalts, MET 01210 and NWA 032 basalts, the obtained cooling rates are within the range of previously estimated values (Day et al., 2006b; Day & Taylor, 2007). The measured cooling rate is lower than the values obtained from Chang'E 5 basalts $\sim 1\text{--}2 \text{ }^\circ\text{C/h}$ to $86 \text{ }^\circ\text{C/h}$ (Neal et al. 2022; Webb et al. 2022).

A-881757 contains abundant shock features evident throughout the sections (**Figure 3.15**). Some of the most evident features include complete maskelynitization of plagioclase and fractures in pyroxenes (**Figures 3.15a, 3.15b**). Shock metamorphic textures in silica such as internal planar deformation features, formation of diaplectic glass and the appearance of crack-like features were observed silica grains (**Figure 3.15c**). There are visible melt veins and recrystallisation textures (symplectites) depicting formation of localized shock-induced features. All these features indicate heterogeneous shock in the range of >10 to $<60 \text{ GPa}$ (Stöffler and Keil, 1991; Bischoff and Stöffler, 1984; Ohtani et al., 2011; Fritz et al., 2017). These observations are

consistent with the previous shock related studies of A-881757 and its pairs such as MIL 05035 (Joy et al., 2008; Liu et al., 2009; Gyollai et al., 2009).

3.4.3 Petrography, mineral and bulk rock chemistry of other KREEP-free (source) basalts

3.4.3.1 Kalahari 009

Kalahari 009 is a monomict breccia with basaltic mineralogy and composition (**Table 3.2**). It is the oldest mare basalt with an age of 4.35 Ga (Terada et al., 2007). The basaltic clast has a coarse-grained sub-ophitic texture with the constituent grains up to 4 mm. Pyroxene and plagioclase are the primary phases of the rock, while olivine and other phases are accessories. Like A-881757, olivine and pyroxene in Kalahari 009 are Fe-rich, and silica occurs in symplectite. The pyroxene and plagioclase show a compositional range of $Wo_{6-41}Fs_{22-67}$ and An_{95-72} , respectively (Sokol et al., 2008). The meteorite is a VLT basalt with unusually low REE abundance (**Figure 3.16** and **Table 3.2**).

3.4.3.2 Luna 24 ferrobasalts

Luna 24 ferrobasalts are soil fragments with ophitic pyroxene and olivine phenocrysts. Other accessory phases are spinels, ilmenite, feldspar, and silica. Pyroxene composition varies from Ca-poor ($Wo_{12}Fs_{36}$) to Ca-rich ($Wo_{25}Fs_{50}$). Olivine is zoned from Fo_{60} to Fo_5 (Vaniman and Papike, 1977). Plagioclase shows compositional variation from An_{96} to An_{86} (Vaniman and Papike, 1977). The soil fragments are low-Ti and marginally high-Al and low-K. The REE abundance of these basaltic rock fragments is low and shows LREE depletion (**Figure 3.16** and **Table 3.2**), similar to sample A-881757 (Ma et al., 1978).

3.4.3.3 Northwest Africa (NWA) 032

NWA 032 is a low-Ti unbrecciated basalt with subophitic-ophitic magmatic textures. The phenocryst population is composed predominantly of olivine (Fo_{65-60}), pyroxene ($\text{Wo}_{20-40}\text{Fs}_{50-60}$ and $\text{Wo}_{10-20}\text{Fs}_{75-85}$ domains), and a small amount of chromite along with a groundmass of feldspar ($\sim\text{An}_{85}$), pyroxene ($\text{Wo}_{15-25}\text{Fs}_{75-99}$), ilmenite, troilite, and trace metals (Fagan et al., 2002). The REE concentrations yield a well-defined Eu anomaly (**Figure 3.16**), and an LREE enriched pattern (Fagan et al., 2002).

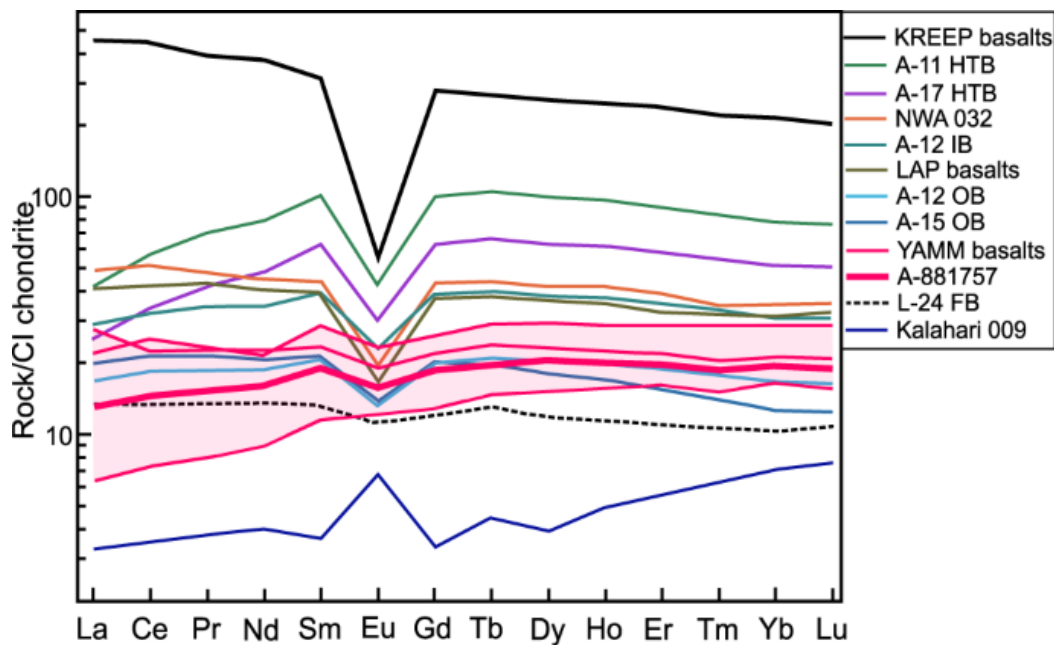


Figure 3.16 Measured REE abundance of A-881757 compared with other YAMM, lunar meteorites and selected Apollo mare basalts. Chondrite-normalized rare earth element plots for YAMM (red), Kalahari 009 (blue), Luna 24 ferrobasalts (FB; dashed line), NWA 032 (orange), LAP basalts (yellow), along with Apollo 12 and Apollo 15 olivine basalts, Apollo 12 ilmenite basalts, Apollo 11 and Apollo 17 high-Ti basalts and KREEP basalts. YAMM basalts along with Luna 24 ferrobasalts and Kalahari 009 show depleted REE pattern while there is a lack of prominent Eu anomaly in YAMM and Luna 24 ferrobasalts, which are distinct from Apollo mare and KREEP basalts. Data Sources: A-881757 (this study); Y-793169 (ref. Warren and Kallemeyn, 1993); MIL 05035 (ref. Liu et al., 2009)); MET 01210 (ref. Day et al., 2006a); Luna 24 ferrobasalts (Vaniman and Papike, 1977); Kalahari 009 (ref. Sokol et al., 2008); Apollo and KREEP basalts (Warren and Taylor, 2014). Abbreviations are A-11 HTB: Apollo 11 high-Ti basalts; A-17 HTB: Apollo 17 high-Ti basalts; A-12 IB: Apollo 12 ilmenite basalts; A-12 OB: Apollo 12 olivine basalts; A-15 OB: Apollo 15 olivine basalts; L-24 FB: Luna 24 ferrobasalts.

3.4.3.4 LaPaz Icefield (LAP) basalts

Low-Ti lunar mare basalt meteorites consist of LAP 02-205, -224, -226, -436, and LAP 03-632, collectively known as LAP basalts. They are holocrystalline basalts containing similar proportions of pyroxene, plagioclase (An_{79-93}), ilmenite, troilite, and free silica, in addition to variable quantities of K-rich glass, ulvöspinel, chromite, phosphates, Fe-Ni metals, baddeleyite, fayalitic ($<Fo_{20}$) and relatively Mg-rich (Fo_{20-67}) olivine (Day et al., 2006b). Pyroxenes show comparable variation from the Mg-rich cores to extremely Fe-rich rims: $Wo_{9-41}Fs_{21-90}$ (LAP 02205), $Wo_{8-39}Fs_{23-86}$ (LAP 02224) and $Wo_{8-40}Fs_{22-87}$ (LAP 02226) (Joy et al., 2005). Plagioclase composition varies from: An_{91-81} (LAP 02205), An_{90-84} (LAP 02224) and An_{90-84} (LAP 02226) (Joy et al., 2005). These meteorites are low-Ti, low-Al, and low-K basalts (**Figure 3.1** and **Table 3.2**). They show elevated REE abundances relative to the other low-Ti basalts (**Figure 3.16**; Day et al., 2006b).

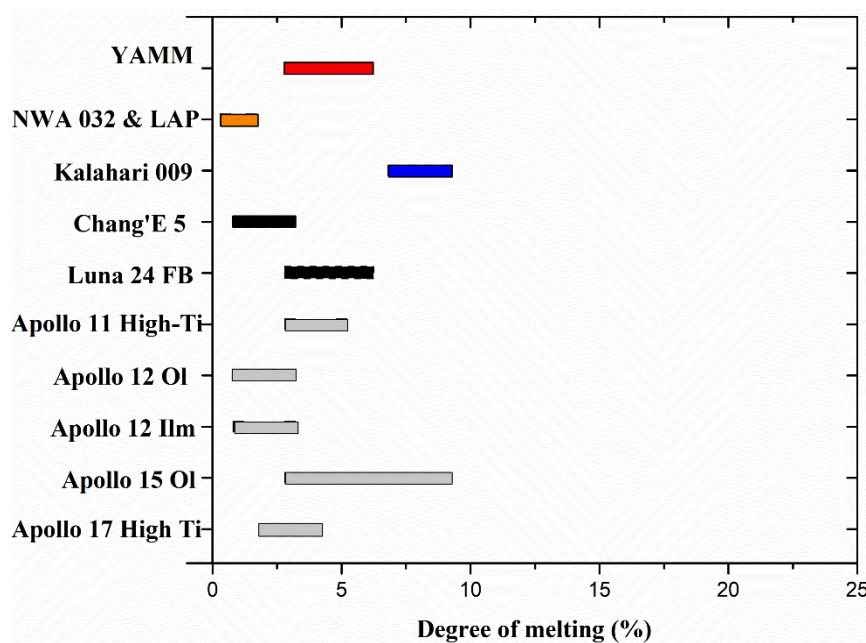


Figure 3.17 The calculated degree of melting for YAMM and other KREEP-free (source) rocks compared to Apollo mare basalts using trace element modeling. Data for degree of melting of the Apollo mare basalts are from Hallis et al., (2014), and the remaining samples are from this study (Methods).

3.4.4 Estimation of parental melt and source composition

To understand the source conditions, the studied samples must represent a parental melt in chemical equilibrium with the mantle source. Earlier studies based on isotopes including Sm-Nd, Rb-Sr, U-Pb, and Lu-Hf have highlighted the depleted mantle source characteristics of YAMM and other non-KREEP basalts (Misawa et al., 1993; Nyquist et al., 2007; Sokol et al., 2008; Liu et al., 2009; Borg et al., 2009; Elardo et al., 2014) (**Figure 3.17**). Since the studied rocks are Fe-rich (Mg# 33-49), estimation of their parent melts is challenging. The low Mg# can either account for the result of extensive fractional crystallization (Grove and Vaniman, 1977; Coish and Taylor, 1978; Day et al., 2006b) or a product of (low-degree) partial melting of heterogeneous Fe-rich mantle (Ryder and Marvin, 1978; Borg et al., 2009; Elardo et al., 2014) (**Figure 3.18**). To address this problem, I examined whether the rocks represent the original melt composition or show any signs of modification via processes such as assimilation and/or crystal fractionation. The approach was first to identify if there is any KREEP component in these rocks by considering the rare earth element (REE) composition. Then, tested any assimilation effect in the studied rocks by considering REE in the most abundant silicate phase pyroxene and plotting the rocks in isotopic ratio diagrams. Finally, it was assessed whether the rocks went through extensive fractionation processes to yield their high Fe-content bulk by considering the exchange coefficients of Fe-Mg between the melt and the most Mg-rich silicate phases that crystallized first from the melt.

Previous studies have shown that changes in the parental melt composition can be traced from their REE, as the distinct source characteristics and magmatic processes would significantly affect the REE composition of parent melt (Day et al., 2006b; Hallis et al., 2014). The absence of characteristically high ratios of HFSE/LREE (HFSE: high field strength element) and LREE/HREE of urKREEP in the studied rocks (A-881757 and other YAMM meteorites) suggest they are devoid of the KREEP component (Warren and Wasson, 1979; Elardo et al., (2014); this study). Also, using the approach of Day et al. (2006b), Similarly, I tracked the assimilation effect, if any, through the

evolving REE composition of pyroxene. A systematic variation of REE in the pyroxenes of MIL 05035 (La/Yb= 0.06-0.17; Joy et al., 2008; Liu et al., 2009) and of the LAP basalts (La/Yb = 0.14-0.26; Day et al., 2006b) was observed, which is consistent with the fractionation trend further implying that no assimilation has occurred in these rocks. Lastly, a plot for the $^{87}\text{Rb}/^{86}\text{Sr}$ source region versus $^{147}\text{Sm}/^{144}\text{Nd}$ source region provides additional evidence for these rocks' unassimilated source (Figure 3.17).

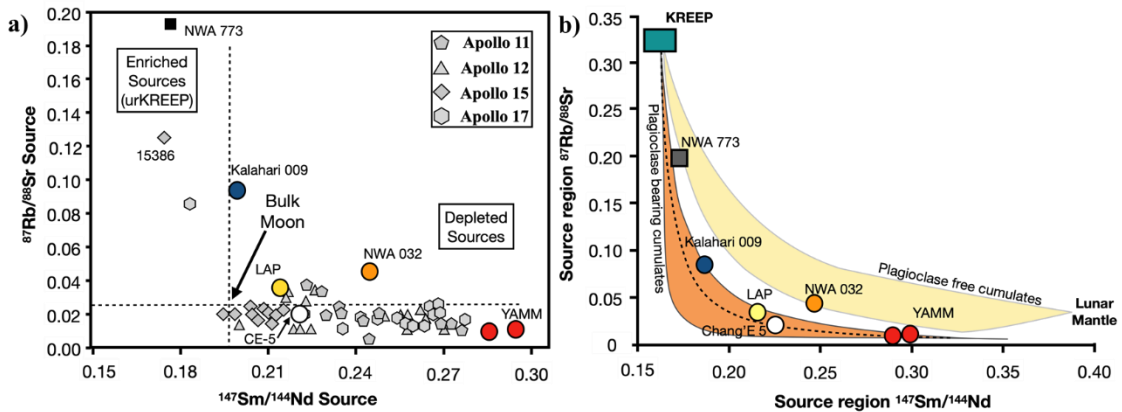


Figure 3.18 Calculated $^{87}\text{Rb}/^{86}\text{Sr}$ versus $^{147}\text{Sm}/^{144}\text{Nd}$ for source regions of Apollo mare basalts and meteorites. a) Illustration of the relationship of KREEP-free (source) to KREEP-related samples (after Borg et al., 2009). YAMM basalts (MIL 05035 and A-881757) are the most depleted variety among the lunar samples. b) The figure describes the mixing line of the KREEP (adapted from Borg et al., 2009). Most non-KREEP samples plot far away from the KREEP basalts providing evidence of an unassimilated source. Data Source: Plot of $^{87}\text{Rb}/^{86}\text{Sr}$ versus $^{147}\text{Sm}/^{144}\text{Nd}$ of lunar basalt source regions calculated using a single-stage model with an initial lunar $^{87}\text{Sr}/^{86}\text{Sr}$ ratio of LUNI = 0.69903 (Nyquist et al., 1973; Nyquist, 1977) and considering the age of the Moon as 4558 Ma. The $^{147}\text{Sm}/^{144}\text{Nd}$ ratios of lunar basalt sources are calculated assuming a two-stage chondritic evolution. In this model, the Moon follows a path of chondritic evolution until 4.42 Ga and then differentiates, forming the source regions of lunar basalts (Nyquist et al., 1992, 1995). Data are from the same sources as given in Figure 3.2.

Next, it was assessed whether the whole-rock composition of the samples is in equilibrium with the observed mineral (core) composition, using widely utilized exchange coefficients, $K_{D,Fe-Mg}^{Ol-melt} = 0.32 \pm 0.03$ (Delano, 1980) and $K_{D,Fe-Mg}^{Pyx-melt} = 0.28 \pm 0.03$ (Longhi, 1992) for lunar settings. YAMM, Kalahari 009 and Luna 24 show signs of partial mineral (olivine and pyroxene) accumulation while olivine and pyroxene composition of NWA 032 and LAP basalts are in-equilibrium with the whole rock

(Figure 3.19). The accumulation of minerals restricts these samples to be fractionated products.

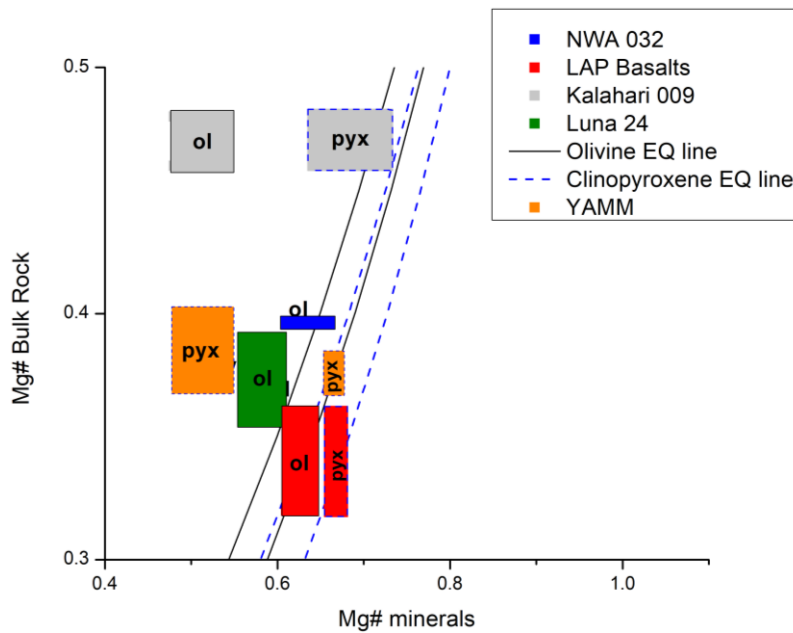


Figure 3.19 Plot of Mg# of the bulk rock versus Mg# of the olivine and pyroxene in different KREEP-free (source) rocks (similar to Rhodes diagram of Putirka, 2008). Black and dashed-blue lines represent olivine-basaltic melt $Kd_{Fe-Mg} = 0.32 \pm 0.03$ (Delano, 1980) and clinopyroxene-basaltic melt $Kd_{Fe-Mg} = 0.28 \pm 0.03$ (Longhi, 1992), respectively, indicating equilibrium olivine and pyroxene composition with basalt. The bulk compositions of Luna 24 ferrobasalts, NWA 032, and LaPaz (LAP) basalts are in equilibrium with the observed olivine and clinopyroxene composition, suggesting the samples approach a melt composition. However, Kalahari 009 and YAMM basalts show some signs of olivine and pyroxene accumulation. The data sources are the same as in **Figure 3.1**.

As the measured whole-rock composition most likely reflects an original melt composition, therefore, the parental melt composition of each rock is discussed in the following sub-sections. Later, using an appropriate parental melt composition, I deduce a probable source composition of each studied rock by performing REE modelling under the backdrop of the lunar magma ocean (LMO) hypothesis (Section 3.3.4; Snyder et al., 1992; Borg et al., 2009; Elardo et al., 2011; Hallis et al., 2014). This REE modelling initially assumes that the LMO has a source composition of 3 x CI for the REE (Hughes et al., 1989) and then calculates the amount of partial melting required to produce each basalt group from the best fit source composition (Section 3.3.4; Snyder

et al., 1992; Borg et al., 2009; Elardo et al., 2011; Hallis et al., 2014). As YAMM, Kalahari, and Luna 24 ferrobasalts show a slight negative to slight positive Eu-anomalies, the best fit mineralogy was obtained close to 75-80 % LMO crystallization (percent solid) (**Figure 3.4**), because plagioclase reaches a liquid phase at this point (Snyder et al., 1992). Northwest Africa 032 and LAP basalts show a high REE abundance ($\sim 40\text{-}50\times\text{CI}$ of LREE and $\sim 30\text{-}43\times\text{CI}$ of HREE) with a prominent negative Eu-anomaly, suggesting their source must have formed after the plagioclase separation (much after 78 % crystallization) during the LMO crystallization (**Figure 3.16**). The estimated best fit mineralogy for NWA 032 and LAP basalts was obtained at 86 % crystallized solid (PCS) with $\sim 1\%$ TIRL (**Figure 3.4**). The trace element modelling results of each sample are discussed in the following sub-sections.

3.4.4.1 YAMM basalts

A-881757 and MIL 05035 both show a similar bulk major-element composition. The MELTS model was run at oxygen fugacity (IW-1) relevant to the Moon. For the bulk composition of A-881757 (Mg# 38.3), the first appearing silicate phase is the pyroxene of Mg# 69. However, the most magnesian pyroxene in the studied A-881757 sections is Mg# 54, likely suggests a possible cumulate component within the sample. The analysis of the bulk composition of MIL 05035 also shows a similar result. The presence of the cumulate component is also favoured by the coarse-grained texture as well as the lower abundance of incompatible trace elements ($\sim 6\times\text{CI}$ abundance of LREE and $\sim 18\times\text{CI}$ HREE) than in selected parental melt Apollo mare basalts ($> \sim 60\times\text{CI}$ for LREE and $> \sim 40\times\text{CI}$ HREE) (**Figure 3.16**). Moreover, the La/Sm versus La and Ce/Yb versus Yb diagrams (**Figure 3.20**) highlight the partial melting relations in the clan members rather than fractional crystallization trends. Based on its lowest ITE abundance within the clan, MIL 05035 was closest to primitive parental melt composition. The measured low-ITE and low Mg# of YAMM basalts suggest that the modal mineralogy of the mantle forming these basalts must be low in an early formed olivine component and be comprised of later crystallized minerals such as orthopyroxene and low-Ca pyroxenes (high clinopyroxene/olivine ratio). The retention

of a limited quantity of plagioclase is also required to produce the observed small negative Eu anomalies in these samples. The deduced modal mineral abundance (17 vol.% olivine + 23 vol.% orthopyroxene + 59 vol.% pigeonite + 1 vol.% plagioclase) for the YAMM's parental melt fits best with a source formed at 75-80 % LMO crystallization (75-80 PCS). Similar modelled mineralogy at 75-80 PCS have been suggested by experimental and thermodynamical models of LMO crystallization (Rapp and Draper, 2018; Johnson et al., 2021). The trace element modelling attempted here shows that the source of these basalts underwent approximately 3-6% partial melting (modal melting) of the mantle with the composition of 75-80 PCS + 1% TIRL (**Table 3.7** and **Figure 3.16**), which supports earlier analytical and experimental observations (Joy et al., 2008; Liu et al., 2009; Arai et al., 2010).

3.4.4.2 Kalahari 009

The observed maximum Mg-rich olivine and clinopyroxene in Kalahari 009 is F_{048-50} and Mg# ~70, respectively (Sokol et al., 2008). The calculated olivine composition (F_{074}) is not present in the sample, in equilibrium with the whole rock (Mg# ~49). Instead, the observed pyroxene of Mg#70 suggests conditions close to equilibrium. There can be two possibilities. The most magnesian clinopyroxene is in equilibrium with the parental melt. Otherwise, Kalahari 009 got fractionated from a more primitive parent magma than its bulk. The difference in the whole rock (Mg# 49) and the observed mineral composition suggests the accumulation of more mafic minerals. It restricts them from being the product of extensive fractional crystallization (**Figure 3.19**). Furthermore, extreme fractional crystallization seems least likely, as Kalahari 009 contains unusually low ITE (~ 3×CI abundance of LREE and ~8×CI abundance of HREE) (**Figure 3.16**). For these reasons, it was assumed that the whole rock composition of Kalahari 009 closely approximates the parental melt composition, although it may contain a cumulate component, which we also subtracted in our calculations.

The relatively high Mg# (~49) of Kalahari 009 compared with other KREEP-free (source) basalts indicates that the clinopyroxene (pigeonite)/olivine ratio in the mantle source of Kalahari 009 must be lowest among the studied KREEP-free (source) basalts. The REE composition of Kalahari has a slight positive Eu anomaly suggesting that the source might have formed after plagioclase appeared on the liquidus (i.e., after 75 PCS) and the observed positive Eu anomaly is resultant of retention of plagioclase in the mantle source due to incomplete plagioclase separation. The deduced modal mineral abundance of Kalahari 009 source at 75-80 PCS is 30 vol.% olivine + 23 vol.% orthopyroxene + 40 vol.% pigeonite + 7 vol.% plagioclase. The parental melt composition of Kalahari 009 indicates approximately 7-9% partial melting (modal melting) of early cumulate (75-80 PCS + 1% TIRL) (**Figure 3.4**).

3.4.4.3 Luna 24 ferrobasalts

Luna 24 shows a similar compositional and mineralogical trend to YAMM basalts and other studied samples. They have low Mg# (35.7) with primary olivine (~Fo₅₈) as well as pyroxene core (Mg# ~60) which are in equilibrium with the bulk rock (**Figure 3.19**). Assuming a bulk rock with a low ITE concentration close to a parental composition (**Figure 3.16**), the trace element modelling implies approximately 3-6% partial melting (modal melting) of the source at 75-80 PCS + 1 % TIRL. The low Mg and low-ITE in the Luna 24 ferrobasalts suggest that the mantle source of these basalts is rich in clinopyroxenes (pigeonite and small amount of augite). The best fit source mineralogy assuming a modal melting scenario for Luna 24 ferrobasalts was obtained at 75-80 PCS contains 25 vol.% olivine, 23 vol.% orthopyroxene, 48 vol.% pigeonite, 2 vol.% augite and 2 vol.% plagioclase (**Figure 3.4**). The modelled mantle mineralogy shows minor plagioclase retention which is consistent with the result from previous studies (Ryder and Marvin, 1978) and is likely because of Al-rich nature of these rocks. Ma et al. (1978), based on observation of varying REE coupled with nearly constant Eu and Sc, also arrived at similar conclusion that small amount of clinopyroxene and plagioclase retained in the mantle source of Luna 24 ferrobasalts.

3.4.4.4 NWA 032 and LAP basalts

Whole-rock Mg# for NWA 032 (38-40; Fagan et al., 2002; Zeigler et al., 2005) and LaPaz basalts (34–38; Day et al., 2006b) suggest that they are in equilibrium with their primary crystallizing mineral phase, i.e., olivine cores, Fo₆₀₋₆₅ and Fo₅₈₋₆₄, respectively. Unlike previous samples, NWA 032 and LAP basalts show an elevated ITE abundance (**Figure 3.16** and **Table 3.2**). However, based on Sm-Nd and Rb-Sr isotopic studies (Borg et al., 2009; Elardo et al., 2014), it has been suggested that the elevated abundance of these samples is not related to KREEP enrichment but rather a low degree of partial melting of Fe-rich mantle (**Figure 3.2**). Following this logic, the whole rock composition was assumed to closely approximate the parental melt composition of both NWA 032 and LAP basalts. Despite the isotopic difference between NWA 032 and LAP basalts (**Figure 3.2**), the modal mineralogy of their sources at 86 PCS is somewhat similar. The 86 PCS source has previously been suggested to be mantle source of many Apollo mare basalts, however, those mare basalts are Mg-rich compared to NWA 032 and LAP basalts. This is indicative that the mantle source of these basalts contains late crystallized Fe-rich components of the LMO, with high abundance of clinopyroxenes (pigeonite and augite) relative to early formed olivine and orthopyroxenes. The modelled source comprises of 10 vol.% olivine + 23 vol.% orthopyroxene + 46 vol.% pigeonite + 21 vol.% augite for NWA 032 and 10 vol.% olivine + 23 vol.% orthopyroxene + 46 vol.% pigeonite + 20-21 vol.% augite + ≤ 1 vol.% plagioclase for LAP basalts. The results obtained for these samples assuming modal melting suggest a very low degree (~0.7-1.5 %) of partial melting in the 86 PCS + 2% TIRL source can generate the REE abundance of NWA 032 and LAP basalts (**Figure 3.4**), similar to the results of Borg et al. (2009).

3.4.5 Parent melt composition of Apollo mare basalts

Some of the Apollo mare basalts are considered to represent near-primary partial melts composition. The samples for comparing their formation *P-T* condition with the studied samples on the basis of: (i) Mg# in their bulk composition, (ii)

abundance of the REE and their chondrite-normalized patterns, and (iii) from previously chosen parent melts (Neal et al., 1994; Schnare et al., 2008; Hallis et al., 2014). To consider being a parent melt composition, the samples with the highest bulk Mg# and lowest bulk REE abundance were chosen among different groups and subgroups of the Apollo mare basalts. There are high Mg# samples, although those samples are not basaltic rocks and are either clasts within regolith breccias, rake fragments or drill core fragments, which are not considered further as parent melts.

Low- to intermediate-Ti (0-6 wt% TiO₂) mare basalts are found within the collections of Apollo 12 and Apollo 15. In Apollo 12, olivine, pigeonite and ilmenite basalts comprise the three low-Ti varieties. Among the Apollo 12 olivine basalts, 12002 and 12020 are considered non-cumulate high Mg# (55-57) and have low REE abundances. Previous studies have considered these two samples as representative of parent melt composition (Hallis et al., 2014). The highest reported bulk Mg# for the pigeonite basalts is lower and the REE abundances are higher when compared to the olivine basalts. Based on petrochemical and textural variations, Apollo 12 pigeonite basalts were suggested to derive from the olivine basalts (Snyder et al., 1997). In addition, the Apollo 12 pigeonite basalts have also been suggested to have undergone modification either by assimilation or fractional crystallization (Neal et al., 1994; Snyder et al., 1997; Schnare et al., 2008). The mare basalts of Apollo 15 largely comprise of two varieties: olivine-normative basalts and quartz-normative basalts. Among the olivine basalts, 15555 contains high bulk average Mg# (i.e., 48 with the highest value 52) and a low total REE abundance among the olivine basalts. Consequently, 15555 was selected as the parent melt composition of Apollo 15 olivine basalts. This sample has previously been suggested as a parent melt composition (Schnare et al., 2008; Hallis et al., 2014). Schnare et al. (2008) proposed that the pigeonite basalts are the fractionated products of the olivine basalts. Among the Apollo 12 ilmenite basalts, sample 12016 shows a non-cumulate texture, highest Mg#, and lowest REE abundances. Therefore, the *P-T* conditions of low-Ti ilmenite basalts was estimated from sample 12016. These samples were also selected as parental melt composition by previous studies (Hallis et al., 2014). Thus, among Apollo mare basalts the *P-T* condition of the parent melt of olivine basalts and ilmenite basalts, i.e., 12002,

12020, 12016 and 1555, were estimated and compared with the studied samples (**Table 3.6**).

The studied rocks are low-Ti basalts and, as such, they are compared with the low-Ti Apollo basalts. However, the *P-T* conditions of high-Ti (> 6 wt % TiO₂) mare basalts from the collections of Apollo 11 and Apollo 17 are also estimated. The highest Mg# (51-55) and lowest REE abundances are found in 10050 and 74275 in Apollo 11 and Apollo 17 samples, respectively. These samples are considered to be non-cumulate parent melts (Hallis et al., 2014). The estimated *P-T* conditions of these samples are shown in **Table 3.6**.

3.4.6 Feasibility of REE modelling and choosing mineral modes of mantle source

The presented chemical modelling of REE of the older A-881757 (YAMM), Kalahari 009 and Luna 24 ferrobasalts mantle sources are 75-80 PCS + 1% TIRL (**Figure 3.4**). The REE pattern in these three samples have a distinctness in that they are all LREE depleted (viz., LREE/HREE < 1), and display very small Eu-anomalies (either positive or negative or null). In contrast, mantle sources of the younger NWA 032 and LAP basalts are 86 PCS + 2% TIRL (**Figure 3.4**). The younger basalts, which exhibit different REE concentrations and patterns than the older KREEP-free (source) rocks, are somewhat similar to that of the Apollo basalts. As mentioned in the previous section, the REE compositions of the crystalline products (mineral phases) of the LMO are taken from the experimental partition co-efficient values (McKay, 1986; Phinney and Morrison, 1990; McKay et al., 1991; Yao et al., 2012). A non-significant difference in REE concentrations and patterns among A-881757 (YAMM), Kalahari 009 and Luna 24 ferrobasalts (**Figure 3.16**) can be attributed to the slight variation in the mantle modal mineralogy in their respective sources (**Figure 3.4**). The samples A-881757 (YAMM), Kalahari 009 and Luna 24 ferrobasalts display a very small Eu-anomaly (either positive or negative or null) because of minor quantities of plagioclase in their

source(s). The size of the Eu-anomaly indicates the plagioclase variation within the source (Neal and Taylor, 1992; Snyder et al., 1992; Hallis et al., 2014). Therefore, it was noticed that in a range of 75-80 PCS + 1% TIRL, the source of A-881757 (YAMM), Kalahari 009 and Luna 24 ferrobasalts with slightly variable modal abundances are capable of producing the low variation in Eu-anomaly and the REE pattern among them. In contrast, NWA 032 and LAP basalts show large negative Eu-anomalies, indicating plagioclase undersaturated or very low plagioclase bearing mantle sources (Neal and Taylor, 1992; Hallis et al., 2014). Additionally, the REE patterns in the samples A-881757 (YAMM), Kalahari 009 and Luna 24 ferrobasalt have a distinctness in that they are all LREE depleted ($LREE/HREE < 1$), unlike some Apollo mare basalts and NWA 032 and LAP basalts (dominantly, $LREE/HREE > 1$). However, the observed difference in Mg# of A-881757 (YAMM) (Mg# 38-40), Kalahari 009 (Mg# ~49) and Luna 24 ferrobasalts (Mg# ~36) is perhaps suggestive of varying proportions of later crystallized clinopyroxene (pigeonite and augite) and olivine in the mantle source.

The estimated mantle modal mineralogy ($Ol_{17-30}Op_{x23}Pig_{40-60}Aug_{0-2}Plag_{1-7}$) for the KREEP-free (source) older basalts range is much different for the KREEP-free (source) NWA 032 and LAP basalts with modal mineralogy of $Ol_{10}Op_{x23}Pig_{46}Aug_{20-21}Plag_{0-1}$ (**Table 3.5** and **Figure 3.16**). Noteworthy to mention here is that the calculated plagioclase abundance in the source of A-881757 (YAMM), Kalahari 009 and Luna 24 ferrobasalts is up to 7%. The plagioclase-bearing mantle source (up to ~8% plagioclase) has been previously suggested for other low-Ti/high-Al basalts such as 12038, 14321, Luna 16 and VLT Luna 24 basalts (Dickinson et al., 1985; Dasch et al., 1987; Neal and Taylor, 1992). This shows that the amount of plagioclase varies from source to source and is primarily dependent on the observed Eu-anomaly and the REE pattern. In addition, the measured isotopic abundance in the studied samples also suggest the plagioclase-bearing mantle source (**Figure 3.17**). Based on measured high-Al (>11.5 wt.%; **Table 3.2**) and very low REE abundances in Luna 24 ferrobasalts and Kalahari 009, such compositions would not be consistent with the assimilation of plagioclase rich crustal materials, as Eu abundance and Rb/Sr ratios would show considerable variations. This supports the notion that the aluminous nature of these basalts is a source

feature. In the model of LMO crystallization, plagioclase becomes saturated at ~75 PCS, consistent with experimental results of Rapp and Draper, (2020) and modelling results of Johnson et al. (2021). The variable modal mineralogy of source and their plagioclase content emphasizes the inherent complexities in the lunar magma ocean and highlights the heterogeneity in the lunar mantle.

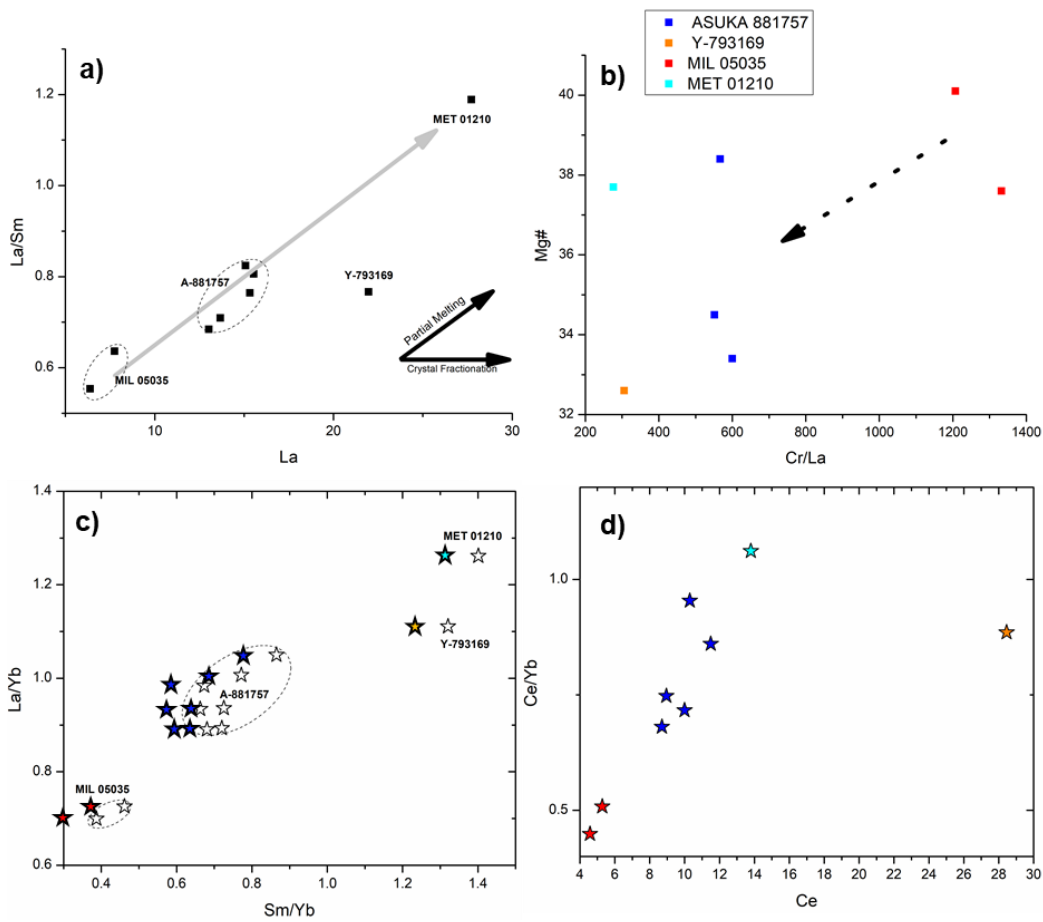


Figure 3.20 Plot showing partial melting relation of YAMM meteorites and primitive nature of MIL 05035. a) La/Sm versus La plot for YAMM meteorites, MIL 05035, A-881757, MET 01210 show a partial melting relation while Y-793169 shows signs of fractional crystallization. b) Mg# plotted against Cr/La measured in the YAMM meteorites. The high Cr/La ratio in MIL 05035 suggests it to be the most primitive among YAMM clan members. c) La/Yb vs Sm/Yb measured in the YAMM meteorites showing a partial melting relation in the YAMM clan. d) Ce/Yb versus Ce/Yb plot for YAMM meteorites, MIL 05035, A-881757, MET 01210 show a partial melting relation while Y-793169 shows signs of fractional crystallization.

The source mineralogy of A-881757 (YAMM), Kalahari 009 and Luna 24 ferrobasalts has more pigeonite compared to the early formed olivine and is likely to be more Fe-rich. With the advancement of LMO crystallization, the equilibrium crystallization gave way to fractional crystallization at about 50-70 PCS (Snyder et al., 1992; Elkins-Tanton et al., 2011; Elardo et al., 2014; Charlier et al., 2018; Rapp and Draper, 2018; Johnson et al., 2021). This would have the effect of forming chemical layering in the upper lunar mantle, the deeper Mg-rich mantle to shallower Fe-rich mantle. This study shows that the studied samples originated within the shallower mantle than the Apollo mare basalt melts (e.g., low-Ti 12002, 12020, 15555, and high-Ti 10050, 12016, 74275). However, a limited number of Apollo basalts also exhibit low Mg#, which has been explained through extensive fractionation (Snyder et al., 1991, 1992; Neal and Taylor, 1992; Neal et al., 1994; Hallis et al., 2014). Therefore, the Fe-rich Apollo basalts might not necessarily represent a shallow source, instead they are fractionated from their parental melt composition. However, their formation P - T condition is not retrievable. Therefore, shallow Fe-rich mantle is the most probable mantle source for the low-titanium and REE-depleted YAMM, Kalahari 009 meteorites, and Luna 24 ferrobasalts.

The modal mineralogy and its Fe-rich nature is also supported by experimental and modelling studies following fractional crystallization of Taylor Whole Moon (TWM) composition (Rapp and Draper, 2018; Johnson et al., 2021). In fact, the chosen modal source mineralogy also supports some of the remote sensing observations as well. Pyroxene rich mantle at shallow depth (~100 km) has been previously suggested by remote sensing observations within the SPA basin (Melosh et al., 2017; Moriarty et al., 2021). Indeed, the high proportion of pyroxene in the KREEP-free (source) basalt mantle source(s) suggests mantle with pyroxene > olivine. Pyroxenite-rich mantle has been previously proposed by Ringwood and Essene (1970) based on the analysis of some Apollo 11 basalts.

3.4.7 Reconciliation of estimated pressure (P) and temperature (T) for KREEP-free (source) samples

The formation pressure and temperature are estimated following the procedure described in Methods, and the results are provided in **Table 3.6 (Figures 3.5a, 3.26)**. To obtain the liquid composition (Mg#) in equilibrium with the observed Mg# in minerals, the MELTs algorithm was applied to the whole rock composition.

The phase diagram mode of pMELTS was chosen as a primary method for calculating P and T . The obtained results are the combined effects of evolving bulk composition and other associated primary minerals rather than any single mineral and/or mineral-melt partitioning. The estimated pressure and temperature obtained from thermobarometry and the pMELTS model show minor differences, depending on the chosen methods. Error in some thermobarometry calculations possibly occurs because the clinopyroxene-liquid and clinopyroxene-only thermobarometry rely on equations that are sensitive to the Al(VI) component and the components containing Na. Some of the analysis lacks Na and K data, thus affecting the thermobarometry calculations.

3.4.7.1 A-881757 and other YAMM meteorites

The pyroxene cores with Mg# (50-54) were chosen. A phase diagram mode of pMELTS obtains the P and T for the composition similar to the pyroxene cores between 0.3-0.8 GPa and 1100-1190°C. This range lies between estimates from clinopyroxene-liquid thermobarometry, 0.5-0.6 GPa and 1140-1160°C, and clinopyroxene-only thermobarometry, 0.4-0.8 GPa, and 1100-1120°C, assuming the standard error of estimate (SEE) in each method. Accounting results from all the methods, the P and T of the YAMM meteorite clan ranges within 0.3-0.8 GPa and 1100-1190°C, respectively (**Table 3.6**).

3.4.7.2 Kalahari 009

The data for whole-rock and mineral composition of Kalahari 009 were taken from Sokol et al. (2008). Using the highest Mg# olivine and pyroxene composition, the pMELTS phase diagram mode calculates P and T within the range of 0.7-0.8 GPa and 1215-1235°C. Using an appropriate liquid composition, which is in equilibrium with the observed minerals, the olivine-liquid thermometry results show a temperature range of 1195-1225°C, while clinopyroxene-liquid yields P - T , 0.7-1.0 GPa and 1215-1235°C and clinopyroxene-only estimate P - T between 0.8-1.0 GPa and 1195-1225°C. The broad range of P - T for Kalahari 009 lies within 0.7-1 GPa and 1195-1235°C (Table 3.6).

3.4.7.3 Luna 24 ferrobasalt

The Luna ferrobasalt composition taken from Vaniman and Papike (1977) is used for thermobarometric calculations. The clinopyroxene-only thermobarometer yields an estimated formation pressure of ~ 0.6 GPa and temperature of ~ 1155°C. This result is close to the experimental value, 1180°C and 0.4-0.5 GPa (Grove and Vaniman, 1977).

3.4.7.4 NWA 032

The P - T for NWA 032 was estimated from the whole rock and mineral data of Fagan et al. (2002). The phase diagram mode for the NWA bulk composition calculates a formation temperature of 1170-1190°C at a pressure of 0.3-0.5 GPa. The olivine-liquid thermometry on the pressure range obtained using the phase diagram method shows a formation temperature of 1180-1200°C. Due to the lack of clinopyroxene data, other thermobarometry methods could not be applied.

3.4.7.5 LAP basalts

Compositions of LAP basalts data were taken from Day et al. (2006b). The results of the phase diagram method on LAP 02205 bulk composition suggest formation

P - T of 0.5-0.6 GPa and 1180-1200°C, respectively. Thermobarometry were performed on the minerals with the most magnesian olivine and pyroxenes. The results of olivine thermometry for pMELTS estimated pressure suggests a formation temperature range of 1170-1180°C. The estimated temperature is 1160°C at 0.43 GPa, based on clinopyroxene-only thermobarometry for pyroxenes of LAP 03632 basalt (**Table 3.6**). The obtained results are similar to the experiments (1150-1200°C at <0.6 GPa) performed by Elardo et al. (2015).

3.4.8 Formation P - T of Apollo mare basalts

To be internally consistent, the P - T calculation by pMELTS and thermobarometry were also estimated the parental melt compositions (e.g., low-Ti 12002, 12020, 15555, and high-Ti 10050, 12016, 74275) of different Apollo sample suites. The obtained results for these samples suggest that the observed differences in the P - T conditions of the studied rocks and the Apollo mare basalts are real as there is no method bias associated with the presented models (**Table 3.6**). This study further demonstrates that the formation P - T obtained by pMELTS closely matches the results from multiple saturation point (MSP) experiments of Apollo samples. For example, the calculated P - T for 15555 in this study is ~ 1.0 GPa and ~ 1350°C for 15555, while earlier experiments by Kesson, (1975) and Walker et al. (1977) deduced 1.0-1.2 GPa and 1300-1350°C for the same sample composition. Several recent studies compare the model (such as pMELTS, MAGPOX, and Perple_X) calculations with the MSP experiments in detail (Elardo and Astudillo Manoslava, 2021; Astudillo Manosalva and Elardo, 2022). These studies have found their results are close to experimental values. In fact, the time-consuming and expensive experiments show a single datum in P - T - X space, while the equilibrium thermodynamic models offer a mean to extrapolate the experimental results seamlessly across various composition and P - T space.

3.5 Discussion

3.5.1 *Origin of symplectites and pre-symplectite composition*

The reconstructed symplectite composition is similar to the range of previously reported metastable lunar pyroxferroite (Liu et al., 2009). The results of the symplectite reconstructions for A-881757 are shown in **Table 3.8**. Symplectites of A-881757 do not show any textural association with mesostasis phases, suggesting an independent origin. The three types of symplectites suggests progressive Fe-enrichment and successive breakdown of unstable pyroxferroite in A-881757 (Lindsley et al., 1972). Type-3 symplectite resembles compositionally to primary pyroxene while type-1 symplectite is compositionally similar to lunar pyroxferroite (**Figure 3.13** and **3.14**). The gradational compositional variation of type-3 to type-1 symplectite suggest their formation by an endogenous process within a closed system (**Figure 3.13b**). The occurrence of symplectitic assemblage fayalite, hedenbergite and silica has been previously reported in Apollo mare basalts (e.g. 10044 and 12064; Griffiths et al., 2014), and mare basalt meteorites (e.g. NWA 10957 and MIL 05035; Liu et al., 2009; Wu and Hsu, 2020). It is important to note that the majority of these samples are Fe-rich ($Mg\# \leq 40$) and have a relatively coarse basaltic texture.

Due to the low oxygen fugacities during crystallization (e.g., IW-1), lunar basalts underwent extreme FeO-enrichment (Fenner Trend), which is illustrated by the sharp fractionation trends in the study by Pernet-Fisher et al. (2014) of 10003 ($Mg\# 38$). Slow cooling and the bulk Fe-rich nature of the rocks hosting symplectites seemingly favours extreme Fe-enrichment, which subsequently results in the formation of symplectites (Pernet-Fisher et al., 2014). In contrast, the Mg-rich, rapidly cooled samples tend to inhibit the extreme fractional crystallization of pyroxenes. Experiments have shown that pyroxferroite becomes stable at pressures ≥ 10 kbar (Lindsley and Burnham, 1970). However, at low pressure pyroxferroite breaks down into a three phase assemblage of hedenbergite pyroxene + fayalitic olivine + silica (Lindsley et al., 1972). The breakdown of pyroxferroite in Fe-rich samples could either occur as a result of reheating by impact shock (Hui et al., 2011; Liu et al., 2009), or during cooling of

the rock (Aramovich et al., 2002). Although, sample A-881757 shows wide-ranging evidence of shock such as fractures and melt veins, most of these features appear to have formed after symplectite formation, cross-cutting the earlier formed symplectites (**Figure 3.14**). These observations imply that symplectites in A-881757 were formed from pyroxferroite during slow cooling and prior to impact-induced shock.

3.5.2 Formation conditions of pyroxene sector zoning in A-881757

Chemical profiles across the zoned pyroxene in A-881757 (**Figures 3.10, 3.11 and 3.21**) enable assessing the formation condition of sector zoning on a detailed studied pyroxene crystal. In terrestrial magmatic conditions, clinopyroxene sector zoning has been experimentally constrained to form at low degrees of magma undercooling (Kouchi et al., 1983; Masotta et al., 2020, MacDonald et al., 2022) and utilized to obtain information on magma history, triggering mechanisms of eruptions, and ascent rates on Earth (Ubide et al., 2021). In lunar pyroxenes, sector zoning has been reported for mare basalts samples 10047 (Mg# ~39-40), 10058 (Mg# ~37), 10062 (Mg# ~35), and 12021 (Mg# ~37) (Hollister and Hargraves, 1970; Boyd and Smith, 1971). All these samples have Fe-rich bulk compositions and their modal mineralogy is dominated by pyroxene, like A-881757, indicating a possible role of bulk compositional effects.

The tetrahedral substitution of Al for Si is depicted in **Figure 3.10**. Substitution of Ti in the M-sites is approximately half of the Al-substitution for Si. This indicates coupled substitution of $(\text{Ti}^{4+})^{\text{VI}} + 2\text{Al}^{\text{IV}} \rightarrow 2\text{Si}^{\text{IV}} + (\text{ }^{2+})^{\text{VI}}$ between different co-existing sectors and also implies the predominately quadrivalent nature of Ti. The content of Al, Ti and Cr increases in the region dominated by Ca (**Figure 3.21**). Similar observations have been made in terrestrial and other lunar pyroxenes, in which Al, Ti and Cr in Ca-rich pyroxenes are highly soluble (Evans and Moore, 1968; Boyd and Brown, 1969; Boyd and Smith, 1971). In order to examine substitution of Al, Ti and Cr in the M1 site, the atomic Al-(2Ti+Cr) was plotted for the analytical points on the sector

zoned pyroxenes (**Figure 3.22**). The regions, where the value is positive, depicts abundance of sufficient Al to balance the octahedral substitution of Ti^{4+} and Cr^{3+} , typically showing Tschermak-type substitution. The negative values, dominant near the outer rims, suggest an unusual substitution that might be caused by the presence of reduced Ti^{3+} and Cr^{2+} , as observed by Boyd and Smith (1971). A-881757 pyroxenes are therefore distinct compared to the Mg-rich Apollo basalts in that they may accommodate Ti^{4+} in the tetrahedral site, which has only been observed in highly reduced low Ti/Fe Apollo 11 samples (e.g., Burns et al., 1972). The presence of Ti^{3+} and Cr^{2+} indicates extreme reduction during crystallization of pyroxene rims, which is

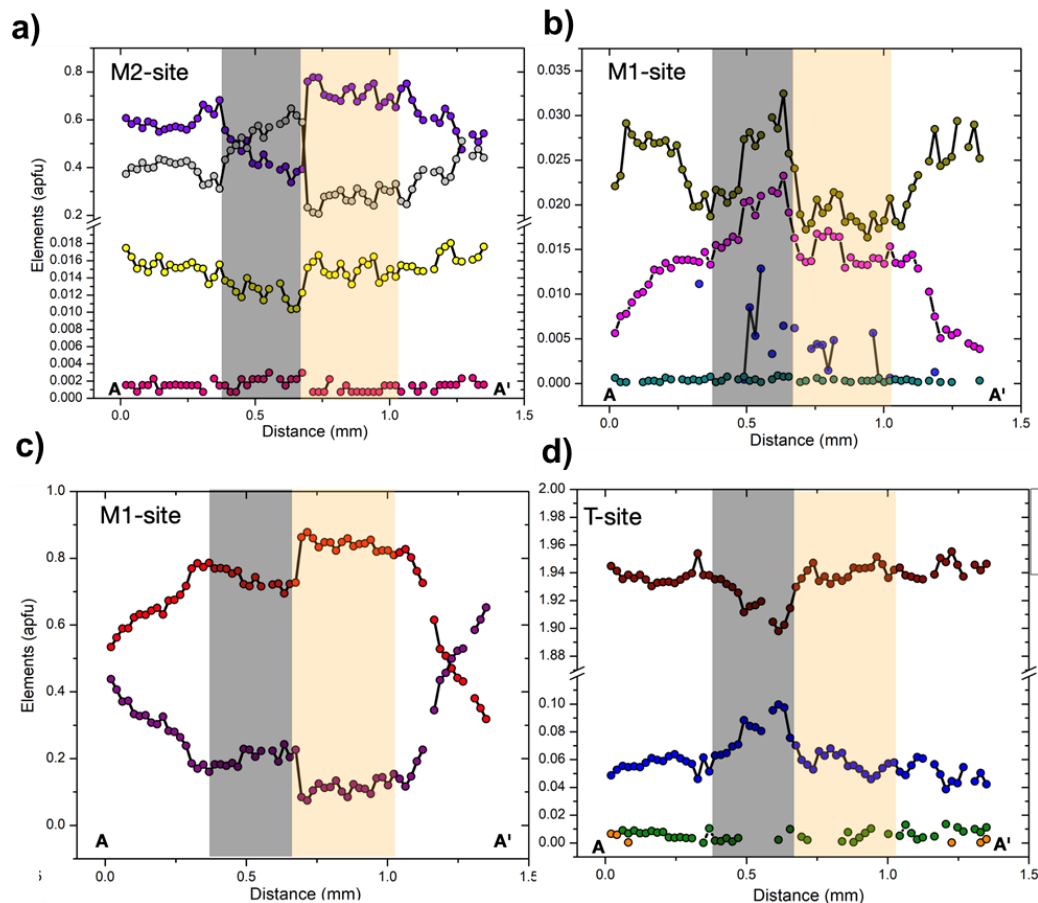


Figure 3.21 The site-specific variation of elements along traverse in A-881757 sector zoned pyroxenes (a-d). The partitioning of elements in octahedral (M1, M2) and tetrahedral sites (T) of A-881757 pyroxene along transect A-A' shown in Figure 3.9a.

also supported by the presence of Fe metal in A-881757 (*Section 4.3.2*).

The site distribution calculation of Morimoto (1988) was applied to the studied sector zoned pyroxenes in A-881757 by calculating the partitioning of cations in octahedral (M1, M2) and tetrahedral (T) sites (**Figure 3.21**) and compare these with the hour-glass sector zoned clinopyroxenes from the Holohaurn tholeiitic eruption in Iceland and recent alkaline eruptions in Mt. Etna, Sicily, Italy (**Figure 3.23**) (Neave et al., 2019; Ubide et al., 2019b). The octahedral M1 sites of A-881757 pyroxenes are occupied by Fe^{3+} , Ti^{4+} , Cr^{3+} , V^{4+} , Mg^{2+} and subordinate Fe^{2+} . In contrast to the terrestrial pyroxenes, there is further Fe^{2+} incorporation into the M2 site of A-881757. In the tetrahedral site, cations Si^{4+} , Al^{3+} , Fe^{3+} reside with Ti^{3+} in A-881757 pyroxenes (**Figure 3.21, 3.23**). The strong partitioning of Si^{4+} and Al^{3+} cations in the Ca-rich and Ca-poor sectors is observed in A-881757, similar to clinopyroxenes of alkaline setting in Mt. Etna. At Etna and other terrestrial alkaline settings, sector zoning does not impose a strong effect on the partitioning of Ca; the sectors are compositionally homogeneous across each other in highly charged cations like Al or Ti (Ubide et al., 2019a, b).

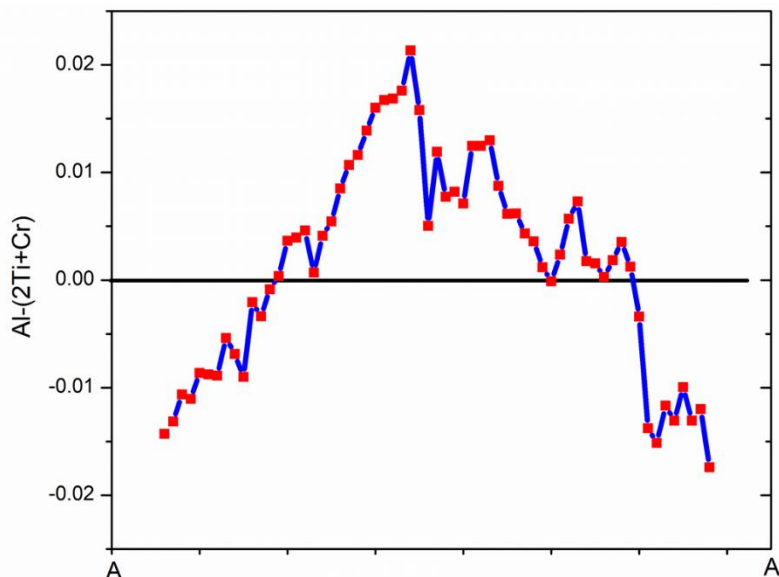


Figure 3.22 Plot of $\text{Al}-(2\text{Ti}+\text{Cr})$ for sector zoned pyroxenes along AA' (**Figure 3.9a**) showing affinity toward Ca-rich and Fe-poor sectors. Alumina, Ti and Cr are concentrated in the Ca-rich augite also depicted in **Figure 3.10a**.

However, unlike Mt. Etna sector zoned clinopyroxenes, Ca and Fe partitioning in the M2 sites of A-881757 sector zoned pyroxenes is more prominent (**Figures 3.10, 3.23**).

The sector zoning also has an effect in the partitioning of REE and HFSE in different sectors (**Figure 3.11, 3.12**) and their pattern is similar to partitioning behaviour of Al in tetrahedral and Fe in M1 sites. To understand the effect of crystallographic control, the quantitative major and trace elemental variations in A-881757 sector zoned pyroxenes was evaluated. It has been observed in terrestrial clinopyroxenes that REE+Y and HFSE concentrations systematically increase with increasing tetrahedral substitution of Al due to charge imbalanced configurations caused by cation substitution in tetrahedral and octahedral sites (Mollo et al., 2018 *and references therein*). Compared to the enrichment in terrestrial alkaline setting of Mt. Etna, the A-881757 pyroxenes show only slight enrichment (**Figure 3.12**). The primary difference between the terrestrial-alkaline and A-881757 clinopyroxene may come from the fact that the studied sector zoned clinopyroxenes are Fe-rich and possibly crystallized under different oxygen fugacity (fO_2) conditions. Melt composition and oxidation state may impose a more limited sector partitioning in lunar pyroxenes relative to terrestrial alkaline pyroxenes.

Within the context of limited sectoral partitioning, the incorporation of REE+Y in A-881757 sector-zoned clinopyroxene correlates with tetrahedral Al (**Figures 3.11, 3.12**), as observed in terrestrial settings (Sun and Liang, 2012; Dygert et al., 2014; Mollo et al., 2018; MacDonald et al., 2022). The slightly stronger partitioning of HFSE such as Zr^{4+} , Hf^{4+} and V^{4+} in the M1 site when compared to other low charged cations highlights the charge control on partitioning (Gaetani and Grove, 1995; Sun and Liang, 2012; Ubide et al., 2019b; **Figure 3.12**). From a crystal-chemical viewpoint, the HFSE enter the smaller M1 octahedral site and the correlation observed between HFSE partitioning and Al results from replacement of Mg^{2+} by Fe^{3+} and/or Al^{3+} in terrestrial settings (Mollo et al., 2018). In A-881757 clinopyroxenes, there is no Fe^{3+} or Al^{3+} in the M1 site, where Mg^{2+} is mostly replaced by Fe^{2+} , minimising charge imbalance and therefore the incorporation of HFSE relative to terrestrial settings (**Figure 3.11 and 3.12**). Similar partitioning behaviour has previously been observed in Fe-rich basaltic melts (Dygert et al., 2014). Therefore, apparently, the key driving mechanism of trace element partitioning in lunar A-881757 sector zoned pyroxenes is the achievement of local charge neutral configurations. Limited charge imbalance in the lunar setting due

to Fe-rich bulk composition and low oxygen partial pressure may lead to more limited sector partitioning in clinopyroxene.

Experimental studies have highlighted that sector zoning in clinopyroxenes is caused by the interplay between thermodynamic conditions and kinetic effects during crystal growth (Kouchi et al., 1983; Lofgren et al., 2006; Schwandt and McKay, 2006; Mollo et al., 2013). Boyd and Smith (1971) suggested that the formation and preservation of sector zoning requires conditions similar to those prevailing in a magma chamber. In terrestrial magmatic settings, clinopyroxene acquires sector-zoning during moderately rapid growth at low degrees of undercooling ($\sim \Delta T < 45^\circ C$), as experimentally shown by Kouchi et al. (1983), Masotta et al., (2020) and MacDonald et al. (2022). Notably, the studied sample A-881757 is coarser than all the previous lunar samples reported for sector zoning. The coarse-grained nature of pyroxene and plagioclase in A-881757 suggest low nucleation rates. Under low prevailing oxygen fugacity of the Moon and a slow estimated cooling rate, the crystals content is expected to be low in A-881757. This inference is consistent with experimental results (Mollo et al., 2013) reporting lower crystal content with decreasing oxygen fugacity and cooling rate. In natural terrestrial settings, Ubide et al. (2019a, b) suggested that conditions favouring the formation of hour-glass sector zoning include cooling and potential convection at the reservoir margin, and magma mixing and upward migration of magma in the plumbing system. Considering that sector zoning in A-881757 pyroxenes occurs in crystal cores, hour-glass sector zoning in A-881757 pyroxene may either have formed during crystallisation at the reservoir margin or upon upward ascent along a dyke, imposing a mild thermal regime and low degree of undercooling.

3.5.3 Crystallization history of A-881757 and other YAMM meteorites

The sequence of crystallisation inferred from the petrography and mineral chemistry of A-881757 suggests that Fe-poor pigeonite and augite crystallized first.

The simultaneous occurrence of augite and pigeonite phases in the pyroxene cores corresponds to a crystallisation temperature close to ~ 1100 °C (Lindsley, 1983). This was soon followed by crystallisation of Fe-rich augite and plagioclase with minor ulvöspinel. Mesostasis and pyroxene symplectite (pyroxferroite breakdown product) phases formed during the last stage of crystallization.

Consistent with the results from pyroxene mineral chemistry, the MELTS model calculations of the bulk composition of A-881757 at 1 bar and IW-1 yielded liquidus temperature ~ 1167 °C (**Figure 3.16**), which is slightly higher than the experimental results (~ 1160 °C) of Arai et al. (2006). The obtained temperature is lower than some previous experimental results on Apollo mare basalts such as low-Ti olivine basalts 15555 (~ 1350 °C; Walker et al., 1977), or 12040 (>1230 °C; Green et al., 1971). However, the formation temperature of A-881757 is somewhat close to the Fe-rich (Mg# 36) very low-Ti Luna 24 basalt (~ 1180 °C; Grove, 1978).

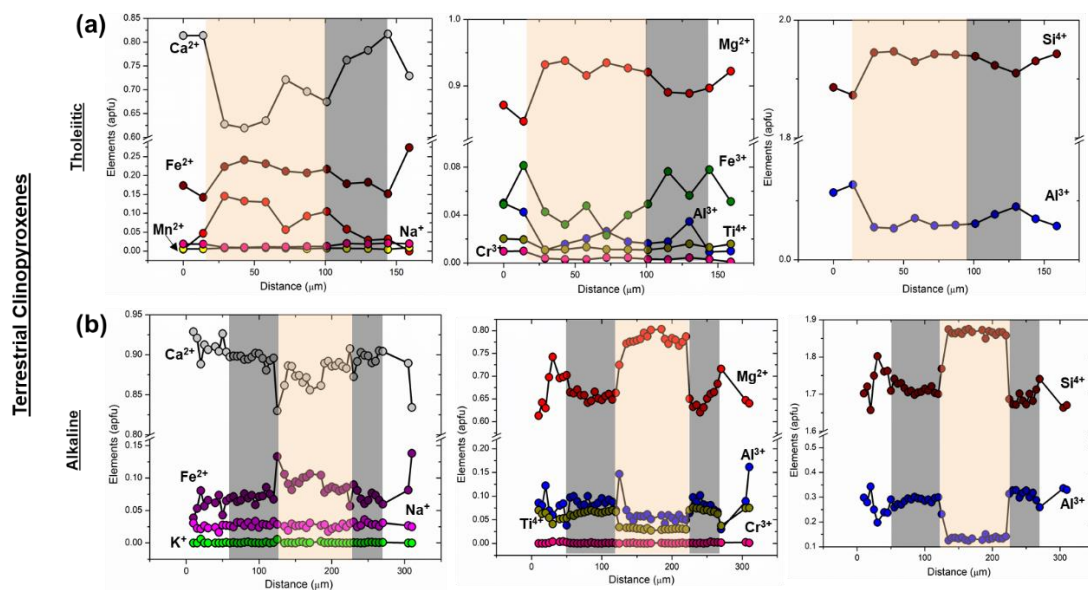


Figure 3.23 The site-specific variation of elements along traverse in terrestrial sector zoned pyroxenes, in both tholeiitic (a) and alkaline (b) clinopyroxene. The elemental variation seen in terrestrial hour-glass sector zoned clinopyroxenes from tholeiitic Holohaurn eruption in Iceland and alkaline Mt. Etna, Sicily, Italy (Data source: Neave et al., 2019 and Ubide et al. 2019a). Note that at Etna and other terrestrial alkaline settings, sector zoning does not impose a strong effect on the partitioning of Ca, homogeneous across sectors relative to highly charged cations like Al or Ti (Ubide et al., 2019a, b).

The first phase to crystallise in the model is low Ca-pyroxene with Mg# 67, while the bulk composition (Mg# 36) suggests that equilibrium pyroxene should have Mg# 54; perhaps indicating the cumulate component of A-881757 and MIL 05035. The pyroxene was soon followed by spinel (Mg# ~27 and Cr# ~67). Although present in limited amounts (~0.02 vol. %), spinel of this composition is not found in any of the studied sections of A-881757 and MIL 05035. However, Y-793169, a member of the YAMM group, contains Cr-spinel (< 1 vol.%). The atypical absence of spinel in A-881757 and MIL 05035, compared to the majority of Apollo and Luna basalts may indicate that spinel occurs as tiny sub-micron size inclusions in host pyroxenes and in the matrix in small quantities that could not be detected, or that early-crystallized chromites disappeared in a peritectic reaction of liquid, chromite and pyroxene, as experimentally shown by Arai et al. (2006) for A-881757.

Plagioclase is the third phase to join the liquidus at ~1142 °C with An₉₀. Appearance of plagioclase can also be marked by the changing Ti/Al ratio along with co-crystallisation of pyroxene and plagioclase (**Figure 3.7b**). Another important difference in the model and observed crystallization is the appearance of olivine at 1092 °C with Mg# ~30. Notably, this appearance of olivine is marked by the disappearance of orthopyroxene in the model calculations. This discrepancy might be explained by

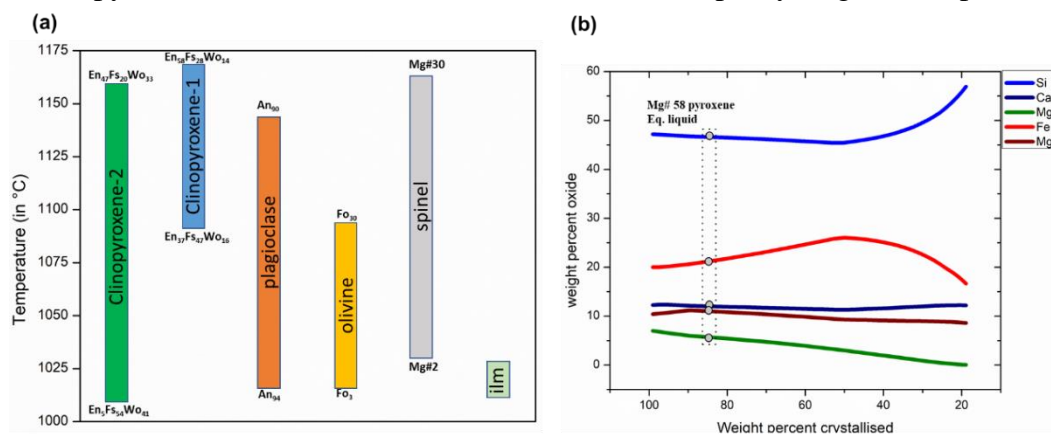


Figure 3.24 Crystallization model calculations using the MELTS algorithm. (a) The sequence of crystallization with compositional variations within the minerals obtained from the MELT's model run at 1 bar. (b) The evolution of bulk composition of A-881757 with crystallization. The gray dot shows the composition of pyroxene in equilibrium with the Mg# 58 pyroxene at 1 bar pressure.

the peritectic reaction of olivine: olivine + melt = low-Ca pyroxene (Longhi and Pan, 1989). Ilmenite appears at ~ 1027 °C, as the late forming phase in the model. The results of the MELTS modelling (**Figure 3.24**) suggest that the YAMM clan has been produced by a common parent melt and can be related by a common liquid line of descent (LLD). With the highest Mg# pyroxene (66), Y-793169 was perhaps crystallized close to equilibrium with a minor cumulate component ($< \sim 1$ vol. %), while A-881757 and MIL 05035 possess a significant cumulate component (~ 10 -20 vol. %).

3.5.4 Petrogenetic model for A-881757

3.5.4.1 Description of the modelled phase diagram for A-881757

The resulting phase diagram in P - T space (0-12 kbar and 1000-1500 °C) of sample A-881757 is given in **Figure 3.25** and **Figure 3.26**. The high temperature liquidus line is defined by the first appearance of olivine (Ol) at lower pressure (< 3 kbar) and spinel (Spl) at higher pressure (> 3 kbar). The cross-over of low to high pressure phase changes corresponds to the invariant point [ol, spl] at ~ 3 kbar and ~ 1270 °C. At the successive lower temperatures, first augite (Aug) and then pigeonite (Pig) become stable along with olivine and spinel (**Figures 3.25, 3.26**). Another high temperature invariant point [ol, aug] occurs at ~ 9 kbar and ~ 1300 °C. Both clinopyroxene phases occur throughout the total range of calculated pressure. At subsequent low temperatures, the Al-bearing minerals, plagioclase (Plag) and garnet (Grt) become stable at lower- (below 6.0-6.5 kbar) and higher-pressure (above 6.0-6.5 kbar) domains, respectively (**Figure 3.25**). The stability of garnet at higher pressure as shown by this model calculations is consistent with the results of other thermodynamic models (Johnson et al., 2021) and experimental calculations (Elardo et al., 2011). A phosphate phase whitlockite (Whit) is stable at further lower temperatures below 1200 °C throughout the total range of calculated pressure. Finally, the stability field of silica (Qtz) is defined at > 7 kbar and < 1080 °C.

The modal isopleths of remaining melt fraction X_{total} is shown by dotted lines (**Figure 3.26a**). The remaining melt fraction in the ol+sp+aug+melt stability field

ranges between ~10 vol. % crystallization at high temperature to ~30% vol. % crystallization at low-temperature, when the pigeonite becomes stable. The calculated chemical isopleths of X_{Mg} for olivine (**Figure 3.25c**) and clinopyroxene (**Figure 3.25b**) are temperature sensitive and approximately follow their respective phase boundaries. The maximum calculated values of X_{Mg} isopleths are 63 for olivine, 72 for augite, and 55 for pigeonite. The X_{Wo} isopleths for augite show variation from Wo_{24} at higher P - T to Wo_{42} at lower P - T , while pigeonite X_{Wo} isopleths are sub-parallel to the pigeonite stability field with variation from Wo_{19} at higher P - T to Wo_{13} at lower P - T . (**Figure 3.26b**). The X_{An} isopleths for plagioclase are typically pressure sensitive and vary between 92 – 88 (**Figure 3.26a**).

3.5.4.2 Calculation of formation P - T

The pMELTS (Ghiorso et al., 2002; Asimow and Longhi, 2004; Smith and Asimow, 2005) model calculations and traditional thermobarometric approaches (Putirka, 2008; Wang et al., 2021) were applied to estimate the formation P - T of A-881757 (YAMM), KREEP-free (source) samples, and Apollo basalt parental melts (Section 3.3). The formation of A-881757 and YAMM basalts initiated at 0.3-0.8 GPa P and 1100-1190°C T . By comparison, the calculated P - T of the oldest mare basalt Kalahari 009 is 0.7-1.0 GPa, and 1195-1235°C (**Figures 3.5a, 3.26**). Collectively, formation of the KREEP-free (source) mare basalts in the lunar mantle range between 0.3-1.0 GPa (~60-200 km) and 1100-1235°C (**Figure 3.5a** and **Table 3.6**). The estimated P - T conditions are significantly lower when compared to that obtained for the melt compositions of the Apollo mare basalts (1310-1410°C at 0.9-1.3 GPa; **Table 3.6**). The calculated P - T values for the Apollo samples are similar to the experimentally derived results (Elkins-Tanton et al., 2004; Elardo et al., 2015). The experimentally-derived P - T conditions of the Apollo picritic glasses are even higher (1430–1560°C at 1.3-2.5 GPa; Elkins-Tanton et al., 2004; Elardo et al., 2015 and references therein) than the lunar basalts. Among the returned lunar samples, only Luna 24 ferrobasalts show a similar P - T range (0.4-0.5 GPa and 1180°C) (Grove and Vaniman, 1978). Within the

context of heterogeneous lunar mantle, the lower estimated temperatures can be attributed to the lower Mg# (48-32) than the Apollo mare basalts, although the bulk composition of the KREEP-free (source) rocks suggest that they were in equilibrium with their lunar mantle sources. To understand this disparity in the formation conditions

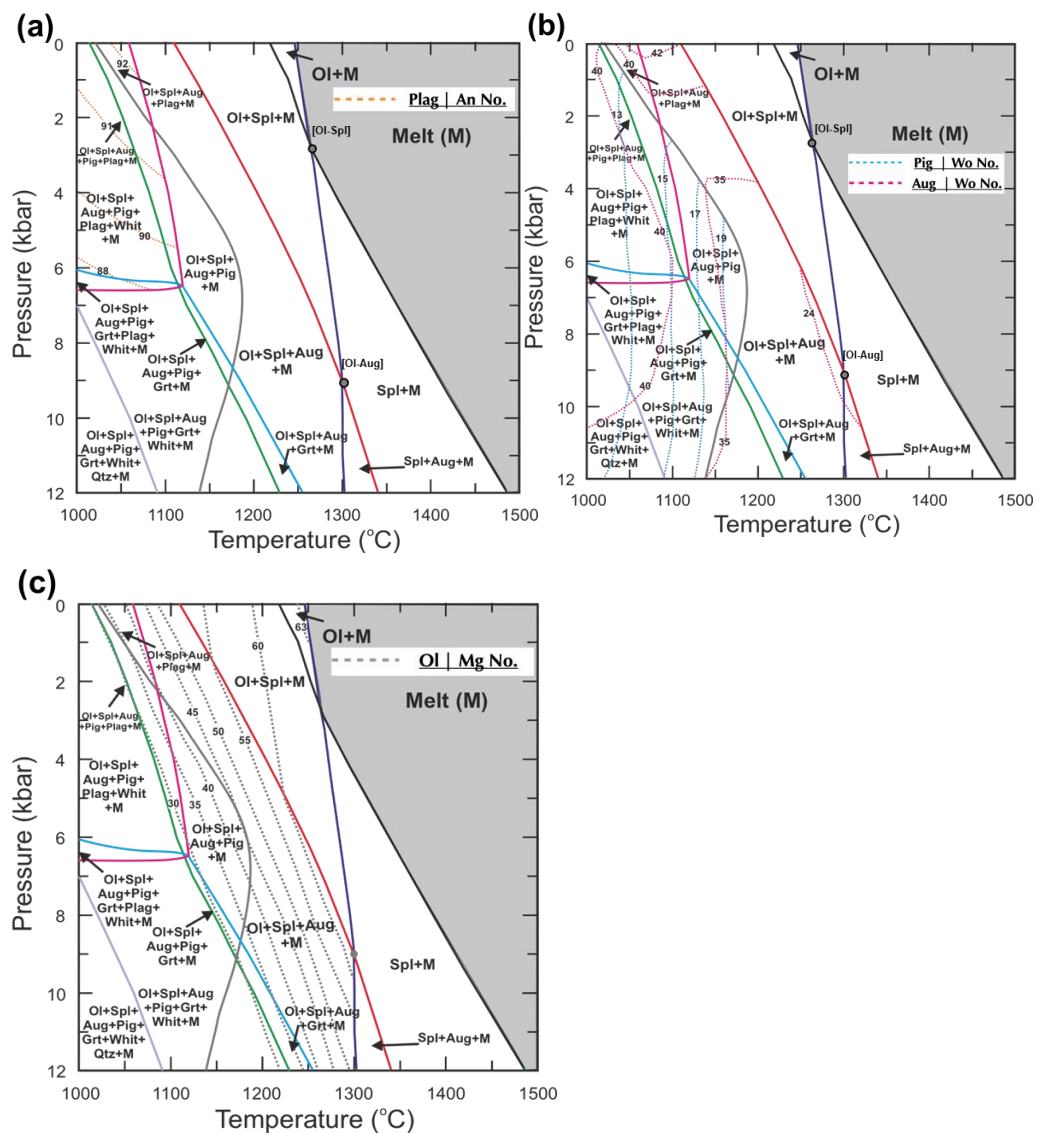


Figure 3.25 Calculated phase diagram of A-881757 with stable phase saturation curves, highlighting equilibrium phase assemblages at different P - T conditions along with modal isopleths (a) X_{an} (Ca/Ca+Na+K) isopleths for plagioclase showing variations from 88-92 in orange dashed lines. (b) The modal X_{Wo} isopleths for clinopyroxenes. (c) The modal isopleths of X_{Mg} for olivine shown by gray dotted lines. Abbreviations are: Grt = garnet; Spl = spinel; Whit = whitlockite; M = melt phase; Ol = olivine; Pig = pigeonite; Aug = augite; Plag = plagioclase.

between the KREEP-free (source) basalts and the Apollo mare basalts, mantle potential temperature (T_p) was calculated to examine likely thermal conditions.

3.5.4.3 Possible P - T path of A-881757 crystallization

It has been shown that the YAMM basaltic melt formed from a shallow pyroxene-rich mantle with maximum formation depths of ~160 km. Following this, it is expected that the YAMM basalts magma would undergo crystallization with lowering of P - T . Here the possible crystallization path of the YAMM basalts is described. Using the presence of stable fields of different minerals at variable P - T along with the petrographic observations, a possible evolutionary P - T path labelled as S1 to S3 (**Figure 3.25b**), was constrained. Considering the low modal abundance of primary olivine and spinel in the model calculation ($X_{\text{total}} < 2\%$ vol.%), the possibility of exchange reactions in early formed olivine and chromite is high due to large fraction of interacting surrounding melt (**Figure 3.25a**). The intersection of isopleth-58 of $X_{\text{Mg}}(\text{Aug})$ and isopleth-55 of $X_{\text{Mg}}(\text{Pig})$ provides a robust constrain to the first crystallized Mg-rich clinopyroxenes at 3-5 kbar pressure and ~1130-1180 °C temperature in A-881757 (**Figure 3.25b**). The minimum depth of initiation of crystallization of A-881757 took place at 60-100 km, considering that 10 kbar pressure corresponds to a depth of 200 km, using the lunar pressure depth relationship. In order to reach the P - T regime corresponding to the coexisting Mg-rich early-formed clinopyroxenes, there may be several likely paths for the A-881757 melt. However, all the possible S1 paths would finally lead to either a continued cooling in a near isobaric condition or decreasing P - T path to the starting point of S2. Plagioclase has compositional ranges from An_{95-86} , while the model calculation estimates the maximum value (92) of X_{An} isopleth at the lowest pressure and highest temperature in the plagioclase field. This indicates that the high-An plagioclase must have crystallized at or near the surface. The adiabatic rise (**S2**) of the early clinopyroxene bearing melt most likely correlates with the high-Mg clinopyroxenes and high-An plagioclase isopleths (**Figure 3.26a**). Finally, plagioclase along with clinopyroxenes were the dominant

phases at the near surface crystallization (**S3**) in this studied sample A-881757. Most of the crystallization (>50%) took place on or near the surface.

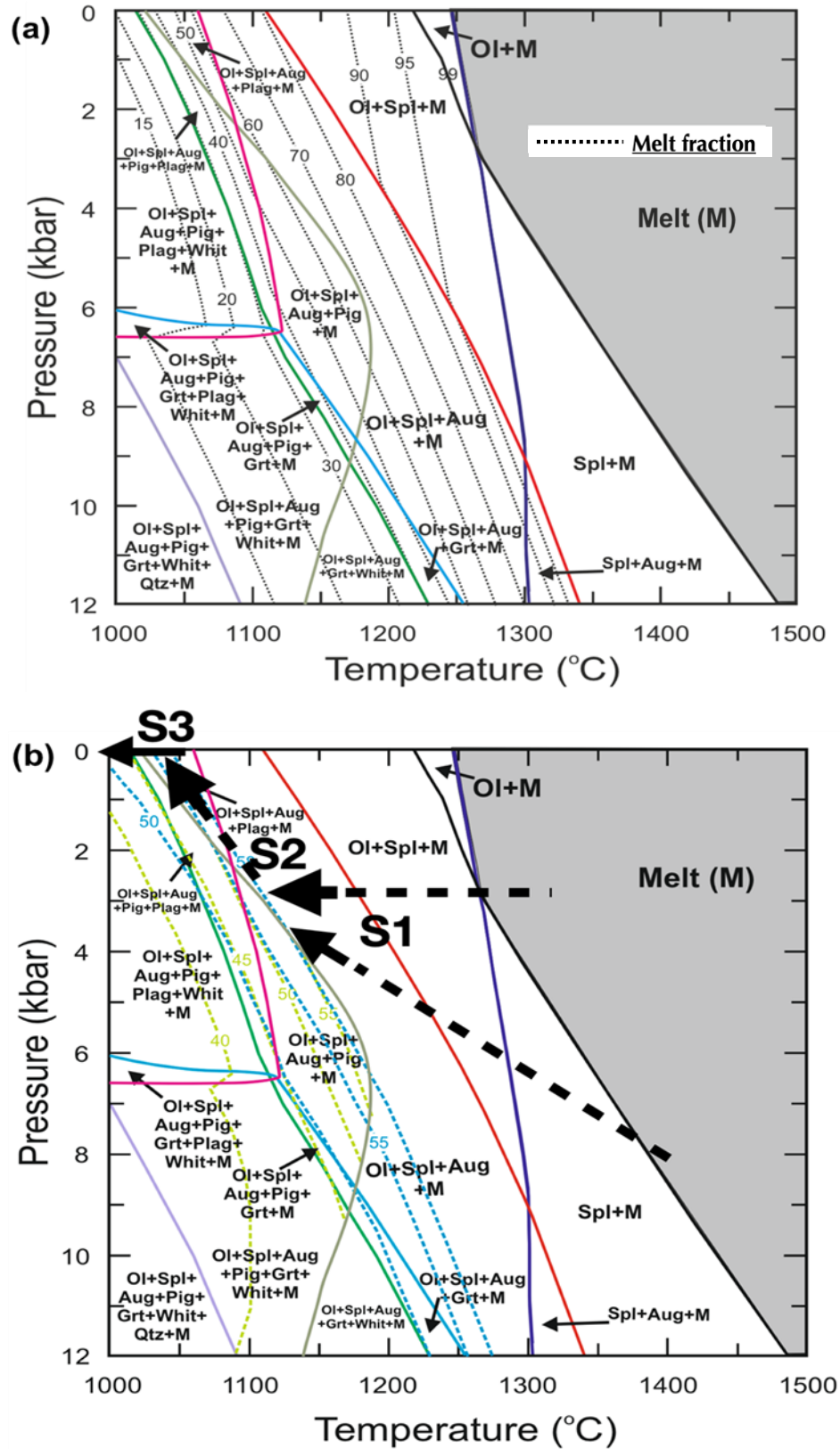


Figure 3.26 Calculated phase diagram of A-881757 with stable phase saturation curves, indicating equilibrium phase assemblages at different P–T conditions along with modal isopleths. (a) The black dashed lines denote the modal isopleths (wt. %) of remaining melts (X_{total}). (b) The modal chemical isopleths for X_{Mg} for clinopyroxene. The green dashed lines belong to pigeonite while blue belongs to augite. The coexistence of augite and pigeonite provide tight constrain on the P–T conditions of A-881757. black bold lines of (b) indicate the evolutionary P–T path with S1 to S3 stages of A-881757 crystallization from parent magma. The continuous lines indicate nearly constrained P–T path, whereas the dashed lines corresponds to the plausible P–T paths. For example, the initial high-T S1 stage can be a near isobaric or a decreasing P–T path between 3.0–9.0 kbar. The modal isopleths of X_{Mg} for olivine shown by gray dotted lines. Abbreviations are: Spl = spinel; Whit = whitlockite; M = melt phase; Ol = olivine; Pig = pigeonite; Aug = augite; Plag = plagioclase; Grt = garnet.

Earlier studies have performed numerous multiple saturation experiments on liquid compositions of Apollo basalts and pyroclastic glasses (Green et al., 1971; Kesson, 1975; Walker et al., 1977; Longhi, 1992; Elkins-Tanton et al., 2011). The equilibrium *P–T* phase diagram of such liquids show similar mineral assemblages with olivine as the first crystallizing phase in most Mg-rich parental liquids. The stability fields of different minerals show wide variation due to difference in the starting bulk composition. At high pressures (>10 kbar) pyroxene becomes the first crystallizing phases in parent melts of the high-Mg Apollo basalts (e.g., 15555, 12002). The modelling presented here suggests a shallow crystallization *P–T* condition for A-881757 and other YAMM meteorites. Similar results of shallow *P–T* have been obtained experimentally for Luna 24 ferrobasalts, meteorites LAP 02205 and NWA 032 (e.g., Grove and Vaniman, 1977; Elardo et al., 2014; 2015). All of these rocks are relatively Fe-rich (Mg#<40) and show equilibrium bulk composition with little or no signs of fractional crystallization (Norman and Ryder, 1980; Elardo et al., 2014). The *P–T* modelling suggests that the basalts away from the PKT region, e.g., older (> 3.8 Ga) KREEP-free (source) meteorites A-881757 vis-à-vis YAMM basalts crystallized in at conditions distinct from high-Mg Apollo mare basalts. Following the distinct mantle source and melting mechanism, this further constrains the crystallization processes in the YAMM meteorites and old KREEP-free (source) basalts.

3.5.5 Mantle potential temperature and surface heat flux

The result presented here indicates that the KREEP-free (source) basalts were sourced from a cooler lunar mantle than the mantle source of Apollo mare basalts. Estimates of average T_p , considering ~1-9% partial melting (**Figure 3.18**), correcting for the average P - T using lunar mantle adiabatic gradient, and correcting for the effect of latent heat of fusion on T (Section 3.3.8), ranges from 1110-1250°C for the KREEP-free (source) basalts (**Table 3.6**). The highest T_p of 1210-1250°C is yielded by the oldest (~4.36 Ga) Kalahari 009, followed by 1110-1200°C by YAMM basalts (~3.9 Ga), and 1160-1170°C by Luna 24 ferrobasalts. The youngest NWA 032 and LAP basalts yield 1150-1190°C T_p . These values are, however, lower than that of our calculations (1295-1385 °C for Apollo basalts) and the results obtained for picrites (1350–1450°C) from previous studies (Elkins-Tanton et al., 2004; Putirka, 2016). Even when the error (up to $\pm 50^\circ\text{C}$; **Table 3.6**) is considered in the calculated T_p , there remains a significant difference in T_p (100-200°C) between the generally older KREEP-free (source) and younger PKT samples. Such differences can be explained in terms of the distinct

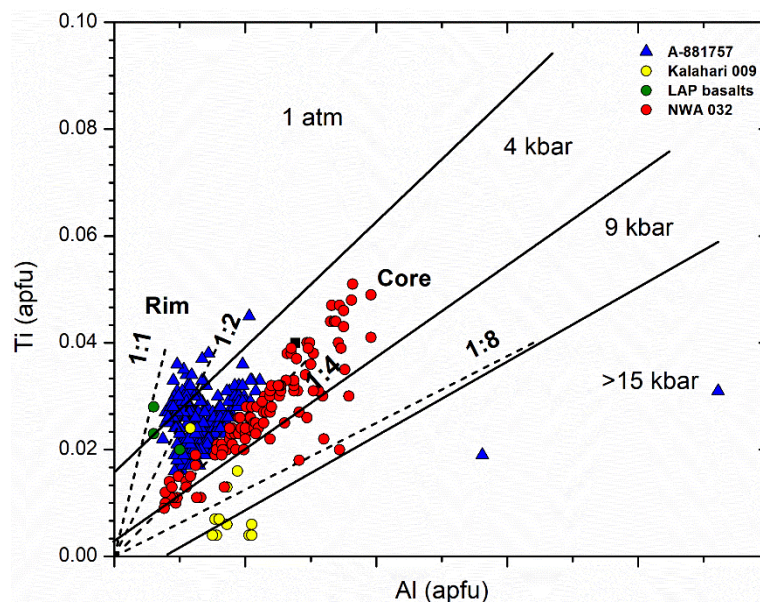


Figure 3.27 Al-Ti geobarometer in clinopyroxene of KREEP-free (source) basalts. The plots of molar Al versus Ti of pyroxenes in studied rocks over the pressure-sensitive partitioning lines of Al and Ti in clinopyroxene. The calibrated partitioning lines are experimentally-derived from controlled high-pressure (Nekvasil, 2004). The estimated pressure shows results similar to the phase diagram mode of pMELTS and thermobarometry.

evolution of the KREEP-free (source) basalts in comparison to the later mare basalts, highlighting the regional differences between PKT and non-PKT regions.

Lower T_p and shallower depth of formation of the KREEP-free (source) basalts in comparison to the Apollo basalts imply lower surface heat flow (56-63 mW/m²) possibly due to KREEP-free (source) magmatism compared to that at the PKT region (64-67 mW/m²; **Table 3.6**), assuming magma stalling at 40 km depth for both cases (**Figure 3.5** and **Table 3.6**). In all likelihood, the studied PKT mare basalts were stalled at greater depths beneath the surface (Elkins-Tanton et al., 2004; Elardo et al., 2015) while the YAMM basalts were emplaced at shallower depths, which influences surface heat flow. The high heat flow at the PKT region was plausibly controlled by mantle overturn induced KREEP accumulation at source, or by some other process. The low T_p obtained for the non-PKT samples even at 3.9 Ga can explain the likely causes of the lower mare basalt fill at the South Pole Aitken basin and Feldspathic Highland Terrane than the PKT region, where T_p was elevated even up to 3.3 Ga.

Calculated high T_p and elevated surface heat flow values obtained from Apollo mare basalts indicate they reflect a localized thermal anomaly possibly near the PKT region. Colder T_p and lower heat flows of KREEP-free (source) regions, having low-Th (YAMM, Kalahari 009 and Luna 24 ferrobasalts), obtained from samples of varying ages and localities may likely provide higher fidelity information on the global thermal regime. These results also support the long-standing idea that the lunar mantle was thermally heterogeneous at various scales (Solomon and Head, 1980; Wiczorek and Phillips, 2000; Elkins-Tanton et al., 2004). The lower degree of melting and relatively Fe-rich source of KREEP-free (source) rocks in comparison to the PKT mare basalts may indicate that a shallower Fe-rich mantle is more ubiquitous for the KREEP-free (source) basalts than the deeper mantle source of PKT-region basalts. These results are also supported by recent remote sensing observations of pyroxene-rich mantle at shallow depth (~100 km) (Melosh et al., 2017; Moriarty et al., 2021). Indeed, the high proportion of pyroxene in the KREEP-free (source) basalt mantle source(s) suggests mantle with pyroxene > olivine rather than peridotite.

3.5.6 A possible melting mechanism for KREEP-free (source) basalts

The melting regimes in most terrestrial bodies, including Earth, Mars, Venus, and Mercury suggest the dominance of partial melting either by decompression of adiabatically rising melts, from thermally anomalous, hot and buoyant portions of the mantle, or by lowering the solidus with addition of H₂O-dominated volatiles (flux) into the mantle. In contrast, it has been widely accepted that lunar mantle melting was aided by heating from radioactive elements in KREEP materials to generate mare basalts. The calculation shows that the primary radioactive elements (K, Th, and U) can produce heat in the order of $\sim 10^9$ J/g/y for the terrestrial planets, corresponding to 1°C increase of temperature over $\sim 10^7$ years for 1g of peridotite. Considering an end-member case of extreme (100%) enrichment of the urKREEP layer in the Moon's mantle, 1°C temperature rise in 1g peridotite can take place over a period of $\sim 10^5$ years. In the previously studied lunar returned samples and meteorites, the maximum KREEP-enrichment observed is <40% in a few lunar samples and meteorites (Lin et al., 2012; Hallis et al., 2014) (e.g., 15382, 15386, SaU 169). If we assume this maximum case as the enrichment of urKREEP layer in the Moon's mantle, then the increase of temperature by 1°C could have taken place between 10^7 - 10^5 years.

To melt the Moon's mantle, however, the supplied heat by radioactive source must also cross the latent heat of fusion of minerals and rocks, which is few hundred times more than the specific heat required to bring the minerals and rocks up to their melting temperatures. Further, dissipation of heat or thermal decay would hinder the melting process. This makes the production of sufficient melt even more difficult. Furthermore, being incompatible, the heat-producing elements would largely concentrate in the melt and escape, leaving the residual mantle too depleted to melt further and produce the volcanism observed at the lunar surface (Turcotte and Ahern, 1978).

An estimated total mare basaltic fill volume on the Moon is $\sim 8.6 \times 10^6$ km³ (Needham and Kring, 2017). Here, the energy stored in the 10 km KREEP-rich layer is

calculated and further, it was evaluated whether the energy budget was enough to generate the mare basalts on the lunar surface, as a first order approximation. Assuming the density as 3270-3460 kg/m³ and the latent heat of crystallization as 4×10⁵ J/kg of basalts, the first order estimate made here indicates that the total energy required to produce ~2.9×10¹⁰ kg mare basalts is ~1.2×10²⁵ J (or 3.3×10⁹ TWh). In contrast, the total energy obtained from the radiogenic heat, for an assumed 10 km thick global urKREEP layer with a density close to ilmenite bearing cumulates (~3719 kg/m³), is only 5.49×10⁷ TWh, which is not a sufficient (< 2%) total energy budget. The radioactive materials are concentrated within the PKT region, while the calculated volume of mare volcanism is probably more substantial as some of the older volcanic signatures are buried as cryptomare. Radioactive heating might have played an important role in generating the PKT KREEP basalts but the generally limited KREEP component seen in most Apollo mare basalts suggest that the energy generated by radioactive materials alone cannot be a major driving force for lunar magmatism. This contrasts with the earlier studies by Wieczorek and Phillips, (2000), which postulated radioactive and internal heating as the driving mechanisms for melting in the PKT terrane assuming a completely molten (KREEP) layer between the lunar crust and mantle, globally. This model of mare basalt generation is strictly valid for KREEP-rich samples (residing in the PKT region) with unusually high amounts of KREEP addition, which have been questioned on the basis of the variable depth of mare basalt generation and the viability of heating mechanisms, e.g., adiabatic decompression versus conductive heating, to form a small amount of melt generated at variable depths in the mantle source regions (Elkins-Tanton et al., 2002, 2004). Alternatively, impact-induced decompression might have also engendered melting of the lunar mantle, given the coincidence of YAMM basalts' crystallization ages with the Late Heavy Bombardment (LHB).

A perhaps more likely scenario is that the latent heat of lunar formation together with the interior heat sources were sufficient to engender low degree partial melting of pre-existing mafic LMO cumulates, at least until the youngest Chang'E 5 basalt volcanism (~2.0 Ga) (Qian et al., 2021). These result shows that the formation

mechanism of KREEP-free (source) basalt volcanism cannot solely due to heating by radioactive elements. Nevertheless, the oldest KREEP-free (source) basalts, those originated from the shallowest depths, most probably underwent low-pressure decompression type melting pyroxene-rich mantle in contrast to the traditional idea that they were the “byproducts” of lunar mantle overturn.

3.5.7 Conclusions and implications for ancient volcanism on the Moon

The unbrecciated lunar basaltic meteorite A-881757 along with the YAMM meteorite group provide an opportunity for detailed study of cryptomare magmatism, whose age is generally older (the oldest known sample is Kalahari 009 of ~ 4.3 Ga; Terada et al., 2007) than the Apollo mare basalts. Cryptomare deposits of different ages are widely identified at or near the lunar surface (Whitten and Head, 2015b). The cryptomare deposits likely formed away from the anomalous PKT region (Hawke and Bell, 1982; Schultz and Spudis, 1979; Head and Wilson, 1992; Arai et al., 2010). The cryptomare deposits are of varied chemical composition, e.g., the Mg-rich cryptomare regions (Whitten and Head, 2015a). Based on the chemical compositions of dark-haloed craters associated with the cryptomare regions and Kalahari 009, the cryptomaria are considered to be of the VLT type (Giguere et al., 2003; Hawke et al., 2005; Terada et al., 2007), which is consistent with the YAMM basalts. They are hidden mare deposits buried under a thick lava flow or formed in a hypabyssal setting (Arai et al., 2010). The estimated thickness of the lava flow based on the calculated cooling rates are unusually large by mare standards (Arai et al., 2010). The petrographic and mineral chemical study of the hour-glass sector zoned (in mm-scale) coarse clinopyroxene grains and exsolution lamellae in pyroxene points to conditions of low degree undercooling possibly within a reservoir margin. Since cryptomare deposits on the lunar surface are generally completely buried, their presence as dykes or sills seems viable, imparting slower cooling rates (0.06 – 0.3 °C/hr) to coarse crystals (up to 2 mm). Apollo basalts typically cooled at the rate of 0.16-20 °C/hr (Lofgren et al., 1975; Takeda et al., 1975),

forming lava flows, typically, ≤ 30 m thick (Takeda et al., 1975; Neal and Taylor, 1992; Arai et al., 2010). Given the Fe-rich bulk and presence of hourglass sector-zoned coarse pyroxenes, the YAMM cryptomare basalts may have been viscous and undergone polybaric crystallization in comparison to the Apollo PKT mare basalts where crystallization primarily occurred on the surface.

YAMM and Kalahari 009 basalts originated from a KREEP-free (source) Fe-rich upper mantle of the Moon through adiabatic decompression melting. The petrogenesis of these KREEP-free (source) samples are thus distinct than the PKT mare basalts especially those which are KREEP rich. The Fe-rich REE-poor cryptomare basalts were then evolved as highly viscous magma slowly cooled in a hypabyssal setting. Seeing the compositional variation of pyroxenes in the cryptomare region, Whitten and Head (2015a) postulated probable volcanic, magmatic or source heterogeneity related processes responsible for the observed mineralogic variation between PKT mare and cryptomare basalts. This study has presented evidence and interpretations of such process-based variations between the PKT mare and cryptomare basalt formation and volcanism on the Moon.

Table 3.1 Representative electron microprobe analyses of minerals in A-881757, 88a&b.

Phases	Pyroxene					Plagioclase		
	<i>Augite field</i>	<i>Pigeonite field</i>	<i>Rim-1</i>	<i>Rim-2</i>	<i>Within Symplectite</i>	<i>Primary</i>	<i>Rim</i>	<i>Rim near symplectite</i>
SiO₂	49.79	49.83	48.38	47.85	47.85	44.47	46.62	49.85
TiO₂	1.13	0.91	0.84	0.90	0.85	0.00	0.06	0.07
Al₂O₃	2.30	1.95	0.91	0.97	0.86	34.88	33.12	31.28
Cr₂O₃	0.77	0.65	0.17	0.13	0.12	0.00	0.02	0.02
FeO	17.76	20.74	31.50	33.38	34.67	0.53	0.68	0.72
MnO	0.32	0.38	0.47	0.44	0.48	0.00	0.00	0.03
MgO	12.17	13.04	7.35	6.72	5.75	0.10	0.03	0.06
CaO	15.82	12.40	10.12	9.84	9.45	18.95	17.40	15.57
Na₂O	0.05	0.03	0.01	0.00	0.01	0.48	1.38	2.13
K₂O				0.01		0.00	0.13	0.34
P₂O₅				0.05		0.00	0.02	0.00
NiO				0.00		0.00	0.00	0.05
V₂O₃	0.03	0.02	0.02		0.02			
Total	100.14	99.94	99.77	100.28	100.06	99.41	99.46	100.12
Oxygen	6.000	6.000	6.000	6.000	6.000	8.000	8.000	8.000
Si	1.908	1.920	1.956	1.942	1.956	2.069	2.160	2.281
Ti	0.033	0.026	0.026	0.027	0.026	0.000	0.002	0.003
Al	0.104	0.088	0.043	0.046	0.041	1.912	1.809	1.687
Cr	0.023	0.020	0.005	0.004	0.004	0.000	0.001	0.001
Fe	0.569	0.668	1.065	1.132	1.185	0.021	0.026	0.028
Mn	0.010	0.012	0.016	0.015	0.017	0.000	0.000	0.001
Mg	0.695	0.749	0.443	0.406	0.350	0.007	0.002	0.004

114 Understanding KREEP-free (source) volcanism on the Moon using Lunar
basaltic meteorites

Ca	0.650	0.512	0.438	0.428	0.414	0.945	0.864	0.763
Na	0.004	0.002	0.001	0.000	0.000	0.043	0.124	0.189
K	0.000	0.000	0.000	0.001	0.000	0.000	0.008	0.020
P	0.000	0.000	0.000	0.002	0.000	0.000	0.001	0.000
Ni	0.000	0.000	0.000	0.000	0.000	0.000	0.000	0.002
V	0.001	0.000	0.000	0.000	0.000			
Total	3.997	4.000	3.994	4.003	3.995	4.997	4.997	4.977
Mg#	0.55	0.53	0.29	0.26	0.23			
Wo/Or	33.8	26.4	22.3	21.6	21.1	0.0	0.8	2.0
En/Ab	36.1	38.6	22.6	20.5	17.8	4.4	12.5	19.5
Fs/An	30.1	35.1	55.1	57.9	61.1	95.6	86.8	78.5

Table 3.1 *continued*

Phases	Olivine				K-Ba-Feldspar		Spinel	
	<i>Primary- Ms</i>	<i>Ilmenite rim</i>	<i>close to FeS</i>	<i>Symplectite</i>	<i>close to silica</i>	<i>close to FeS</i>	<i>Primary</i>	<i>included in Ms</i>
SiO₂	30.76	30.77	30.82	30.99	55.19	53.84	0.04	0.05
TiO₂	0.08	0.35	0.08	0.13	0.34	0.27	29.05	20.44
Al₂O₃	0.01	0.04	0.01	0.00	19.62	19.30	5.28	6.28
Cr₂O₃	0.02	0.07	0.01	0.02	0.00	0.00	5.20	20.85
FeO	64.12	63.73	64.22	63.42	0.45	2.29	59.02	50.68
MnO	0.88	0.81	0.82	0.87	0.01	0.00	0.40	0.40
MgO	3.71	3.91	3.70	4.07	0.00	0.00	0.49	0.25
CaO	0.27	0.28	0.27	0.24	0.44	0.64	0.03	0.01
Na₂O	0.00	0.02	0.02	0.00	0.28	0.42	0.21	0.65
K₂O					11.62	11.53		
BaO					12.05	11.74		
Total	99.86	99.97	99.95	99.73	100.00	100.00	99.71	99.61
Oxygen	4.000	4.000	4.000	4.000	8.000	8.000	4.000	4.000
Si	1.010	1.006	1.011	1.014	2.780	2.741	0.001	0.002
Ti	0.002	0.009	0.002	0.003	0.013	0.010	0.795	0.557
Al	0.000	0.001	0.000	0.000	1.165	1.158	0.226	0.268
Cr	0.000	0.002	0.000	0.001	0.000	0.000	0.149	0.597
Fe	1.760	1.743	1.760	1.735	0.019	0.098	1.796	1.535
Mn	0.025	0.022	0.024	0.024	0.001	0.000	0.012	0.012
Mg	0.182	0.190	0.179	0.198	0.000	0.000	0.027	0.013
Ca	0.010	0.010	0.010	0.008	0.024	0.035	0.001	0.000
Na	0.000	0.001	0.001	0.000	0.027	0.041	0.015	0.046
K					0.747	0.749		
Ba					0.238	0.234		
Total	2.988	2.984	2.988	2.983	5.012	5.065	3.023	3.031
Mg#	10.0	9.6	9.1				1.5	0.9

Table 3.1 *continued*

Phases	Ilmenite			Silica			
	<i>Primary</i>	<i>in Mesostasis</i>	<i>with Olivine rim</i>	<i>Within mesostasis</i>	<i>Close to Kfs</i>	<i>close to FeS</i>	<i>Within melt veins</i>
SiO₂	0.00	0.03	0.02	98.15	98.53	98.95	97.58
TiO₂	53.87	52.65	53.23	0.17	0.15	0.17	0.13
Al₂O₃	0.02	0.02	0.03	0.69	0.59	0.34	0.71
Cr₂O₃	0.08	0.29	0.18	0.01	0.00	0.00	0.01
FeO	45.37	45.74	45.36	0.68	0.37	0.21	0.83
MnO	0.44	0.47	0.51	0.00	0.02	0.00	0.01
MgO	0.62	0.30	0.30	0.01	0.00	0.00	0.01
CaO	0.04	0.11	0.00	0.15	0.06	0.01	0.20
Na₂O	0.00	0.00	0.08	0.08	0.06	0.06	0.06
K₂O				0.27	0.31	0.18	0.28
Total	100.43	99.61	99.70	100.20	100.09	99.91	99.80
Oxygen	3.000	3.000	3.000	2.000	2.000	2.000	2.000
Si	0.000	0.001	0.000	0.988	0.990	0.994	0.987
Ti	1.009	1.000	1.007	0.001	0.001	0.001	0.001
Al	0.001	0.001	0.001	0.008	0.007	0.004	0.008
Cr	0.002	0.006	0.003	0.000	0.000	0.000	0.000
Fe	0.945	0.966	0.954	0.006	0.003	0.002	0.007
Mn	0.009	0.010	0.011	0.000	0.000	0.000	0.000
Mg	0.023	0.011	0.011	0.000	0.000	0.000	0.000
Ca	0.001	0.003	0.000	0.002	0.001	0.000	0.002
Na	0.000	0.000	0.004	0.002	0.001	0.001	0.001
K				0.004	0.004	0.002	0.004
Total	1.990	1.996	1.992	1.010	1.008	1.005	1.010
Mg#	2.4	1.2	1.1				

Table 3.1 *continued*

Phases	Glass		Fusion crust	Melt Vein		Fe-Ni metal		FeS	
	<i>K-Si</i>	<i>K-Ca</i>		<i>close to ilmenite- ulvospinel</i>	<i>close to symplectite</i>	<i>close to pyroxene</i>	<i>close to ilmenite and spinel</i>		
SiO₂	77.99	79.00	47.75	45.91	48.47	Fe	95.07	98.35	62.12
TiO₂	0.35	0.52	1.73	1.12	1.82	S	0.01	0.00	35.92
Al₂O₃	11.86	12.28	7.95	10.31	14.39	Ni	3.14	0.04	0.01
Cr₂O₃	0.01	0.04	0.27	0.16	0.14	Co	0.88	0.14	0.00
FeO	0.65	1.54	22.37	25.18	19.30	Cr	0.01	0.12	0.00
MnO	0.00	0.03	0.30	0.35	0.26				
MgO	0.00	0.02	7.43	5.74	4.43				
CaO	0.20	5.72	11.55	11.57	11.38				
Na₂O	0.15	0.53	0.00	0.03	0.02				
K₂O	8.73	0.97							
V₂O₃			0.19	0.29	0.29				
Total	99.94	100.64	99.52	100.66	100.48	Total	99.11	98.64	98.05

Table 3.2 Bulk rock chemistry of A-881757 and other associated lunar rocks.

Sample	A- 881757 , 88	A- 881757	A- 881757 , 80a	A- 881757 , 80b	MIL 05035	Y- 793169	MET 01210	Kalahar i 009	NWA 032	La Paz lunar meteorites	LAP 02205	LAP 02205	Luna 24 Ferroba salt (24109, 78)	NWA 773	urKRE EP		
Refs	This study	\pm SD	Yanai, (1991)	Warren and Kallem eyn, (1991)	Warren and Kallem eyn, (1991)	Joy et al. (2008)	Arai et al. (2010)	Warren and Kallem eyn, (1991)	Joy et al. (2005)	Day et al. (2006a)	Sokol et al. (2008)	Borg et al. (2009), Ziegler et al. (2007)	Elardo et al. (2014)	Day et al. (2006b)	Ma et al. (1977)	Valenci a et al. (2018)	Warren and Taylor (2014)
<i>wt. %</i>																	
SiO ₂	47.54	0.3	45.36	47.06	47.06	48.4	47	46	44	46.9	46.2	44.7	44.3	46			
TiO ₂	1.35	0.01	1.66	2.45	2.45	0.9	1.44	2.19	1.55	1.76	0.45	3	2.89	3.11	1.3		
Al ₂ O ₃	10.33	0.05	11.49	9.96	10.01	8.85	9.26	11.1	16.6	12.7	12.8	9.32	13.6	9.95	11.6		
FeO	20.6	0.12	21.72	22	22.51	20.7	22	21.2	16.46	17	16	22.2	18.4	21.8	22.4		
MnO	0.39	0.002	0.25	0.34	0.34	0.33	0.32	0.32	0.22	0.31	0.27	0.28	0.24	0.3	0.26		
MgO	7.16	0.03	6.47	6.2	6.3	7.79	7.44	5.75	6.2	6.13	8.53	7.97	5.18	6.32	7		

Table 3.2 *continued*

CaO	12.22	0.11	11.99	11.47	11.75	12.1	11.8	11.1	13	14.3	10.7	10.6	11.8	11.4	12.3
Na ₂ O	0.24	0.001	0.5	0.25	0.25	0.21	0.26	0.27	0.2	0.35	0.53	0.35	0.53	0.39	0.29
K ₂ O	0.04	0.008	0.04	0.04	0.04	0.01	0.03	0.06	0.06	0.05	0.19	0.09	0.13	0.1	0.02
P ₂ O ₅	0.13	0.008	0.05			0.02	0.05		0.13	0.08		0.09	0.12	0.17	
Total	100.0		99.5	99.8	100.7	99.3	99.6	98.0	98.4	99.6	95.7	98.6	97.2	99.9	
Mg#	38.3		34.7	33.4	33.3	40.1	37.6	32.6	40.2	39.1	48.7	39.0	33.4	34.1	35.8
S(%)	0.009		0.19					0.055							

Table 3.2 continued

Sample	A-881757, 88	A-881757	A-881757, 80a	A-881757, 80b	MIL 05035	Y-793169	MET 01210	Kalahari 009	NWA 032	La Paz lunar meteorites	LAP 02205	Luna 24 Ferrobasalt (24109, 78)	NWA 773	urKREEP			
Refs	This study	± SD	Yanai, (1991)	Warren and Kalle meyn, (1991)	Warren and Kalle meyn, (1991)	Joy et al. (2008)	Arai et al. (2010)	Warren and Kalle meyn, (1991)	Joy et al. (2005)	Day et al. (2006)	Sokol et al. (2008)	Borg et al. (2009), Ziegler et al. (2007)	Elardo et al. (2014)	Day et al. (2006)	Ma et al. (1977)	Valencia et al. (2018)	Warren and Taylor (2014)
ppm																	
Li	7.52	0.07															
Be	0.30	0.04				8.45	9.63		8.07								
B	1.20	0.05															
Sc	95.40	1.46		97	96			109	53.4	53	55	61	48.3	52.8	47	24.4	19.5
V	78.91	1.50		24.9				107	59.8	73	116	132		92	177		
Cr	1780.7	17.66		13.5		2257.9	2052.3				2700	2614		0.29	2606.8	5071	1366
Co	22.89	0.24			24.3	23.8	28.1		31.8		26.5	40.6	38	35.4	36	84	92
Ni	8.49	0.14			<35	8.27	11		212		10	49.2	268	42.4	80	195	236
Cu	8.30	0.19				5.21	9.64		23.4			34.2		18.6			
Zn	3.80	0.20		1.72	<35	1.81	16.9		37.4			30.5		27.5		17	16
Ga	3.16	0.04		2.2(8)	2.8	3.07	2.96		19.1		2.2	4.31		3.74			
Ge	1.62	0.04		0.039		1	0.12										
Rb	0.71	0.04				0.57	0.49		1.34		7	1.78		1.67			
Sr	121.14	0.50		128	112	113	105		163		110	132		109		57	50
Y	29.71	0.19				19.7	22.1		36.8	5.5		65.71	64.9	57			

Zr	60.57	0.28	97	< 110	32.3	36.4	190	103	3.5	14.46	206	236	172		128	160
Nb	3.70	0.04			1.94	1.15		1.07		0.675	15.26		11.9			
Cs	0.02	0.00			0.02	0.03		0.09		0.07	0.05		0.03		0.07	0.05
Ba	53.68	0.26	65	50	28.40	25.8		80.8	79	66	371	133	122		120	124
La	3.14	0.04	3.7	3.3	1.87	1.54	5.3	6.69	5.39	0.8	11.75	11.5	9.97	2	8.5	10.1
Ce	8.96	0.06	10	8.7	5.28	4.58	15.6	13.8	14.6	2.2	31.77	32	26.3		22.4	25.7
Pr	1.44	0.02			0.81	0.75		2.12			4.52	4.47	4.04			
Nd	7.61	0.09	7.7	7.8	4.59	4.24	10.2	10.7	9.8	1.9	21.21	21.4	19.1		21.3	14.8
Sm	2.92	0.03	3.08	2.96	1.87	1.77	4.4	3.58	3.6	0.56	6.73	6.26	6.05	1.9	3.9	4.22
Eu	0.92	0.01	1.08	1.03	0.82	0.72	1.37	1.11	1.03	0.4	1.13	1.01	0.98	0.58	0.34	0.29
Gd	3.86	0.04			2.54	2.65		4.54		0.7	8.9	7.28	7.81			
Tb	0.74	0.01	0.83	0.84	0.52	0.56	1.1	0.91	0.85	0.17	1.66	1.52	1.44	0.44	0.79	0.82
Dy	5.29	0.08	5.5	6	3.66	3.93	7.5	5.85		1	10.73	10.4	9.35	2.8		
Ho	1.13	0.02	1.24	1.39	0.82	0.88	1.63	1.26		0.28	2.35	2.19	2			
Er	3.28	0.06			2.33	2.66		3.63			6.46	6.56	5.4			
Tm	0.49	0.01			0.36	0.39		0.53			0.9	0.88	0.84			
Yb	3.26	0.04	3.8	3.48	2.83	2.78	4.8	3.54	3.36	1.2	5.86	6.65	5.3	1.9	2.8	2.63
Lu	0.47	0.01	0.56	0.54	0.40	0.39	0.72	0.52	0.519	0.19	0.893	0.88	0.82	0.29	0.39	0.37
Hf	1.95	0.04	2.26	2.18	1.21	1.03		2.37	2.66	0.4783	5.05		4.5	1.1	3.11	3.72
Ta	0.22	0.00	0.31	0.28	0.10	0.06		0.10		0.0388	0.8		0.6		0.4	0.45
W	0.06	0.00			0.31	0.01		0.69			310				0.2	0
Pb	0.15	0.00			0.42	0.39		0.55					0.71			
Th	0.48	0.01	0.48	0.44		0.28		0.86	0.85	0.09	2.01		1.79		1.31	1.58
U	0.11	0.00				0.07		0.32	0.23	0.14	0.46		0.45		0.28	0.37
La/Yb	0.67		0.68	0.66	0.46	0.39	0.77	1.32	1.12	0.47	1.40	1.21	1.31	0.74	2.12	2.68
La/Sm	0.68		0.76	0.71	0.64	0.55	0.77	1.19	0.95	0.91	1.11	1.17	1.05	0.67	1.39	1.52

Table 3.3 Representative minor and trace analysis of pyroxenes, plagioclase, symplectites and olivine in A-881757 (in $\mu\text{g/g}$, if not mentioned otherwise)

Phases	<i>Pyroxene</i>													
	Prm_core		Prm_core		Prm_mid		Prm_rim		Prm_rim		Rim near symplectite		Rim near symplectite	
Elements		1σ		1σ		1σ		1σ		1σ		1σ		1σ
Si (wt.%)	23.39		22.48		24.37		25.17		26.10		25.89		26.00	
Sc	145.8	1.99	143.1	1.96	177.8	2.43	142.4	1.95	151.1	2.07	131.7	1.80	139.8	1.91
V	201.0	3.26	196.9	3.20	177.0	2.87	115.7	1.88	73.3	1.19	32.0	0.52	38.0	0.62
Co	35.3	0.59	28.0	0.47	40.5	0.68	33.5	0.56	35.0	0.59	33.2	0.56	41.2	0.69
Ni	9.5	0.16	16.1	0.27	11.5	0.19	4.5	0.08	2.9	0.05	6.4	0.11	10.6	0.18
Cu	n.d.	-	2.8	0.14	2.9	0.15	2.9	0.15	3.2	0.17	22.2	1.15	68.3	3.54
Zn	8.2	0.18	n.d.	-	9.2	0.20	n.d.	-	n.d.	-	n.d.	-	11.0	0.24
Ga	0.9	0.02	0.8	0.02	1.4	0.03	1.5	0.03	1.2	0.02	2.9	0.06	3.5	0.07
Ge	n.d.	-	n.d.	-	n.d.	-	n.d.	-	n.d.	-	n.d.	-	n.d.	-
Rb	n.d.	-	n.d.	-	n.d.	-	n.d.	-	5.3	0.13	n.d.	-	n.d.	-
Sr	3.8	0.08	10.8	0.23	10.4	0.22	15.8	0.34	41.7	0.89	33.7	0.72	46.7	1.00
Y	10.3	0.17	12.3	0.20	16.8	0.27	23.7	0.39	21.0	0.34	111.5	1.82	169.9	2.77
Zr	4.3	0.07	11.4	0.19	9.7	0.16	35.3	0.59	34.7	0.58	189.4	3.17	378.9	6.33
Nb	n.d.	-	0.5	0.01	0.2	0.00	1.5	0.03	1.4	0.03	0.8	0.01	7.3	0.13
Cs	n.d.	-	n.d.	-	n.d.	-	n.d.	-	0.3	0.01	0.2	0.01	0.1	0.00
Ba	0.0	0.00	2.3	0.04	1.7	0.03	9.1	0.17	91.8	1.68	34.4	0.63	28.3	0.52
La	0.1	0.00	0.4	0.01	0.4	0.01	1.1	0.02	3.2	0.05	4.8	0.08	7.3	0.12
Ce	0.4	0.01	1.3	0.02	1.2	0.02	3.4	0.06	8.4	0.14	17.8	0.30	27.6	0.47
Pr	0.1	0.00	0.3	0.00	0.3	0.00	0.5	0.01	1.1	0.02	3.6	0.06	5.3	0.09
Nd	1.0	0.02	1.8	0.03	1.9	0.04	3.5	0.06	4.9	0.09	20.7	0.38	35.5	0.65
Sm	0.6	0.01	0.8	0.01	1.3	0.02	1.8	0.03	1.8	0.03	10.0	0.19	16.5	0.32

Eu	0.0	0.00	0.2	0.00	0.1	0.00	0.2	0.00	0.6	0.01	0.8	0.01	1.1	0.02
Gd	0.9	0.02	1.4	0.03	2.1	0.04	2.5	0.05	2.5	0.05	15.4	0.29	24.1	0.45
Tb	n.d.	-	n.d.	-	n.d.	-	0.5	0.01	0.5	0.01	2.9	0.05	4.6	0.09
Dy	1.9	0.04	2.0	0.04	3.0	0.06	4.0	0.07	3.5	0.06	19.8	0.36	30.5	0.56
Ho	0.4	0.01	0.4	0.01	0.7	0.01	0.8	0.01	0.8	0.01	4.2	0.07	6.3	0.11
Er	1.2	0.02	1.4	0.02	2.0	0.04	2.6	0.04	2.6	0.04	11.9	0.21	17.5	0.30
Tm	0.2	0.00	0.2	0.00	0.3	0.01	0.4	0.01	0.4	0.01	1.7	0.03	2.6	0.04
Yb	1.6	0.03	1.5	0.02	2.0	0.03	2.7	0.04	2.8	0.04	10.7	0.17	15.9	0.25
Lu	0.2	0.00	0.2	0.00	0.3	0.01	0.4	0.01	0.4	0.01	1.6	0.03	2.3	0.04
Hf	0.3	0.00	0.4	0.01	0.5	0.01	1.0	0.02	1.2	0.02	7.2	0.12	17.8	0.30
Ta	n.d.	-	n.d.	-	n.d.	-	0.1	0.00	0.1	0.00	n.d.	-	0.4	0.01
W	n.d.	-	0.0	0.00	n.d.	-	n.d.	-	0.1	0.00	n.d.	-	n.d.	-
Pb	0.0	0.00	0.1	0.00	0.1	0.00	0.1	0.00	0.5	0.02	0.3	0.01	0.3	0.01
Th	n.d.	-	0.0	0.00	0.1	0.00	0.1	0.00	0.7	0.01	0.4	0.01	0.3	0.01
U	n.d.	-	0.0	0.00	0.1	0.00	0.0	0.00	0.1	0.00	0.0	0.00	0.0	0.00

Table 3.3 *continued*

Phases	Plagioclase							
	Prm_core		Prm_Core		Prm_rim		Prm_rim	
Elements		<i>1σ</i>		<i>1σ</i>		<i>1σ</i>		<i>1σ</i>
Si (wt.%)	20.78	-	20.46		21.25		24.69	
Sc	1.8	0.02	1.7	0.02	2.1	0.03	n.d.	-
V	2.3	0.04	2.2	0.04	1.7	0.03	0.4	0.01
Co	27.7	0.46	21.6	0.36	21.9	0.37	n.d.	-
Ni	1.6	0.03	1.1	0.02	n.d.	-	n.d.	-
Cu	2.8	0.15	2.5	0.13	3.0	0.15	2.2	0.12
Zn	17.7	0.38	14.1	0.30	14.4	0.31	n.d.	-
Ga	7.2	0.14	6.5	0.13	8.2	0.16	17.5	0.35
Ge	n.d.	-	n.d.	-	n.d.	-	n.d.	-
Rb	n.d.	-	n.d.	-	n.d.	-	n.d.	-
Sr	349.8	7.47	351.9	7.52	383.5	8.19	1140.2	24.36
Y	0.2	0.00	0.2	0.00	0.2	0.00	0.7	0.01
Zr	n.d.	-	0.1	0.00	n.d.	-	n.d.	-
Nb	n.d.	-	n.d.	-	n.d.	-	n.d.	-
Cs	n.d.	-	n.d.	-	n.d.	-	n.d.	-
Ba	20.0	0.36	21.5	0.39	23.9	0.44	215.5	3.93
La	0.1	0.00	0.2	0.00	0.2	0.00	0.9	0.01
Ce	0.2	0.00	0.3	0.00	0.4	0.01	1.6	0.03
Pr	0.0	0.00	0.0	0.00	0.0	0.00	0.2	0.00
Nd	n.d.	-	0.2	0.00	0.3	0.00	1.1	0.02

Sm	n.d.	-	n.d.	-	n.d.	-	n.d.	-
Eu	1.9	0.03	1.7	0.03	2.1	0.04	7.7	0.14
Gd	n.d.	-	n.d.	-	0.1	0.00	0.2	0.00
Tb	n.d.	-	n.d.	-	n.d.	-	n.d.	-
Dy	n.d.	-	n.d.	-	n.d.	-	n.d.	-
Ho	n.d.	-	n.d.	-	0.0	0.00	n.d.	-
Er	n.d.	-	n.d.	-	n.d.	-	0.0	0.00
Tm	n.d.	-	n.d.	-	n.d.	-	n.d.	-
Yb	n.d.	-	0.0	0.00	n.d.	-	0.0	0.00
Lu	0.0	0.00	n.d.	-	n.d.	-	n.d.	-
Hf	n.d.	-	n.d.	-	n.d.	-	n.d.	-
Ta	n.d.	-	n.d.	-	n.d.	-	n.d.	-
W	n.d.	-	n.d.	-	n.d.	-	n.d.	-
Pb	0.2	0.01	0.0	0.00	0.0	0.00	0.0	0.00
Th	n.d.	-	n.d.	-	n.d.	-	n.d.	-
U	n.d.	-	n.d.	-	n.d.	-	n.d.	-

Table 3.3: *continued*

Phases	Symplectites						Olivine	
	Type-1		Type-2		Type-3			
Elements	1σ		1σ		1σ		1σ	
Si (wt. %)	25.24		25.24		22.64		14.26	
Sc	109.8	0.01	143.0	0.01	101.0	0.01	40.8	0.00
Ga	2.0	0.00	2.2	0.00	1.5	0.00	0.8	0.00
Ge	n.d.	-	n.d.	-	n.d.	-	n.d.	-
Rb	0.8	0.00	0.5	0.00	0.5	0.00	0.8	0.00
Sr	29.7	0.02	28.1	0.02	22.2	0.01	7.2	0.00
Y	115.3	0.06	145.1	0.08	89.7	0.05	52.7	0.03
Zr	135.5	0.07	90.3	0.05	58.4	0.03	63.7	0.03
Nb	0.4	0.00	0.8	0.00	1.5	0.00	1.1	0.00
Ba	16.9	0.01	24.3	0.02	27.7	0.02	29.4	0.02
La	3.2	0.00	3.5	0.00	2.6	0.00	2.9	0.00
Ce	12.5	0.01	13.3	0.01	9.2	0.01	7.3	0.01
Pr	2.4	0.00	2.5	0.00	1.7	0.00	1.2	0.00
Nd	15.0	0.01	16.2	0.02	10.3	0.01	6.5	0.01
Sm	7.5	0.01	7.4	0.01	4.9	0.00	2.7	0.00
Eu	0.8	0.00	0.8	0.00	0.6	0.00	0.2	0.00
Gd	12.1	0.01	13.5	0.01	8.2	0.01	3.7	0.00
Tb	2.5	0.00	2.9	0.00	1.7	0.00	0.9	0.00
Dy	19.7	0.02	23.7	0.02	14.0	0.01	6.9	0.01
Ho	4.6	0.00	5.7	0.01	3.3	0.00	1.8	0.00
Er	14.8	0.01	19.2	0.02	11.4	0.01	7.4	0.01
Tm	2.7	0.00	3.4	0.00	2.1	0.00	1.5	0.00
Yb	20.0	0.02	24.7	0.03	15.1	0.02	11.9	0.01

Lu	3.5	0.00	4.3	0.00	2.7	0.00	2.0	0.00
Hf	5.3	0.01	3.0	0.00	2.2	0.00	3.2	0.00
Ta	n.d.	-	n.d.	-	0.6	0.00	n.d.	-
Pb	0.2	0.00	0.2	0.00	0.2	0.00	0.5	0.00
Th	0.5	0.00	0.4	0.00	0.3	0.00	1.3	0.00
U	0.1	0.00	0.1	0.00	0.1	0.00	0.5	0.00

Table 3.4 The mineral REE partition coefficients used in model calculations.

	Olivine^a	Orthopyroxene^b	Augite^b	Pigeonite^c	Plagioclase^d
La	0.0001	0.0007	0.0446	0.0009	0.0418
Ce	0.0001	0.0015	0.0733	0.0017	0.0302
Pr					
Nd	0.0001	0.0055	0.1544	0.0058	0.0236
Sm	0.0006	0.0143	0.251	0.011	0.017
Eu	0.0007	0.0204	0.2952	0.0068	1.2
Gd	0.001	0.0281	0.3377	0.021	0.0105
Tb	0.002	0.0376	0.3758	0.027	0.0095
Dy	0.003	0.0487	0.4071	0.034	0.0089
Ho					
Er	0.008	0.0714	0.4402	0.055	0.0077
Tm					
Yb	0.019	0.0913	0.4426	0.087	0.0065
Lu	0.03	0.0995	0.4368	0.11	0.0068

^a- McKay, (1986); ^b-Yao et al., (2012); ^c- McKay et al., (1991); ^d- Phinney and Morrison, (1990)

Table 3.5 Estimated trace element compositions of the YAMM basalts, Kalahari 009, NWA 032, LAP basalts and Luna 24 ferrobasalts. The assumed source mineralogy for each meteorite and melting model are described in Methods, respectively.

YAMM basalts							
	Source composition (78 PCS + 1% TIRL)	3% batch melting	6% batch melting	3%+TIRL	4%+TIRL	A- 881775	MIL 05035 (Liu et al., 2009)
La	0.32	10.26	6.19	16.92	13.27	13.02	6.38
Ce	0.33	10.8	6.53	17.54	13.79	14.46	7.39
Pr				15.34	7.99	8.63	22.58
Nd	0.36	11.84	7.39	18.16	14.45	16.07	8.95
Sm	0.45	13.64	9	19.72	16.05	19.03	11.52
Eu	0.53	14.81	10.3	17.98	15.15	15.71	12.24
Gd	0.63	16.4	11.65	22.77	19.06	18.65	12.81
Tb	0.69	16.04	11.86	21.96	18.65	19.61	14.75
Dy	0.80	15.84	12.01	21.65	18.55	20.69	15.36
Ho				19.95	15.59	14.53	22.32
Er	1.08	16.75	13.49	22.51	19.72	19.79	16.07
Tm				18.64	14.95	13.80	20.31
Yb	1.35	16.52	13.98	22.69	20.13	19.34	16.48
Lu	1.54	16.27	13.97	22.17	19.77	18.94	15.58

Kalahari 009				
	Source composition (78 PCS + 1% TIRL)	7% fractional melting	9% fractional melting	Kalahari 009 (Sokol et al., 2008)
La	0.49	4.65	3.15	3.31
Ce	0.48	4.67	3.17	3.55
Pr				
Nd	0.49	4.52	3.05	4.01

La	0.18	10.54	5.93	8.29
Ce	0.20	10.75	6.29	
Pr				
Nd	0.26	11.34	6.83	
Sm	0.35	12.34	7.74	12.37
Eu	0.37	10.72	6.87	9.86
Gd	0.50	14.17	9.3	
Tb	0.54	13.71	9.21	11.59
Dy	0.61	14	9.63	10.95
Ho				
Er	0.81	14.85	10.66	
Tm				
Yb	1.00	15.19	11.3	11.26
Lu	1.16	15.25	11.61	11.59

Table 3.6 Estimated formation P-T, mantle potential temperature and heat flow for A-881757 and other KREEP-free (source) basalts. Abbreviations are LT: low-Ti basalt; IT: intermediate-Ti basalt; HT: high-Ti basalt. Data sources: ^aElardo et al., (2015); ^bElkins-Tanton et al., (2005); ^cElkins-Tanton et al. (2011); ^dHallis et al., (2014). * Results with single available composition

Sample	Olivine thermometry	Clinopyroxene-liquid thermobarometry		Clinopyroxene-only thermobarometry		Phase diagram-pMELTS		P and T range		Experimental Results		Degree of melting	T _p (°C)	Heat flow (mWm ⁻²)		
	T (°C)	P (GPa)	T (°C)	P (GPa)	T (°C)	P (GPa)	T (°C)	P (GPa)	T (°C)	P (GPa)	T (°C)	(%)		at <1 km	at 40 km	at 60 km
A-881757 /YAMM	-	0.5-0.6	1140-1160	0.4-0.8	1100-1120	0.3-0.8	1110-1190	0.3-0.8	1100-1190			3-6	1110-1200	2216-2380	56-59	37-40
Kalahari 009	1195-1225	0.7-1.0	1215-1235	0.8-1.0	1195-1225	0.7-0.8	1215-1235	0.7-1.0	1195-1235			7-9	1210-1250	2401-2523	60-63	40-42
Luna 24 ferrobasalts	-	-	-	0.6*	1155*			0.6	1155	0.4-0.5 ^a	1180 ^a	3-6	1160-1170	2250-2373	56-59	37-40
NWA 032	1180-1200	-	-	-	-	0.3-0.5	1170-1190	0.3-0.6	1170-1200	<0.6 ^b	1150-1200 ^b	0.7-1.5	1160-1190	2290-2371	57-59	38-40
LAP basalts	1170-1180	-	-	0.4*	1160*	0.5-0.6	1180-1200	0.4-0.6	1160-1200	0.55 ^b	1150-1200 ^b	0.7-1.5	1150-1190	2308-2390	58-59	38-40
12002 (LT)						1.2-1.3	1390-1410			1.2-1.4 ^c	1370 ^c	1-3^d	1355-1385	2655-2705	66-68	44-45
12020 (LT)	1390					1.1-1.2	1390-1400					1-3^d	1360-1380	2670-2700	67	44-45
15555 (LT)	1295-1310					1.0	1350			1.0-1.2 ^c	1300-1350 ^c	3-9^d	1330-1370	2630-2700	66-67	44-45
12016 (IT)						0.9-1.2	1350-1380					1-2^d	1325-1350	2615-2650	65-66	44
10050 (HT)						1.0-1.1	1310-1320					3-5^d	1295-1315	2525-2575	63-64	43
74275 (HT)						0.9-1.0	1300-1320			1.0-1.2 ^c	1290-1315 ^c	2-4^d	1295-1310	2545-2580	64	42-43

Table 3.7 Average modal abundances (Vol.%) of major silicate phases in Asuka-881757 and other YAMM basalts.

<i>References</i>	A-881757		MIL 05035				Y-793169			MET 01210		
	This Study	<i>Yanai and Kojima (1991)</i>	<i>Joy et al. 2008</i>	<i>Liu et al. 2009</i>	<i>Arai et al. 2007</i>	<i>Takeda et al. 1993</i>	<i>Arai et al., (2010)</i>					
Clast Info/section No.	,88a	,88b		,31	,34	,6	,40	,29	,33	,36		
Area (cm ²)	0.55	0.57		0.60	1.44	1.08	1.03	1.00	0.92	0.81		
Pyroxene	55.9	53.6	59.00	53.95	61.36	66.9	66.4	58.7	69.2	63.4	56.0	59-70
Plagioclase/maskelynite	33.4	32.2	30.00	36.27	24.82	29.0	20.2	35.0	17.2	29.5	42.0	17-35
Olivine/Fayalite	2.1	2.9		0.60	3.50	1.9	0.0					
Silica	0.8	1.5		0.83	1.13	0.3	0.8					
Spinel	0.5	1.0	<5	0.16	0.84	0.5	4.3				1.0	
Ilmenite	0.6	1.0	6.00	0.54	0.82		2.6				1.0	
Troilite	0.2	0.2	<5	0.21	0.16	0.2						
Phosphate	0.2	0.2		0.65	0.06							
Opaque phases/Glass	0.1	0.1	<5	0.57	0.53			6.3	13.6	7.0	2.0	
Symplectite	6.2	7.5	<5	6.24	6.77	1.2	8.4					
Mesostasis component sum	4.5	6.0		3.55	7.06							

Table 3.8 Reconstructed bulk compositions of symplectites in A-881757 (88a & 88b).

<i>ID</i>	Symplectite T-1		Symplectite T- 2	Symplectite T-3								
	<i>SMP-1</i>	<i>MM3</i>	<i>SMP-1</i>	<i>SMP-1</i>	<i>SMP-2</i>	<i>SMP-3</i>	<i>SMP-4</i>	<i>SMP-5</i>	<i>SMP-6</i>	<i>SMP-8</i>	<i>MM-1</i>	<i>MM-2</i>
Olv (vol. %)	38.52	39.79	32.51	17.42	20.22	21.45	20.10	18.66	22.60	30.91	23.89	24.18
Pyx (vol. %)	32.34	36.00	37.03	61.25	58.11	57.28	59.26	60.08	56.52	46.23	56.61	51.72
Silica (vol. %)	27.51	22.28	27.71	16.72	18.05	19.59	19.19	19.35	19.17	19.46	18.60	22.44
(wt.%)												
SiO₂	50.42	48.13	51.86	50.82	50.70	51.00	51.12	51.53	50.57	48.92	50.04	51.54
TiO₂	0.41	0.44	0.47	0.76	0.71	0.69	0.71	0.73	0.68	0.57	0.67	0.63
Al₂O₃	0.50	0.55	0.58	0.99	0.93	0.90	0.93	0.95	0.88	0.72	0.87	0.81
Cr₂O₃	0.03	0.03	0.03	0.05	0.05	0.05	0.05	0.05	0.05	0.04	0.05	0.04
FeO	39.55	41.10	37.13	33.08	33.97	34.07	33.57	32.93	34.65	38.20	35.27	34.63
MnO	0.54	0.56	0.51	0.45	0.46	0.47	0.46	0.45	0.47	0.52	0.48	0.47
MgO	2.99	3.15	2.98	3.33	3.29	3.25	3.26	3.26	3.26	3.24	3.28	3.16
CaO	5.48	6.02	6.40	10.78	10.10	9.77	10.10	10.33	9.62	7.89	9.52	8.84
Na₂O	0.02	0.03	0.03	0.05	0.04	0.04	0.04	0.05	0.04	0.03	0.04	0.04
Total	99.95	100.02	100.00	100.30	100.26	100.23	100.25	100.26	100.22	100.13	100.22	100.16

Chapter 4

Insights to lunar crustal diversity from lunar regolith breccia meteorites Y-981031, Y-983885 and Y-86032.

4.1 Introduction

The Moon can be thought of as a "memory stone" that has preserved a chronological record of the geological processes that have shaped planetary bodies in our solar system. Previous chapter focused on unbrecciated basaltic lunar meteorite Asuka 881757, the results highlighted the importance of lunar meteorites, especially those which are likely formed away from the PKT region, in providing an unbiased perspective and new insights to the formation and evolution of the Moon. In this chapter, I focus more on the lunar surface and crustal composition on the backdrop of unexplored lunar regolith breccias.

Our understanding of the mineralogical and chemical composition of lunar crust is essentially from the samples obtained robotic and human-crewed missions. Remote sensing datasets such as Clementine, Lunar Prospector (LP) and Kaguya (K) Gamma Ray Spectrometer (GRS), Chandrayaan-I Moon mineralogical mapper (M³), and Kaguya Spectral Profiler datasets provide an additional information in a large spatial scale. Several efforts have been made by utilizing compositional information from the samples and mapping the lithologies globally (Wang and Pedrycz, 2015). However,

every such efforts are biased by the spatially limited sampling of the Lunar surface. Lunar meteorites, as the complimentary samples provide a better global representation of the compositional diversity of the lunar surface. Among the available lunar meteorites, the brecciated samples (also called as regolith breccia) provide an overview of the regional geology and compositional variations within the lunar crusts (Warren and Humphrys, 2003; Warren et al., 2005; Gross et al., 2014).

The lunar regolith breccia meteorites are made up complex blend of lithic clasts, mineral fragments and groundmass materials of near surface lithologies which are possibly sourced from a varied lunar parent rocks (Day et al., 2006a; Korotev et al., 2009; Joy and Arai, 2013). The data obtained from these compositionally variable feldspathic and basaltic clasts, have provided us new additional insights and helped us in clearing some of the preconceived notion about the geochemical evolution of the Moon (Korotev, 2005). These include, i) correction of the hypothesis which suggested the age relation between high Ti and low-Ti basalt suites obtained from Apollo sample suites that the low-Ti basalts formed after the high Ti basalts as the melting regime becomes deeper with time (Warren and Taylor, 2014); ii) better constrained timing of basaltic volcanism with a more extended period from ~4.35 Ga (Kalahari 009; Terada et al., 2007; Sokol et al., 2008) to ~2.9 Ga (NWA 032; Borg et al., 2009), while the timing of basaltic volcanism was believed to be confined to majorly between ~3.8 to ~3.2 Ga based on returned lunar basalts; iii) improvement of the poor representation of returned Mg-suite rocks in the lunar highlands and bulk crustal aluminium content by the lunar meteorites (Korotev et al., 2003; Neal, 2009); iv) identification of the new lithologies such as magnesian anorthosite and spinel troctolite and confirmation of some remotely sensed lithologies such as pure anorthosites (Gross and Treiman, 2011; Nagaoka et al., 2014; Gross et al., 2014). Despite of significant detailed research on the lunar crust, we still find unusual and exotic clasts within the lunar breccias (Joy et al., 2014; Zeng et al., 2018; Xue et al., 2019). Therefore, there is continued need to analyse more and more samples especially lunar breccias to better understand the lateral and vertical heterogeneity in the lunar crust. In this chapter, lunar regolith breccia meteorites recovered near and around Yamato mountains in Antarctica by Japanese Antarctic Research Expeditions (JARE) between 1980-1999, were studied. Three lunar

meteorites namely Yamato (Y)-981031, Y-983885 and Y-86032 were examined. A detailed investigation of petrography, mineralogy and bulk chemistry of these samples is discussed. The bulk chemistry data of the lunar meteorite and GRS data from Lunar Prospector was also compared to identify potential source crater for these three regolith breccia meteorites.

4.2 Sample Description

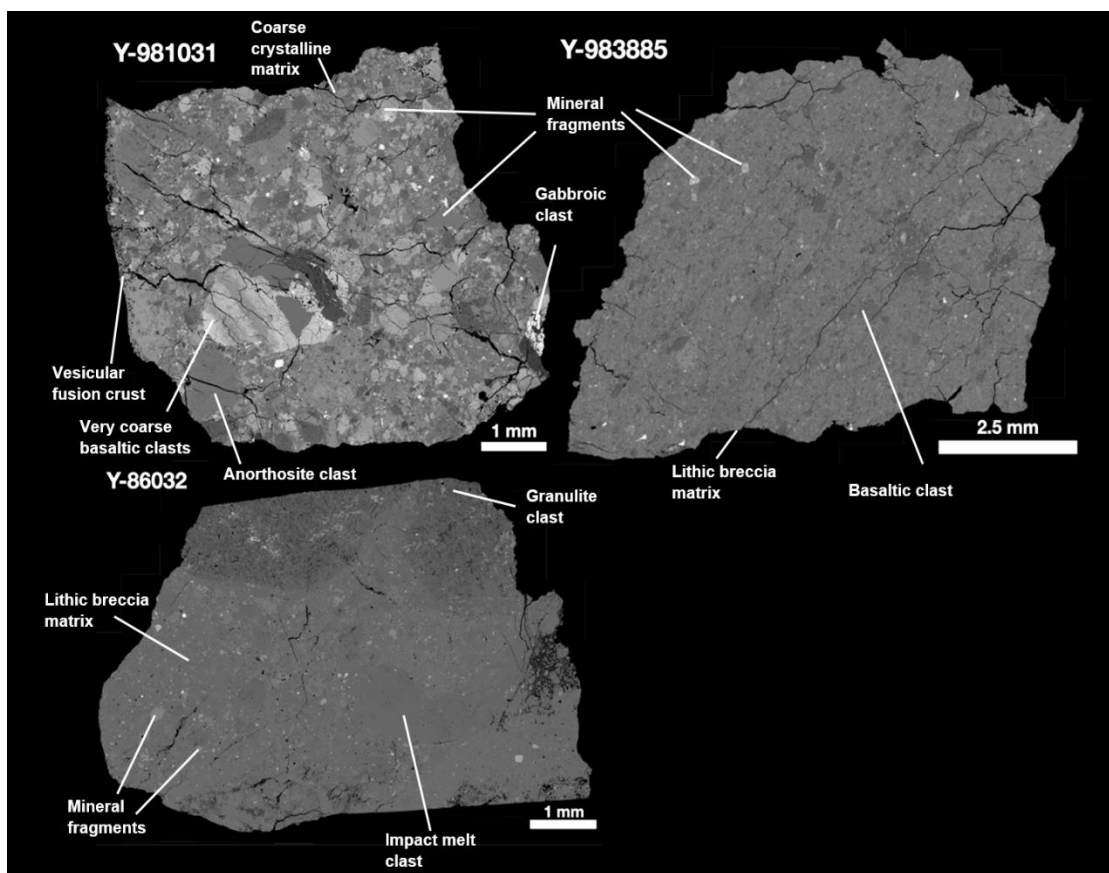


Figure 4.1 Backscattered electron images of the polished thick sections of Y-981031, Y-983885 and Y-86032.

All three samples show difference in their overall geochemistry. Sample Y-981031, discovered in Antarctica during JARE-39 (1998-1999) expedition. This meteorite was earlier classified as anorthositic regolith breccia but later found to contain more olivine and pyroxene bearing basaltic clasts than anorthositic clasts (<10 %) in the matrix fragments (Sugihara et al., 2004). Preliminary characterization studies now classify this rock as Anorthosite bearing basaltic regolith breccia (Arai et al., 2002).

The ages of Y-981031 mare affinity phosphates have been measured to be 3.5 Ga (Terada et al., 2007), however the anorthositic components might be older. High noble gas content measured in the sample indicate their derivation from a mature regolith (Lorenzetti et al., 2005).

Sample Y-983885 was also found in during JARE-39 expedition. The sample was recovered from surface ice around the Yamato mountains, Antarctica. This meteorite is classified as basalt-bearing anorthositic regolith breccia containing numerous clasts and mineral fragments (Arai et al., 2005). Y-983885 also found to contain a small KREEP component that is evident by its elevated rare earth element concentration (Warren and Bridges, 2004). Previous studies have reported that the bulk composition (Si, Ca and K) of Y-983885 meteorites is distinct from the Apollo samples of the PKT region and it has been suggested that this sample may have been obtained from the South Pole Aitken basin (Corrigan et al., 2009). The noble gas measurement in this sample indicates its derivation from a mature regolith (Miura et al., 2006; Lorenzetti et al., 2003). Be, Al and Cl isotope measurement in Y-983885 suggest ejection age of 0.045 Ma with short transit time of (<0.02 Ma) and terrestrial age of (0.045 Ma) (Nishiizumi et al., 2009). U-Pb ion microprobe measurement on the phosphate grains of Y-983885 yielded ages ~4.0 Ga (Arai et al., 2008).

Sample Y-86032 was discovered in 27th JARE expedition in 1986. Two more similar samples Y-82192 and Y-82193 (now defined as paired) was recovered from the close proximity to Y-86032 (Takeda et al., 1989). This sample is classified as Anorthosite fragmental breccia (Takeda et al., 1989; Yamaguchi et al., 2004, 2010). The sample is measured to have very low concentration of rare earth elements and high bulk Al concentration, unusual when compared to other lunar anorthositic breccias (Palme et al., 1991; Karouji et al., 2006). Nyquist et al., (2006) and Yamaguchi et al., (2010) argued that the ancient clasts present in Y-86032 sample might have originated far from the PKT region, and possibly in the far side of the Moon. The isotopic studies ³⁹Ar–⁴⁰Ar, Rb–Sr, and Sm–Nd suggest sample Y-86032 to be among some of the oldest lunar samples with ages ~4.4 Ga (Nyquist et al., 2006). The low concentration of the noble gases in this samples suggest their derivation from immature deep (>5m) regolith

(Nyquist et al., 2006). The cosmic ray exposure ages based on multiple studies averaged ~8-10 Ma (Eugster and Niedermann, 1988; Eugster, 1989; Nyquist et al., 2006).

4.3 Methods

One polished thick section of each sample Y-981031, Y-983885,74 and Y-86032 were obtained from National Institute of Polar Research (NIPR), Japan for petrographic and mineralogical examination. The thick sections were gold coated for 1 min and analyzed first at NIPR SEM facility and later EPMA facility at Physical Research Laboratory, Ahmedabad.

4.3.1 Petrography

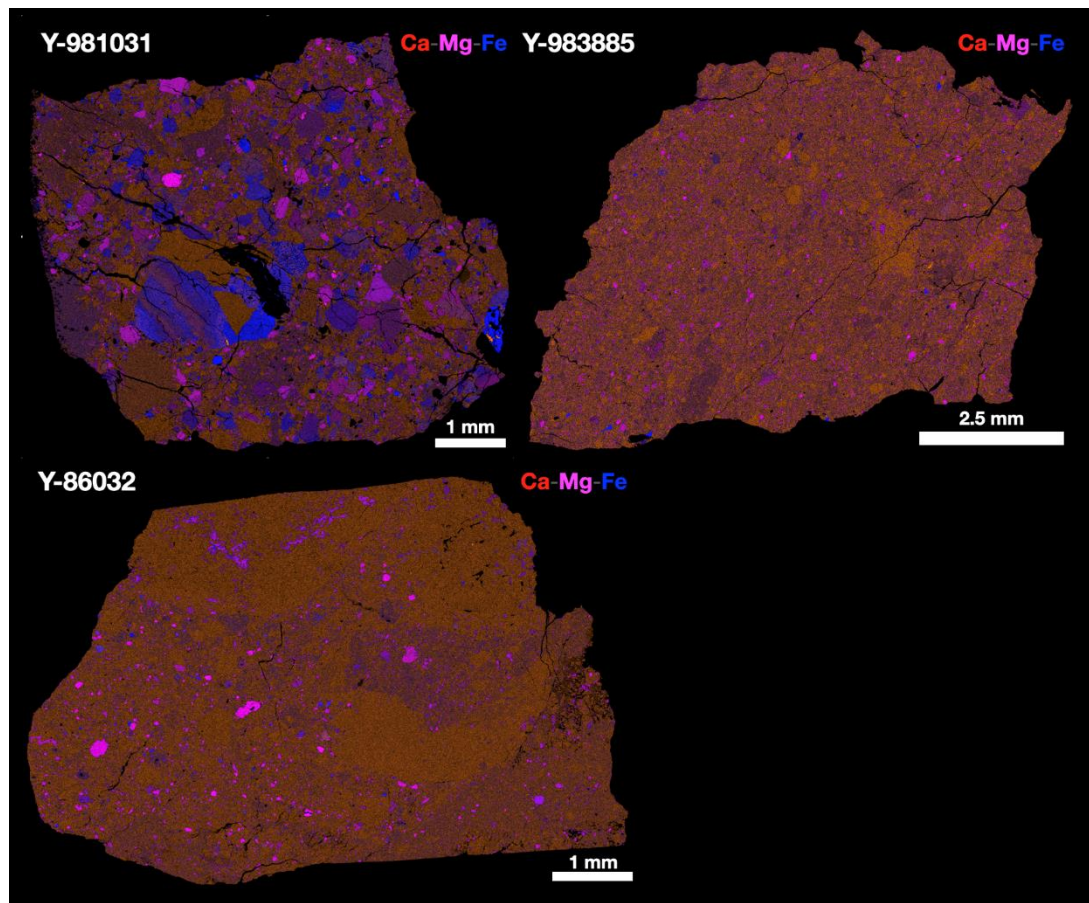


Figure 4.2 Combined Ca-Mg-Fe X-ray images of studied regolith breccia meteorites.

The whole section back scattered electron images (**Figure 4.1**) and X-ray images (**Figure 4.2**) were obtained from JEOL JSM-7100F field emission scanning

electron microscope equipped with an energy dispersive spectrometer (Oxford Aztec Energy) at the NIPR. The images mosaic was done using *Mosaic-J* tool in *Image J* free software by manually overlapping different images. The X-ray images were combined using *Image J* software by assigning a specific color to a channel for each element and merging them together. The modal recombination was later performed using thresholding of the phases in the grayscale by assigning a specific DN value (from 0-255). The DN value for a particular phase is kept fixed. The relative errors in modal abundance are usually associated with the choice of the threshold which is calculated ~1-3% for major phases and ~10% for minor phases.

4.3.2 In situ mineral composition

The quantitative chemical composition of mineral and phases within the samples were determined using JEOL JXA 8530F Plus Hyper Probe at PRL. The spot and line analysis on different phases were performed. Phases such as olivine, pyroxene, plagioclase, silica, ilmenite, and spinel were measure with a beam current of 10 nA by focused beam. Metals and oxides were analyzed with combination of beam current ranging from 5-10 nA with a beam diameter ranging from (<1-5 μm). During analysis of plagioclase, Na loss was observed leading to slightly poor stoichiometric proportion of Na in some analysis. All the analyses were performed at 15 kV and data were reduced using a ZAF correction procedure. The typical count times for all the elements was 30s except for Na which was kept 10s. The details regarding crystals and standard were discussed in **Chapter 2**.

4.3.3 In situ trace element composition

LA-ICPMS facility at National Geophysical Research Institute, Hyderabad (NGRI) was utilized to measure the trace element composition of mineral in the studied sections. The same thick section which was previously utilized for the EPMA analysis, was used by removing the gold coating. The analysis spots were marked on the whole

section images and the value of the Si was noted to use as internal standard in the LA-ICPMS measurements. All the analysis was performed with 50 μm spot size. BCR-2g, NIST SRM 612 and GJ-1 were for monitoring the quality of data during the experiments. The measurement protocol is detailed in Section 2.3.2.

4.3.4 Bulk major and trace element composition

The bulk chemical composition was obtained on representative powdered samples provided by NIPR. The instrument *Thermo Scientific iCAP-Q* housed at Physical Research Laboratory, Ahmedabad and at Scripps Isotope Geochemistry Laboratory (SIGL), Scripps Institution of Oceanography, were used for the bulk major and trace element analysis. A ~ 50 mg aliquot of homogenized sample powder was digested in Teflon-distilled concentrated HF (4 mL) and HNO₃ (1 mL) for >72 h on a hotplate at 150 °C, along with total procedural blanks and terrestrial basalt and andesite standards (AGV-2, BHVO-2). Samples were sequentially dried and taken up in concentrated HNO₃ to destroy fluorides, and then diluted to a factor of 50,000 for major-element determination and 5000 for trace-element determination followed by doping with 1 ppb indium to monitor instrumental drift during analysis. Major-element abundances were obtained in low resolution KED mode. For major-elements, Si was

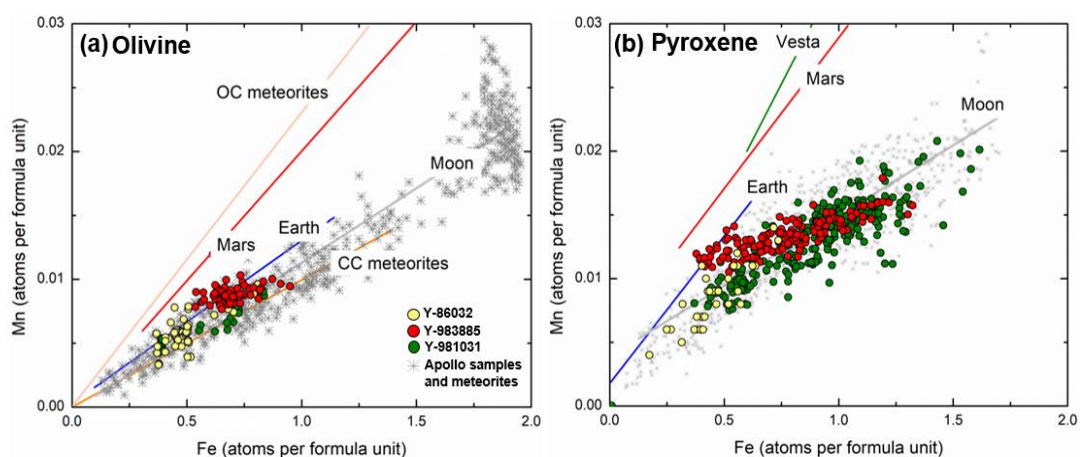


Figure 4.3 Fe/Mn ratio in the olivine (a) and pyroxene (b) of studied meteorites confirming their lunar origin. The gray data corresponds to previously studies Apollo samples. The different color line are the best fitted compositions of different planetary bodies of the Solar System. Data Source: This study, Joy et al. (2014).

derived by difference, with reproducibility of other elements measured on the BHVO-2 reference material being better than 3%, except Na₂O (6.9%).

4.4 Lunar Origin

All the studied meteorites are classified as lunar based on their mineral composition and lithic components and their overall similarity to previously analyzed Apollo samples and lunar meteorites. One of the primary pieces of evidence of having a lunar origin is the presence of Fe-Ni metal in these samples. The highly reducing

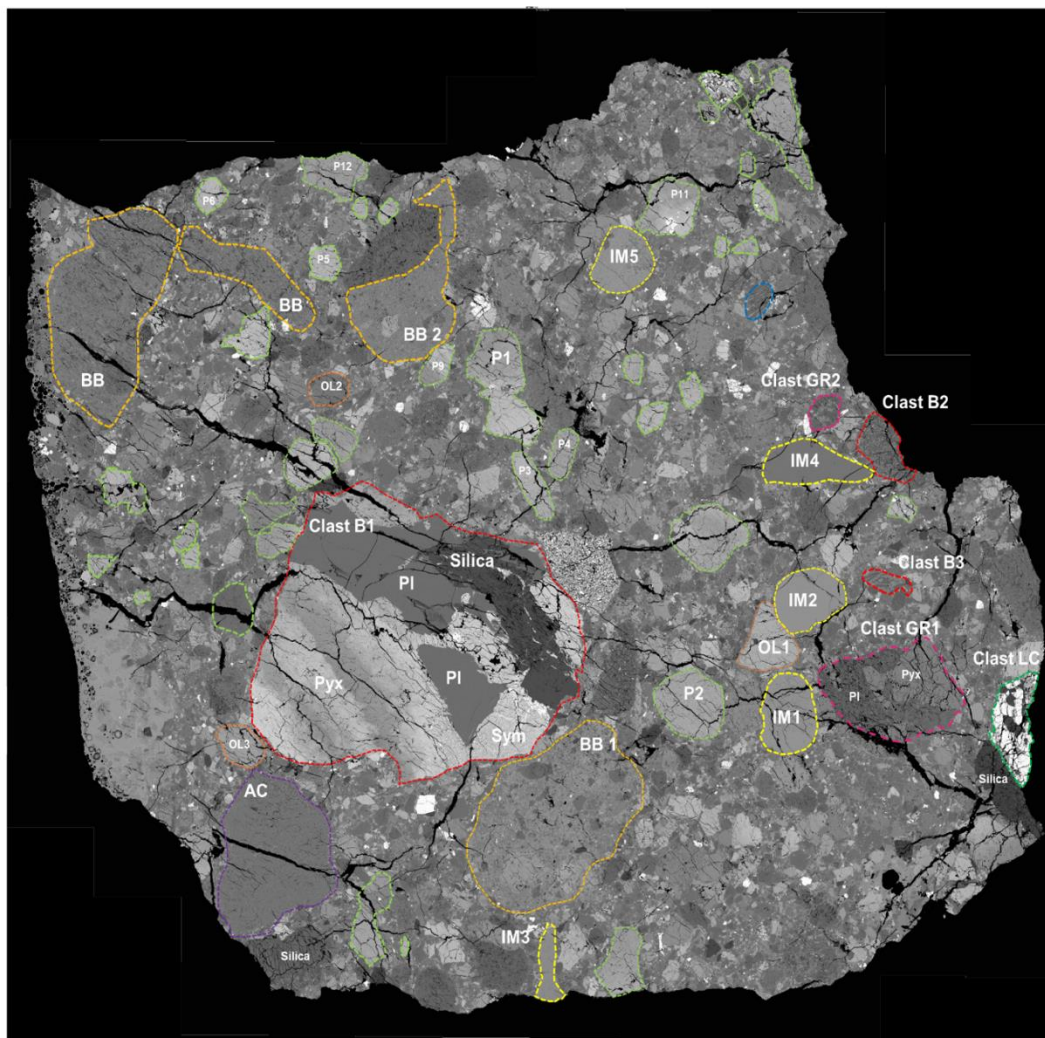


Figure 4.4 Backscattered electron image of sample Y-981031 showing variety of clasts present in the sample. The basaltic clasts are marked as red dashed line. Brecciated clasts are marked as orange dashed line and Impact melt clast as yellow dashed line. Pyroxene clast as green dashed line. Anorthosite clast as purple dashed line. Granulite clast as pink and evolved basalt as green dashed line.

environment/low oxygen fugacity of the Moon favors the formation of metal (Papike et al., 1991; Day, 2020). Fe/Mn ratios of olivine and pyroxene in the studied sections are consistent with the lunar sample mafic mineral trends (**Figure 4.3**) further supporting a lunar origin for the Y-981031, Y-983885 and Y-86032.

4.5 Petrography and Mineral Chemistry Results

4.5.1 Sample Y-981031

The size of the Y-981031 section is $\sim 6.6 \times 7.6$ mm (**Figure 4.4**). Texturally, it is a lithic polymict regolith breccia also referred sometimes as fragmental regolith breccia (using terminology of (Stöffler and Keil, 1991)). The presence of glass spherule in the sample suggest their regolith nature (clast IM in **Figure 4.4**). The grain size of clasts ranges from 0.3-0.9 with few clasts reaching up to 1-2 mm size (**Figure 4.4**). The sample is composed of basaltic clasts (< 2 mm) and anorthosite (granulitic) lithic clasts, fragments of symplectites and mineral clasts of angular pyroxene, olivine, plagioclase, other non-silicate phases such as ilmenite, and troilite set in a glassy matrix.

The sample also contains several impact melt breccia clasts (BC in **Figure 4.4**) of varying grain size and composition. A highly vesicular fusion crust is also seen on the sample. Overall, the sample is dominated by basaltic component when compared to other two breccia samples.

4.5.1.1 Basaltic clasts

The basalts are the most common clasts among the lithic clast population in Y-981031. Basaltic clasts show wide range of textures and compositions (Table 1). The textures range from gabbroic (length ≤ 1.0 -2.0 mm) (Clast B1) to very fine grained (< 0.1 mm) sub ophitic (Clast B2) (**Figure 4.5c**). The largest basaltic clast (Clast B1) is $\sim 2.2 \times 2.0$ mm and contains relatively coarse pyroxene, plagioclase, silica and symplectite phases. The pyroxene shows a composition range of $W_{0.17.9-32.2}En_{4.2-47.1}Fs_{26.1-70.5}$ (**Figure 4.6**). The pyroxene shows strong zoning and exsolution lamellae

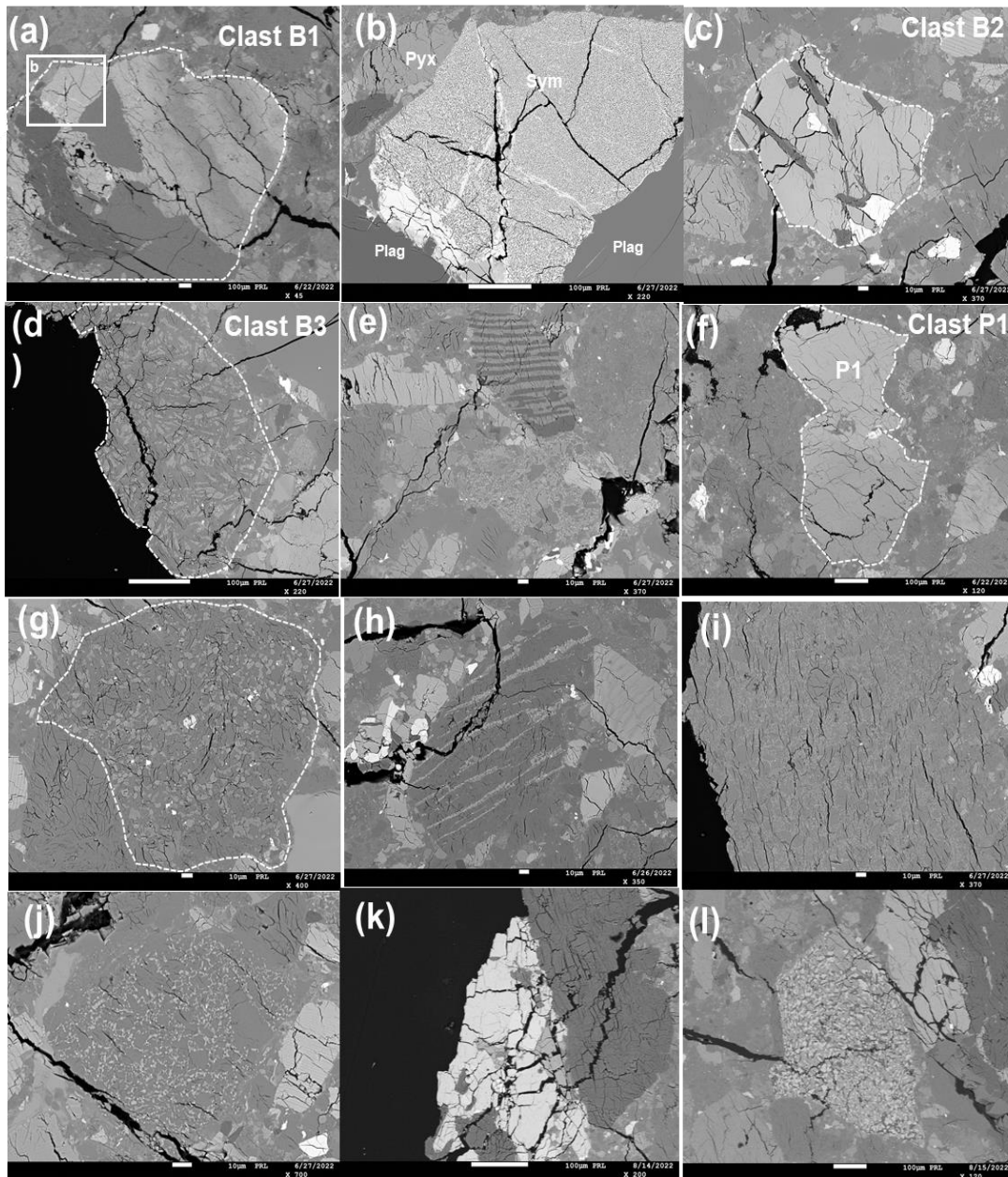


Figure 4.5 Backscattered electron images of clasts and components in Y-981031. (a) VLT basalt B1 with relatively coarse exsolution. (b) Fine grained symplectite present in clast B1. (c) small clast B2 containing fayalitic olivine. (d) clast B3 showing ophitic texture. (e) Si-K-feldspar clast showing texture of liquid immiscibility. (f) isolated pyroxene clast containing dark augitic composition below and light pigeonitic composition above. (g) small gabbroic anorthosite clast with pyroxene embedded within anorthosite. (h) recrystallized fragment of grabbroic anorthosite. (i) fine grained melt with inclusions of plagioclase showing sign of thermal erosion . (j) clastic melt small clast plagioclase in a much finer matrix. (k) clast of Fayalite and silica showing composition of late mesostasis phase. (l) symplectite clast showing vermicular pyroxene, olivine and silica.

(up to 0.2 mm thick), coarser than most of the Apollo mare basalts. The light and dark

bands of coexisting pigeonite and augite is clearly resolvable in BSE image (**Figure 4.5a**). The plagioclase grains of clast B1 show a narrow compositional range from $An_{90.3}$ to $An_{92.8}$. This Fe-rich pyroxene also grades into fine grained symplectite textures of hedenbergite, silica and olivine, formed possibly by breakdown of pyroxferroite (**Figure 4.5b**). A very large (length ~ 1.0 mm) irregular, heavily fractured silica grain

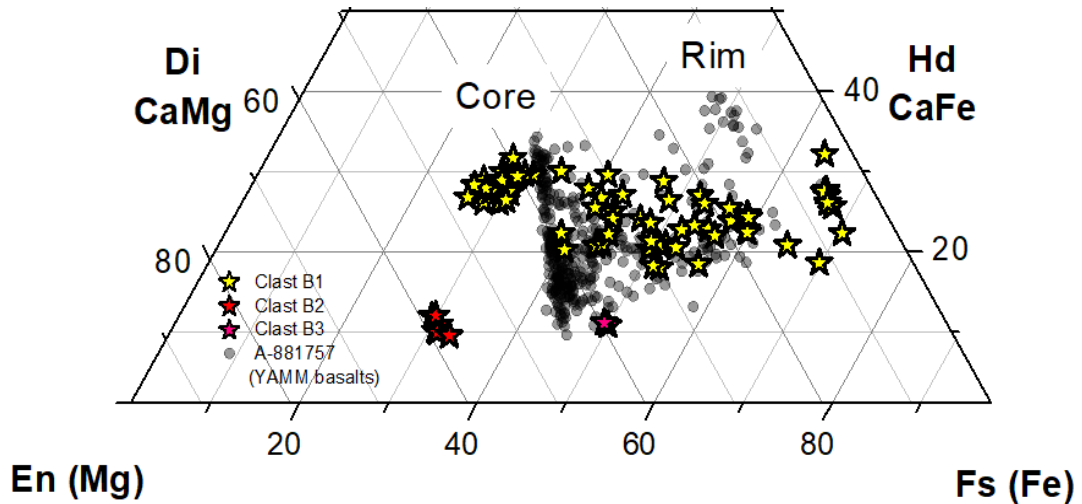


Figure 4.6 Pyroxene chemistry from selected clasts in sample Y-981031. Basaltic clast B1 show composition similar to A-881757, while basaltic clast B3 has more Mg composition.

and small grains of ilmenite and troilite are also found in the clast B1.

Clast B2 ($\sim 0.4 \times 0.3$ mm) is sub ophitic basalt with elongated plagioclase and pyroxene grains. The pyroxene composition in clast B2 has range of $Wo_{10-12}En_{58-60}Fs_{29-31}$, which is more Mg rich than the clast B1. Plagioclase in the clast B2 shows composition $An_{92.0-93.1}Ab_{7.1-6.5}Or_{0.9-0.4}$. Ilmenite and troilite (few microns in size) are present as accessory phase. Clast B3 is very small ($\sim 0.3 \times 0.1$ mm) skeletal grain with a relatively restricted mineral composition. Pyroxene, primarily pigeonite, has composition of $Wo_{10.8-11.3}En_{38.9-40.3}Fs_{48.8-50.2}$. Plagioclase has restricted composition of An_{90-92} , similar to that in clast B1. All three-basalt clasts of Y-981031 falls in a distinct range showing that each of them might have different origin. Pyroxene composition in two basalt clasts (B1 and B3) falls within the compositional range of YAMM basalts while the pyroxenes of basalt clast B2 falls on the Mg rich side. However, the low Ti

composition of pyroxenes in the basaltic clasts ($\text{TiO}_2 \sim 0.25 - 0.73$ wt.%; **Table 4.2**) supports their very low Ti nature.

The relatively coarse-grained basaltic clast B1 with slightly Mg rich composition closely matches with some other unbrecciated basalts such as EET 87521/96008, QUE 94281, Y-793274, Y-793169, MET 01210, MIL 05035 and A-881757. The compositional evolution of pyroxene in Clast B1 is similar to previously analyzed low Ti/ Very low Ti basalts (Joy et al., 2014). In the Al/Ti versus Mg# (Mg/Mg+Fe) plot, the basaltic clast B1 overlaps the range of Dhofar basaltic clasts and other VLT lunar meteorites (**Figure 4.7a**). The flatter portion of the plots (at Mg# ~ 0.45) can be explained by the co-crystallization of plagioclase without ilmenite being a cotectic phase. Similar compositional trends have previously been observed in case of YAMM basalts, Apollo 17 VLT as well as other VLT lunar basalts (Korotev et al., 2009). The Mg# correlates well with Ti# (Ti/Ti+Cr) and pyroxenes in the basaltic clasts follow a VLT trends similar to other lunar basalts (**Figure 4.7b**). Other than pyroxene and plagioclase the only basaltic clast B1 contains silica and symplectites (**Figure 4.5 a-e**). The symplectite associated with the clast B1 is fine-grained assemblage of hedenbergite, silica and olivine. The bulk composition of the symplectite is attempted using broad beam analysis of 10 μm diameter and overall composition plot near very

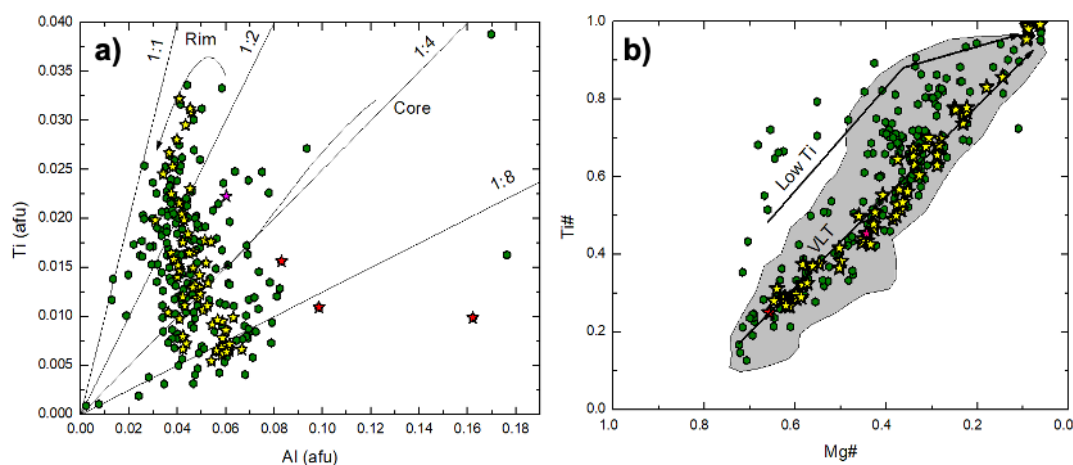


Figure 4.7 Compositional evolution trend of pyroxene in Y-981031. a) Ti versus Al composition of pyroxenes b) Ti versus Mg# composition of pyroxene in Y-981031. Green color corresponds to pyroxene clasts, grey regions from VLT basalts (Joy et al., (2008) and star symbols correspond to basaltic clasts: Yellow- B1, Red-B2 and Pink- B3.

Fe-rich pyroxene or pyroxferroite suggesting its crystallization from pyroxferroite breakdown (Lindsley et al., 1972).

The trace element abundance of basalt clast B1 was also measured using LA-ICPMS. The relatively coarse grain nature of clast B1 enable us to measure the abundance of trace element in pyroxene, plagioclase and symplectite. The trace element variation seen in the clast B1 pyroxene is given in **Figure 4.8** and Table 4.6. The progressive increment of REE concentration from core to the rim of the pyroxene clast suggest the progressive fractional crystallization. The plagioclase trace elemental abundance of the clast B1 is also measured to highlight strong Eu anomaly in the sample. The REE composition of symplectite closely matches with the composition of the rim of the pyroxene again suggesting their formation by breakdown of metastable pyroxferroite.

4.5.1.2 Feldspathic clasts

Feldspathic clasts are the next dominant lithic clasts in the sample Y-981031. The texture of these clasts is typical granulitic and dominantly composed of anorthositic and pyroxene and olivine. One relatively coarse granulite clast GR1 (~ 0.8 × 0.6 mm) is found in the sample and rest of the granulitic clasts are very small (**Figure 4.4**). The

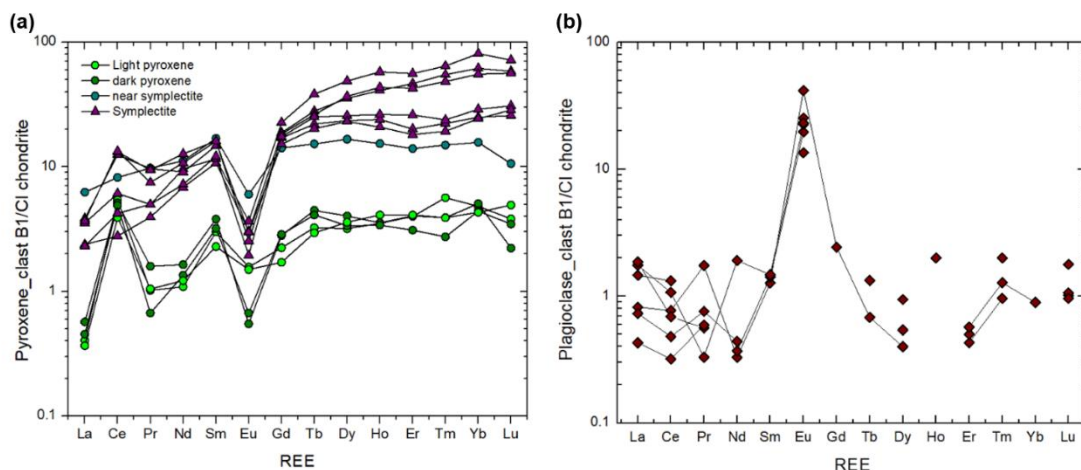


Figure 4.8 REE composition of minerals of clast B1. (a) pyroxene core to rim including broad beam pyroxene symplectite REE composition. The REE composition clearly show progressive REE enrichment from core to rim. Ce anomaly highlighted might indicate some terrestrial weathering in the sample. (b) REE concentration of plagioclase fragments show strong positive Eu anomaly as expected.

granulitic clast contains pyroxene of compositional range $Wo_{32.0-34.6}En_{51.6-52.4}Fs_{13.0-16.4}$ and plagioclase of composition $An_{87\pm 0.4}$ (Table 4.2). The Ti/Al ratio of 0.5 in the clast GR1 indicates late stage crystallization of pyroxene after the plagioclase separation within these clasts. The composition of the granulitic clast GR1 is similar to the granulitic clasts of MET 01210 and Dhofar group of meteorites (Day et al., 2006a; Joy et al., 2014).

4.5.1.3 Glass spherules and breccia clasts

The sample Y-981031 also contains glassy melt clasts. The textures of most of these clasts are glassy with no fracture (**Figure 4.4**). The four glass spherules found in the sample show circular to irregular shapes and their size ranges from 0.4 to 0.7 mm in length. Their composition shows large variation in Al_2O_3 (9.8 – 26.2 wt. %) and FeO (4.7 – 14.1 wt. %) (Table 4.2). As two processes are known to produce the glass beads on the Moon: impact melting of lunar surface materials (impact origin) and pyroclastic volcanism (volcanic origin), origin of these melt clasts were examined following the criteria (e.g., the petrographic features, MgO/ Al_2O_3 ratios and Ni content) proposed by Delano (1986) and Zeigler et al. (2006) to distinguish these two different types of glasses. IM1, IM3 and IM4 display homogeneous texture and have MgO/ Al_2O_3 of 0.56, 0.75 and 0.32 respectively, such low MgO/ Al_2O_3 is suggestive of impact origin of these melts. The impact melt origin of these clasts is also supported by high Ni (~100-110 ppm) in these melt clasts. The impact melt clast IM2, on the other hand show MgO/ Al_2O_3 ~1.56 which is consistent with the ratios of Apollo volcanic glasses (i.e., MgO/ Al_2O_3 > 1.25; Zeigler et al., (2006). The low average Ni abundance (~26.4 ppm) in this clast also support its volcanic origin.

The impact melt breccia of both glassy and crystalline type is present in Y-981031. These breccia clasts are clast bearing and contains mineral fragments of variable sizes (0.1 – 0.3 mm) enclosed in a glassy matrix. The pyroxene is low Ca with composition of $Wo_{10.5}En_{56}Fs_{33.6}$ and plagioclase have composition of $An_{93.6\pm 0.4}$. The breccia also contains numerous Fe-Ni metal with Ni rich composition reaching up to 6.5 wt. %.

The trace element abundance of the impact melt as well as breccia clasts were also measured. The breccias due to their clastic nature shows the composition of dominant constituent phase(s). For example, the breccia BB1 has highly positive Eu anomaly while rest of the clasts show LREE ($[La/Sm]_{cn} = 0.83$; $[La/Yb]_{cn}=0.72$ and $[La/Lu]_{cn}=0.89$) positive pattern with negative Eu anomaly (**Figure 4.9**). The impact melt clasts show variable composition, but are less incompatible element rich than Apollo impact melt from Korotev et al., (2009). (**Figure 4.9**).

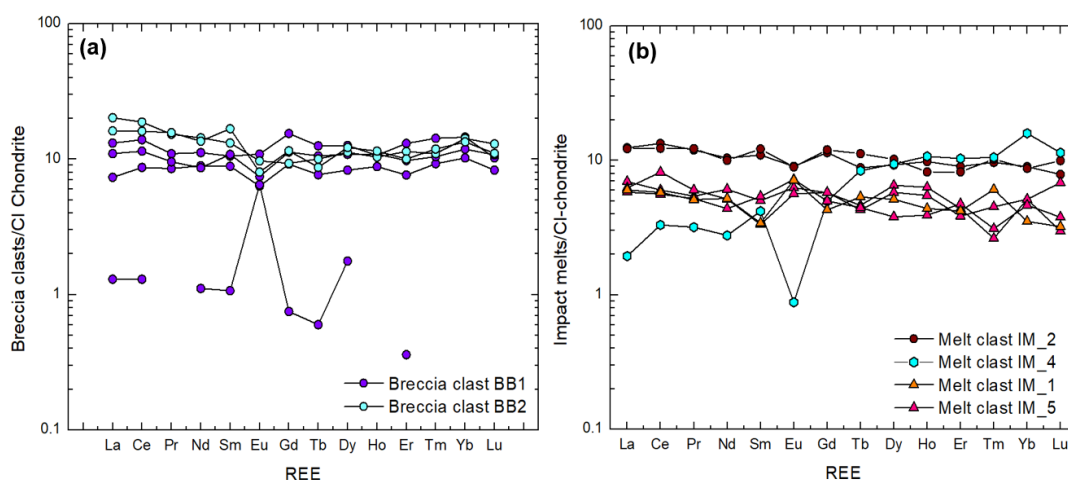


Figure 4.9 Trace elemental abundance in breccia and impact melt clast of Y-981031 measured using broad (55-60 μm) laser beam over the clasts. (a) Broad beam analyses of breccia clast BB1 and BB2 show dominance of pyroxene with only one data of clast BB1 show anorthositic composition. (b) Impact melt clasts (IM-1,2,4 and 5) REE composition. Most impact melts except for IM-4 show negligible Eu anomaly.

4.5.1.4 Mineral clasts and Matrix fragments

Pyroxene is the most dominant mineral fragment present in the sample and occupies largest proportion. The majority of the pyroxene mineral clasts compositions typically show mare basalt affinity (**Figure 4.6**). Some of the pyroxenes show relatively coarse-grained texture (~ 1.0 mm in length) and thick exsolution lamellae. Dark and light bands are relatively coarse while the width of exsolution lamellae in other pyroxene fragments (~ 1 μm) falls in same category as pyroxene in other lunar basalts and brecciated meteorites (**Figure 4.5f**). The width of the exsolution lamellae is often related to the indication of cooling rate. The observed varying exsolution lamellae is indicative of very slow cooling rate of these pyroxenes. The composition of pyroxenes is given in Table 4.2.

The fragments of symplectites and mesostasis are also found throughout the sections. Pyroxene symplectites show variable texture and composition. The symplectite fragment reaches up to a size of ~0.6 mm. The texture and composition of the symplectite suggest their composition tending towards a Fe rich pyroxene composition (Table 4.2). The sample also contain a clast (**Figure 4.5k**) of mesostasis containing fayalitic olivine (Fa₈₉) and silica (Table 4.2). While fayalitic olivines are

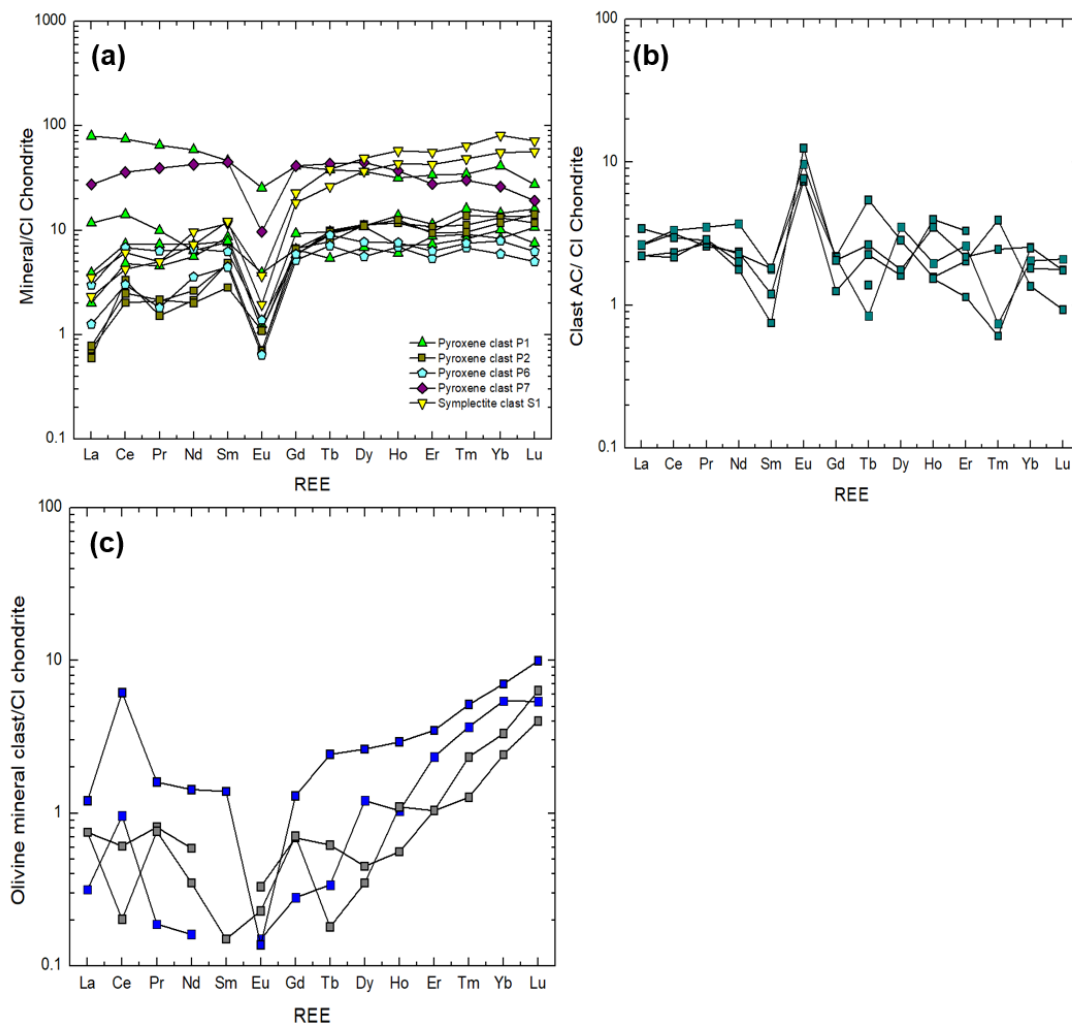


Figure 4.10 Chondrite normalized REE composition of mineral fragments in Y-981031. (a) Pyroxene mineral fragments (P1, P2, P6 and P7) show variable REE composition with pyroxene symplectite (S1) having highest abundance and stronger Eu anomalies. (b) REE abundance of anorthositic fragment (AC) showing homogeneous composition from core to rim. (c) REE composition of two olivine mineral fragments in Y-981031.

found associated with symplectites and mesostasis, Mg rich monomineralic olivine clasts are also found in the section. The composition of olivine ranges from Fo₈₁₋₅₈.

They occur as large mineral fragments with length up to ~0.4 mm with numerous fractures.

Other mineral fragments include plagioclase clast which has length ~ 1.0 mm. The composition of the plagioclase fragments show variability from An₈₇ - An₉₇. Ilmenite fragments (~0.2 mm) and troilites are dispersed among the sample both within the lithic clast and as isolated mineral fragment. Fe-Ni metal is also abundant in the section and occur as irregular small grain within the matrix. While majority of metal grains have low Co, few Co rich grain, similar to metal grains observed in LaPaz basalts by Day et al., (2006b) is also found in sample Y-981031. The fusion crust of the sample varies in composition, depending on the host mineral that melted and converted as the crust. The compositions of all the discussed phases are given in Table 4.2. The matrix of the Y-981031 are welded by agglutinate fragments and small mineral clasts with compositions identical to the mineral clasts and lithic fragments described. The trace element composition of pyroxenes shows variable REE composition, indicating the clasts probably represent various stages of magma evolution.

4.5.2 Sample Y-983885

Y-983885 sample (~ 6.6 × 10.8 mm) is a polymict regolith breccia containing lithic clasts, isolated mineral fragments, glass spherules - all embedded in a dark fine-grained glassy matrix. In contrast to Y-981031, the sample has only few lithic clasts over ~0.5 mm across and most of the clasts and mineral fragments are small ~100-200 μm. The sample is composed of variety of lithic clasts including KREEP rich clast (IMB 3), impact melt breccia clasts (IMB 1-7), VLT basalts (BB 1-3), feldspathic clasts (FC1-3) and relatively coarser granulite clasts (~1.0 mm; clast GC), with varied textures. The individual minerals within the breccia in decreasing order of abundance are pyroxene, plagioclase, olivine, ilmenite, troilite and Fe-Ni metal grains.

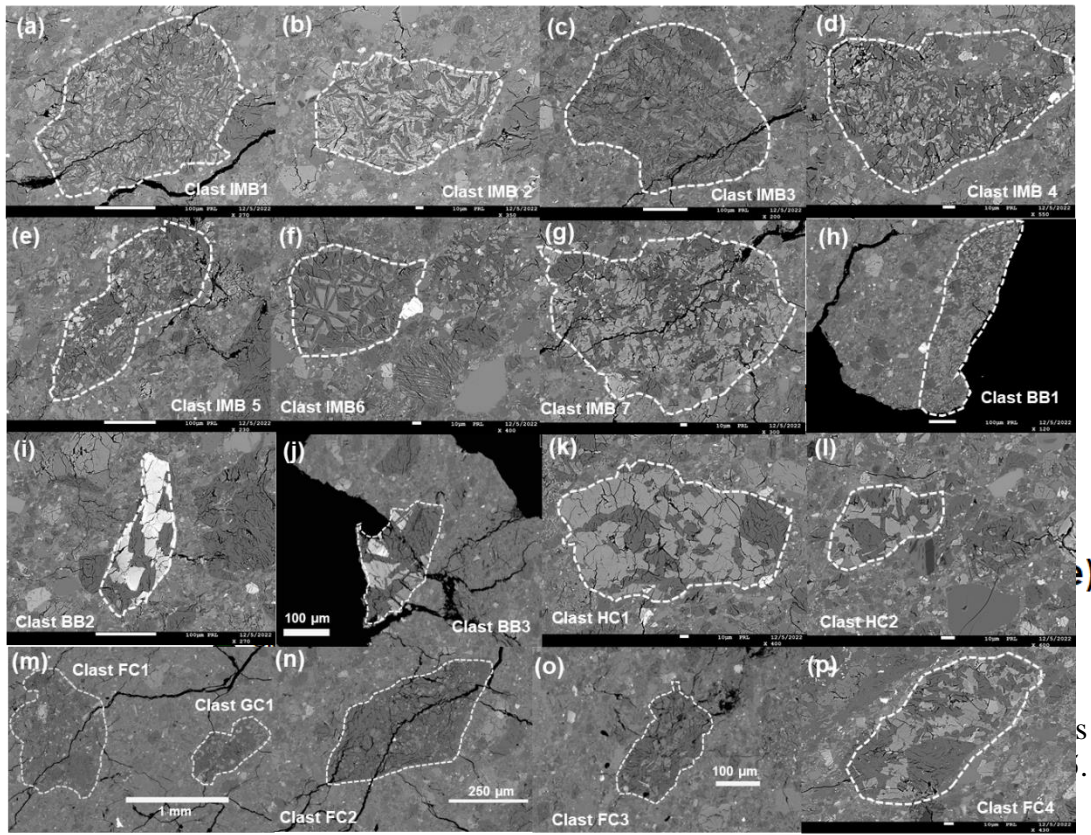


Figure 4.11 Crystalline impact melt clast (IMB), basaltic clasts (BB) and feldspathic clasts (FC) in lunar regolith breccia meteorite Y-983885. BSE images showing (a-g) reannealed, metamorphic textures in crystalline IMBs, (h-j) basaltic clasts with ophitic to gabbroic textures, (k) pyroxene dominant clast HC1 with compositional similarity to Mg suite norite, (l) granular clast HC2 compositional similar to anorthosites, (m-p) feldspathic clasts and granulitic clast (m; GC 1) in the Y-983885.

4.5.2.1 Crystalline impact melt and basaltic clasts

Y-983885 contains numerous small crystalline impact melt clasts with textures ranging from reannealed, metamorphic (IMB_1 to 5), to ophitic (IMB_6) and sub-ophitic (IMB_7) (**Figure 4.11**). They look texturally similar to crystalline impact melt rocks that formed from large-degree impact melting events which is also evident from presence of melted (recrystallized) minerals within these clasts (Koeberl et al., 1991; Taylor et al., 1991). Some clasts are likely to inherited (less modified) from target rock(s). Some of crystalline melt breccias (IMB_2, 4 and 6) also incorporate minor metallic components, which are probably originated from projectile that caused the impact event (**Figure 4.11**; Norman and Nemchin, 2014). The crystalline impact melt

breccias composed of pyroxene with compositional range of $Wo_{5.8-28.6}En_{50-60.2}Fs_{16.4-33.5}$, olivine (Fo_{62-74}) and plagioclase with $An_{89.8-98.2}$ (Table 4.3; **Figure 4.12**).

Among basaltic fragments, the ophitic basaltic clasts, BB1 ($\sim 0.76 \times 0.18$ mm) contains olivine of composition Fo_{68-70} , pyroxene with compositional range of $Wo_{9.8-14.6}En_{41.5-58}Fs_{32.2-44.0}$ and plagioclase grain have compositional range from $An_{91.5}$ to $An_{93.6}$. The gabbroic basalts, BB2 and BB3, contains no olivine and have pyroxenes of relatively evolved compositions $Wo_{13.6-30.7}En_{14.8-24.2}Fs_{46.8-71.6}$ (**Figure 4.11, 4.12**; Table 4.3 and Table 4.8). The Ti/Al ratio of the basaltic clasts vary as a function of impact-induced metamorphic grade in many clasts (**Figure 4.14**). For crystalline basalts, the Ti/Al ranges from 0.5 to 0.25 which is consistent with early pyroxene crystallization followed by plagioclase.

A broad beam laser ablation inductively coupled plasma mass spectrometry measurement of minerals and clasts in Y-983885 were also made to understand their trace elemental composition. The pyroxenes show variety of composition with pattern suggestive of magmatic fractionation (**Figure 4.13a**). The average composition over three 55 μ m spot on the clast IMB_3 suggests that the clast is a KREEP rich variety (**Figure 4.13b**).

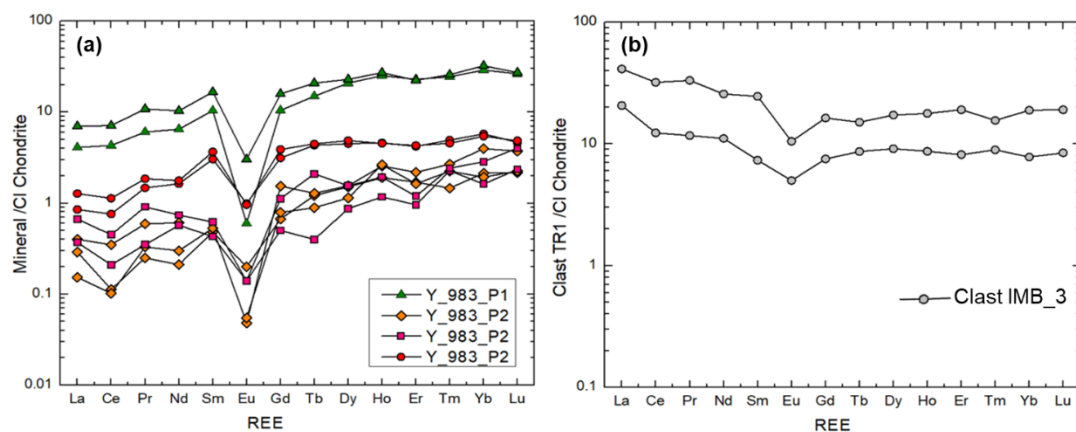


Figure 4.13 Trace elemental variation in (a) pyroxene mineral fragments and (b) bulk composition of crystalline impact melt clast IMB_3 of Y-983885 measured using broad beam of ~ 55 μ m showing REE rich composition.

4.5.2.2 Feldspathic anorthosite, Magnesium suite and Granulitic clasts

Four lithic clasts (Clast FC_1-4) have been recognized as feldspathic on the basis of their plagioclase abundance (>75 vol. %; **Figure 4.11m-o**). All the feldspathic clasts contain dominant minerals plagioclase, followed by pyroxene and olivine. The compositional ranges of pyroxene are toward the Mg rich end member ($Wo_{3.2-22.2}En_{55.0-72.2}Fs_{22.8-34.2}$). The olivine composition varies from Fo₅₅ to Fo₇₃ while plagioclase composition shows a range of An_{87.8-97.4}. In contrast to feldspathic clasts, Clast HC1 has slightly higher modal abundance of pyroxene than plagioclase. The compositional range of clast HC1 pyroxene ($Wo_{11.6-12.4}En_{57.90-58.4}Fs_{29.7-29.8}$) and plagioclase (An_{92.4.8-94.7}) falls between the field of previously reported Mg suite clasts and Ferroan anorthosite (**Figure 4.11, 4.18**). Clast HC2 show granular texture similar to clast HC1, and also have similar pyroxene composition but with slightly higher anorthitic plagioclase An_{96.2} (Table 4.8; **Figure 4.18**). Sample Y-983885 also contains granulite (GC1) showing granoblastic texture. The plagioclase composition of granulite clasts is in the range of An_{94.4-94.9}. The olivine composition in the clast is Fo₆₅ while pyroxene show narrow compositional range of $Wo_{8.56-37.7}En_{45.4-63.7}Fs_{16.8-27.2}$.

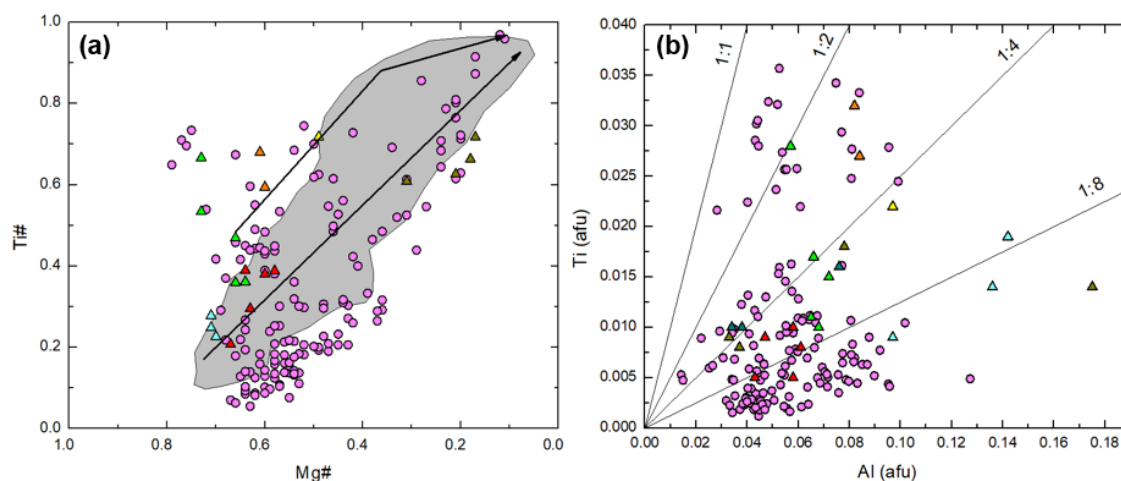


Figure 4.14 Compositional evolution trend of pyroxenes in Y-983885. (a) Mg# versus Ti composition of pyroxene mineral fragments in Y-983885 (b) Al versus Ti composition of pyroxenes. Pink circles correspond to pyroxene mineral fragments and filled triangles (Yellow-clast IMB_7; Dark Yellow-clast IMB4; Cyan-clast IMB1; Orange-clast BB3; Dark green-clast IMB_6) are pyroxenes in basaltic clasts. Grey region is field of lunar basalt pyroxenes from Joy et al., (2008).

4.5.2.3 Matrix and mineral fragments

The matrix of Y-983885,74 section is predominantly mafic in composition, dominated by pyroxene and olivine of both igneous and metamorphic affinity. The compositional range of pyroxenes in the matrix show large variations from orthopyroxene to pigeonite and augite (**Figures 4.12, 4.13**). Some isolated grains of pyroxene reveal exsolution lamellae of width $\sim 2\text{-}3\ \mu\text{m}$, smaller in comparison to that of Y-981031. The olivine grains in the sample have compositional range of $\text{Fo}_{36.8-76.5}$. Plagioclase grains occur as metamorphosed anorthitic fragment within a compositional range of An_{87-98} .

Minor mineral fragments include ilmenite, Fe-Ni metal, troilite and silica. Ilmenite in the samples is very rare and usually associated with the basaltic fragments. There are abundant Fe-Ni metal grains in Y-981031 and all of them show high Ni/Co ratio, indicating a meteoritic origin of these grains (for details refers to Section 5.5.1).



Figure 4.15 Lithologies of sample Y-86032 seen under optical camera (left panel) and microscope (right panel).

4.5.3 Sample Y-86032

Y-86032 sample is a feldspathic lunar meteorite classified as feldspathic regolith breccia. Previous studies have argued, based on low Th content that the origin of these meteorites is far away from the Procellarum KREEP Terrane (PKT) region (Nyquist et al., 2006; Yamaguchi et al., 2010). It is one of the most studied samples among the all the three samples discussed in this chapter. Nyquist et al., (2006) have reported an

ancient anorthositic clast in these sample which was previously not observed in Apollo and Luna samples. The study also calculated the age of this rock and have a reported age of ~ 4.4 Ga based on Ar-Ar and Sm-Nd isotopic systematics. A recent work by Ito et al., (2022) also reported the similar ancient Pb-Pb age of this meteorite. Analysis of pyroxenes in two different lithologies yielded different Pb-Pb dates: 4426.4 ± 5.6 Ma from Dark Gray lithology, and 4386.2 ± 3.7 Ma from Gray lithology, indicating that the pyroxene in each fragment has different formation timing (Ito et al., 2022). Therefore, the old reported ages of the Meteorite Y-86032 suggest it to record the formation of earliest crust on the Moon.

The studied section of Y-86032 ($\sim 4.6 \times 7.3$ mm) also contains previously reported lithologies: Light Grey, Dark Grey, Grey and White units (**Figure 4.15**). The clast inventory includes anorthositic breccia, impact melt and granulitic clast, and

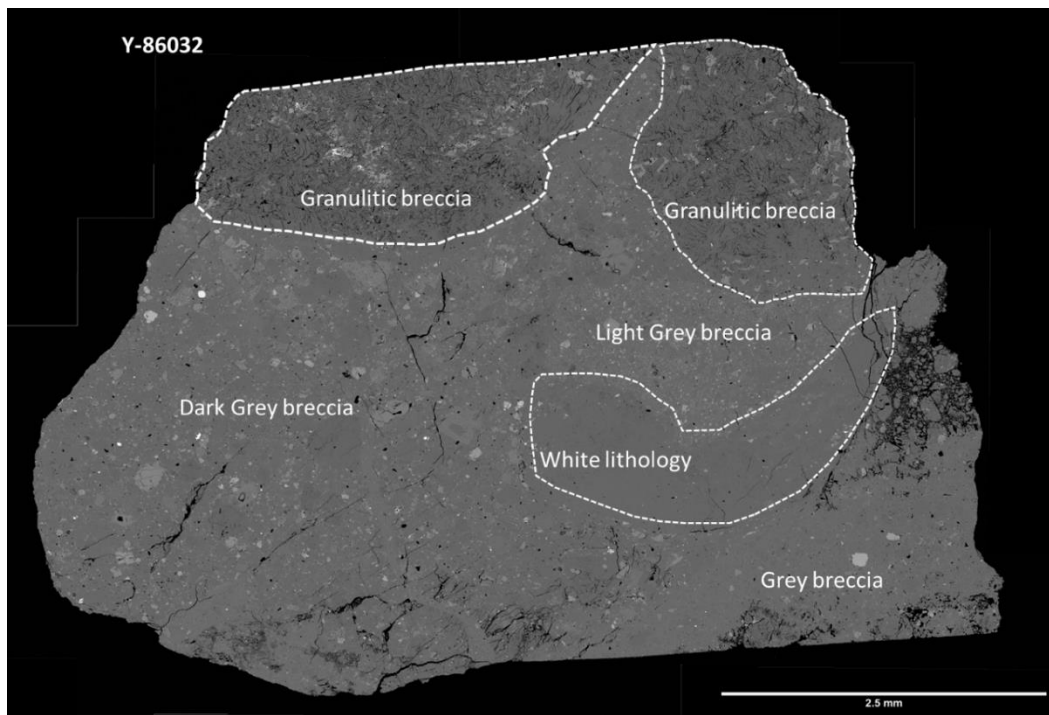


Figure 4.16 Backscattered electron images of Y-86032 marking granulitic breccia (GB1 (left) and GB2 (right)), and lithologies identified in optical images (Dark grey, white, grey and light-grey lithology).

several mineral fragment of olivine, pyroxene, plagioclase, ilmenite and spinel, similar to the observations from previous studies. In contrast to the previously discussed samples Y-981031 and Y-983885, Y-86032 has very few lithic clasts and

contains a few isolated mineral clasts of olivine embedded in the glassy anorthositic matrix. No basaltic clast was observed in this section, only three basaltic clasts have been reported until now in the samples depicting the rarity of basaltic clasts in these samples. The presence of glass spherules in the sample suggests them to be a regolith breccia but their scarcity indicate that they are an immature variety unlike Y-981031.

The White (W) lithology occurs as sub rounded fragment (~1.0 mm diameter) in between the other lithologies with sharp boundaries between two. The visual appeal of the W-lithology suggests it to be monomineralic feldspar. Light grey (LG) lithology surround the white and grey lithology and have gradational boundary with Dark grey (DG) lithology. The clast in the LG lithology appears to be deformed and have no well-defined boundaries. Previous studies suggest LG lithology is the deformed mixture of breccia clast and clastic matrix lithified together as a result of shock. The LG lithology is predominantly anorthositic and granulitic breccia containing a few small mafic mineral clasts. The DG defined domain in the section is clastic matrix composed of igneous, metamorphic, brecciated and mineral fragments of olivine, pyroxene, plagioclase and spinels. The impact melt domains highlighted in previous studies are not well defined in this section and their boundaries appear to be diffused in other lithologies.

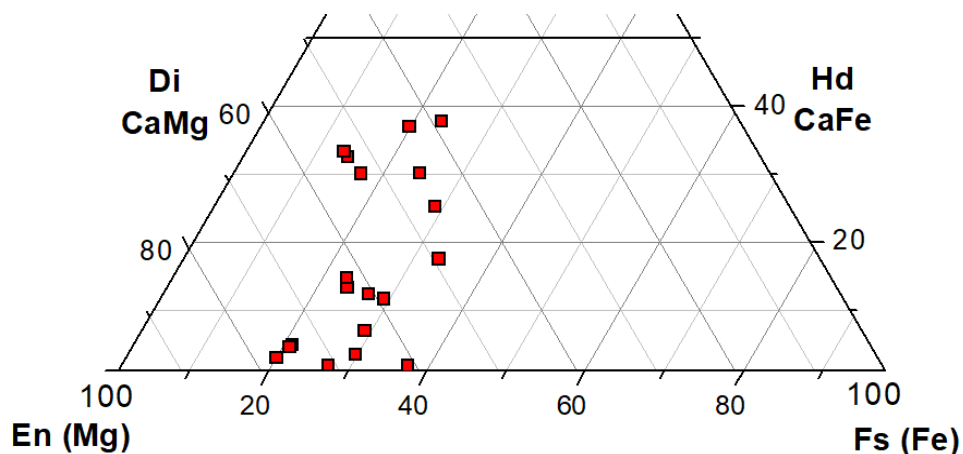


Figure 4.17 Compositional variation observed in isolated pyroxene grains (marked as red) of Y-86032.

4.5.3.1 Granulitic breccia

The section contains two granulite units (marked as granulitic breccia in **Figure 4.16**) showing granoblastic texture with clast size up to ~2.7 mm long. They also contain mafic silicate unit intermingled at locations (**Figure 4.16**). The pyroxene composition shows a range of $Wo_{11.7-37.1}En_{43.2-59.1}Fs_{19.7-29.2}$. Olivine have restricted composition of Fo_{64-63} . Plagioclase compositions in the granulitic breccia are $An_{94.9-96.3}$. Ilmenite and spinels are also present as accessory phases sharing boundaries with plagioclase and pyroxene (Table 4.4).

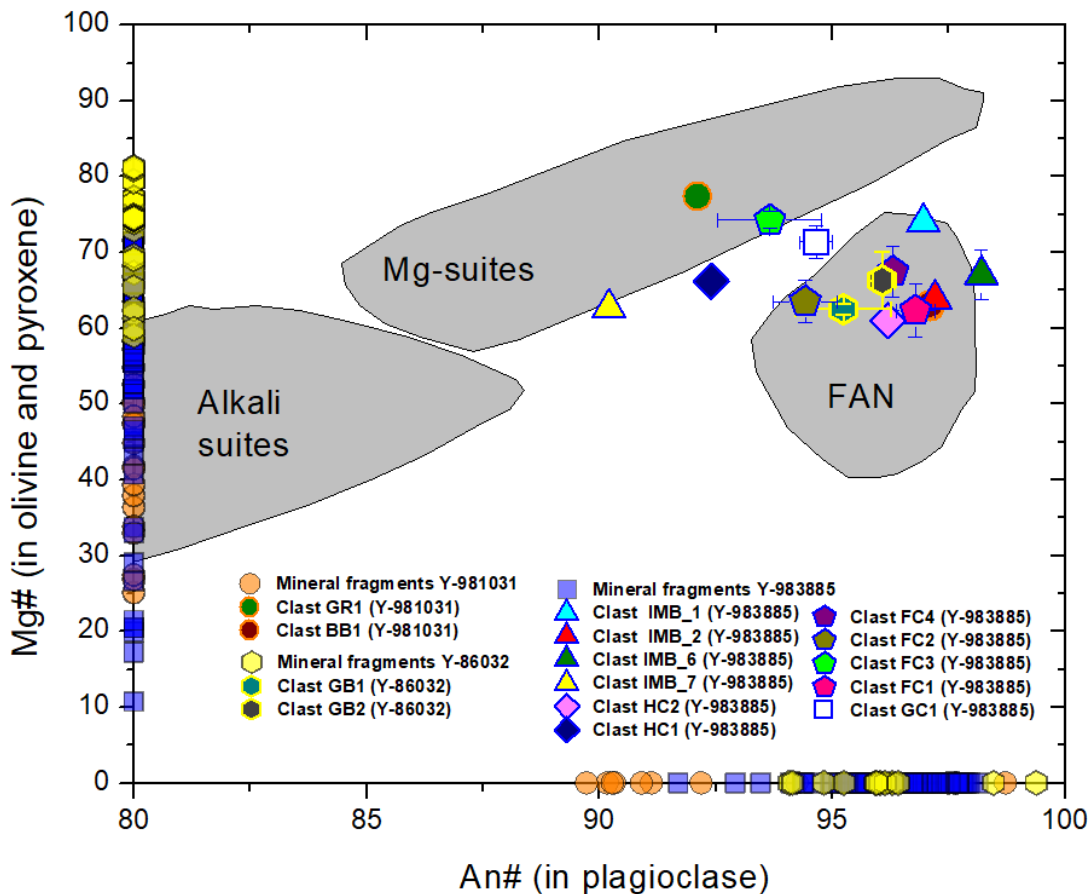


Figure 4.18 Plot of An# $[(Ca/Ca+Na+K) \times 100]$ in plagioclase mineral fragments (plotted over axes) and clasts versus Mg# $[Mg/(Mg+Fe) \times 100]$ in olivine and pyroxene mineral fragments (plotted over axes) and clasts of the studied lunar breccias. Fields showing pristine Apollo rock suites are from James et al., (1989), Warren, (1993), Mercer et al., (2013) and Joy et al., (2014). Data are given in Table 4.7.

4.5.3.2 Mineral clast and matrix fragments

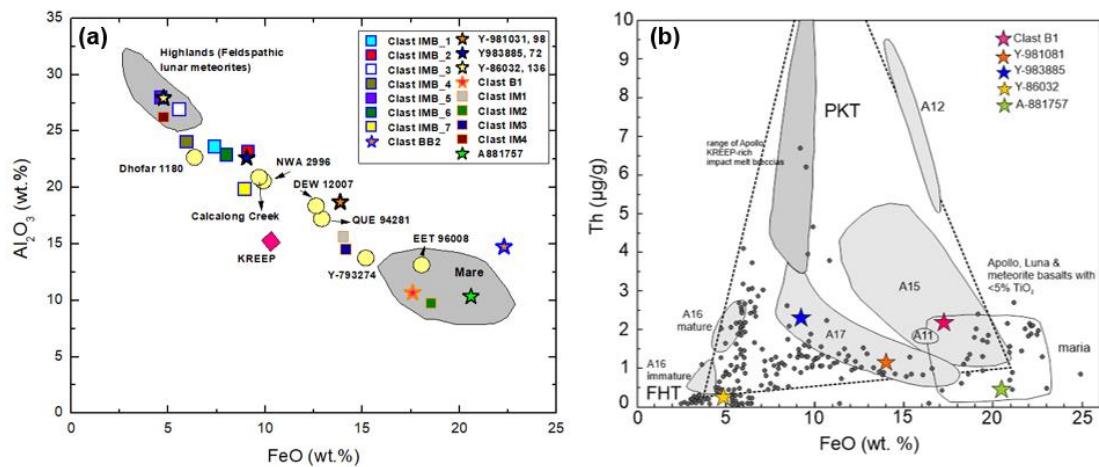


Figure 4.19 Bulk rock chemistry of the studied rock compared with Lunar samples and meteorites. (a) FeO versus Al₂O₃ for the studied samples and clasts in this thesis. Samples plotting in the mare basalts region are A-881757 and clast B1. Clast BB2 is an evolved mare basalt plotted away from Mare region. while rest of the bulk samples and impact melt clasts plot in varied range of mixing between basalt (mare basalt) and anorthosite (highland) end-members. Data Source: Lunar meteorites data are taken from a range of literature sources (Warren 1989; Koeberl et al. 1991; Jolliff et al. 1998; Anand et al. 2003; Hill and Boynton, 2003; Zhang and Hsu, 2009; Mercer et al. 2013; Collareta et al. 2016). (b) Comparison of studied samples in FeO versus Thorium compositional space containing Apollo samples (grey shaded fields) and meteorites (grey points). Data Source: Korotev, (2021) and references therein.

Although fewer, the mineral clasts of olivine, pyroxene, plagioclase and other accessory phases are spread all throughout the sample. The olivine composition in the sample is in the range of Fo₅₉₋₈₁. A line analysis performed over an olivine grain reveals homogenous composition. Plagioclase composition is in the range of An₉₂₋₉₆. Pyroxenes in the sample compositionally vary from orthopyroxene, pigeonite to augite and show a range of Wo_{1.8-37.9}En_{45.4-74.0}Fs_{14.2-37.2}. (**Figure 4.17**)

4.6 Bulk Composition

The bulk composition of all three lunar meteorites (Y-981031 ~0.53 g; Y-983885 ~0.57; Y-86032 ~ 0.49 g) were measured using representative homogenized powder provided by NIPR. The bulk composition of the individual breccia sample represents the variable degree of mixing of different lithologies present. Y-981031 is high Al₂O₃

(18.69 wt.%), very low-Ti ($\text{TiO}_2 = 0.58$ wt. %), low K ($\text{K}_2\text{O} = 0.08$ wt. %) and low Th (1.16 ppm) rock with the chemical composition closest to basalts among the three meteorites (Table 4.1). Measured bulk composition is consistent with the previous measurements (Kaiden and Kojima, 2002; Karouji et al., 2002, 2006; Korotev et al., 2009). The composition of mineral fragments and clasts in Y-981031 also suggest the dominance of basaltic components with few highland fragments (**Figure 4.18**). The composition of Y-981031 closely matches with meteorites QUE 94281, DEW 12007, NWA 4884 and EET 96008/87521 and are likely to be paired with these meteorites (**Figure 4.19**; Zeng et al., 2018). The FeO/MnO ratio (~ 82.35) of Y-981031 falls in the field of typical lunar meteorites (**Figure 4.3**). The REE pattern of Y-981031 indicates LREE enrichment ($[\text{La}/\text{Sm}]_{\text{cn}}=1.37$ and $[\text{La}/\text{Yb}]_{\text{cn}}=2.02$) along with a small Eu anomaly ($\text{Eu}/\text{Eu}^* = 0.73$). The REE concentration ($\sim 16\text{-}33 \times \text{CI}$) of the sample also matches with the above-mentioned meteorites. The high Ni (~ 153 ppm) concentration in the sample is suggestive of chondritic meteorite contamination.

Sample Y-983885 is also classified as high Al_2O_3 (22.62 wt.%), very low -Ti ($\text{TiO}_2 = 0.49$ wt. %), low K ($\text{K}_2\text{O} = 0.13$ wt. %) and low Th (2.35 ppm) rock, similar to the

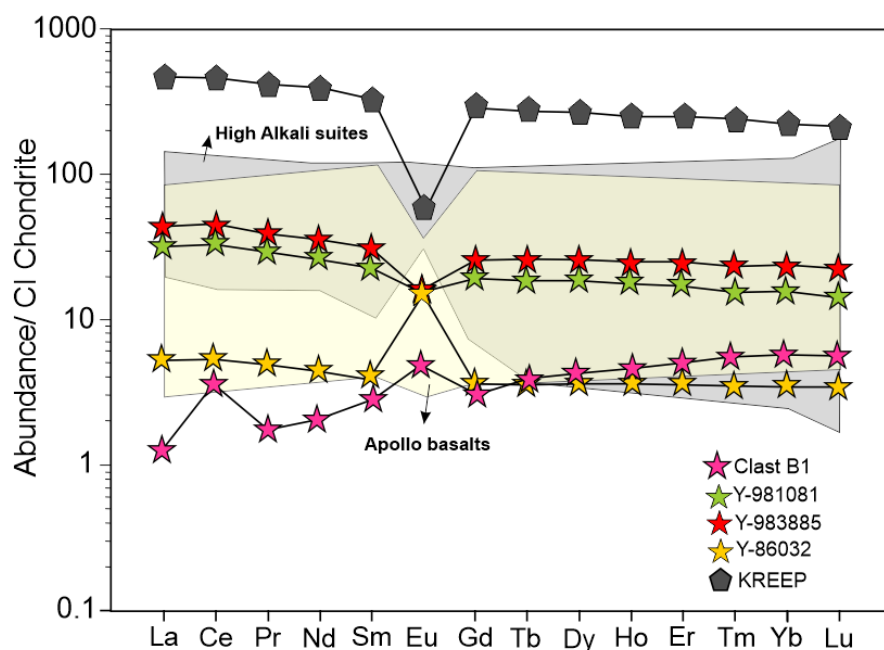


Figure 4.20 Bulk rare earth element (REE) abundances of lunar meteorite Y981031, Y-983885, Y-86032 and clast B1. The bulk rock Apollo mare basalts (dark gray area; Papike et al., 1998), bulk rock Apollo alkali suite samples (yellow area; Wieczorek et al., 2006), and high-K KREEP (Warren, 1989)

lunar meteorite Calcalong Creek (**Figure 4.19** and Table 4.1). The REE abundance ($\sim 24\text{--}45 \times \text{CI}$) of Y-983885 is highest among the three studied samples. The measured REE abundance in Y-983885 is, however, lower than the meteorite Calcalong Creek suggesting their derivation from two distinct locations on the Moon. The REE pattern is LREE ($[\text{La}/\text{Sm}]_{\text{cn}}=1.43$ and $[\text{La}/\text{Yb}]_{\text{cn}}=1.85$) enriched with very strong Eu ($\text{Eu}/\text{Eu}^* = 0.53$) anomaly (**Figure 4.20**). The meteorite also shows a high Ni abundance suggesting chondritic meteorite contamination (Table 4.21). The composition of mineral fragments in the sample suggest both mixed high Mg# and low Mg# fragments in the sample, as suggested by the bulk composition (**Figure 4.18**).

Sample Y-86032 is very high Al_2O_3 (27.93 wt.%), very low -Ti ($\text{TiO}_2 = 0.19$ wt.%), low K ($\text{K}_2\text{O} = 0.01$ wt. %) and low Th (0.21 ppm) rock with composition typical to feldspathic lunar meteorites. Measured composition of the major and trace elements

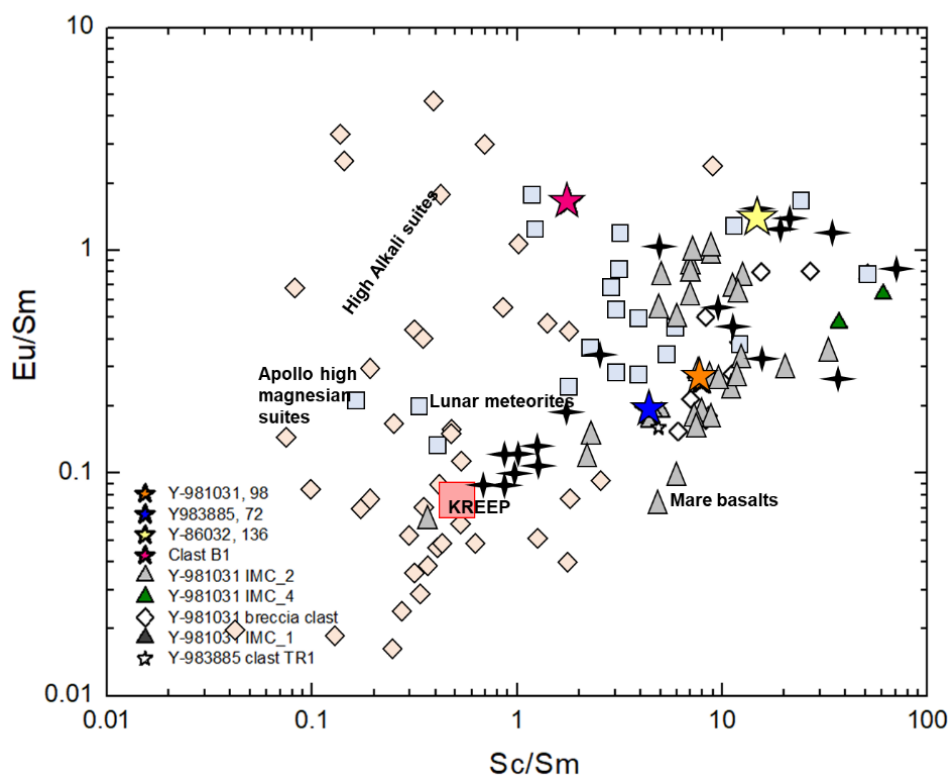


Figure 4.21 Sc/Sm versus Eu/Sm measured in the bulk rock and clasts of studied samples compared with Apollo ancient magmatics (High Mg suites and High Alkali suites), Apollo mare basalts, lunar meteorites and Apollo impact melt breccias (IMB, marked as “+”). Data Sources – Apollo high-Mg suite, high-Alkali suite and bulk lunar meteorite composition - Wieczorek et al., (2006), Joy et al., (2006, 2008), Joy et al., (2010a, b), High K-KREEP - Warren, (1989), Apollo impact melt breccias (IMB)- Jolliff, (1998) and Korotev, (1994)

is consistent with the previous studies (Korotev et al., 2009; Yamaguchi et al., 2010). Major element composition of Y-86032 shows similarities with its pairs Y-82192, ALHA 81005, and MAC 88105 (**Figure 4.19**). REE composition of Y-86032 is lowest among the analyzed samples and is supportive of the fact that they are likely derived from KREEP poor region such as Feldspathic Highland Terrane (FHT). The composition of mineral fragments shows dominance of high Mg# and high An# component in the sample, as expected from a highland derivative rock (**Figure 4.18**).

Using modal recombination, the basaltic clast BB2 in Y-983885 sample is also studied. The basalt is dominated by ~51 vol.% pyroxene and ~49 vol.% plagioclase. The reconstructed bulk composition of clast BB2 suggest it to be a low Ti (TiO_2 ~0.17 wt.%), high Al (Al_2O_3 ~14.7 wt. %) and low K (K_2O ~0.03 wt.%). In the plot of FeO versus Al_2O_3 , this basalt plots away from the mare region possibly indicating it unusual nature. In addition, the evolved nature of pyroxene and low bulk Mg# (~17) of the clast may reflect an evolved nature of this basaltic clast. Further, the composition of clast B1 in Y-981031 is also calculated using modal recombination (Table 4.1). The basaltic clast B1 is the coarsest basalt in Y-981031 with pyroxene and plagioclase occupying >76 vol.% and rest of the region is occupied by silica and symplectites. The reconstructed bulk composition of the clast B1 suggest it to be a low-Al (Al_2O_3 ~10.6 wt.%), very low-Ti (TiO_2 ~0.27 wt.%) and low K (K_2O ~0.05 wt.%) basalt. The low Mg# of the reconstructed composition suggests it to be an Fe-rich basalt variety similar to YAMM basalts described in the previous chapter. The reconstructed REE composition (~2-6 \times CI) of clast B1 shows negligible to slight positive Eu anomaly, indicating their KREEP-poor nature. Ce anomalies in the clast B1 could be a possible reflect terrestrial weathering as seen in several Antarctic meteorite samples “finds” (Floss and Crozaz, 1991). The low-Mg and KREEP-poor nature of the clast B1 suggest that the YAMM basalt like lithology are not uncommon on the Moon.

4.7 Identifying Potential Source Regions of Y-981031, Y-983885 and Y-86032 from the lunar surface

The studied meteorites are all regolith breccias with chemistry different to each other suggesting their derivation from three distinct locations on the Moon. I compare

the bulk rock chemistry, mare basalts and impact melt composition of these samples to understand their correlation with available present database of the Apollo samples and lunar meteorites. Later, the bulk composition of these rocks with the global remote sensing GRS datasets were compared to identify possible source region of these rocks. The bulk composition of brecciated meteorites especially regolith breccias provide an averaged overview of the compositional heterogeneity of a region and therefore provide a much robust comparison with the orbiter datasets.

4.7.1 Evidence from bulk rock chemistry, impact melts, and mare basalts

The bulk rock chemistry of the rocks reveals the differences in the studied meteorites. The meteorites fall in variable degree of mixing of two end member of the lunar surface i.e., highland and mare (**Figure 4.19**). Sample Y-981031 has highest VLT mare component while sample Y-86032 has highest highland component among the studied meteorites. In FeO versus Th plot, samples plot in three distinct regions corroborating with their derivation from three distinct locations on the Moon (**Figure 4.19**). It also highlights the fact that these meteorites are not from the PKT region (**Figure 4.19b**).

Mare basalts on the near side sampled by the Apollo, Luna and Chang'E 5 mission contains variable composition from VLT to low-Ti to high-Ti, with large range of model crater count ages (Wilhelms et al., 1987). I did not find any high Ti mare basalt component in the studied sample section, which is also consistent with most of the previous studies except few occurrences in meteorites Dhofar 1428, ALHA81005 and MAC 88105 (Robinson et al., 2012; Joy and Arai, 2013 and Xue et al., 2019). Therefore, it is likely that these samples were not sourced from high-Ti regions on the Moon such as Mare Tranquillitatis, Oceanus Procellarum and interior regions of Mare Moscoviense on the lunar far side. The VLT basalts are common in regions such as Mare Frigoris, northern regions of Mare Imbrium and many reported cryptomare regions (**Korotev, 2012; Joy et al., 2014**).

Impact melts on the Moon has been sampled by Apollo missions (12, 14, 15, 16 and 17; Korotev, 1994; Jolliff, 1998; Joy et al., 2014). These Apollo impact melts represents degree of mixing between feldspathic rocks and varieties of KREEP rich lithologies such as KREEP basalts, Mg suite and High alkali suites (**Figure 4.20**). The bulk composition of the studied sample show impact melts with low Ti and low-K compositions. The typical average impact melts composition from the Apollo have high REE concentration ($\sim 25\text{-}400 \times \text{CI}$) while the impact melts compositions of the sample Y-981031 not matches with the Apollo samples suggesting that the meteorite sample originated from a non-PKT source region (Jolliff, 1998; Korotev, 1994).

Impact melt breccias in the sample have composition reflecting the mixing between a feldspathic end-member and a ferroan high Sc/Sm rock type with small amount of KREEP (**Figure 4.20**). These melt breccias do not appear to have melted an Apollo like Mg-suite or high alkali suites with KREEP-rich lithologies. However, these meteorites are rather compositionally similar to the lunar feldspathic meteorites and intermediate-Fe rich melts like the Dhofar group meteorites (Joy et al., 2010b, 2014). These differences additionally indicate that the studied meteorite samples were not originated from the PKT region, and were likely sourced from a different low to moderate Th, Fe-rich region of the Moon, particularly the feldspathic highland terrane (FHT) or the South Pole-Aitkin (SPA) basin terrane.

4.7.2 Evidence from remote sensing datasets

Remote sensing dataset has offered us insight into the global geochemical variation on the Moon. I compare the bulk composition of the studied lunar meteorites Y-981031, Y-983885 and Y-86032 with the global elemental datasets obtained by GRS instrument on board Lunar Prospector (LP), following a protocol similar to (Corrigan et al., 2009; Calzada-Diaz et al., 2015). I applied several level comparisons (First FeO, TiO₂ and Th, followed by CaO, MgO, Al₂O₃, and SiO₂) to the global dataset assuming that the meteorite samples were derived from a compositionally homogeneous terrane exposed on the scale of individual pixels. I used 7 elements (FeO, TiO₂ and Th, Al₂O₃, CaO, MgO and SiO₂) in the GRS data and compared the average bulk composition of

the samples that includes the compositional data reported by previous studies. LP-GRS dataset elements provide elemental compositions along with the error matrices associated with all the 7 elements.

I calculated the error associated with each GRS pixel taking the square root of the diagonal matrix. The calculated errors corresponding to each pixel is also incorporated while searching for the possible source location. Each sample is searched for matching range of sample bulk composition values in LP-GRS and their corresponding latitude and longitude are recorded. First, the LP-GRS obtained FeO, TiO₂ and Th (~60 km × 60 km) concentrations were compared with the sample average composition because these elements are the basis of classification of lunar terranes. A second level of filtering is applied matching the measured bulk Ca concentration representing lunar highland. This filtering is later followed by Mg, Al and Si filtering which further constraints the source region of the meteorites. The matching latitude and longitude are exported and later plotted using Arc GIS software.

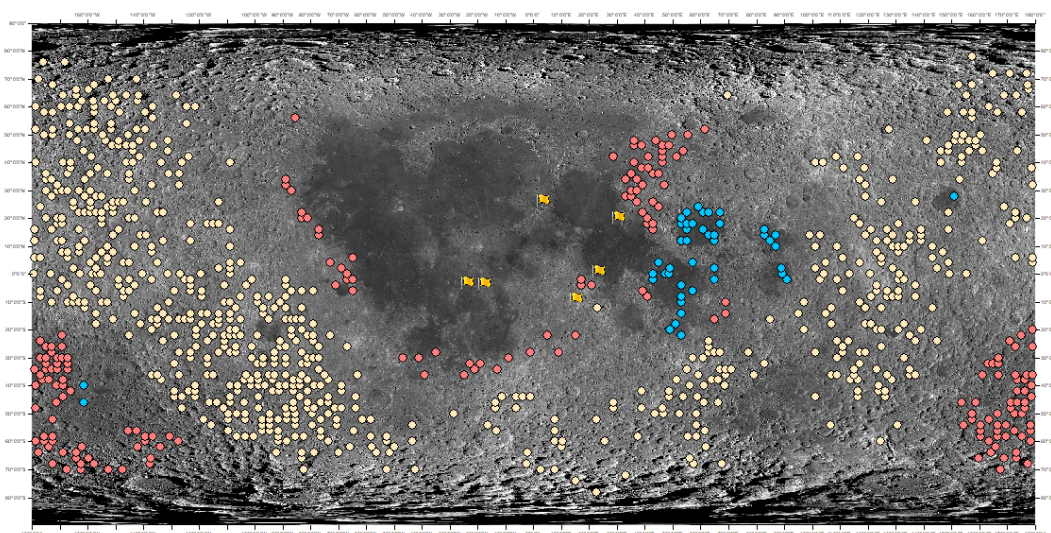


Figure 4.22 Fe-TiO₂-Th filtered possible source locations of the studied samples. Blue - Y-981031, Red - Y-983885 and Yellow - Y-86032.

As suggested by the bulk rock chemistry of the studied meteorites, none of the matched sample locations falls in the PKT region. The results of the first order filtering clearly corroborate the results from the bulk rock chemistry (**Figure 4.22**). Sample Y-86032, with highland like composition, matches with highlands on the near and far side of the Moon. The sample Y-86032 has previously been suggested to derive from the

lunar far side (Nyquist et al., 2006). The matching algorithm also suggest it to derive from lunar far-side with highest probability matching with its derivation from regions surrounding Oriental basin. With the presence of high abundance of anorthitic plagioclase in Y-86032, achieving a pure anorthositic composition, the identified source regions are also matching with the previously suggested regions (Ohtake et al., 2009) that have high probability of pure anorthosites. Sample Y-981031 with proportionately high mare content only matches with a few GRS pixels. This is likely because as most of the mare basalt regions are Th enriched and only a few regions have mare basalts exposed with low Th. Sample Y-981031 composition matches with the compositions near Mare Crisum and Mare Fecunditatis. VLT basalt, and gabbroic clasts in Y-981031 resemble with some of the lithologies identified at Luna 24 sites (Taylor et al., 1978).

Y-983885 bulk composition matched with regions near Apollo 17 landing sites and SPA basin. Corrigan et al., (2009) have previously suggested based on CaO and SiO₂ abundance that this sample is likely to be derived from the SPA basin. Here the designed matching algorithm suggests that indeed there is high possibility for this sample to be derived from the SPA basin however, this possibility is not exclusive as some of the regions near Apollo 17 landing site also matches with the bulk composition of Y-983885.

The results presented in this study argue that the samples are indeed of non-PKT origin and therefore highlight the importance of studying meteorites to understand a global perspective of lunar evolution. Return sample from other terranes of the moon like SPAT are utmost importance to forward our understanding of the Moon. The possible source regions deduced from the matching algorithm will provide a coarse estimate of the source region. These non-PKT samples can further be explored in terms of their mineralogy, petrology, and mare basalt chemistry to not only provide additional insight to lunar geochemistry but also to calibrate the instruments onboard future missions to the Moon.

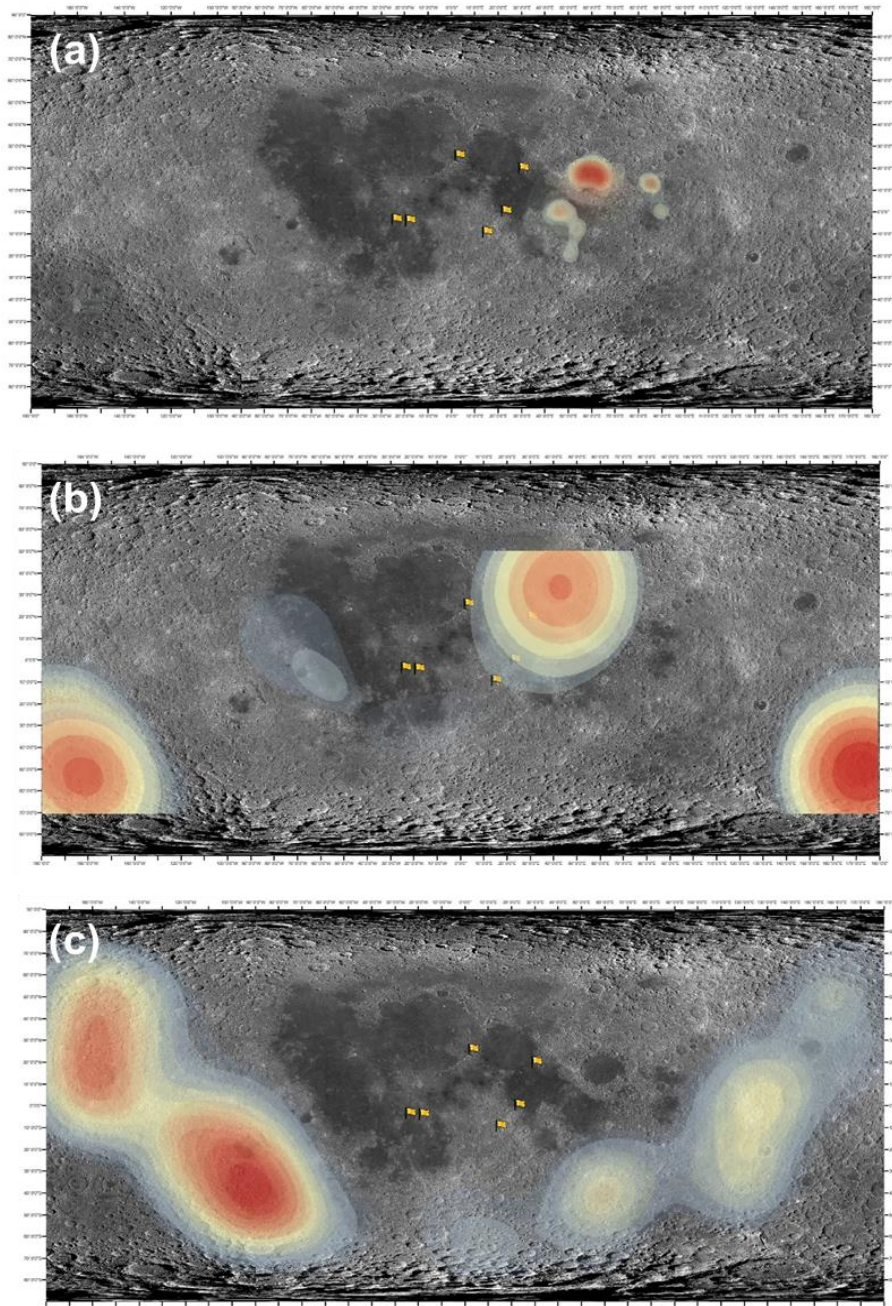


Figure 4.23 Identification of lunar regolith with similar composition to the studied meteorites. All the data are shown in cylindrical projections of the map of the Moon with 0° latitude and 0° longitude at the centre. The bulk composition of all the meteorites are taken from this study and previous studies on the sample. The yellow flags are marked as Apollo landing sites. The density plot here marks the probability of region to be a potential source region of a meteorite. a) Sample Y-981031 matches with regions of Mare Fecunditatis and Mare Crisium. b) Sample Y-983885 show high probability of being sourced from SPA region and region towards north of Mare Crisium. c) Sample Y-86032 show high probability of being sourced from highland region near Mare Orientale.

Table 4.1 Bulk rock chemistry of sample Y-981031, Y-983885, Y-86032 and clast B1.

Sample	Y-981031, 98	Y983885, 72	Y-86032, 136	Clast B1
Method	ICPMS	ICPMS	ICPMS	Modal
SiO2	44.84	45.68	46.39	55.84
TiO2	0.58	0.49	0.19	0.32
Al2O3	18.69	22.62	27.93	10.67
FeO	13.87	9.04	4.76	17.60
MnO	0.17	0.12	0.07	0.25
MgO	9.04	7.98	5.11	3.79
CaO	12.27	13.49	15.17	11.14
Na2O	0.40	0.36	0.37	0.32
K2O	0.08	0.13	0.01	0.05
P2O5	0.08	0.09	0.01	0.16
Total	100.00	100.00	100.00	100.13
Mg#	53.7	61.1	65.7	27.74
<i>ppm</i>				
Li	7.96	9.95	3.42	-
Be	0.76	1.48	0.24	-
B	11.24	7.11	2.17	-
Sc	27.69	20.61	8.79	5.41
Ti	3430.62	2896.74	1173.42	2.50
V	87.05	53.23	25.96	1.08
Cr	1769.32	1337.73	722.16	0.31
Mn	1282.31	886.90	487.30	-
Co	41.26	32.52	16.97	0.04
Ni	153.17	403.70	163.86	-
Cu	5.53	6.97	5.69	-
Zn	13.25	21.36	6.36	-
Ga	5.00	4.61	4.31	0.32
Ge	1.09	1.10	0.47	-
Se	0.11	0.17	0.04	-
Rb	2.08	3.91	0.34	0.02
Sr	123.31	129.36	161.80	5.76
Y	27.66	39.54	5.77	4.03
Zr	115.83	155.73	19.70	1.91
Nb	6.56	11.39	1.30	0.81

Table 4.1 continued

Mo	0.02	0.14	-	-
Cs	0.10	0.17	0.02	0.15
Ba	88.74	130.10	23.34	2.90
La	7.71	10.72	1.25	1.36
Ce	20.41	27.58	3.35	3.91
Pr	2.73	3.72	0.46	1.79
Nd	12.37	16.51	2.08	2.19
Sm	3.51	4.69	0.60	3.05
Eu	0.91	0.89	0.84	5.03
Gd	4.07	5.46	0.75	3.17
Tb	0.71	0.98	0.13	4.17
Dy	4.72	6.61	0.92	4.51
Ho	0.99	1.39	0.20	5.00
Er	2.85	4.09	0.59	5.05
Tm	0.40	0.61	0.09	5.85
Yb	2.60	3.94	0.59	5.88
Lu	0.36	0.56	0.08	5.91
Hf	2.59	3.65	0.47	2.33
Ta	0.30	0.50	0.07	1.02
W	0.17	0.29	0.03	0.61
Pb	0.62	1.11	0.13	0.01
Th	1.16	2.35	0.21	2.06
U	0.29	0.59	0.05	2.30

Table 4.2 Quantitative EPMA data for silicate, oxide, and other accessory phases in Y-981031

ID	Clast B1										
	Phases			Pyroxene						Plagioclase	Silica
	Dark band	Dark band	Dark band	Contact b/w light and dark	Contact b/w light and dark	light band	light band	light band	Core	Core	Broad beam
SiO ₂	52.31	52.15	51.96	50.97	51.58	49.18	48.53	47.73	45.54	100.33	48.80
TiO ₂	0.25	0.23	0.34	0.33	0.25	0.44	0.67	0.73	0.02	0.12	0.29
Al ₂ O ₃	1.36	1.39	1.32	1.25	0.97	1.01	0.89	0.77	33.55	0.27	0.40
Cr ₂ O ₃	0.59	0.60	0.53	0.45	0.39	0.37	0.18	0.12	0.02	-	-
FeO	17.15	17.30	19.45	20.84	24.19	29.41	32.62	39.49	0.55	0.04	41.81
MnO	0.34	0.31	0.36	0.35	0.39	0.50	0.45	0.50	-	0.01	0.53
MgO	15.91	15.39	13.24	11.86	13.55	9.43	6.13	3.73	0.15	-	1.56
CaO	12.71	13.36	14.24	14.19	9.64	9.63	10.76	8.35	18.20	0.02	6.08
Na ₂ O	0.04	0.06	0.05	0.02	-	0.04	-	0.01	1.01	0.02	-
K ₂ O	-	-	-	-	-	-	-	-	0.12	0.14	0.01
Total	100.66	100.78	101.45	100.26	100.95	100.01	100.22	101.42	99.13	100.93	99.47
Mg#	62.3	61.3	54.8	50.4	49.9	36.4	25.1	14.4			6.2

ID	Clast B2		Clast B3		Clast P1						
	Pyroxene	Plagioclase	Pyroxene								
SiO ₂	51.90	46.14	52.276	46.245	48.908	51.453	51.195	47.794	50.532	49.286	50.628
TiO ₂	0.56	0.07	0.627	0.06	0.653	0.376	0.305	0.756	0.312	0.566	0.349
Al ₂ O ₃	1.88	31.30	2.461	33.374	0.547	1.636	1.028	0.773	1.271	3.907	1.507
Cr ₂ O ₃	0.43	0.03	0.767	0.026	0.106	0.562	0.361	0.157	0.556	1.054	0.57
FeO	17.88	1.25	12.682	0.402	35.18	16.828	24.217	32.511	22.85	15.678	18.967
MnO	0.26	0.02	0.246	0.024	0.546	0.236	0.316	0.388	0.308	0.282	0.259
MgO	20.21	1.50	17.956	0.162	7.25	13.167	12.312	6.907	11.524	11.754	11.795
CaO	5.73	17.63	13.068	18.299	6.503	15.37	10.984	9.38	12.295	17.027	15.864
Na ₂ O	0.04	0.67	0	0.709	0.03	0.017	0.033	0.018	0.079	0.081	0.051
K ₂ O	0.04	0.21	0.002	0.059	0	0	0.001	0.006	0	0	0
Total	98.92	98.82	100.085	99.36	99.723	99.645	100.752	98.69	99.727	99.635	99.99
Mg#	66.84		72		26.9	58.2	47.5	27.5	47.3	57.2	52.57

Phases	Clast P2		Clast P3	Clast P4	Clast P5			Clast P6
	Pyroxene							
SiO ₂	50.35	49.86	48.94	51.26	49.83	48.77	50.22	49.96
TiO ₂	0.69	0.74	0.50	0.36	0.54	0.69	0.49	0.63
Al ₂ O ₃	0.83	0.76	0.78	3.72	0.55	1.16	0.91	0.76
Cr ₂ O ₃	0.22	0.16	0.29	1.02	0.21	0.25	0.31	0.23
FeO	24.55	28.58	31.41	18.58	34.02	28.53	28.99	31.85
MnO	0.34	0.40	0.41	0.29	0.47	0.37	0.39	0.41
MgO	12.90	13.04	9.01	19.97	11.67	10.40	11.54	8.79
CaO	8.64	5.55	8.43	5.22	3.68	8.79	7.93	8.25
Na ₂ O	0.03	0.01	0.03	0.00	0.04	0.08	0.06	0.07
K ₂ O	0.00	0.01	0.00	0.03	0.00	0.00	0.00	0.01
Total	98.54	99.10	99.79	100.43	101.01	99.05	100.83	100.97
Mg#	48.4	44.8	33.8	65.7	37.9	39.4	41.5	33.0

Table 4.2. *Continued*

Phases	<u>Clast OL1</u>	<u>Clast OL2</u>	<u>Clast OL 3</u>	<u>Clast LC</u>		<u>IM1</u>	<u>IM2</u>	<u>IM3</u>	<u>IM4</u>
	Olivine	Olivine	Olivine	Silica	Olivine				
SiO ₂	36.00	39.71	36.56	99.35	30.35	46.23	45.99	46.32	46.44
TiO ₂	0.11	0.03	0.08	0.14	0.04	0.84	0.39	0.65	0.28
Al ₂ O ₃	0.02	0.18	0.09	0.64	0.06	15.68	9.78	14.56	26.28
Cr ₂ O ₃	0.02	0.01	0.05	0.08	0.01	0.27	0.47	0.49	0.09
FeO	35.48	17.88	31.82	0.68	63.99	14.01	18.52	14.13	4.74
MnO	0.37	0.18	0.32	0.00	1.27	0.22	0.18	0.26	0.06
MgO	27.90	42.42	31.08	0.00	4.45	8.83	15.29	10.90	8.34
CaO	0.15	0.06	0.13	0.03	0.26	13.19	9.04	11.07	14.91
Na ₂ O	0.03	0.03	0.00	0.11	0.00	0.06	0.04	0.24	0.17
K ₂ O	0.00	0.01	0.00	0.27	0.01	0.02	0.03	0.18	0.05
Total	100.08	100.50	100.14	101.35	100.44	99.33	99.73	98.80	101.35
Mg#	58.4	80.9	63.5	0.0	11.0	52.9	59.5	57.9	75.8

Table 4.2. *continued*

ID	Clast GR1		Clast BC 1 and BC2		
	Phases	Pyroxene	Plagioclase	Pyroxene	Plagioclase
SiO ₂	51.64	45.98	53.99	45.41	37.10
TiO ₂	0.79	0.03	0.45	0.00	0.04
Al ₂ O ₃	1.36	34.40	1.01	34.82	0.09
Cr ₂ O ₃	0.57	0.00	0.34	0.00	0.04
FeO	9.19	0.24	19.91	0.90	32.25
MnO	0.20	0.00	0.30	0.04	0.34
MgO	17.69	0.23	18.91	0.40	31.00
CaO	16.93	17.60	4.91	18.43	0.15
Na ₂ O	0.04	1.22	0.04	0.49	0.00
K ₂ O	0.03	0.21	0.00	0.02	0.02
Total	98.43	99.92	99.85	100.50	101.05
Mg#/An#	77.4	92.1	62.9	97.2	63.1

Table 4.3 Major element composition of impact melt basalts, basalts and granulite clast in sample Y-983885.

ID	Clast IMB_1				Clast IMB_2			Clast FC_4			Clast IMB_4		Clast IMB_5		Clast IMB_7	
	Plag	Plag	melt - pyx	melt - pyx	melt- ol	plag	melt- pyx	plag	melt- ol	melt- pyx	plag	melt- pyx	plag	melt- pyx	melt- pyx	plag
SiO ₂	43.98	44.70	52.74	52.81	36.64	44.44	54.59	44.51	36.86	52.80	44.49	50.95	43.79	51.41	51.54	45.55
TiO ₂	0.00	0.02	1.71	1.69	0.03	0.00	2.00	0.03	0.04	0.33	0.01	0.69	0.06	0.266	0.28	0.06
Al ₂ O ₃	35.01	34.09	9.13	11.36	0.15	34.45	8.71	34.63	0.28	2.24	33.59	4.06	34.11	3.784	1.36	33.37
Cr ₂ O ₃	0.00	0.03	0.55	0.99	0.52	0.02	0.54	0.02	0.07	1.07	0.00	0.85	0.05	0.754	0.63	0.00
FeO	0.46	0.94	17.31	13.80	30.92	0.55	15.15	0.66	29.93	16.60	0.71	16.95	0.36	13.761	20.45	0.51
MnO	0.01	0.01	0.11	0.12	0.13	0.05	0.08	0.00	0.09	0.13	0.00	0.09	0.00	0.067	0.09	0.03
MgO	0.06	0.28	3.34	4.63	30.73	0.16	2.83	0.15	31.29	21.55	0.36	18.54	0.06	19.978	19.28	0.06
CaO	19.11	19.49	15.46	15.05	0.50	19.16	14.97	19.39	0.32	5.48	19.16	6.94	19.14	8.04	5.50	18.21
Na ₂ O	0.38	0.27	0.10	0.21	0.00	0.30	0.07	0.38	0.01	0.01	0.49	0.02	0.51	0.047	0.03	0.93
K ₂ O	0.01	0.02	0.08	0.15	0.00	0.01	0.15	0.05	0.01	0.00	0.05	0.01	0.09	0	0.00	0.24
Total	99.02	99.85	100.51	100.79	99.62	99.12	99.07	99.81	98.91	100.21	98.85	99.09	98.16	98.11	99.15	98.96
Mg#/An#	96.5	97.4	25.6	37.4	63.9	97.2	25.0	96.3	65.1	69.8	95.3	66.1	94.9	72.1	62.7	90.2

ID	Clast BB1			Clast IMB_6			Clast BB2		Clast IMB_8		Clast HC1		Clast IMB_3	
	pyx	plag	ol	plag	pyx	ol	plag	pyx	plag	pyx	plag	pyx	plag	pyx
SiO ₂	51.81	45.80	38.02	44.50	53.59	37.96	48.99	48.00	45.87	50.84	45.09	52.95	45.43	46.54
TiO ₂	0.54	0.02	0.05	0.01	0.34	0.04	0.03	0.30	0.09	1.12	0.04	0.37	0.02	0.21
Al ₂ O ₃	2.89	33.72	0.06	35.33	0.79	0.12	29.54	0.69	29.96	1.82	34.31	1.56	32.01	18.01
Cr ₂ O ₃	0.50	0.02	0.13	0.00	0.45	0.02	0.00	0.11	0.04	0.50	0.00	0.64	0.03	0.27
FeO	19.95	1.10	26.89	0.39	21.01	26.97	2.48	41.12	1.97	20.40	0.32	18.63	1.01	13.59
MnO	0.13	0.02	0.15	0.00	0.11	0.14	0.00	0.16	0.00	0.12	0.00	0.11	0.03	0.05
MgO	20.25	0.47	35.03	0.19	21.72	34.33	0.08	4.79	2.60	17.92	0.06	20.51	1.32	10.56
CaO	4.77	18.44	0.29	19.97	2.92	0.18	17.43	6.13	17.43	6.39	18.66	6.12	18.55	10.56
Na ₂ O	0.02	0.61	0.01	0.20	0.01	0.00	0.92	0.00	0.36	0.04	0.76	0.04	0.38	0.01
K ₂ O	0.01	0.10	0.00	0.01	0.00	0.00	0.06	0.00	0.03	0.04	0.14	0.00	0.02	0.09
Total	100.85	100.28	100.62	100.59	100.95	99.75	99.53	101.29	98.35	99.19	99.37	100.92	98.81	99.90
Mg#/An#	64.4	93.8	69.9	98.2	64.8	69.4	91.0	17.2	96.2	61.0	92.4	66.2	96.3	58.1

Table 4.4 EPMA composition of minerals in Y-86032

(wt.%)	Pyroxene			Olivine			Plagioclase		
SiO ₂	52.02	52.63	53.60	36.71	37.98	39.32	44.44	44.26	44.31
TiO ₂	0.97	0.17	0.75		0.01	0.04	0.02	0.04	0.01
Al ₂ O ₃	1.21	2.18	1.59	0.01	0.03	0.02	33.99	33.63	33.35
Cr ₂ O ₃	0.49	0.73	0.60	-	0.06	0.09	0.03	0.05	0.00
FeO	17.92	14.60	8.81	34.49	22.77	17.43	0.13	0.13	0.24
MnO	0.29	0.29	0.19	0.38	0.28	0.22	0.00	0.00	0.00
MgO	20.68	22.11	18.98	28.92	37.71	42.16	0.08	0.06	0.07
CaO	5.70	6.52	16.19	0.00	0.05	0.12	19.54	19.02	19.88
Na ₂ O	0.01	0.05	0.14	-	-	-	0.45	0.62	0.43
K ₂ O	0.02	0.02	0.04	0.02	0.02	0.03	0.02	0.05	0.03
Total	99.30	99.31	100.88	100.53	98.91	99.44	98.69	97.86	98.31
Mg#/An#	67.3	73.0	79.3	59.9	74.7	81.2	95.9	94.1	96.1

(wt.%)	Spinel		Ilmenite
SiO ₂	0.06	0.80	0.08
TiO ₂	12.84	23.30	54.03
Al ₂ O ₃	7.49	5.82	0.10
Cr ₂ O ₃	35.36	31.16	0.28
FeO	38.68	35.16	40.24
MnO	0.34	0.34	0.44
MgO	3.85	3.38	4.10
CaO	0.00	0.00	0.00
K ₂ O	0.04	0.03	0.02
Total	98.65	99.99	99.29
Mg#	15.1	14.6	15.4
2Ti (%)	34.4	52.7	-
Al (%)	15.7	10.3	-
Cr (%)	49.8	37.0	-

Table.4.5 Trace elemental composition of mineral in clast B1

<i>Elements</i>	Dark band: Augite		Light band: Pigeonite		Pyroxene near symplectite		Symplectite		Plagioclase	
Sc	97.74	± 22.92	97.58	± 22.99	73.64	± 17.02	64.65	± 5.51	-	
Ti	1619.3	± 395.45	3521.02	± 862.47	5509.2	± 1330.73	2252.75	± 205.63	108.3	± 30.53
V	395.27	± 87.09	212.12	± 47.05	11.54	± 2.56	3.08	± 0.52	-	
Cr	4326.42	± 1306.81	2584.17	± 785.62	106.43	± 31.65	39.61	± 4.49	-	
Co	57.03	± 15.49	62.31	± 17.07	43.32	± 11.37	47.63	± 2.83	1.83	± 0.9
Ni	24.44	± 11.09	16.02	± 7.35	5.47	± 2.57	12.81	± 3.18	-	
Ga	0.82	± 0.33	1.48	± 0.48	2.86	± 0.82	1.76	± 0.45	20.41	± 4.89
Sr	1.95	± 0.28	8.32	± 1	12.16	± 1.4	7.53	± 1.13	368.62	± 15.3
Y	5.88	± 0.97	12.79	± 2.06	48.19	± 7.48	126.18	± 33.91	0.077	± 0.077
Zr	3.42	± 0.63	18.83	± 3.18	49.28	± 7.99	51.53	± 8.85	-	
Nb	-		0.72	± 0.13	0.8	± 0.14	0.47	± 0.15	-	
Ba	-		7.7	± 1.56	2.2	± 0.53	8.33	± 1.2	73.68	± 9.44
La	0.111	± 0.036	0.7	± 0.13	1.61	± 0.28	1.29	± 0.15	0.3	± 0.12
Ce	4.22	± 0.69	5.39	± 0.88	16.45	± 2.55	5.85	± 1.12	0.74	± 0.21
Pr	0.078	± 0.027	0.437	± 0.076	1.4	± 0.21	0.68	± 0.14	0.24	± 0.1
Nd	0.98	± 0.31	3.12	± 0.86	8.31	± 2.1	6.86	± 1.28	0.23	± 0.24
Sm	0.38	± 0.15	1.21	± 0.35	4.04	± 1	2.67	± 0.52	0.29	± 0.3
Eu	0.036	± 0.022	0.171	± 0.047	0.417	± 0.093	0.318	± 0.077	3.63	± 0.55
Gd	0.94	± 0.21	1.68	± 0.28	5.49	± 0.71	6.94	± 0.87	0.74	± 0.43
Tb	0.132	± 0.029	0.299	± 0.04	1.26	± 0.11	2.22	± 0.28	0.039	± 0.039
Dy	0.87	± 0.17	2.57	± 0.35	8.2	± 0.95	18.6	± 2.39	0.15	± 0.15
Ho	0.209	± 0.042	0.616	± 0.079	2.5	± 0.26	4.91	± 0.68	-	
Er	0.85	± 0.15	1.61	± 0.21	6.91	± 0.72	13.92	± 1.42	-	
Tm	0.072	± 0.024	0.342	± 0.053	1.07	± 0.14	2.29	± 0.51	-	
Yb	0.6	± 0.16	2.13	± 0.4	7.39	± 1.26	20.09	± 6.56	-	
Lu	0.105	± 0.028	0.339	± 0.055	1.25	± 0.17	2.74	± 0.56	-	
Hf	-		0.62	± 0.12	2.47	± 0.38	0.76	± 0.16	-	
Ta	0.0049	± 0.005	0.031	± 0.011	0.053	± 0.016	-		-	
W	0.053	± 0.039	-		0.272	± 0.099	0.102	± 0.06	-	
Th	0.034	± 0.019	0.098	± 0.026	0.65	± 0.12	0.323	± 0.08	-	
U	0.0115	± 0.0083	<0.019	± 0.012	0.153	± 0.035	0.118	± 0.042	-	

Table 4.5 continued

Elements	Pyroxene										Plagioclase		Clast TR-1								
Sc	92.51	±	42.59	101.77	±	51.46	97.43	±	54.36	213.39	±	85.4	-	15.47	±	9.06	27.76	±	17.22		
Ti	3172.23	±	434.77	2400.3	±	345.8	4051.46	±	608.68	7499.32	±	964.01	1123.4	±	436.65	1876.43	±	289.67	3987.49	±	630.26
V	338.22	±	175.61	328.04	±	187.28	148.98	±	94.05	138.58	±	62.45	37.1	±	8.09	46.3	±	30.31	78.93	±	55.39
Cr	4857.43	±	3042.81	5618.75	±	3814.76	3039.27	±	2246.54	2056.16	±	1141.44	1482.84	±	117.48	1297.56	±	987.55	2578.12	±	2082.1
Co	25.73	±	7.72	29.17	±	9.8	32.57	±	12.28	19.79	±	5.07	30.29	±	7.99	31.64	±	12.48	38.71	±	16.58
Ni	11.11	±	1.18	10.97	±	1.72	17.83	±	1.84	2.11	±	0.59	281.16	±	89.72	257.71	±	20.13	339.43	±	26.73
Ga	0.6	±	0.43	0.87	±	0.64	0.9	±	0.67	2.01	±	1.12	-	5.94	±	4.39	3.51	±	2.74		
Sr	1.51	±	0.51	9.1	±	3.41	7.93	±	3.35	4.85	±	1.38	117.19	±	19.55	122.5	±	53.87	133.8	±	64.29
Y	3.57	±	1.79	5.22	±	2.95	11.84	±	7.55	48.89	±	20.54	6.07	±	1.97	22.19	±	14.79	44.97	±	32.8
Zr	3	±	2.22	6.43	±	5.43	4.79	±	4.67	27.23	±	16.55	18.89	±	4.6	145.26	±	148.76	175.13	±	199.38
Nb	0.047	±	0.02	0.214	±	0.09	0.027	±	0.018	0.061	±	0.028	4.38	±	1.6	4.37	±	1.54	12.28	±	4.68
Ba	-			-			-			-			52.11	±	15.16	78.41	±	104.32	169.99	±	253.87
La	0.148	±	0.081	0.24	±	0.15	0.47	±	0.33	1.5	±	0.66	2.55	±	1.07	7.58	±	5.5	15.15	±	12.19
Ce	0.33	±	0.2	0.43	±	0.3	1.08	±	0.86	4.12	±	1.94	7.17	±	2.64	11.78	±	9.84	30.66	±	28.85
Pr	0.081	±	0.091	0.12	±	0.16	0.25	±	0.34	0.83	±	0.8	0.96	±	0.59	1.6	±	2.24	4.55	±	6.8
Nd	0.44	±	0.15	0.53	±	0.21	1.26	±	0.46	4.6	±	1.16	3.18	±	2.26	7.87	±	2.84	18.26	±	6.93
Sm	-			0.144	±	0.098	0.84	±	0.37	2.4	±	0.8	1.85	±	1.87	1.7	±	0.77	5.68	±	2.47
Eu	0.0048	±	0.0058	0.012	±	0.015	0.083	±	0.074	0.052	±	0.038	1.13	±	0.84	0.44	±	0.39	0.91	±	0.85
Gd	0.24	±	0.27	0.34	±	0.42	1.19	±	1.57	3.2	±	2.92	-	2.3	±	3.17	4.99	±	7.4		
Tb	0.051	±	0.058	0.12	±	0.15	0.26	±	0.35	0.86	±	0.83	-	0.5	±	0.7	0.87	±	1.31		
Dy	0.44	±	0.26	0.59	±	0.39	1.85	±	1.29	7.93	±	4.07	2.34	±	1.84	3.48	±	2.51	6.57	±	5.01
Ho	0.22	±	0.1	0.164	±	0.084	0.39	±	0.2	2.14	±	0.85	0.32	±	0.34	0.74	±	0.39	1.51	±	0.83
Er	0.41	±	0.1	0.3	±	0.1	1.07	±	0.3	5.72	±	1.13	0.9	±	0.95	2.03	±	0.6	4.75	±	1.4
Tm	0.08	±	0.022	0.086	±	0.029	0.162	±	0.043	0.87	±	0.16	-	0.318	±	0.09	0.55	±	0.15		
Yb	0.48	±	0.19	0.71	±	0.31	1.35	±	0.58	7.17	±	2.45	1.29	±	1.35	1.93	±	0.87	4.69	±	2.12
Lu	0.086	±	0.087	0.15	±	0.17	0.18	±	0.21	1	±	0.91	-	0.32	±	0.38	0.73	±	0.89		
Hf	0.127	±	0.069	0.24	±	0.14	0.24	±	0.14	0.58	±	0.27	1.91	±	1.51	2.08	±	1.17	4.09	±	2.36
Ta	0.0095	±	0.0069	0.017	±	0.014	-			0.0045	±	0.005	-	0.21	±	0.13	0.49	±	0.32		
Th	-			0.037	±	0.084	0.026	±	0.063	0.11	±	0.2	1.14	±	0.66	0.86	±	2.16	3.17	±	8.46
U	0.02	±	0.041	0.013	±	0.03	0.017	±	0.041	<0.030	±	0.022	-	0.17	±	0.4	0.56	±	1.34		

Table 4.6 Trace elemental composition of minerals and clast (analyzed as broad beam) in Y-983885.

Elements (ppm)	Pyroxene				Olivine	
Sc	28.51 ±	6.76	32.91 ±	6.6	17.78 ±	4.01
Ti	963.28 ±	317.04	2836.52 ±	957.91	1787.52 ±	583.87
V	127.43 ±	11.37	86.75 ±	7.01	63.58 ±	5.46
Cr	4101.63 ±	337.61	2613.17 ±	194.55	1977.69 ±	161.07
Co	32.51 ±	6.83	18.96 ±	3.65	16.83 ±	3.45
Ni	30.09 ±	11.16	7.93 ±	3.33	13.77 ±	5.1
Sr	3.34 ±	0.77	0.62 ±	0.18	0.39 ±	0.13
Y	11.27 ±	1.97	7.1 ±	1.15	18.09 ±	2.92
Zr	9.47 ±	1.23	14.67 ±	1.29	18.39 ±	1.49
Nb	0.57 ±	0.22	0.187 ±	0.072	-	
Ba	4.04 ±	1.48	0.15 ±	0.15	0.3 ±	0.18
La	1.2 ±	0.27	0.141 ±	0.055	0.132 ±	0.044
Ce	3.03 ±	0.92	0.58 ±	0.19	0.47 ±	0.15
Pr	0.45 ±	0.16	0.076 ±	0.038	0.09 ±	0.036
Nd	2.35 ±	0.69	0.56 ±	0.21	0.28 ±	0.13
Sm	0.9 ±	0.48	0.37 ±	0.19	0.38 ±	0.17
Eu	0.067 ±	0.069	0.056 ±	0.041	0.019 ±	0.02
Gd	0.86 ±	0.48	0.65 ±	0.29	1.17 ±	0.4
Tb	0.21 ±	0.12	0.112 ±	0.059	0.27 ±	0.13
Dy	0.99 ±	0.54	1.57 ±	0.64	2.74 ±	1.11
Ho	0.49 ±	0.24	0.33 ±	0.14	0.9 ±	0.37
Er	1.5 ±	0.7	0.93 ±	0.38	2.63 ±	1.03
Tm	0.173 ±	0.096	0.225 ±	0.088	0.54 ±	0.19
Yb	1.14 ±	0.6	1.37 ±	0.54	2.91 ±	1.11
Table 4.6 continued						
Lu	0.19 ±	0.13	0.143 ±	0.068	0.54 ±	0.23
Hf	0.6 ±	0.37	0.34 ±	0.18	0.78 ±	0.36
Pb	-		0.037 ±	0.04	0.42 ±	0.24
Th	0.15 ±	0.092	-		-	
U	0.07 ±	0.061	-		0.02 ±	0.017

the lunar surface

Table 4.7 Compositional ranges and textures of representative lithic clasts studied in this thesis.

Clasts	Dimensions (mm)	Textures	Pyroxene	Olivine	Plagioclase	Glass y melt
<u>Y-981031 clasts</u>						
<i>Basaltic clast</i>						
B1	2.25 x 2.07	gabbroic	Wo _{17.9-32.2} En _{4.2-47.1} Fs _{26.1-70.5}	-	An _{90.3-92.8}	x
B2	0.42 x 0.34	sub-ophitic	Wo ₁₀₋₁₂ En ₅₈₋₆₀ Fs ₂₉₋₃₁	-	An _{92.0-93.1}	x
B3	0.34 x 0.11	skeletal	Wo _{10.8-11.3} En _{38.9-40.3} Fs _{48.8-50.2}	-	An ₉₀₋₉₂	x
<i>Granulitic clast</i>						
GR1	0.83 x 0.64	granular	Wo _{32.0-34.6} En _{51.6-52.4} Fs _{13.0-16.4}	-	An ₈₇₋₉₀	x
<i>Breccia clast</i>						
BB1	1.25 x 0.98	fragmental	Wo _{10.5} En ₅₆ Fs _{33.6}	-	An _{93.2-94}	x
<u>Y-983885 clasts</u>						
<i>Crystalline Impact melt clasts</i>						
IMB_1	0.45 x 0.28	Reannealed ophitic	-	Fo ₇₄	An _{96.2-97.4}	Yes
IMB_2	0.25 x 0.16	Reannealed ophitic	-	Fo ₆₄	An _{97.2}	Yes
IMB_3	0.44 x 0.36	Reannealed ophitic	-	-	An _{96.1-96.7}	Yes
IMB_4	0.18 x 0.16	Reannealed ophitic	-	-	An _{95-95.8}	Yes
IMB_5	0.45 x 0.16	Reannealed ophitic	-	-	An _{94.4-96.3}	Yes
IMB_6	0.16 x 0.13	ophitic	Wo _{5.8-28.6} En _{54.5-60.9} Fs _{16.4-33.2}	Fo ₆₉	An _{96.3-98.2}	Yes
IMB_7	0.34 x 0.24	Sub ophitic	Wo _{6.3-16.7} En _{50.0-60.2} Fs _{33.2-33.5}	Fo ₆₂₋₆₉	An _{89.8-92.0}	Yes
<i>Basaltic clasts</i>						
BB1	0.77 x 0.19	ophitic	Wo _{9.8-14.6} En _{41.5-58} Fs _{32.2-44.0}	Fo ₇₀	An _{91.5-93.6}	x
BB2	0.26 x 0.11	gabbroic	Wo _{13.6-24.8} En _{14.8-23.3} Fs _{51.9-71.6}	-	An _{93.6-92.8}	x
BB3	0.28 x 0.15	gabbroic	Wo _{26.7-30.7} En _{22.5-24.2} Fs _{46.8-49.0}	-	An _{96.2-96.9}	x
<i>Feldspathic clast</i>						
FC1	1.2 x 1.0	Poikilitic	Wo _{3.2-13.2} En _{56.9-62.6} Fs _{29.9-34.2}	Fo _{55.0-63.4}	An _{96.4-97.4}	x
FC2	0.65 x 0.34	granular	Wo _{4.2-8.8} En _{66.8-72.2} Fs _{23.4-24.3}	Fo ₇₃	An _{92.9-95.3}	x
FC3	0.17 x 0.13	Poikilitic	Wo _{9.0-11.3} En _{57.6-58.7} Fs _{31.0-32.2}	Fo ₆₀	An _{87.8-89.2}	x
FC4	0.23 x 0.10	granular	Wo _{11.3-22.2} En _{55.0-61.8} Fs _{22.8-26.9}	Fo ₆₅	An _{95.7-96.3}	x
Clast HC1	0.27 x 0.14	gabbroic/granular	Wo _{11.6-12.4} En _{57.9-58.4} Fs _{29.7-29.9}	-	An _{92.4-94.7}	x
Clast HC2	0.1 x 0.05	gabbroic/granular	Wo _{12.6-13.5} En _{52.3-52.7} Fs _{33.2-33.5}	-	An _{96.2}	x
<i>Granulite clast</i>						
GC1	0.85 x 0.44	granoblastic	Wo _{8.56-37.7} En _{45.4-63.7} Fs _{16.8-27.7}	Fo ₆₅	An _{94.4-94.9}	x
<u>Y-86032 clasts</u>						
<i>Granulite clast</i>						
GB1	3.52 x 1.35	granular	Wo _{11.6-37.1} En _{43.1-59.1} Fs _{19.7-29.2}	-	An _{95.9-96.3}	x
GB 2	2.01 x 1.68	granular	Wo _{9.95-37.1} En _{43.1-56.3} Fs _{19.7-33.6}	-	An _{94.9-96.1}	x

4.8 Summary and Conclusion

The chapter provide a comprehensive mineralogical and petrological investigation of three compositionally distinct regolith breccia meteorite. The studied samples Y-981031, Y-983885 and Y-86032 are the product of impact cratering events, which affected several types of target rocks and mingled them together to form regolith breccia. Collectively, they show varied degree of mixing of highland and mare materials with basaltic, granulitic, troctolitic clast and isolated mineral fragments of pyroxene, plagioclase, anorthosite and other accessory phase such as ilmenite, sulfides, spinels. Sample Y-981031 contains a relatively coarse-grained basalt (clast B1) with exsolution lamellae of size (0.5 mm) larger than Apollo mare basalts. The texture, composition and bulk chemistry of the clast closely matches with the YAMM meteorites, however, the clast B1 has less REE abundance and more Th concentration which suggest that they are not exactly part of YAMM clan. Sample Y-983885 contains number of impact melt, basaltic, feldspathic, and granulitic clasts with range of composition and textures. Sample Y-86032 contains several distinct lithologies dominated by anorthosite. The sample is measured to represent one of the oldest crusts on the Moon.

The bulk composition of the studied sample and clasts highlight their unique chemistry when compare to previously analyzed Apollo samples. Composition of impact melts, basalts and breccias in the sample suggest their derivation from non-PKT regions. The compositional matching algorithm applied on the average measured bulk composition of meteorites and Lunar Prospector GRS global elemental abundance to identify the possible source region of the meteorites. The results confirm the samples to have a non-PKT origin. Sample Y-983885 was likely derived from the region Mare Crisium. Sample Y-86032 is probably sourced from highland regions with high probability to originate from Mare Orientale basin. Sample Y-983885 has high chances of being sourced from the SPA basin of the Moon. This sample and its constituent lithic clasts and mineral fragments are likely to represent the compositional diversity of the SPA basin.

The following chapter will utilise the petrographic information of samples presented in this and previous chapter to understand the highly siderophile abundance on the Moon. As shown here, these sample are representative of the unsampled regions of the Moon, therefore measuring the highly siderophile abundance in these sample will help to better constrain the abundance of the HSE on the Moon.

Chapter 5

Abundance of Highly Siderophile Elements in the Lunar Mantle and Crust from meteorites

5.1 Introduction

Highly Siderophile elements (HSE: Re, Os, Ir, Ru, Rh, Pt, Pd, and Au) are important tracers for the understanding of the formation and accretion of planetary bodies (e.g., Walker, 2009; Day et al., 2016). Experimental studies have shown that these elements have a higher affinity for the metal than for silicate, and under low-pressure conditions, their metal-silicate partition coefficient value ranges to values greater than $\sim 10^4$ (**Figure 5.1**; Mann et al., 2012). Assuming that terrestrial planetary bodies accreted from chondritic materials, then calculations suggest that ~ 98 - 99% of the HSE were preferentially incorporated into planetary cores during primary differentiation (Palme and O'Neill, 2013). This property of the HSE is practically utilized to trace fundamental processes such as planetary accretion, core formation, differentiation, and late accretion in the planets and asteroids (Day et al., 2007, 2010; Puchtel et al., 2008; Walker, 2009; Fischer-Gödde and Becker, 2012; Sharp et al., 2014; Day and Walker, 2015; Liu et al., 2015; Righter et al., 2015; Day et al., 2016; Gleißner and Becker, 2017, 2019; McIntosh et al., 2020; Day and Paquet, 2021). However, the absolute and relative abundances of the HSE in planetary materials are also affected by several mantle and crustal processes such as melting, fractional

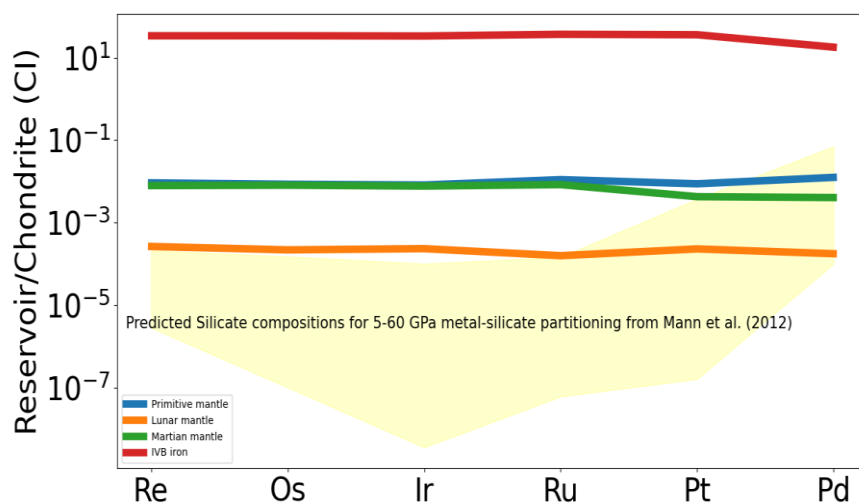


Figure 5.1 Highly Siderophile Elements (except monoisotopic Rh and Au) abundance in different planetary bodies (cf. Day et al., 2016). Baseline distributions of the HSE in the Earth, Moon, Mars and IVB magmatic iron. The pattern of the HSE abundance in terrestrial, martian and lunar mantle do not match the predicted silicate compositions after core formation (Mann et al. 2012) suggest that some addition of the HSE from impactor is required to explain the observed abundance.

crystallization, metasomatism, crust-mantle remixing, as well as later impact processing (Day et al., 2016). The conundrum of the elevated HSE abundances in planetary mantles, their abundances in planetary materials and our current understanding has been discussed in detail in *Section 1.6* of this thesis. Here, the HSE abundances is discussed only in the context of lunar settings. The HSE abundance of the Moon is interpreted from returned samples and lunar meteorites from a wide array of rock types. These include anorthosites, Mg-suites rocks, impact melt breccias, regolith breccias and igneous volcanic rocks (**Figure 5.2**). However, it is important to note that despite the primary role of core formation in the fractionation of the HSE, lunar samples do not appear to record solely the effect of this process (Walker et al., 2004; Day et al., 2007; Day & Walker, 2015). Lunar rocks tend to show a broadly chondritic relative abundance of the HSE (**Figure 5.3**) with long-term Re/Os and Pt/Os isotopic ratios within $\pm 10\%$ of chondrites. Day et al. (2010) have shown that crust-mantle partitioning behavior of the Earth and Moon have remarkable similarities. These observations conclusively suggest that there were processes other than metal-silicate partitioning acting on the Moon, the most likely of which is the late accretion of chondritic impactors (Chou, 1978; Wanke, 1981), that are responsible in modifying

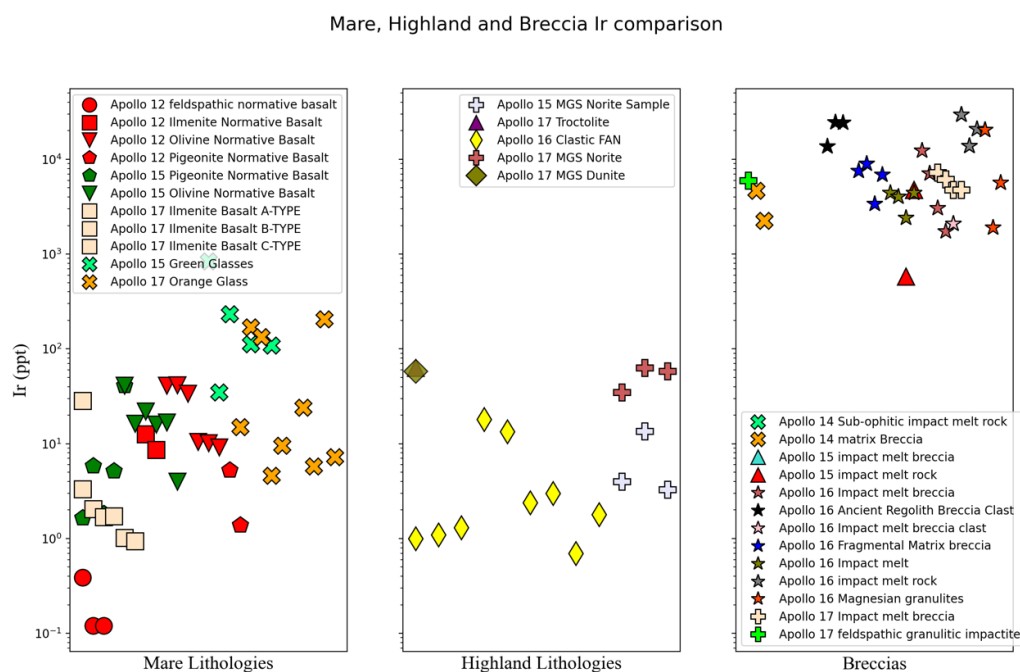


Figure 5.2 Comparison of Ir composition of lunar mare lithologies, highland lithologies and breccias. Data Source: Day et al., (2016) and references therein.

the distribution of the HSE in planetary mantles. Further in this chapter, the mantle and crustal abundance of the the HSE is discussed as understood from previous analysis of the Apollo samples and lunar meteorites.

5.1.1 Lunar Mantle

Similar to other planetary mantles, the HSE abundance of the Moon's silicate fraction is higher than the predictions from experimental studies of metal-silicate partitioning (**Figure 5.1**). Most importantly, due to lack of bonafide mantle rocks, the HSE in the lunar mantle are estimated using derivative melts, such as mare basalts (Day et al., 2007; Day and Walker, 2015). This method has drawbacks as lunar basalts and their HSE contents are likely affected by multiple process including degree of melting, crystal-liquid fractionation, and presence or absence of residual metals and sulfides, during their ascent to the surface.

However, in the absence of bonafide mantle rocks, derivative melts sampled as mare basalts and pyroclastic glasses are the only materials available with which to estimate the mantle HSE abundances. Pyroclastic glasses with high MgO are thought

to be sourced from deep lunar mantle (> 400 km) via high degree of partial melting (Shearer and Papike, 1999). In terrestrial settings, high MgO melts (e.g. picrites and komatiites) have the HSE abundances broadly similar to their mantle sources, because they result from partial melting to such high degree where all the sulfide host minerals from the source mantle gets incorporated into the melt (Barnes et al., 1985; Rehkämper et al., 1999). Earlier studies based on the measurement of Ir content in picritic, high-Ti orange and low-Ti green glasses suggested that the HSE concentration sampled by the picritic glasses are similar (~ 2 to 4 times depleted than their terrestrial counterparts) to those in the terrestrial mantle (Ringwood, 1992). However, this interpretation has been questioned on the grounds that these samples might not be pristine but rather have surface-correlated HSE enrichments (e.g., Chou et al., 1975). Surface correlation and elevated HSE concentrations have been associated with meteoritic contamination on the exterior portion of the glass beads, after their emplacement. Later experiments conducted by Walker et al. (2004) showed that the HSE abundance in the lunar pyroclastic glasses are much lower than previous estimates made by Ringwood (1992).

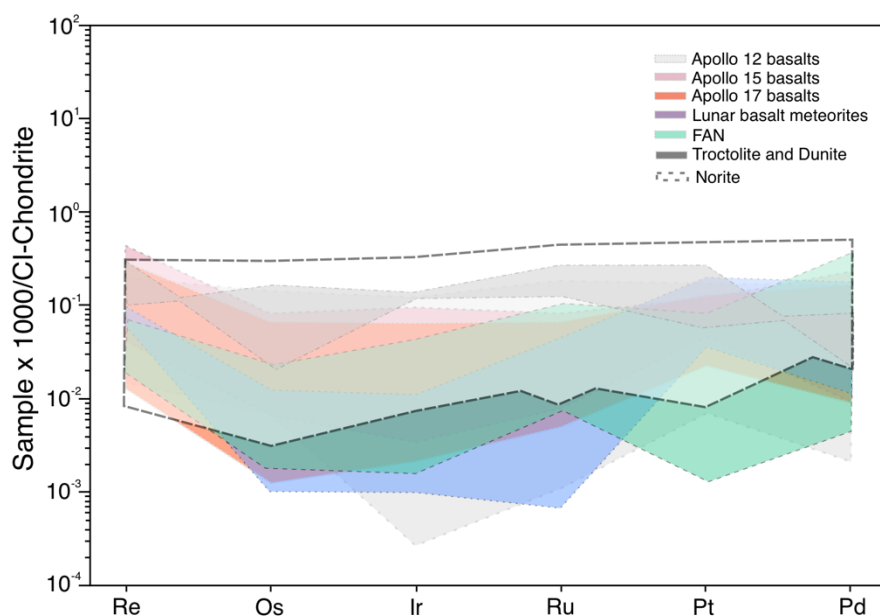


Figure 5.3 The HSE pattern in lunar pristine rocks. Data Source: Day et al., (2007), Day et al., (2010), and Day and Walker, (2015).

5.1.1.1 Pristinity of the samples

Observations from lunar crustal samples have revealed the importance of identifying samples free from any impactor contamination. The Os isotopes and HSE content has conventionally been used to characterize the pristine and non-pristine composition based on the fact that most possible impactor such as chondrites and iron meteorites have much higher HSE concentration than the lunar crustal rocks and, therefore, even a small meteoritic addition will cause a significant increase in the overall HSE concentration in the sample (**Figure 5.3**; Warren, 1993). The HSE are sensitive to impactor addition especially for rocks with low initial HSE abundances. In addition to the HSE, Os isotope composition is also diagnostic of impactor contamination as chondrites and iron meteorites have limited variability in their Re/Os and $^{187}\text{Os}/^{188}\text{Os}$ composition. The difference also becomes robust from the observation that HSE relative abundances and ratios of lunar basalts are non-chondritic during magmatic processing (Day et al., 2010). A recent study by Day (2020) proposed that the Ni/Co ratio in metal grains of lunar samples can also be used to differentiate the exogenous and endogenous components in the sample. In addition to the above-mentioned evidence, the low incompatible element abundance (exception of KREEP

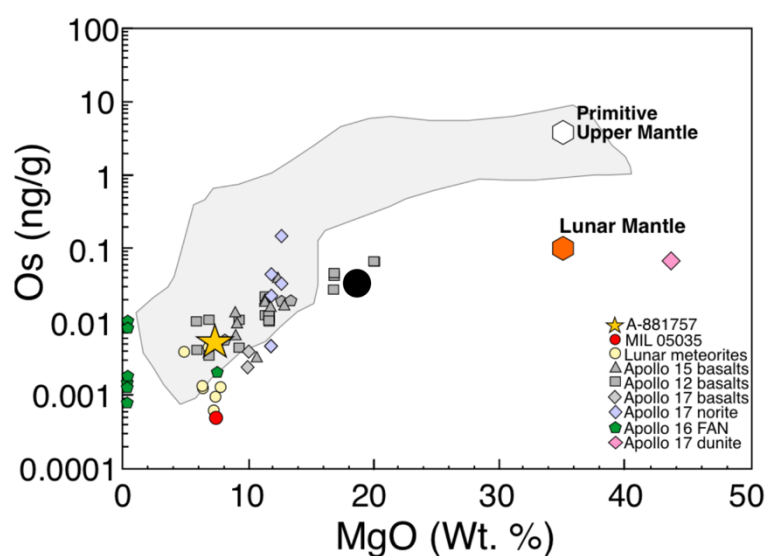


Figure 5.4 MgO (wt.%) versus Os (ng/g) for lunar mare basalts, FAN and MGS rocks shown along with terrestrial lavas. The compositions of Earth's primitive upper mantle (Becker et al., 2006) and lunar mantle (Day et al., 2007) is estimated assuming similar MgO abundance for both mantles. Data Source: this study; Day et al., (2007, 2010); Walker et al., (2004).

basalts), coarse granularity, phase homogeneity, coarse exsolution lamellae, cumulate

texture, and unradiogenic $^{87}\text{Sr}/^{88}\text{Sr}$ composition, are some other criteria to assess the sample “pristine” (Warren and Wasson, 1980; Warren, 1993). Assessment of the pristine nature of any lunar sample is imperative when using such samples to estimate the lunar mantle composition.

5.1.1.2 Regolith contamination and metal-sulfide retention in mare basalt source regions

The estimation of lunar mantle HSE abundances using pristine mare basalts have been questioned on the grounds of possible contamination from the HSE-rich mega-regolith (Brenan et al., 2019). The present-day lunar surface environment contains evidence of regolith materials strongly affected by impacts (e.g., as sampled by lunar regolith breccia meteorites), which show significantly high HSE abundances (ppb) compared to mare basalts and pristine lunar crustal lithologies (ppt) (Walker, 2009; Day et al., 2016). Even (<1%) contamination from this megaregolith would have a significant effect on the mare basalt HSE abundances. Any HSE abundance estimation for BSM using such impact-contaminated rock would represent the maximum possible value. Brenan et al. (2019) suggested the hot Mg-rich magmas along with the fractionated basalt are prone to regolith contamination. These authors used melting models assuming ($\sim 0.0002 \times \text{CI}$; Day et al., 2007) HSE in the lunar mantle and the melts is then mixed with possible contaminants ($\sim 1\%$ Orgueil composition) from the mega-regolith. However, Day and Paquet (2021) noted that there is a surprising threshold in the case of the Ir value (~ 50 ppt) for mare basalts especially with the samples having > 10 wt.% MgO. If the hot Mg-rich materials are more prone to impact contamination, as suggested by Brenan et al. (2019), a reasonable expectation would be a large range of Ir concentrations, which was not observed. Second, the inter-elemental HSE ratio of impact melt rocks on the Moon usually vary within the chondritic range. However, the mare basalt meteorites especially the low-Mg ones show high Pd/Ir for a given Ir content. Therefore, if regolith contamination has actually affected these samples, the pronounced high Pd/Ir should have been overprinted by chondritic low

Pd/Ir. Additionally, low Ru/Ir and Pd/Ir observed in case of the high MgO Apollo 15 mare basalts cannot be explained by the regolith contamination model.

In addition to this, if mare basalt sources had residual metals and sulfides along with contamination from mega-regolith, then mare basalts cannot be used as a proxy to the bulk silicate moon (BSM) composition. Therefore, the BSM's HSE content will essentially remain unconstrained. The possibility of metal and sulfide retention in the mare basalt sources has been explored by Day (2018) using elements of similar incompatibility. For instance, W, U and Th behave similarly during partial melting and fractional crystallization, but W is a moderate siderophile element and U and Th are strongly incompatible lithophile trace elements. If mare basalt sources had any metal left in the source after partial melt extraction, W concentration with respect to Th or U should be lower than the source lacking residual metal. Using Apollo 11, 12, 15 samples and lunar meteorites, Day (2018) demonstrated that most of the samples follow a linear correlation between W and U, with U/Th approximately the same as for those of the chondrites, terrestrial samples and the lunar surface (**Figure 5.5a**). This implies that there is no significant modification of the W/U ratio and metal is not a residual phase in mare basalt mantle sources.

Sulfide retention is also theoretically possible in mare basalt mantle sources due to extremely low fO_2 conditions of the Moon. One of the key parameters controlling sulfide retention is S-saturation of parental magmas, usually expressed as SCSS (Sulfur Content at Sulfide Saturation). SCSS is understood to be dependent on the changes in FeO content of the melt. In lunar settings, FeO content differs from source to source and during magmatic differentiation. It has been observed that SCSS of the lunar samples rapidly changed during melt extraction and emplacement of the mare basalts, which further lead to sulfur retention (Brenan et al., 2019). Following this scenario, BSM HSE abundance would have been more than what is estimated from the mare basalts, i.e., \sim Bulk Silicate Earth HSE/4. However, it is important to note that eruption dynamics of mare basalts, their emplacements are not well understood, which imply this interpretation to be circumstantial. In this line, the behavior of Cu and Yb in mare basalts has also been observed (Day, 2018) (**Fig 5.5b**). Copper is a moderately volatile element and behaves as chalcophile while Yb is a refractory lithophile element. A

positive correlation between Yb and Cu indicates that the mare basalt parental melts were likely undersaturated with respect to sulfur (Day, 2018).

While the debate still persists, the samples studied in this thesis would be extremely important to address some of these issues like regolith contamination at the non-PKT regions of the Moon.

5.1.1.3 Estimation of HSE abundances in the lunar mantle

Extensive research has been done on terrestrial samples to understand the composition of the HSE in mantle and crustal reservoirs. The primary method of obtaining the mantle abundance is through projection of the measured HSE to hypothetical undepleted mantle composition termed as Primitive Mantle or “PM”. The PM composition is estimated either by using the compatible Mg or melt depletion indicator Al. However, due to lack of availability of direct mantle samples, lunar mantle HSE abundance is calculated either by using HSE-MgO co-variations (**Figure 5.4**) or inter-elemental HSE co-variation. HSE-MgO covariations works on the assumption that the compatible HSE can be regressed to ~35 wt.% MgO composition of the mantle (Day et al., 2007). This method can distinguish the non-pristine materials as these samples plot at higher values than the usual HSE abundances for a given MgO. Inter-elemental HSE co-variation utilizes two HSE of contrasting compatibility with an assumption that with increasing degree of melting, incompatible HSE or incompatible/compatible HSE ratios will decrease until when the incompatible/compatible ratio will approximately be equal to the source. This method does not require MgO content but does require samples to be pristine and free from impactor contamination. While both the HSE-MgO and interelement co-variation methods provide similar results, the inter-element co-variation method has been shown to give non-chondritic Re/Os and Pd/Os for the estimated lunar and martian mantle composition (Day et al., 2016). MgO-HSE co-variation methods, however, predicts broadly chondritic-relative abundances of the HSE (Becker et al., 2006; Day et al., 2007) and so are favored. Using the MgO-HSE co-variation method, the HSE abundance in the lunar mantle from large dataset of HSE abundances in mare basalts

and unbrecciated lunar meteorites was estimated. I have compiled the present estimated HSE abundance in the *Section 5.5.3*.

5.1.2 Lunar exterior

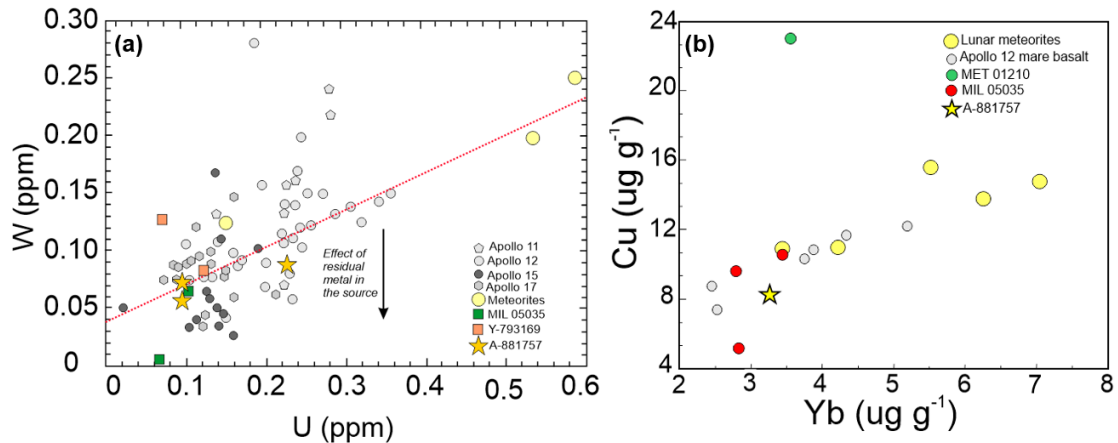


Figure 5.5 (a) U versus W concentrations in lunar basalts from Apollo 11, 12, 15, 17 along with YAMM basalts and other lunar meteorites. Most of the samples (except some Apollo 12 samples), including YAMM basalts show linear correlation between W and U refuting the metal retention in the source of these basalts. (b) Cu versus Yb for Apollo 12 mare basalts, lunar meteorites including YAMM basalts. Except MET 0210, Apollo 12 mare basalts and YAMM basalts show strong correlation indicating no sulfur retention in the source. The high Cu abundance of MET 01210 is possible result of impactor contamination. Data Source: This study, Day, (2018) and references therein.

The lunar crust is an exceptional test bed which records billion years of interaction history of the airless Moon with space. The primary crust on the Moon is thought to have formed as a result of large-scale differentiation of partially to completely molten silicate Moon (Smith et al., 1970; Wood et al., 1970). This anorthositic crust formation was later followed by an intrusive mafic Mg-suite lithology. These rocks preserve important information regarding the crust-mantle differentiation in the Moon. However, this information can be overprinted by meteoritic contamination. Lunar crustal samples collected during sample return missions and as lunar meteorites show plenty of evidence of impactor materials (Walker et al., 2004; Puchtel et al., 2008; Fischer-Gödde and Becker, 2012; Sharp et al., 2014; Liu et al., 2015; Gleißner and Becker, 2017, 2019; McIntosh et al., 2020). Thus, the lunar crust

enables us to look into both endogenous and exogenous processes occurring in and on the Moon.

Analysis of pristine lunar samples have previously been attempted by several studies using Radiochemical Neutron Activation Analysis (RNAA) and have accounted for the lunar primeval crustal HSE abundance ($n=41$; <3 to 198 pgg^{-1} Os, 1 to 130 pgg^{-1} Ir, <130 to 1200 pgg^{-1} Pd, <0.3 to 17 pgg^{-1} Re; Higuchi and Morgan, 1975; Hertogen et al., 1977; Warren and Wasson, 1978, 1980; Wolf et al., 1979; Warren et al., 1991; Ebihara et al., 1992). Using isotope dilution methods, HSE in the lunar pristine rocks have also been measured (Day et al., 2010). HSE abundances of the pristine lunar crustal lithologies like Ferroan Anorthosite (FAN) and Mg-suite rocks were estimated to be 0.000003 to $0.00006 \times \text{CI chondrite}$ and 0.00002 - $0.0001 \times \text{CI chondrite}$, with chondritic Re/Os and non-chondritic inter-elemental ratios (high Pd/Ir ≥ 22 ; Re/Ir ≥ 0.2) (Day et al., 2010). Chondritic impactors are likely to have had very high HSE content (~ 235 to 1008 ngg^{-1} for Ir; Day et al., 2016). The overall ~ 3000 - $50,000$ times difference in the HSE abundance makes them extremely sensitive tracers of meteoritic contamination. In the case of speculative cometary impactors, the predicted HSE abundance can be 30-500 times more than the pristine lunar crust (Yamamoto, 1985).

Impactor contaminated rocks such as impact melt breccias, lunar regolith breccia meteorites and impact melt coats have been analyzed to understand the flux, nature and the HSE characteristics of materials that were indisputably accreted late to the Moon (Walker et al., 2004; Puchtel et al., 2008; Fischer-Gödde and Becker, 2012; Sharp et al., 2014; Liu et al., 2015; Gleißner and Becker, 2017, 2019; McIntosh et al., 2020). Most of the conclusions, based on inter-elemental HSE ratios, indicate that the measured composition of the impactors is consistent with either chondrites-like materials or iron meteorites (Higuchi and Morgan, 1975; Hertogen et al., 1977; Warren et al., 1991; Norman et al., 2002; Puchtel et al., 2008; Fischer-Gödde and Becker, 2012; Sharp et al., 2014; Liu et al., 2015; Gleißner and Becker, 2017, 2019). Two different approaches have been utilized to analyze the HSE abundance in these samples. One method performs measurement on homogenized powders (e.g. Norman et al., 2002) while other analyzes individual sub-fragments (e.g. Puchtel et al., 2008; Fischer-Gödde and Becker, 2012; Gleißner and Becker, 2017; McIntoshMcIntosh et al., 2020).

Homogenized powder analysis provides averaged information of the HSE content and their isotopes in bulk samples. Complementarily, analysis of individual sub-fragments enables examination of the HSE carrier phases and their distribution within the samples. Studies on Impact Melt Breccia (IMB) samples have reported that Re-Os isotopic compositions in several cases are super-chondritic with high Pt/Ir, Pd/Ir and Ru/Ir that differ significantly from the present-day composition of chondrites sampled on Earth (Norman et al., 2002; Puchtel et al., 2008; Sharp et al., 2014; Liu et al., 2015; McIntosh et al., 2020). However, some impact melt rocks from the Apollo 16 mission show the chondritic HSE and $^{187}\text{Os}/^{188}\text{Os}$ isotope compositions (Liu et al., 2015; Gleißner and Becker, 2017). It has been suggested that super-chondritic $^{187}\text{Os}/^{188}\text{Os}$ and high Pt/Ir, Pd/Ir and Ru/Ir in the Apollo IMB demarcates the changes in composition of impactor striking the Moon before 3.5 Ga and after 3.5 Ga. However, alternative explanations are that these could reflect (1) a combination of chondritic and differentiated impactors (Fischer-Gödde and Becker, 2012); (2) mixing of endogenous lunar crustal component with fractionated HSE relative to the chondrites (Norman et al., 2002), or (3) could possibly result from the fractionation of HSE within the impact melts sheets (Day et al., 2016).

In this chapter, the abundance of the HSE in the lunar mantle and crust is targeted using the lunar meteorites discussed in the previous chapters. The bulk chemistry of the studied lunar meteorites clearly depicts their derivation from the regions outside the PKT terrane (*Section 4.7*) and can provide key constraints on the HSE abundance outside the PKT region. The petrogenesis of unique unbrecciated lunar meteorite A-881757, which is distinctly sourced from a pyroxene-rich lunar mantle source, provides key understanding of the HSE abundance in the KREEP-free (source) lunar mantle. The regolith breccia meteorites offer us to examine the nature, flux and composition of the materials striking the unexplored lunar surface away from the PKT.

5.2 Samples

The HSE abundance in four different lunar meteorites, namely A-881757, Y-981031, Y-983885 and Y-86032 were measured. Asuka-881757 (~7.2 wt.% MgO) is an unbrecciated, ~3.9 Ga coarsely crystalline lunar meteorite composed dominantly of pyroxene and plagioclase. The sample is also part of the YAMM clan, which has three

other lunar meteorites, MIL 05035 (unbrecciated coarse), Y-793169 (unbrecciated fine grained) and MET 01210 (basaltic breccia). YAMM basalts are classified as KREEP-free (source) samples and have been argued to represent unique, KREEP-free (source) volcanism outside the PKT, distinct to returned Apollo samples (Srivastava et al., 2022). These low-Ti mare basalt meteorites help us in constraining the HSE abundance of previously unexplored portion of the KREEP-free (source) lunar mantle.

Samples Y-981031, Y-983885 and Y-86032 are regolith breccia meteorites composed of varied lithic clasts and mineral fragments. Their bulk compositions suggest they were derived from the three distinct locations on the Moon (see *Section 4.7*). All the samples show presence of impact melt suggesting their non-pristine nature. The studied sections also contain metals and sulfide phases, which perhaps formed or modified during the impacts. Phosphates in the mare basalt clasts of Y-981031 yielded ages of ~3.5 Ga (Terada et al., 2006), similar to sample EET 87521 and EET 96008. Its paired counterpart Y-793274 have an age of ~4.0 Ga. Phosphates from different clasts of Y-983885 yielded a confirmative age of ~4.0 Ga (Arai et al., 2008). Sample Y-86032 is a feldspathic regolith breccia with the clasts of ages as old as ~4.4 Ga. In chapter 4, it was argued that this sample might have been derived from the far-side of the Moon (*Section 4.7*).

5.3 Analytical Methods

Bulk rock samples of A-881757(89), Y-981031(90), Y-983885(72) and Y-86032(136) were provided by NIPR. A homogeneous powder was prepared using a dedicated agate mortar and pestle. The homogenized powder is further used to measure the bulk major and trace-elements along with the HSE abundance and $^{187}\text{Os}/^{188}\text{Os}$ of the samples. The polished thick sections of A-881757(88a & 88b), Y-981031(100), Y-983885(74) and Y-86032(137) were also studied to determine the composition of metals and sulfides grains using EPMA facility at NIPR and PRL (for details see Chapter 2).

Osmium isotope and HSE abundance measurements were performed at the Scripps Isotope Geochemistry Laboratory (SIGL). Homogenized sample powders and associated total procedural blanks were prepared with appropriate amount of isotopically enriched multi-elemental spike (^{99}Ru , ^{106}Pd , ^{185}Re , ^{190}Os , ^{191}Ir and ^{194}Pt) in single-use pre-cleaned borosilicate Carius tubes. Samples were digested by adding a 1:2 mixture of Teflon distilled HCl and Teflon-distilled purged HNO_3 in the Carius tube. After sealing, the Carius tubes were placed in a convecting oven for 72 hours at a temperature of $270 \pm 1^\circ\text{C}$. Osmium was triply extracted using CCl_4 and then back-extracted into quadruple Teflon-distilled HBr (Cohen and Waters, 1996). Double micro-distillation was performed to further purify the extracted osmium (Birck et al., 1997). The remaining of the HSE were purified from the residual solutions using anion exchange separation techniques (Day et al., 2016).

Osmium isotope measurement was done using a Triton TIMS in negative mode and the other HSE abundances were determined using *Cetac* Aridus II desolvating nebulizer coupled to an iCAPQc ICPMS. Precision on the $^{187}\text{Os}/^{188}\text{Os}$ measurement was determined using only 35pg UMCP Johnson-Matthey standard load and was better than $\pm 0.2\%$ (2SD; 0.11368 ± 27 ; $n = 9$). Osmium measurements were also corrected for oxide interferences, instrumental mass fractionation (assuming the exponential law) using $^{192}\text{Os}/^{188}\text{Os} = 3.0821$, spike addition, and the TAB (total analytical blank). The HSE abundance data were corrected offline for mass fractionation using multiple measurements of a standard solution throughout the run. The external reproducibility on the HSE analyses was better than 0.25% on 0.5 ppb solutions and all the sample data are reported in Table 5.1. Total procedural blanks analyzed run with the samples in two analytical campaigns and from the same batch of Carius tubes had relatively consistent $^{187}\text{Os}/^{188}\text{Os} = 0.140 \pm 0.013$, and (in pg) $\text{Re} = 4.9 \pm 2.0$, $\text{Pd} = 20.5 \pm 5.2$, $\text{Pt} = 3.9 \pm 2.0$, $\text{Ru} = 70 \pm 10$, $\text{Ir} = 2.5 \pm 1.0$ and $\text{Os} = 1.7 \pm 0.8$ ($n = 3$). The uncertainties on concentration measurements were calculated by propagating from external reproducibility on standard measurements, together with associated blank percentages. More detailed explanation of each step is provided in Chapter 2.

5.4 Results

The detailed petrography and mineral chemistry of studied lunar meteorites has already been discussed in Chapter 3 and Chapter 4. Here, the chemistry of metal grains and highly siderophile element abundance and Re-Os isotopic composition (**Table 5.1**) of the samples are detailed.

5.4.1 Composition of metal grains

The studied thick sections of A-881757, 88a and 88b, show anhedral Fe-Ni metal grains: one adjacent to a fracture, sharing boundaries with pyroxene and anhedral troilite; and another associated with ilmenite and spinel. The metals associated with the early formed pyroxenes have ~3.14 wt. % Ni and ~0.88 wt. % Co, while the metals

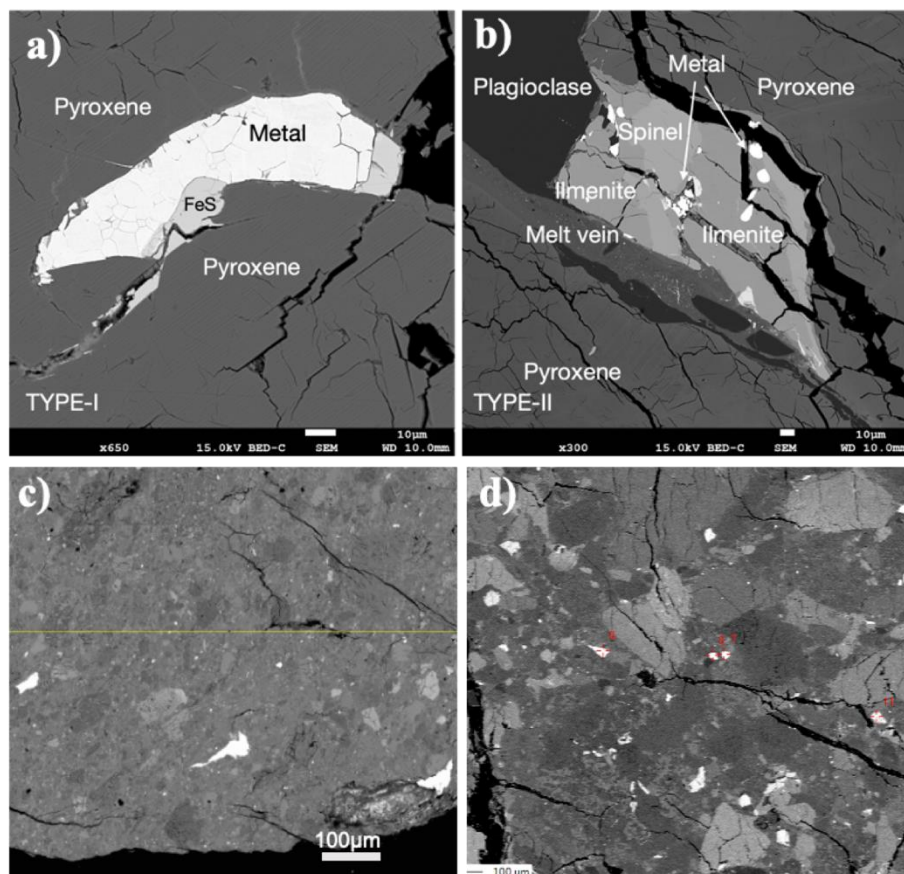


Figure 5.6 Backscattered electron images of metal grains in the studied samples. **a)** Two distinct association of metal is observed in A-881757. TYPE-I metal grains are associated with first formed pyroxenes and plagioclase **b)** TYPE-II metal grains are found close to spinel and ilmenites. **c)** Metal in sample Y-983885 occur as anhedral ~100µm grains. **d)** Sample Y-981031 metal grains (with red cross hairs) found disseminated within the regolith.

associated with ilmenites and spinels have ~ 0.04 wt. % Ni and ~ 0.14 wt. % Co (**Figures 5.6a, 5.6b**).

Among the regolith breccia meteorites, sample Y-981031 and Y-983885 contains numerous FeNi metal grains. However, the studied section of Y-86032 does not contain any FeNi metal phase. Sample Y-981031 has metal grains embedded in matrix as isolated mineral fragments. The Ni and Co composition of metal grains show restricted composition of 3.53-6.91 wt.% Ni and 0.39-0.60 wt.% Co. The metal grains in sample Y-983885 exists as anhedral grains of size ranging from 100-200 μm . The compositional range of Ni and Co in Y-983885 metal grains vary from 2.86-10.59 wt.% and 0.32-0.78 wt.%, respectively (**Figures 5.6c, 5.6d**).

5.4.2 Rhenium-osmium (Re-Os) isotope systematics and highly siderophile element (HSE) abundances

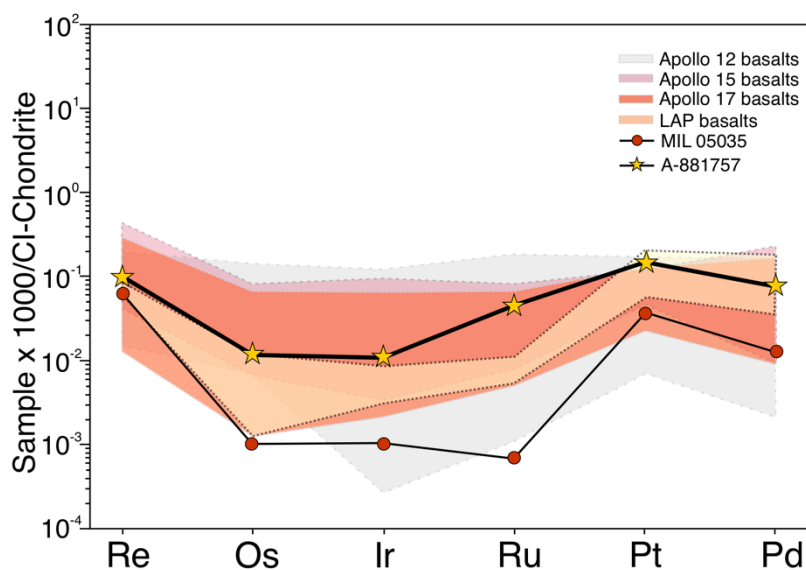


Figure 5.7 The HSE pattern for A-881757 and MIL 05035 compared with previously analyzed Apollo basalts and lunar meteorites. Data Sources: This study; Day et al., (2007); Day and Walker, (2015).

5.4.2.1 Unbrecciated lunar basalt A-881757 and YAMM basalts

Two samples among the YAMM clan have been analyzed for the highly siderophile element (HSE) concentration and Os isotopes so far, A-881757, 89 (~ 7.2

wt.% MgO; this study) and MIL 05035, 20 (7.4 wt.% MgO; Day and Walker, 2015). Both, A-881757 and MIL 05035 show the fractionated HSE pattern as seen in case of low-Mg mare basalt meteorites (Day et al., 2007). However, A-881757 has less fractionated and a higher HSE abundance when compared to its paired counterpart MIL 05035 (**Figure 5.7**). The absolute and relative abundance of the HSE in A-881757 lies at the higher end among previously analyzed mare basalt meteorites while being within the range of values observed for Apollo mare basalts (Day et al., 2007; Day and Walker, 2015). The $^{187}\text{Os}/^{188}\text{Os}$ of A-881757 (0.1247 ± 0.0003) is slightly sub-chondritic but within the error range of MIL 05035 (0.1244 ± 0.0002). Given $\sim 3.8\text{-}3.9$ Ga crystallization ages for YAMM basalts, the dispersion of $^{187}\text{Re}/^{188}\text{Os}$ - $^{187}\text{Os}/^{188}\text{Os}$ reflects the possible disturbance of the Re-Os system in the sample, yielding initial γ_{Os} ($\gamma_{\text{Os}} = [({}^{187}\text{Os}/^{188}\text{Os})_{\text{sample}} - ({}^{187}\text{Os}/^{188}\text{Os})_{\text{Chon}}] / ({}^{187}\text{Os}/^{188}\text{Os})_{\text{Chon}} \times 100$) values from -204 to -1187 (**Figure 5.8**).

5.4.2.2 Lunar regolith breccia meteorites

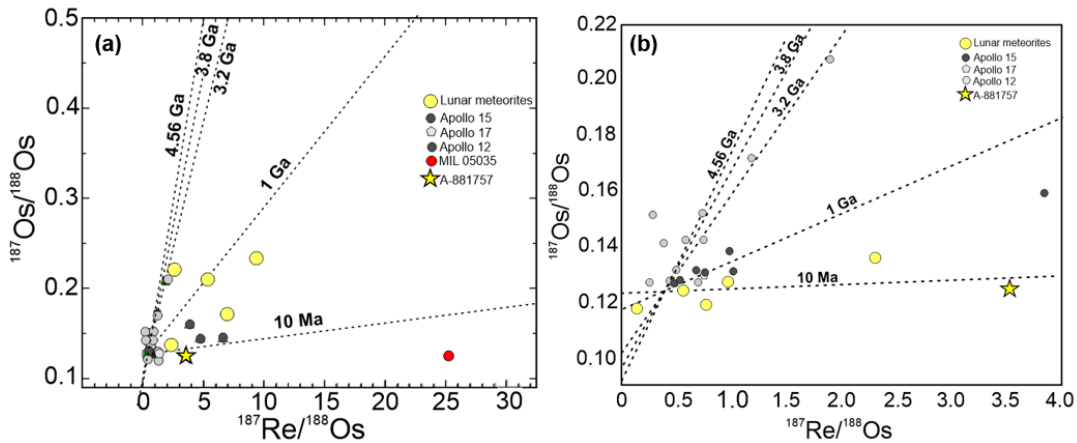


Figure 5.8 $^{187}\text{Re}/^{188}\text{Os}$ versus $^{187}\text{Os}/^{188}\text{Os}$ for YAMM basalts compared with mare basalts with a) $^{187}\text{Re}/^{188}\text{Os} = 0\text{-}32.5$ and b) $^{187}\text{Re}/^{188}\text{Os} = 0\text{-}4.0$. The dotted lines show isochrons, tied to Solar System initial $^{187}\text{Os}/^{188}\text{Os}$. The isochron lines shown for ages 4.56 Ga, 3.2 Ga, 1.0 Ga and 10 Ma. Despite having crystallization age of ~ 3.9 Ga, YAMM basalts (A-881757 and MIL 05035) lie to the right, falling close to 10 Ma isochrons, implying open system behaviour of Re and/or Os. Data Source: This study; Day et al., (2007); Day and Walker, (2015).

The studied regolith breccia meteorites have the HSE concentrations that range from approximately 0.01 to 0.1 times CI chondrite values and most data fall within the range of impact melt breccias, feldspathic granulite and fragmental matrix breccias (Puchtel et al., 2008; Fischer-Gödde and Becker, 2012; Sharp et al., 2014; Liu et al., 2015; Gleißner and Becker, 2017, 2019; McIntosh et al., 2020). They are, therefore, at much higher concentrations than for A-881757. Among all three samples, Y-86032 exhibit relatively flat HSE patterns while Y-981031 and Y-983885 display HSE fractionation (**Figure 5.9**). Sample Y-981031 show enrichment of Pt and Pd and Y-983885 depicts has enrichment of only Pd. Sample Y-983885 have the highest absolute abundance of the HSE among the studied samples, suggesting significant impact contamination.

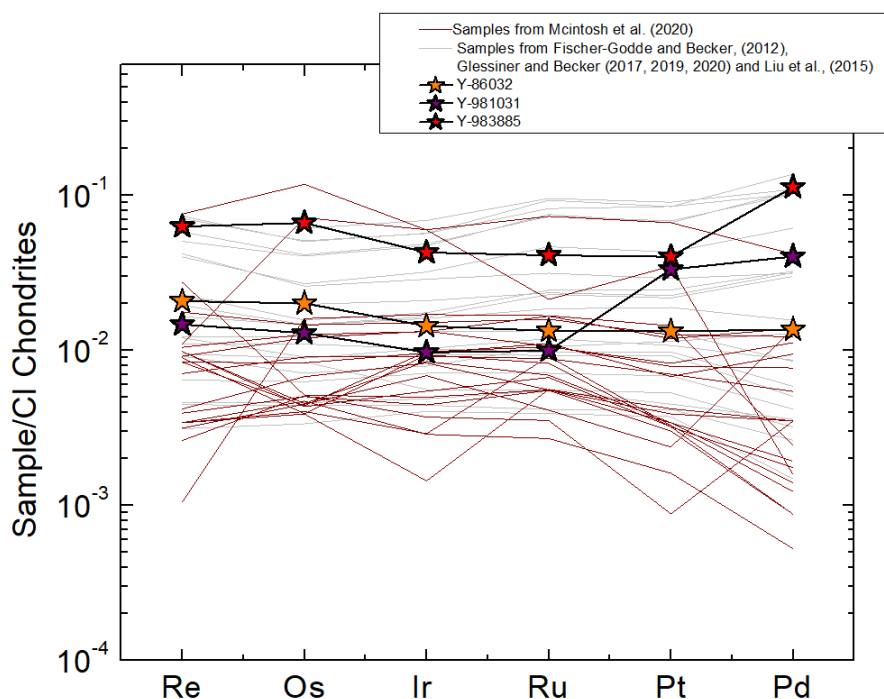


Figure 5.9 Carbonaceous Ivuna (CI) normalized highly siderophile (HSE) abundances for studied regolith breccia meteorites, Y-981031, Y-983885 and Y-86032 compared with previously analyzed impact melt rocks. CI chondrite normalization from Horan et al., (2003).

The HSE composition in the regolith breccias show heterogeneity in their (Pt, Pd, Ru)/Ir ratios (**Figure 5.9**). Sample Y-86032 shows chondritic ratio of all the HSE (Ru/Ir=1.38; Pd/Ir = 1.26 and Pt/Ir = 1.88) and falls in the field of chondrites and impact melt breccias. Sample Y-981031 exhibit non-chondritic ratios of Pd/Ir = 5.51 and Pt/Ir = 6.96. Similar non-chondritic Pd/Ir=3.51 is observed in Y-983885, however, Pt/Ir value falls within chondritic fields. The non-chondritic Pd/Pt and Pt/Ir, have been observed previously in case of Apollo 16 impact melt rocks, Apollo 16 impact melt coats 65035 and lunar meteorite MIL 090034 (Fischer-Gödde and Becker, 2012; McIntosh et al., 2020). Unlike the inter-element HSE concentrations, ratios of $^{187}\text{Os}/^{188}\text{Os}$ for the studied regolith breccia meteorites show chondritic ratio ranging between 0.1265 (~3.5 Ga; Y-981031) – 0.1278 (~ 4.4 Ga; Y-86032). All these measured ratio numbers are

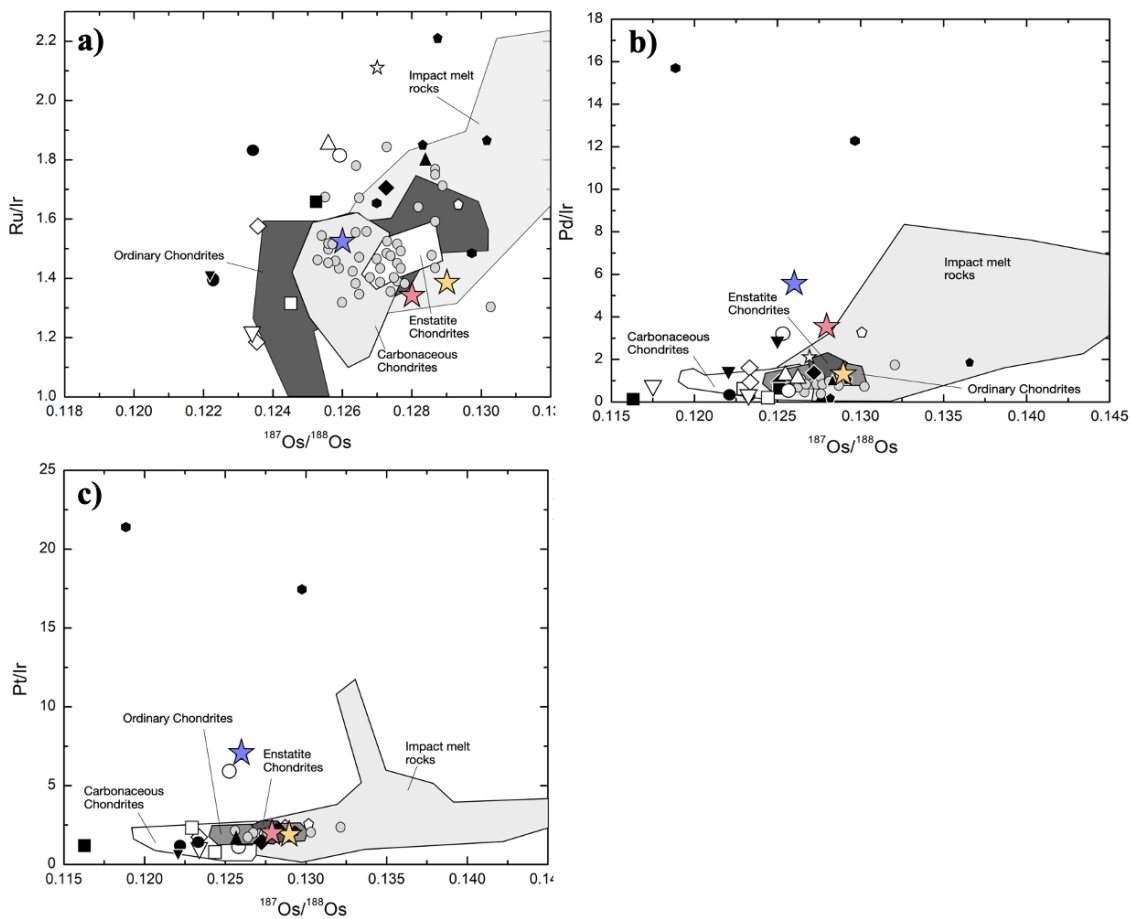


Figure 5.10 Plots of $^{187}\text{Os}/^{188}\text{Os}$ versus a) Ru/Ir b) Pd/Ir and c) Pt/Ir for studied regolith breccia meteorites, Y-981031, Y-983885 and Y-86032, impact melt rocks, lunar anorthositic regolith breccia, impact melt coats and chondrites (cf. McIntosh et al., (2020).

plotted within previously measured $^{187}\text{Os}/^{188}\text{Os}$ values of Apollo 16 and 17 impact melt breccias, feldspathic impactites and terrestrial primitive mantle (**Figure 5.10**).

5.5 Discussion

5.5.1 Origin of metal grains in unbrecciated basalt A-881757 and regolith breccia Y-981031 and Y-983885

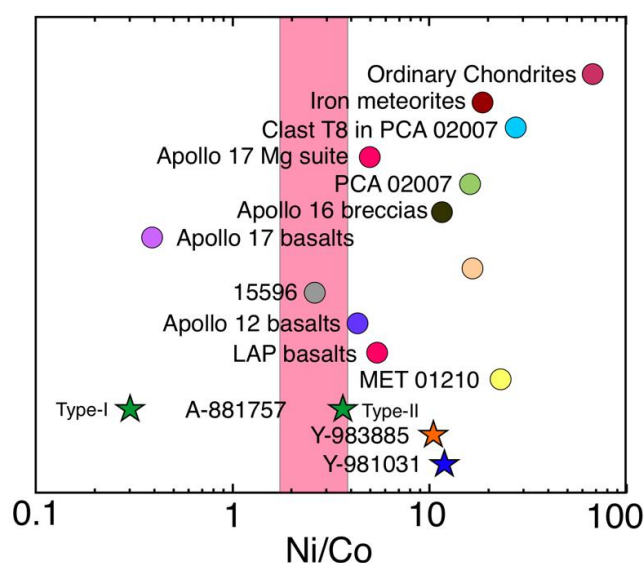


Figure 5.11 Ni/Co ratios in metal grains of the studied samples (marked as colored stars) compared with lunar mare basalts, MGS, impact melt breccias, iron meteorites and chondrites. The red bands is shown the range from terrestrial basalts (Howarth et al. 2017). Data Sources: This study, Day, (2020) and references therein.

The highly reducing conditions ($f\text{O}_2 \sim \text{IW}-1$) within the lunar interior potentially promote the formation of metal grains in lunar rocks. These metal grains could either be a product of magmatic fractionation at reduced conditions or a consequence of impactor striking on the Moon's surface. Thus, it becomes important to understand whether the metal grains present in lunar rocks are result of exogenous or endogenous processes. Nickel/Cobalt (Ni/Co) ratio in the metal grains have been demonstrated to be useful discriminator of these two processes because the most likely impactors such as chondrites and iron meteorites tend to have high Ni/Co (> 20) ratio when compared to metals formed by fractional crystallization of lunar basaltic magmas (Ni/Co < 8) (Day, 2020).

Two distinct associations of metal grains were found in A-881757. One occurs as relatively coarse ~ 100 μm anhedral grains associated with pyroxene and troilite (Type-I) and the other as small grains (~ 10 - 20 μm) occurring between spinel and ilmenite (Type-II) (**Figure 5.6**). Other than A-881757, only brecciated MET 01210 has anhedral metal grains (Arai et al., 2010; Day, 2020). The Ni/Co composition of metal grains can record the effect of impact contamination as most plausible impactors (chondrites and iron meteorites) have relatively high Ni/Co. The average measured Ni/Co composition of metals in A-881757 is 3.6 for Type-I and 0.3 for Type-II (**Figure 5.11**). The average Ni/Co composition of metals in MET 01210 is ~ 23.6 , indicative of exogenous input of chondritic materials (Day, 2020). The measured Ni/Co for A-881757 metal grains indicate that they are pristine, free from impactor contamination. Therefore, A-881757 can be used to estimate BSM HSE contents in non-PKT regions.

Metal grains in regolith breccias Y-981031 and Y-983885 occurs as < 200 μm grains and show Ni/Co composition of 10.40 ± 1.53 ($n=6$) and 11.70 ± 2.84 ($n=20$), respectively (**Figure 5.11**). This value is similar to Ni/Co composition of metal grains present in Apollo 16 impact melt breccias (~ 11.6) but lower than value observed in lunar breccia meteorite MET 01210 (~ 23.6) and PCA 02007 (~ 27). The intermediate Ni/Co of Apollo 16 impact melt breccias has been interpreted as signature of mixing between low Ni/Co endogenous component and high Ni/Co exogenous components (Day, 2020). Therefore, sample Y-981031 and Y-983885 likely preserve some evidence of pre-existing lithologies.

5.5.2 Post-crystallization disturbances and origin of HSE in YAMM basalts

The studied lunar basalt meteorites show deviation to the right of the 3.8 Ga reference isochrons, and plots at or around the 10 Ma reference isochrons in $^{187}\text{Re}/^{188}\text{Os}$ - $^{187}\text{Os}/^{188}\text{Os}$ diagrams (**Figure 5.8**). This behaviour has previously been observed in the case of Apollo mare basalts especially in Apollo 17 suites and have been interpreted to indicate either open-system behaviour of Re by addition, or loss of Os, or modification from cosmic ray exposure (CRE) (Day and Walker, 2015). The

apparent open-system behaviour of the Re-Os isotope system in the YAMM basalts is most likely post-crystallization modification of Re, rather than Os. This is because YAMM basalt samples have relatively unfractionated Os/Ir (Os and Ir show similar geochemical behaviour and normally not strongly fractionated) which is consistent with the observations in Apollo mare basalts and terrestrial igneous systems.

The studied samples, which are exposed to galactic cosmic rays on the airless Moon promotes the production of neutrons. These produced neutrons further interact and get absorbed by other isotopes, usually the ones with large neutron capture cross-sections. The decay of these captured neutron particles further modifies the isotopic composition of the elements experiencing burnout along with the isotopic composition of elements present in “downstream” (Nyquist et al., 1995; Supplementary section S4 of Day and Walker, 2015). Therefore, the observed non-isochronous behaviour may also result from CRE exposure of the samples leading to Re and W burnout. The W/Re ratio of the studied sample is >15000, similar to mare basalts. An earlier study found that the Apollo 12 samples have a strong correlation between CRE ages and $\square^{149}\text{Sm}$ (^{149}Sm has a large effective thermal neutron absorption cross section) but a less pronounced relation in Re concentration and CRE ages (Day and Walker, 2015). Although the correlation is weak, a greater dispersion is seen in the measured Re content versus extensive neutron capture that ultimately suggested the Re modification to some extent. Furthermore, while reducing the data for Re concentration a prior knowledge of the present $^{185}\text{Re}/^{187}\text{Re}$ of the samples is required which in this case is assumed to be the same as the natural ratio. This may lead to potential erroneous calculation and over-estimation of Re in the studied samples. The very low abundance of Re in the samples makes it difficult to provide any conclusive argument here. Moreover, CRE effects on Os abundance, as suggested by Day and Walker (2015), would have been well below the level of measurements. Extreme Re-Os disturbance observed in the case of YAMM basalts is also evident in other mare basalt meteorites (Day and Walker, 2015). Since the studied meteorites are all “finds”, these samples might also have affected by impact removal, fusion melting and their residence time within Antarctic ice layers. Previous studies on highly differentiated achondritic meteorites show evidence of Re-Os disturbance as a result of terrestrial weathering in Antarctica (Day et al., 2012). However, YAMM basalts in general do not exhibit any

observable geochemical evidence of terrestrial weathering such as Ce anomaly. Following from the discussion above and results from previous studies on lunar meteorites, the most likely explanation for the non-isochronous results is the effect of CRE on Re isotopes. In addition to increased Re abundance, YAMM basalts also show elevated abundance of Pt and Pd. The measured abundance of Pt and Pd in A-881757 is higher than the Apollo mare basalts and lunar basaltic meteorites. Such high Pt and Pd abundance are unlikely to result from terrestrial contamination during its residence in Antarctica ($<1 \text{ pgg}^{-1}$ Pt in typical samples; Petaev et al., 2013) or due to any known CRE effects. The elevated Pt and Pd abundances might have resulted from the crystal-liquid fractionation effects, as seen by Day and Walker (2015).

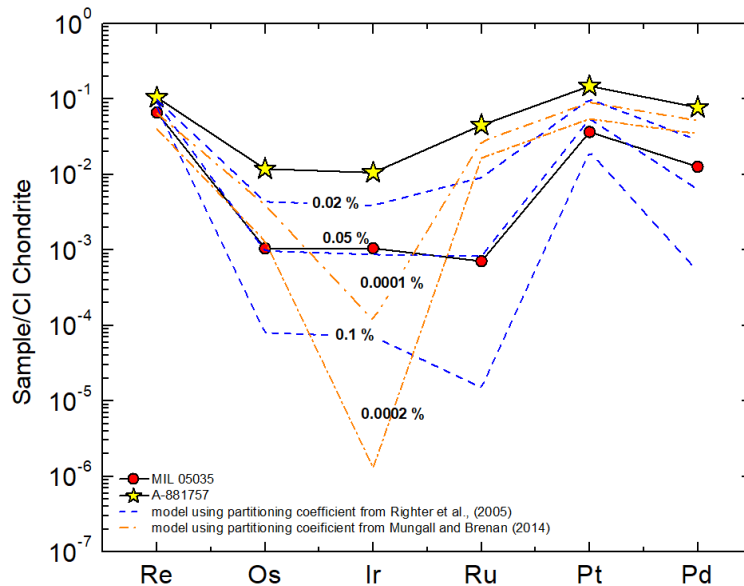


Figure 5.12 Sulfide fractionation model for YAMM basalts using sulfide-silicate partition coefficient from (Blue) Righter et al. (2005) and (Orange) Mungall and Brenan, (2014). The MIL 05035 composition can be produced by 0.0005% - 0.05% sulfide fractionation from A-881757.

A key observational aspect of low-Mg mare basalt meteorites is that they generally show low HSE abundances, more fractionated inter-element HSE variations, and can have super-chondritic $^{187}\text{Os}/^{188}\text{Os}$ in some cases (e.g., LAP basalt meteorites). On the other hand, Apollo mare basalts (high MgO) exhibit chondritic-relative HSE pattern and near-chondritic present day Os isotopic composition. The observed difference can be attributed to the compatibility of HSE during fractional crystallization

(Ir ≥ Os > Ru > Pt > Pd ≥ Re) in lunar magmatic settings (Day et al., 2007; Day and Walker, 2015). A difference in the HSE abundances of MIL 05035 and A-881757 is also observed. In the absence of impact contamination, a few endogenous processes may have been responsible for the variation observed between the bulk HSE abundances of A-881757 and MIL 05035, despite having similar $^{187}\text{Os}/^{188}\text{Os}$. First, the coarse-grained nature of these samples could possibly have led to variable metal or sulfide distribution in aliquots (i.e., more in A-881757 than in MIL 05035). Alternatively, sulfide and/or metal fractionation may have occurred during fractional crystallization of parent magmas. The absence of metal grains in MIL 05035 supports this latter view, that the variations reflect fractional crystallization at 3.9 Ga with very limited corresponding Re/Os fractionation. The model was applied to check the possibility of metal and sulfide fractionation using starting composition of A-881757 (**Figure 5.12**). Due to current limitations in our understanding of the HSE mantle-melt partitioning, sulfide-silicate partition coefficient from Righter et al. (2015) and Mungall and Brenan (2014) were applied. Using partitioning value of Righter et al. (2015), 0.05 % of sulfide fractionation fits well with the composition of MIL 05035. Mungall and Brenan (2014)'s sulfide-silicate melt partition coefficients are very high and therefore require very small amount (0.0005%) of sulfur to best fit MIL 05035 composition. These results support the involvement of crystal-liquid fractionation of sulfide phase in generating difference between the HSE abundance of A-881757 and MIL 05035.

5.5.3 Osmium isotope and HSE abundance in the KREEP-free (source) mantle

The lunar mantle has been suggested to be heterogeneous at varied scale on the basis of major and trace-elemental abundance, mineralogy and isotopic abundance in the returned mare basalts (Neal and Taylor, 1992). This mantle heterogeneity is considered to primarily results from the lunar magma ocean crystallization, and subsequently formed cumulates, followed by density driven global/local mantle overturn leading to mixing of the earlier formed Mg rich mantle cumulates with later Fe-Ti-rich cumulate (e.g., Warren and Taylor, 2014). Among the variety of mare basalts in our returned sample collection, some of the compositional difference can be

explained through fractional crystallization from common parental melts for e.g., Apollo 15 quartz normative basalts have been derived from fractional crystallization of Apollo 15 olivine basalts parental melts (Schnare et al., 2008). This fractional crystallization relationship, however, not applicable for all the mare basalt sample suite because of large difference in their Sr-Nd isotopic composition, indicating mantle source heterogeneity (Nyquist, 1977; Nyquist et al., 1995). Interestingly, despite having large differences in lithophile isotopic systematics, there is no clear systematic differences in the HSE abundance of Apollo 12, 15 or 17 mare basalts that can be attributed to mantle source heterogeneity. Therefore, the sources of Apollo mare basalts are considered to have similar range of HSE abundances suggestive of HSE homogeneity in the lunar mantle. The difference in the inter-elemental ratio within two

A recurring notion emphasized throughout the thesis is the significance of examining samples from areas beyond the regions where previous missions have collected samples. The YAMM basalts have previously been shown to originate at depths shallower than Apollo mare basalts (Srivastava et al., 2022). These low-MgO YAMM basalts are modelled to generate from 3-6% partial melting of pyroxene-rich mantle distinct to Apollo basalt's olivine-rich mantle. YAMM basalts offers us insight to examine the HSE composition of the lunar mantle in parts other than the PKT. The observed Sr-Nd isotope heterogeneity between the KREEP-free YAMM mantle source and KREEP-rich Apollo mare basalts is not evident in Os isotopes, depicting the insensitivity of ^{187}Re - ^{187}Os systematics to Lunar Magma Ocean crystallization. Fractionated HSE patterns observed in case of YAMM basalts is likely result of source mineral partition coefficients and later fractional crystallization. YAMM basalts show no signs of impact contamination and the fractionated inter-elemental HSE ratios refutes the regolith contamination effects. The lunar mantle estimates of HSE contents come from extrapolation of the HSE content in mare basalts to an assumed lunar mantle MgO contents. The obtained bulk silicate Moon HSE abundance estimates being ~40 times less than the BSE, agree with previously proposed estimates (**Figure 5.4a**; Day and Walker, 2015; Day and Paquet, 2021).

5.5.4 HSE compositions of lunar regolith breccia meteorites and composition of late accreted materials beyond PKT

The high contrast in composition of impactor (ppb; chondrites and iron meteorites) and lunar crustal lithologies (ppt; highland rocks and mare basalts) enable us in constraining putative impactor composition and its evolution with time (Fischer-Gödde and Becker, 2012; Gleißner and Becker, 2019; McIntosh et al., 2020). The HSE and $^{187}\text{Os}/^{188}\text{Os}$ composition of the studied samples highlights three distinct variety: Y-86032, an anorthositic regolith breccia indicate flat HSE pattern with chondritic Os isotopic composition; Sample Y-981031, a fragmental regolith breccia, show non-chondritic HSE pattern with highly fractionated Pt and Pd but chondritic $^{187}\text{Os}/^{188}\text{Os}$ composition; Sample Y-983885, a very fine grained regolith breccia sample, depicts chondritic Os composition and nearly flat HSE pattern with only slight Pd fractionation (**Figure 5.9**). The inter-elemental HSE ratios have previously been suggested to be important in diagnosing the possible impactor. Sample Y-86032 HSE inter elemental

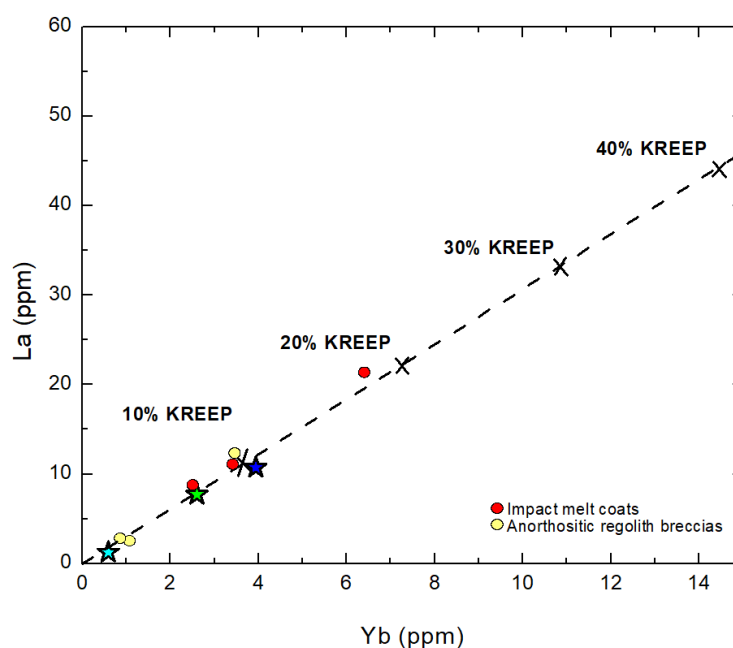


Figure 5.13 Binary mixing between KREEP and pristine lunar crust. 1-10% KREEP is needed to recreate the composition observed in the studied rocks. KREEP composition from Warren (2003) and composition of impact melt rocks is from McIntosh et al., (2020).

ratio consistently points toward ordinary chondrite like composition. While the inter-elemental HSE ratios in the studied samples show either elevated abundance of Pd and

Pt (Y-981031) or that of only Pd (Y-983885). These ratios do not fall in any of the previously reported impactor compositional fields. Furthermore, no significant fractionation in Ru/Ir was observed as seen previously in case of lunar anorthositic regolith breccia MIL 090034 and MIL 090075.

To understand the origin of the HSE in the regolith breccia meteorites, it is important to understand their lithological makeup. Bulk trace element composition of Sample Y-981031 and Y-983885 shows high REE abundances, which is most likely inherited from the endogenous processes in the Moon because chondrites and other possible impactors are not usually REE rich. A binary mixing trend between KREEP and lunar crustal lithologies implies that most of the studied samples lies between 1-10% KREEP mixing trend to generate their La/Yb (**Figure 5.13**). Number of evidences from previous studies indicate that the impact melt rocks may record more than one impact events.

5.5.4.1 HSE inter-elemental ratios: retained late accreted material vs fractional crystallization and metal segregation in impact melt

It has been observed that some HSE may fractionate during impact and post-impact processes leading to loss of impactor information (Day et al., 2016; Gleißner and Becker, 2017; McIntosh et al., 2020). All the three meteorites are distinct in their major, and trace element chemistry and contains both sulfides and metals as minor accessory phases. In-situ LA-ICPMS analysis of the HSE bearing phases such as metals, sulfides and schreibersite have indicated that the fractionation of the HSE can occur even at small scales and masses (Gleißner and Becker, 2017; McIntosh et al., 2020; Day and Paquet, 2021). Although impact related rocks and breccias are dominantly composed of the HSE derived from the impactors, some siderophile elements like S, P, Fe, and Ni can have combination of endogenous (lunar) and exogeneous (meteoritic) origin. Earlier studies suggested that almost half the S and greater than 90% of P in the Apollo 16 impact melts rocks with ~1% CI chondritic composition have signatures of endogenous origin (Gleißner and Becker, 2017). The partitioning behavior of the HSE is influenced by the solid metal - liquid metal

partitioning and can change dramatically in the presence of light elements such as S and P. The presence of P and S also affects the HSE partitioning by lowering HSE melting temperatures to the point where even some refractory silicates may survive. The partitioning experiments however found S has a larger effect in the HSE partitioning in solid metal - liquid metal when compared to P (Corrigan et al., 2009). This may cause the elevated Pd, Pt and Ru in some impact melts rock and regolith breccias.

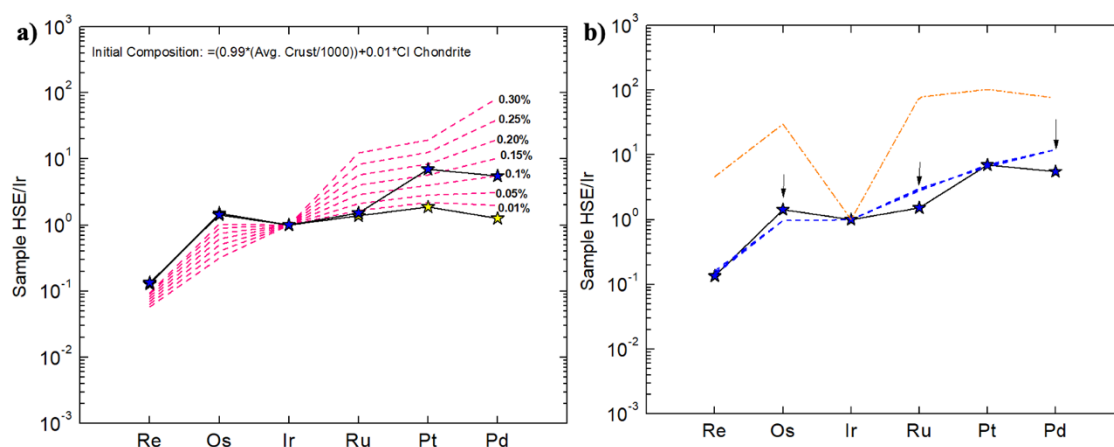


Figure 5.14 Modelled HSE/Ir ratios within an impact melt pool. a) Fe-Ni-S system. b) solid sulfide-liquid silicate. The composition of melt pool is taken as $0.99 \times \text{Average Crust} + 0.01 \times \text{CI Chondrite}$ abundance. The both models failed to match the composition of Y-981031 however, model (a) matches well with the composition of Y-86032. Partition coefficient is taken from Chabot et al., (2015) for solid metal-liquid metal and from Righter et al., (2005) and Mungall and Brenan, (2014) for solid sulfide and liquid silicate.

In order to further investigate whether the observed composition of the HSE in the studied rocks are directly representative of the melt they crystallized from or if large scale crystal fractionation and metal segregation have affected them, the HSE partitioning in solid metal and liquid metal during immiscible Fe-Ni-P-S liquid crystallization (**Figure 5.14**) was modelled. Using partition coefficient of solid metal - liquid metal in Fe-Ni-P-S system from Chabot et al. (2015), evolution of the HSE/Ir ratios was modelled instead of its concentration as the absolute HSE abundance in the liquid metal varies as a function of impactor materials in the impactites and metal content, and therefore not diagnostic of specific impactor compositions. A combination of possible host lithologies (pre-impact pristine lunar crust compositions) and impactors (chondrites and iron meteorites) were utilized to explain the observed HSE fractionation

in Y-981031 and Y-983885. The fractionation of HSE is dependent on (i) the partition coefficient of the HSE, (ii) initial composition of the impact melts, and (iii) increasing fractionation of sulfides and metals. Assuming the contribution of impactors such as chondrites (carbonaceous, ordinary and enstatite) and iron meteorites, the modelled HSE inter-elemental ratio do not fit with the observed inter-elemental ratios in the studied samples. This is mostly because the impactor with the high HSE content and almost no HSE fractionation dilutes the fractionated HSE signature of the lunar crust. Also, it was observed in the model that while segregating sulfides from the impact melts, even if Pd/Ir reaches the desired high values, collaterally other HSE ratios such

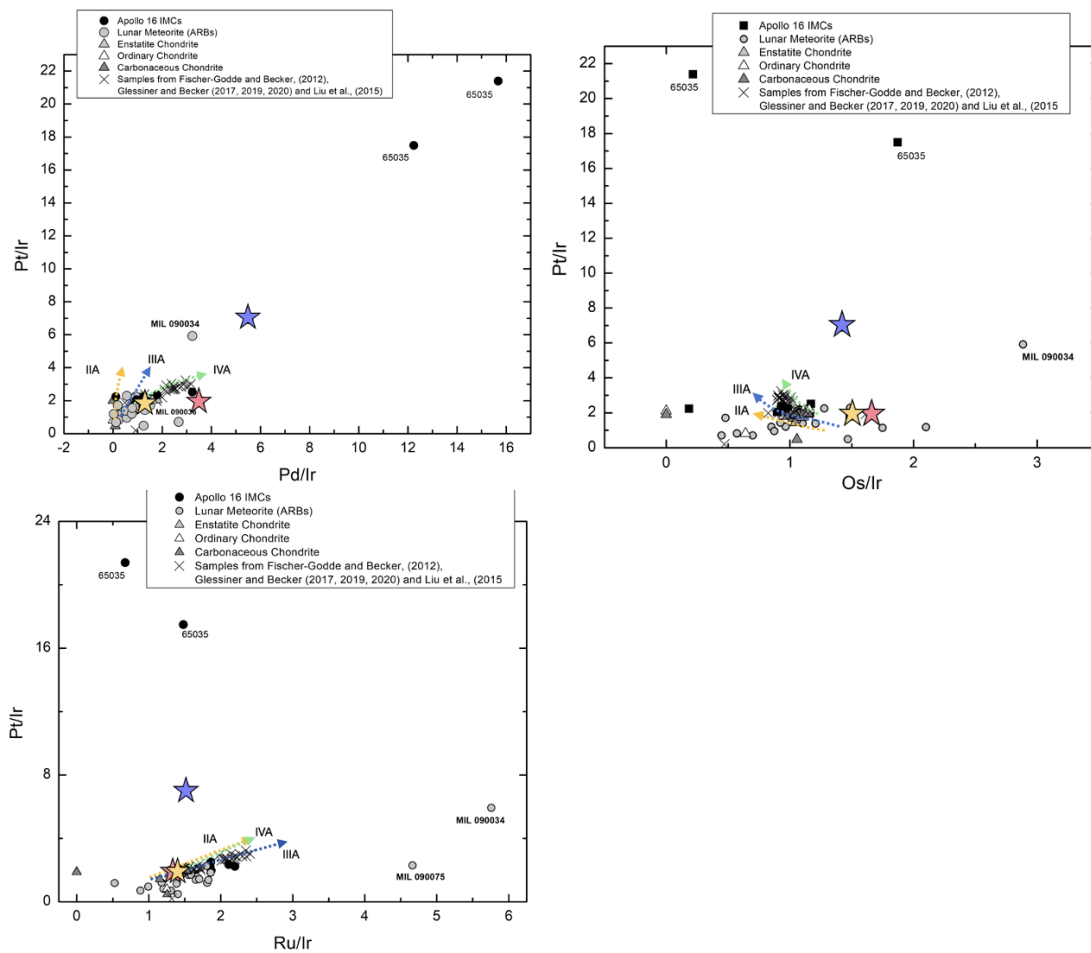


Figure 5.15 Bulk HSE/Ir ratios of the studied samples and other lunar impact rocks. Lunar HSE data taken from Puchtel et al. (2008), Fischer-Gödde and Becker (2012), Sharp et al. (2014), Liu et al. (2015), Gleißner and Becker, 2017, 2019, 2020), McIntosh et al., (2020) and this study. The fractionation trends of magmatic iron meteorite groups (Pernicka and Wasson, 1987; Hoashi et al., 1993; Smolir et al., 1996; Cook et al., 2004; Petaev and Jacobsen, 2004; McCoy et al., 2011) are also plotted for comparison.

as Ru/Ir also started to increase, which is not observed in case of sample Y-983885 and Y-981031 (**Figure 5.14**). The observed high Pd/Ir and Pt/Ir, therefore, cannot be imparted by the chondritic impact melts and subsequent sulfide segregation.

Additionally, none of the samples from asteroid bodies have been observed with such high Pd/Ir or Pt/Ir abundances (Day et al., 2016). Fischer-Gödde and Becker (2012) also observed much higher HSE ratios in Apollo melt breccias than the known chondrites. They suggested possible incorporation of two major HSE rich materials, first a pre-existing impact contaminated granulites and another a component resembling chemically evolved group of IVA iron meteorites. The plot of measured inter-elemental ratios in studied samples do not fall along the magmatic differentiation trend of IIA, IIIA and IVA iron meteorites suggesting that the sample Y-981031 and Y-983885 HSE/Ir ratios does not relate to any of the known impactor composition (**Figure 5.15**).

5.5.4.2 Whether Pd and Pt enrichment is inherited from lunar crustal component? Potential terrestrial analogy

The fractionation of Pd and Pt is not surprisingly new in the terrestrial HSE datasets and pristine lunar rocks. Terrestrial rocks such as komatiites (Pd/Ir \approx 30), pyroxenites (Pd/Ir \approx 120), ocean floor basalts (Pd/Ir \approx 100), continental tholeiites (Pd/Ir \approx 100) record large HSE fractionations. Similar high Pd/Ir fractionation is observed in case of layered intrusion complexes such as Bushveld and Stillwater. Furthermore, even the low Mg mare basalts sampled by lunar meteorites (e.g. A-881757) show Pd and Pt fractionation. Day et al. (2016) highlighted this idea by plotting a mixing trend between lunar crustal compositions of FAN and magnesian suite rocks and CI chondrite compositions that the observed high HSE/Ir ratio might be inherited from lunar crustal components. Given very low abundance of the HSE in the lunar crustal materials compared to the impactor an unusual process is required to concentrate the HSE in the Fe-Ni metal and sulfides to enhance the signature of lunar crustal components in the impact melt rocks. In terrestrial settings, theoretically, such high enrichment is possible by formation of metal-sulfide assemblages in some impact melt rocks with “R-factor” type processes operating to cause significant enrichment from otherwise low HSE abundance sources (Campbell and Naldrett, 1979).

The R-factor type enrichment scenario can be modelled using equation:

$$HSE_{sulfide\ melt} = \frac{HSE_{silicate\ melt} \times D_{silicate}^{Sulfide} \times (R+1)}{R + D_{silicate}^{Sulfide}} \quad (5.1)$$

, where R is the ratio of silicate to sulfide liquid and $D_{silicate}^{Sulfide}$ is the partition coefficient of sulfide and silicate melt (taken from Mungall and Brenan, 2014).

The HSE partitioning in solid metal and liquid metal during immiscible Fe-Ni-S liquid crystallization was further demonstrated (**Figure 5.16**). Using an initial composition of $0.01 \times CI + 0.99 \times R$ -factor-enriched lunar crustal composition (within

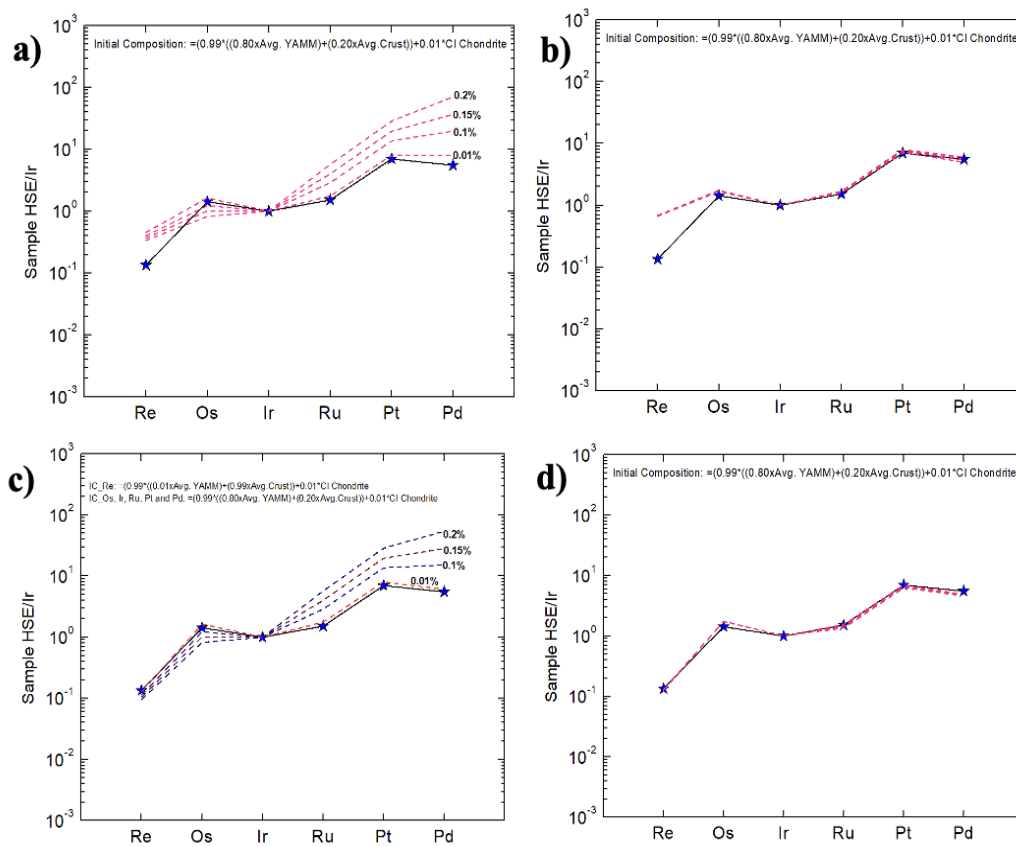


Figure 5.16 Modelled HSE/Ir ratios for solid metal-liquid metal fractionation within an impact melt pool. (a) and (c) Fe-Ni-S system; (b) and (d) Fe-Ni light element free system. The initial composition of the impact melt pool in (a) and (b) is taken as $0.99 \times ((0.80 \times \text{Avg. YAMM}) + (0.20 \times \text{Avg. Lunar Crust})) + 0.01 \times CI$ Chondrite while Re composition in model (c) and (d) is changed to $0.99 \times ((0.01 \times \text{Avg. YAMM}) + (0.99 \times \text{Avg. Lunar Crust})) + 0.01 \times CI$ Chondrite. The crustal composition has been assumed to have undergone enrichment from ‘R-factor’ type process ($R \sim 100$ - 1000 :1). The modelled composition in (a) and (b) well matches with the observed fractionated HSE (except Re) composition of Y-981031. Lowering the Re abundance leading to perfect matching of the observed HSE/Ir ratios in Y-981031. The average lunar crust composition is taken from Day et al., (2010). Partition coefficients are taken from Chabot et al., (2015).

the range of Day et al., 2010) and partition coefficient of solid metal-liquid metal in Fe-Ni-P-S system from Chabot et al. (2015), evolution of the HSE/Ir ratios was modelled. This model successfully mimics the Pd/Ir and Pt/Ir observed in studied samples with R factor between 1000-100. It is also noted that the further sulfur scavenging from this melt can increase the HSE fractionation to very high values. The R-factor enrichment although proposed as a theoretical process is shown to be evident in Ni-sulfide ore deposits (e.g. Sudbury complex; Naldrett et al., 1979; Naldrett and Duke, 1980). The formation of ore deposits as understood from the terrestrial settings requires a perturbation of normal cycle of magma generation (either via partial melting or fractional crystallization), magma transport, magma-rock interaction and crystallization (Arndt et al., 2005). The studies on the Ni-Cu-PGE deposits of the Earth have highlighted the fact that the potential for a magma to form these deposits have little to do with its content of Ni, Cu and PGE, and more on the magma's ability to interact with the crustal wall rocks (Barnes et al., 1985; Arndt et al., 2005). In order to form an economic deposit however, the mantle-derived magma must be capable of being driven to sulfide saturation. The sulfur saturation in a system is governed by its pressure, temperature, bulk composition, fO_2 and fS_2 (Ripley and Li, 2013; Barnes and Ripley, 2016). As S solubility decreases with increased pressure (Mavrogenes and O'Neil 1999), the requirement of S required to bring about saturation rises. Therefore, for saturation to occur either the temperature of the magma must drop and/or the composition of the magma must change. As seen in several terrestrial PGE deposits, most likely, saturation can be attained by the interaction of S-undersaturated magma with S-rich crustal wall rock (Naldrett, 1999; Ripley and Li, 2013; Barnes and Ripley, 2016).

Lunar magmas are sufficiently undersaturated with sulfur (Day et al., 2018; Steenstra et al., 2018) and therefore, they must be driven to sulfide saturation by crustal contamination from the most S-bearing lithologies (0.1-0.2 wt.%; Steenstra et al., 2020) on the Moon i.e. Mare basalts. Among lunar rocks, mare basalts have the most S concentration and within mare basalts with high-Ti basalts richer in S than low-Ti basalts (Steenstra et al., 2017, 2018). In conclusion, the breccias with large mare basalts (basaltic breccias) lithologies are more prone to undergo sulfide saturation than the anorthosite bearing breccias. Among the mare basalts, low MgO and low-TiO₂ mare

basalts appears to have most fractionated abundance of HSE (Day et al., 2007; Day and Walker, 2015) and are capable of imparting the fractionated pattern to their brecciated counterparts. Samples Y 981031 and Y 983885 have high mare basalt contents and are low in Ti. This makes this sample more likely to undergo sulfide saturation and R-factor process enrichment. The fractionated nature of Pd/Ir and Pt/Ir are therefore, indigenous to Moon. During the time when impactor strikes the surface of a body it is understood that ~99% of the body essentially evaporates, such high energy environment creates a local and possibly short lived, impact melt pool which possibly facilitates mineralization and fractional crystallization. The scenario mentioned above suggest that the lunar meteorites Y 981031 and Y 983885 particularly record the HSE fractionation during formation or melt-evolution within large impact melt sheets. Modelling the physicality of such process on the Moon is out of the scope of this paper. Most importantly the modelling results presented here highlights that lunar impact melt rocks may not always preserve impactor compositions with fidelity. A caution is required when using HSE/Ir ratio to predict the composition of impactor on to the Moon.

5.5.5 What we learn new about the lunar HSE inventory

Highly siderophile element abundance in the lunar mantle and crust have been studied for past several decades. The advent of isotope dilution techniques allows high precision measurements of the HSE and Os isotopic composition (Day et al., 2007; Puchtel et al., 2008; Day and Walker, 2015; Day et al., 2016). The compositional constraints on the lunar mantle and crustal abundance has been made using the pristine samples from Apollo sample suites and lunar meteorites (Day et al., 2007, 2010; Day and Walker, 2015; Day and Paquet, 2021). The lunar mantle is suggested to have ~40 times lower HSE abundance than terrestrial (Day et al., 2007; Day and Paquet, 2021). However, still this abundance is higher than the experimental predictions (Mann et al., 2012). Late accretion - continued accretion after the cessation of core segregation (Chou, 1978) - have been invoked to explain the high and flat HSE abundances observed in the Moon as well as in other planetary mantles (Day et al., 2012).

The study of the A-881757 highly siderophile element abundance shed a new and important insight to the HSE abundance of the global Moon. These meteorites are obtained from lunar mantle distinct to Apollo mare basalts and therefore provide vital constraints on the lunar mantle HSE composition. The measured compositions of HSE in A-881757 and its other paired YAMM basalts are in the range of the HSE abundance reported previously for Apollo mare basalts. Also, the measured bulk HSE abundance of A-881757 suggest that the present predicted values of BSM from this study lies well within the values estimated by previous studies (Day et al., 2007; Day and Walker, 2015).

Lunar regolith breccia meteorites Y-981031, Y-983885 and Y-86032 additionally, help us in examining the spatial variability of impactors striking the Moon. The HSE composition of the impact melt rocks have been shown to preserve the chondritic and iron meteorite like signatures (Higuchi and Morgan, 1975; Hertogen et al., 1977; Norman et al., 2002; Puchtel et al., 2008; Fischer-Gödde and Becker, 2012; Sharp et al., 2014; Liu et al., 2015; Gleißner and Becker, 2017, 2019; McIntosh et al., 2020). The observed HSE composition of Y-86032 with flat HSE pattern and chondritic Os isotopic composition is similar to previously analyzed anorthositic regolith breccias MIL 090036 and MIL 090075. The inter-elemental HSE ratio constrain the impactor composition to be ordinary chondrite type. The oldest reported age of the sample Y-86032 is ~4.4 Ga with the farside highland origin. Therefore, measurement on the Y-86032 constrain the HSE composition of oldest far-side lunar crust to have ordinary chondrite type composition. This is in agreement with some previous studies suggesting the impactor composition might have evolved from older ordinary chondrite type composition to later carbonaceous chondrite type (McIntosh et al., 2020). Furthermore, the studies on sample Y-981031 and Y-983885 highlight an important aspect that the impact melt rocks on the Moon may not necessarily record the impactor composition with high fidelity. Several process occurring within the impact melt sheet can overprint the impactor signature. Moreover, the high fractionated HSE/Ir ratio observed in Y-981031 and Y-983885 can be explained by R-factor process similar to what is observed in Sudbury complex in the terrestrial settings. A far-fetched implication from this study could be possible widespread presence of concentrated PGEs inventory within the lunar crust, especially regions that are close to the major lunar basins.

Table 5.1 Re-Os isotope and highly siderophile element concentration in Y-86032, Y-981031, and Y-983885. Re* is calculated based upon the Re/Os ratios required for the Os isotopic composition of the sample to evolve from the solar system initial $^{187}\text{Os}/^{188}\text{Os}$ of 0.09531 at 4.56 Ga (Shirey and Walker, 1998) to the present-day isotopic composition (using $k = 1.666 \times 10^{-11} \text{ yr}^{-1}$).

Sample	Re*	Re	Pd	Pt	Ru	Ir	Os	$^{187}\text{Re}/^{188}\text{Os}$ ($\pm 2\sigma$)	$^{187}\text{Os}/^{188}\text{Os}$ ($\pm 2\sigma$)
<i>(in ppt)</i>									
A-881757	0.45	3.99	44.2	129.9	28.8	4.57	5.46	3.52 ± 0.03	0.1247 ± 0.0003
<i>(in ppb)</i>									
Y-86032, 136	0.89	0.79	7.80	11.60	8.55	6.19	9.27	0.411 ± 0.079	0.1286 ± 7
Y-981031, 90	0.53	0.56	23.04	29.12	6.35	4.18	5.96	0.453 ± 0.059	0.1265 ± 7
Y-983885, 72	2.86	2.40	64.66	35.13	26.20	18.44	30.62	0.378 ± 0.229	0.1278 ± 6

Chapter 6

Summary and Future Work

6.1 Introduction

Our view of the Moon has undergone significant transformation and most of it has started from the Apollo Era. Sample return missions, such as Apollo, Luna, and recent mission Chang'E 5, have provided invaluable understandings of the chemical and thermal evolution of the Moon. Although these missions sampled a plethora of lithologies on the Moon, all of them were brought from regions with unusually high abundances of incompatible elements (such as K, REEs, P) within or adjacent to the Procellarum KREEP Terrane (PKT). Our knowledge about the Moon is primarily based on samples collected during these missions, so our understanding of the Moon is somewhat biased (Shearer and Borg, 2006). Therefore, returning samples from unexplored regions, such as the South Pole Aitken Terrane (SPAT) and Feldspathic Highland Terrane (FHT) of the Moon, are amongst the top priorities for future missions. In this respect, lunar meteorites, with their ever-growing number (>200 stones), allow us to study unexplored regions of the Moon. This thesis utilizes lunar meteorites to understand two important processes that have shaped the Moon throughout the geologic time, i.e., Volcanism and Meteoritic impacts.

Over the past four decades, the conceptual framework of the lunar magma ocean (LMO) model has served as the dominant paradigm for interpreting all lunar data

(Smith et al., 1970; Wood et al., 1970). Typically understood, lunar basalts are formed by partial melting of the mantle, with heating assisted by the mixing of heat-producing incompatible element-rich layers known as “KREEP” (Neal and Taylor, 1992). And it was believed that the high abundance of incompatible trace elements measured in these samples is the tell-tale of the lunar mantle overturn process where KREEP mixes into the source of mare basalts. However, an alternate hypothesis posits that some of the lunar basalts might have a KREEP-free (source) origin where ITE enrichment produced purely through simple magmatic processes such as low-degree melting followed by extensive fractional crystallization (Borg et al., 2009; Elardo et al., 2014; Tian et al., 2021).

In this thesis work, I targeted to understand the magmatic processes that carried the information about the mantle sources and the incipient secondary basaltic crust formation away from the PKT region on the Moon. At first, mineralogical and petrological study of the lunar basaltic meteorite Asuka-881757, which is free from KREEP component, along with paired samples Y-793169, MIL 05035, MET 01210 (together as YAMM) were performed. A detailed petrographic analysis of these samples was targeted. Similar to Asuka-881757, some more KREEP-free (source) basalts with crystallization ages ranging from ~4.35 Ga to ~2.9 Ga (Kalahari 009, NWA 032, Luna 24 ferrobasalts and LAP basalts) were identified. Further, a petrological modelling in all of the KREEP-free (source) basaltic samples were performed to understand their formation conditions on the Moon. Additionally, three lunar meteorites namely Yamato (Y)-981031, Y-983885 and Y-86032 were examined and detailed investigation of petrography, mineralogy and bulk chemistry of these samples was provided. Furthermore, the bulk chemistry data of the lunar meteorite and GRS data from Lunar Prospector were combined to identify potential source crater for these three regolith breccia meteorites.

Next, the external inputs into the lunar crust (\pm mantle) were examined to gauge the interaction of the airless lunar surface with the dynamic solar system environment, eventually to build-up a comprehensive geological history of the Moon. The studied meteorites A-881757, Y-981031, Y-983885 and Y-86032 have potentially been launched away from the PKT region, and therefore provide new insight into meteoroid impacts and volcanism that have shaped the previously unexplored lunar surface

(Korotev et al., 2009; Day et al., 2016). The proxy of highly siderophile elements (HSE: Re, Os, Ir, Ru, Pt and Pd) and Re-Os isotopes in these samples was utilized to understand HSE composition in the lunar crust and mantle. HSE abundance on the Moon has been closely tied with the late accretion conundrum on the Earth-Moon system (Walker, 2009; Day et al., 2016). As most of the HSE estimates on the Moon is based on the returned Apollo samples, analysis of lunar meteorites can provide a stronger constraint on the abundance of HSE in the lunar mantle and crust in a global perspective.

6.2 Understanding KREEP-free (source) volcanism on the Moon using Lunar basaltic meteorites

This work mainly focuses on understanding the petrogenesis of KREEP-free (source) lunar basalts. In this chapter, KREEP-free (source) lunar basaltic meteorite Asuka-881757 (A-881757), which is considered as launch paired with the YAMM (Yamato-793169, Asuka-881757, Miller Range 05035 and Meteorite Hills 01210) meteorite clan was investigated, to explore the early magmatic evolution of the Moon. The mineralogy and petrology of A-881757 was explored and compared it with other similar basaltic meteorites and returned lunar basalts.

Asuka-881757 is an unbrecciated and Fe-rich (Mg# 36), sample with coarse pyroxene (2-8 mm) and plagioclase (1-3 mm) as primary constituents. The coarse pyroxenes of A-881757 preserve mm-scale, near complete hour-glass sector zoning with strong Ca-Fe partitioning, similar to some Fe-rich Apollo basalts. Variation in major, minor and trace elements along the zoned sectors of pyroxene help in constraining the formation conditions. In contrast to the most Mg-rich Apollo basalts, the ferroan meteorite A-881757 contains various types of abundant symplectites (~ 8 vol %) formed by breakdown of pyroxferroite due to slow cooling, resembling a few extreme Fe-rich (Mg# ≤ 40) Apollo basalts. Petrographic observations and thermodynamic modelling of fractional crystallization reveal the following crystallization sequence: Fe-poor pyroxenes \rightarrow co-crystallized plagioclase and Fe-rich pyroxenes \rightarrow assemblage of Fe-augite, Fayalite, Fe-Ti oxides, and other late-stage phases. Combining phase stability at variable P - T with petrographic observations, a

constrain on the minimum depth of formation of A-881757 parent magma (60-100 km) was provided. KREEP-free (source) basalts (such as A-881757 and YAMM) were concluded to have undergone a polybaric crystallization with the coarsest crystals formed at a slow cooling rate within the lunar crust. Crystallization occurred prior to expulsion and eruption at the surface.

The bulk major and trace element chemistry was utilized to deduce the composition of parental melts of A-881757/YAMM basalts. Further, these analyses were extended to other similar KREEP-free (source) basalts. The trace element modelling was performed on the estimated parental melts to understand the mantle source composition of these basalts and to know the degree of partial melting required to generate these basalts. Next, to estimate the formation P - T of the KREEP-free (source) basalts, thermodynamic modelling was applied. In order to maintain the methodological consistency, selected parental melt composition in the Apollo mare basalts suites were also studied for comparison. A similar petrological modelling was performed to estimate their formation P - T of Apollo mare basalts.

The YAMM basalts and other associated KREEP-free (source) basalts are consistent with the formation condition of low degree partial melting of the LMO cumulates. Similarly, the Apollo mare basalts also underwent low degree partial melting of their respective mantle source (Hallis et al. 2014). The formation of the KREEP-free (source) mare basalts in the lunar mantle are significantly lower when compared to that obtained for the melt compositions of the Apollo mare basalts. Similarly, the estimated mantle potential temperatures for KREEP-free (source) basalts indicate that the Moon's mantle source was relatively cooler and had a lower surface heat flow compared to the mare basalts that erupted later. This suggests a fundamental change in the Moon's melting regime between approximately 3.9 and 3.3 billion years ago.

6.3 Lunar crustal diversity as observed from the lunar regolith breccia meteorites Y-981031, Y-983885 and Y-86032

This work focuses on the detailed mineralogical and petrological investigation of the brecciated lunar meteorites. In-situ major and trace element abundance of

different phases were measured in these samples. The petrographic examination of textures and their compositional help in distinguishing the lithic clasts and mineral fragments. The basaltic clast within the breccia samples were further studied in details. The bulk compositional data and the global LP-GRS data were combined to filter out the possible source locations of these meteorite samples.

The studied samples Y-981031, Y-983885 and Y-86032 show varied degree of mixing of highland and mare materials. Sample Y-983885 and Y-981031 show variety of lithic fragments such as low-Ti basalts, high-Al basalts, troctolites, granulites and KREEP basalts. Sample Y-86032 dominantly composed of impact melt and granulitic clasts. Apart from the lithic clast these samples contain numerous olivine, pyroxene, and plagioclase mineral clasts. Bulk Th and FeO concentration in the studied samples suggest their derivation from three distinct locations of the lunar surface. Petrographic observation of Y-981031 and Y-983885 indicates comparatively larger proportions of basaltic than anorthositic materials, in contrast to previous studies (Arai et al., 2002, 2005). The different textures and sizes of exsolution lamellae in pyroxenes suggests varied degree of cooling of the clasts, and crystallization in a range of environments from surface to shallow subsurface or under a thick lava flow.

The basaltic clasts in Y-981031 show compositional similarity to the YAMM basalts both in major and trace elements. It shows relatively coarse grain texture with exsolution lamellae thickness ranging up to ~500 μm suggesting very slow cooling of this basalt. Sample Y-983885 contains basalts with high KREEP contents and is overall the most KREEP rich sample among the three. Overall composition of the lithic clasts and mineral fragments presented here highlights the lithological diversity of the lunar crust. Using elemental abundance from GRS, possible source regions for these samples were highlighted on the surface of the Moon. The result presented here suggests the source region of Y-981031 was in the near side around Mare Crisium and Mare Fecunditatis, while sample Y-86032 composition is suggesting its possible source in the highlands region. There is a high possibility that the sample Y-983885 ejected from the SPA basin. However, this possibility is not exclusive as some of the regions near Apollo 17 landing site can also be the source of Y-983885.

6.4 Understanding the highly siderophile elements abundance in Lunar mantle and crust from Lunar meteorites

The final objective of the thesis deals with the unresolved problem of highly siderophile element overabundance in the lunar interior. The highly siderophile elements and Re-Os isotopes in the unbrecciated mare basalt A-881757 and lunar brecciated meteorites Y-981031, Y-983885 and Y-86032 were measured and compared with the available lunar HSE datasets. The HSE elements have higher affinity to partition in metal and sulfide phases than silicates (Day et al., 2016). Therefore, HSE abundance in bulk sample is primarily controlled by the presence and absence of these phases. Petrographic observations of all the samples were also focused on the identification of sulfides and metal.

Presence of metal in the samples could be result of two independent processes, i.e., internal processes such as fractional crystallization or external processes such as impactor contamination. Following the protocol of Day (2020), Nickel/Cobalt (Ni/Co) ratio in the metal grain of the meteorites were studied to understand their possible origin. This study also provides the HSE abundance data of the samples that are originated away from the PKT region and helps to better constrain on the processes governing the abundance of siderophile elements in the Bulk Silicate Moon (BSM). The HSE/Ir ratios were further utilized to constraint the composition of possible impactors striking the Moon.

The compositional investigation of metals in all the studied meteorites reveals both endogenous and exogenous metals in the samples. Sample A-881757 contains metal with low Ni/Co suggesting its origin from fractional crystallization. Therefore, the measured HSE content of A-881757 gives insight into the HSE abundance of KREEP-free (source) mantle. While two of the regolith breccias Y-981031 and Y-983885 show variable degrees of impactor contamination with high Ni/Co, the sample Y-86032 contains no metals and sulfides phase and is rather dominated by impact melts and granulites. Thus, Y-981031 and Y-983885 provide us some insights to the crustal abundance of HSE as a function of impactor contamination.

The study of meteorites A-881757 and MIL 05035 suggests that HSE is relatively homogeneously distributed among the KREEP-rich and KREEP-free (source) mantle of the Moon and the Re-Os isotopic system is unaffected by mantle melting and crystallization process. The HSE abundance of regolith breccias show two order higher values than that in the basaltic meteorite A-881757. The elevated abundance of HSE in the regolith breccias can be attributed to the possible impactor contamination. The nature of impactors can range from carbonaceous chondrite to iron meteorite. The HSE/Ir ratio of the lunar regolith breccia Y-86032 suggest late accretion of ordinary chondrite type impactor while the samples Y-981031 and Y-983885 records the fractional crystallization and segregation of metal within the impact melt sheets.

6.5 Potential Future Work

The thesis utilizes several methods that can be further applied in other similar lunar samples and datasets to expand our understanding of the Moon. Some of the potential work arising from this thesis are summarized below:

- *Exploring the lunar mantle and crust outside the Procellarum KREEP terrane using lunar meteorites*

This thesis presents an important example of studying lunar meteorites. In the absence of samples from the unexplored regions of the Moon, the lunar meteorites with their ever-increasing number are the keys for the global context. Future studies can target meteorites that are most likely sourced from regions away from the PKT and particularly near SPA regions, and explore their mineralogy and petrology in the context of lunar evolution. Understanding the lunar geochemistry regarding unique lithologies such as pure anorthosites, Mg-spinels, and KREEP-free (source) basalts is fundamentally tied to understand the fundamental problems associated with lunar evolution. This study will also benefit the future proposed landing missions at or near the south pole. Furthermore, the samples such as regolith breccia meteorites can also be utilized as a ground truth for future lunar missions.

- *Understanding lunar volcanism, its evolution, and the role of KREEP*

Although, the potential melting mechanisms and generation of KREEP-free (source) samples has been discussed in this thesis, the role of KREEP in the generation of mare basalt is still uncertain. The melting mechanism of the Moon needs to be assessed thoroughly based on all the possibilities. This would require a detailed investigation of all the suites of mare basalts from sample return and lunar meteorite collection for exploring different parental melts. Further, these parental melts and their modeled source regions should be studied in detail to understand the KREEP mixing and its influence in actively or passively melting these lithologies. Lastly, all this information could be tied together with their age to see any possible evolutionary pattern.

- ***Understanding the highly siderophile element fractionation in lunar settings such as impact melt pools***

It has been observed that some HSE may fractionate during impact and post-impact processes leading to loss of impactor information (Fischer-Gödde and Becker, 2012; Gleißner and Becker, 2017; McIntosh et al., 2020). The HSE fractionation observed in Y-981031 and Y-983885 are the example of the fact that the impact melt rocks do not necessarily record impactor information with fidelity. There is a need to better understand the processes that can fractionate HSE in the lunar settings like the impact melt pools.

- ***Understanding the nature and composition of impactors through time***

Highly siderophile elements are excellent tracers of the impacts on the planetary surface. By knowing the composition of these elements in lunar rocks, we can trace the possible impactor and its composition. This exercise can also be tied together with the (meteorite) samples from other terrestrial bodies such as Mars and Vesta. This way, we can understand the compositional aspects of late accreting materials as the time-integrated record.

Bibliography

- Ahrens C. (2020) Origin of the Moon, Impactor Theory. In *Encyclopedia of Lunar Science* (ed. B. Cudnik). Springer International Publishing, Cham. pp. 1–6.
- Alibert C., Norman M. D. and McCulloch M. T. (1994) An ancient Sm-Nd age for a ferroan noritic anorthosite clast from lunar breccia 67016. *Geochimica et Cosmochimica Acta* **58**, 2921–2926.
- Anand M., Taylor L. A., Neal C. R., Snyder G. A., Patchen A., Sano Y. and Terada K. (2003) Petrogenesis of lunar meteorite EET 96008. *Geochimica et Cosmochimica Acta* **67**, 3499–3518.
- Arai S., Terada K., Arai T., Hidaka H. and Sano Y. (2008) Ion microprobe U-Pb dating of the Yamato-983885 lunar meteorite. *Meteoritics and Planetary Science Supplement* **43**, 5074.
- Arai T. and Maruyama S. (2017) Formation of anorthosite on the Moon through magma ocean fractional crystallization. *Geoscience Frontiers* **8**, 299–308.
- Arai T., Hawke B. R., Giguere T. A., Misawa K., Miyamoto M. and Kojima H. (2010) Antarctic lunar meteorites Yamato-793169, Asuka-881757, MIL 05035, and MET 01210 (YAMM): Launch pairing and possible cryptomare origin. *Geochimica et Cosmochimica Acta* **74**, 2231–2248.
- Arai T., Ishi T. and Otsuki M. (2002) Mineralogical Study of a New Lunar Meteorite Yamato 981031. *Lunar and Planetary Science XXXIII*, #2064.
- Arai T., Otsuki M., Ishii T., Mikouchi T. and Miyamoto M. (2005) Mineralogy of Yamato 983885 lunar polymict breccia with a KREEP basalt a high-Al basalt, a very low-Ti basalt and Mg-rich rocks. *Antarctic Meteorite Research* **18**, 17.
- Arai T., Takeda H., Yamaguchi A. and Ohtake M. (2008) A new model of lunar crust: asymmetry in crustal composition and evolution. *Earth, Planets and Space* **60**, 433–444.
- Arai, T., Hiroshi, T. and Masamichi, M., (2006). Experimental petrology of ancient lunar mare basalt Asuka-881757: Spinel crystallization as a petrologic indicator. *Antarctic Meteorite Research*, vol. **19**, p. 1-19, 19, pp.1-19.
- Arai, T., Misawa, K., and Kojima, H. (2007). Lunar meteorite MIL 05035: mare basalt paired with Asuka-881757. In *38th Annual Lunar and Planetary Science Conference* (No. 1338, p. 1582).

- Aramovich C. J., Herd C. D. K. and Papike J. J. (2002) Symplectites derived from metastable phases in martian basaltic meteorites. *American Mineralogist* **87**, 1351–1359.
- Arndt, N. T., Leshner, C. M., and Czamanske, G. K. (2005). Mantle-derived magmas and magmatic Ni-Cu-(PGE) deposits. *100th Anniversary Volume. Soc. Econ. Geol.* 5-24.
- Asimow P. D. and Ghiorso M. S. (1998) Algorithmic modifications extending MELTS to calculate subsolidus phase relations. *American Mineralogist* **83**, 1127–1132.
- Asimow P. D. and Longhi. J. (2004) The Significance of Multiple Saturation Points in the Context of Polybaric Near-fractional Melting. *Journal of Petrology* **45**, 2349–2367.
- Asphaug E. (2014) Impact Origin of the Moon? *Annual Review of Earth and Planetary Sciences* **42**, 551–578.
- Astudillo Manosalva D. F. and Elardo S. M. (2022) The Accuracy of Perple_X, pMelts, and MAGPOX in Modelling Equilibrium Crystallization of Lunar and Martian Basalt Compositions and Their Multiple Saturation Points. In *LPI Contributions* LPI Contributions. p. 2343.
- Barnes S.-J., Naldrett A. J. and Gorton M. P. (1985) The origin of the fractionation of platinum-group elements in terrestrial magmas. *Chemical Geology* **53**, 303–323.
- Barnes, S.J. and Ripley, E.M., 2016. Highly siderophile and strongly chalcophile elements in magmatic ore deposits. *Reviews in Mineralogy and Geochemistry*, **81**(1), pp.725-774.
- Barr A. C. (2016) On the origin of Earth's Moon. *Journal of Geophysical Research: Planets* **121**, 1573–1601.
- Basu B (2019) Chandrayaan-2 India's daring moon mission. In *Science Reporter*, 14 November 2019, pp 16–19.
- Basu Sarbadhikari A., Babu E. V. S. S. K. and Vijaya Kumar T. (2017) Chemical layering in the upper mantle of Mars: Evidence from olivine-hosted melt inclusions in Tissint. *Meteoritics and Planetary Science* **52**, 251–267.
- Basu Sarbadhikari, A., Babu, E. V. S. S. K., Vijaya Kumar, T., and Chennaoui Aoudjehane, H. (2016). Martian meteorite Tissint records unique petrogenesis among the depleted shergottites. *Meteoritics and Planetary Science*, **51**(9), 1588–1610.
- Beattie P. (1993) Olivine-melt and orthopyroxene-melt equilibria. *Contributions to Mineralogy and Petrology* **115**, 103–111.
- Becker H., Horan M. F., Walker R. J., Gao S., Lorand J.-P. and Rudnick R. L. (2006) Highly siderophile element composition of the Earth's primitive upper mantle:

- Constraints from new data on peridotite massifs and xenoliths. *Geochimica et Cosmochimica Acta* **70**, 4528–4550.
- Bell P. M., Mao H. K., Roedder Ed. and Weiblen P. W. (1975) The problem of the origin of symplectites in olivine-bearing lunar rocks. In *Lunar and Planetary Science Conference Proceedings* pp. 231–248.
- Bence A. E. and Papike J. J. (1972) Pyroxenes as recorders of lunar basalt petrogenesis: Chemical trends due to crystal-liquid interaction. *Lunar and Planetary Science Conference Proceedings* **3**, 431.
- Beynon, J.H. and Brenton, A.G. (1982) *An Introduction to Mass Spectrometry*, University of Wales Press, Cardiff.
- Birck J. L., Barman M. R. and Capmas F. (1997) Re-Os Isotopic Measurements at the Femtomole Level in Natural Samples. *Geostandards Newsletter* **21**, 19–27.
- Bischoff A. and Stöffler D. (1984) Chemical and structural changes induced by thermal annealing of shocked feldspar inclusions in impact melt rocks from Lappajärvi crater, Finland. *Journal of Geophysical Research: Solid Earth* **89**, B645–B656.
- Borg L. E. and Carlson R. W. (2023) The Evolving Chronology of Moon Formation. *Annual Review of Earth and Planetary Sciences* **51**, 25–52.
- Borg L. E., Connelly J. N., Boyet M. and Carlson R. W. (2011) Chronological evidence that the Moon is either young or did not have a global magma ocean. *Nature* **477**, 70–73.
- Borg L. E., Gaffney A. M. and Shearer C. K. (2015) A review of lunar chronology revealing a preponderance of 4.34–4.37 Ga ages. *Meteoritics and Planetary Science* **50**, 715–732.
- Borg L. E., Gaffney A. M., Shearer C. K., DePaolo D. J., Hutcheon I. D., Owens T. L., Ramon E. and Brennecka G. (2009) Mechanisms for incompatible-element enrichment on the Moon deduced from the lunar basaltic meteorite Northwest Africa 032. *Geochimica et Cosmochimica Acta* **73**, 3963–3980.
- Borg L., Norman M., Nyquist L., Bogard D., Snyder G., Taylor L. and Lindstrom M. (1999) Isotopic studies of ferroan anorthosite 62236: a young lunar crustal rock from a light rare-earth-element-depleted source. *Geochimica et Cosmochimica Acta* **63**, 2679–2691.
- Bottke W. F. and Norman M. D. (2017) The Late Heavy Bombardment. *Annual Review of Earth and Planetary Sciences* **45**, 619–647.
- Boyd F. R. and Smith D. (1971) Compositional zoning in pyroxenes from lunar rock 12021, oceanus procellarum. *Journal of Petrology* **12**, 439–464.
- Boyd, F. R., and Brown, G. M. (1969). Electron-probe study of pyroxene exsolution. *Mineralogical Society of America Special Paper*, **2**, 211-216.

- Boyett M., Carlson R. W., Borg L. E. and Horan M. (2015) Sm–Nd systematics of lunar ferroan anorthositic suite rocks: constraints on lunar crust formation. *Geochimica et Cosmochimica Acta* **148**, 203–218.
- Brenan J. M., Mungall J. E. and Bennett N. R. (2019) Abundance of highly siderophile elements in lunar basalts controlled by iron sulfide melt. *Nature Geoscience* **12**, 701–706.
- Burns R. G., Abu-Eid R. M. and Huggins F. E. (1972) Crystal field spectra of lunar pyroxenes. In *Lunar and Planetary Science Conference Proceedings*. p. 533.
- Calzada-Diaz A., Joy K. H., Crawford I. A. and Nordheim T. A. (2015) Constraining the source regions of lunar meteorites using orbital geochemical data. *Meteoritics and Planetary Science* **50**, 214–228.
- Cameron A. G. and Ward W. R. (1976) The origin of the Moon. In *Abstracts of the Lunar and Planetary Science Conference, volume 7, page 120, (1976)*
- Campbell I. H. and Naldrett A. J. (1979) The influence of silicate:sulfide ratios on the geochemistry of magmatic sulfides. *Economic Geology* **74**, 1503–1506.
- Canup R. M. (2004) Origin of terrestrial planets and the Earth–Moon system. *Physics Today* **57**, 56–62.
- Canup R. M. (2012) Forming a Moon with an Earth-like composition via a giant impact. *Science* **338**, 1052–1055.
- Canup R. M. and Asphaug E. (2001) Origin of the Moon in a giant impact near the end of the Earth’s formation. *Nature* **412**, 708–712.
- Carlson R. W. and Lugmair G. W. (1981) Sm–Nd age of lherzolite 67667: implications for the processes involved in lunar crustal formation. *Earth and Planetary Science Letters* **56**, 1–8.
- Carlson R. W., Borg L. E., Gaffney A. M. and Boyett M. (2014) Rb–Sr, Sm–Nd and Lu–Hf isotope systematics of the lunar Mg-suite: the age of the lunar crust and its relation to the time of Moon formation. *Philosophical Transactions of the Royal Society A: Mathematical, Physical and Engineering Sciences* **372**, 20130246.
- Chabot, N.L., Wollack, E.A., Humayun, M. and Shank, E.M. (2015). The effect of oxygen as a light element in metallic liquids on partitioning behavior. *Meteoritics and Planetary Science*, **50**(4), pp.530-546.
- Charlier B., Grove T. L., Namur O. and Holtz F. (2018) Crystallization of the lunar magma ocean and the primordial mantle-crust differentiation of the Moon. *Geochimica et Cosmochimica Acta* **234**, 50–69.
- Chou C.-L. (1978) Fractionation of Siderophile Elements in the Earth’s Upper Mantle. *Lunar and Planetary Science Conference Proceedings* **1**, 219–230.

- Chou C.-L., Boynton W. V., Sundberg L. L. and Wasson J. T. (1975) Volatiles on the surface of Apollo 15 green glass and trace-element distributions among Apollo 15 soils. *Lunar and Planetary Science Conference Proceedings* **2**, 1701–1727.
- Cohen A. S. and Waters F. G. (1996) Separation of osmium from geological materials by solvent extraction for analysis by thermal ionisation mass spectrometry. *Analytica Chimica Acta* **332**, 269–275.
- Coish R. A. and Taylor L. A. (1978) Mineralogy and petrology of basaltic fragments from the Luna 24 drill core. In *Mare Crisium: The view from Luna 24* (eds. R. B. Merrill and J. J. Papike). pp. 403–417.
- Collareta A., D’Orazio M., Gemelli M., Pack A., and Folco L. (2016). High crustal diversity preserved in the lunar meteorite Mount Dewitt 12007 (Victoria Land, Antarctica). *Meteoritics and Planetary Science* **51**:351–371.
- Cone, K. A., Palin, R. M., and Singha, K. (2020). Unsupervised machine learning with petrological database ApolloBasaltDB reveals complexity in lunar basalt major element oxide and mineral distribution patterns. *Icarus*, **346**, 113787.
- Cook, D.L., Walker, R.J., Horan, M.F., Wasson, J.T. and Morgan, J.W., 2004. Pt-Re-Os systematics of group IIAB and IIIAB iron meteorites. *Geochimica et Cosmochimica Acta*, **68**(6), pp.1413-1431.
- Corrigan C. M., Chabot N. L., McCoy T. J., McDonough W. F., Watson H. C., Saslow S. A. and Ash R. D. (2009) The iron–nickel–phosphorus system: Effects on the distribution of trace elements during the evolution of iron meteorites. *Geochimica et Cosmochimica Acta* **73**, 2674–2691.
- Crawford I. A. and Joy K. H. (2014) Lunar exploration: Opening a window into the history and evolution of the inner Solar System. *Philosophical Transactions of the Royal Society A: Mathematical, Physical and Engineering Sciences* **372**.
- Ćuk M. and Stewart S. T. (2012) Making the Moon from a fast-spinning Earth: a giant impact followed by resonant despinning. *Science* **338**, 1047–1052.
- Curran N. M., Joy K. H., Snape J. F., Pernet-Fisher J. F., Gilmour J. D., Nemchin A. A., Whitehouse M. J. and Burgess R. (2019) The early geological history of the Moon inferred from ancient lunar meteorite Miller Range 13317. *Meteoritics and Planetary Science* **54**, 1401–1430.
- Dasch E. J., Shih C.-Y., Bansal B. M., Wiesmann H. and Nyquist L. E. (1987) Isotopic analysis of basaltic fragments from lunar breccia 14321: Chronology and petrogenesis of pre-Imbrium mare volcanism. *Geochimica et Cosmochimica Acta* **51**, 3241–3254.
- Day J. M. D. (2018) Geochemical constraints on residual metal and sulfide in the sources of lunar mare basalts. *American Mineralogist* **103**, 1734–1740.
- Day J. M. D. and Walker R. J. (2015) Highly siderophile element depletion in the Moon. *Earth and Planetary Science Letters* **423**, 114–124.

- Day J. M. D., Brandon A. D. and Walker R. J. (2016) Highly Siderophile Elements in Earth, Mars, the Moon, and Asteroids. *Highly Siderophile and Strongly Chalcophile Elements in High-Temperature Geochemistry and Cosmochemistry* **81**, 161–238.
- Day J. M. D., Floss C., Taylor L. A., Anand M. and Patchen A. D. (2006a) Evolved mare basalt magmatism, high Mg/Fe feldspathic crust, chondritic impactors, and the petrogenesis of Antarctic lunar breccia meteorites Meteorite Hills 01210 and Pecora Escarpment 02007. *Geochimica et Cosmochimica Acta* **70**, 5957–5989.
- Day J. M. D., Pearson D. G. and Taylor L. A. (2007) Highly Siderophile Element Constraints on Accretion and Differentiation of the Earth-Moon System. *Science* **315**, 217–219.
- Day J. M. D., Taylor L. A., Floss C., Patchen A. D., Schnare D. W. and Pearson D. G. (2006b) Comparative petrology, geochemistry, and petrogenesis of evolved, low-Ti lunar mare basalt meteorites from the LaPaz Icefield, Antarctica. *Geochimica et Cosmochimica Acta* **70**, 1581–1600.
- Day J. M. D., Walker R. J., James O. B. and Puchtel I. S. (2010) Osmium isotope and highly siderophile element systematics of the lunar crust. *Earth and Planetary Science Letters* **289**, 595–605.
- Day J. M. D., Walker R. J., Qin L. and Rumble III D. (2012) Late accretion as a natural consequence of planetary growth. *Nature Geoscience* **5**, 614–617.
- Day J. M. D., Waters C. L., Schaefer B. F., Walker R. J. and Turner S. (2016) Use of Hydrofluoric Acid Desilicification in the Determination of Highly Siderophile Element Abundances and Re-Pt-Os Isotope Systematics in Mafic-Ultramafic Rocks. *Geostandards and Geoanalytical Research* **40**, 49–65.
- Day, J. M. D. (2020). Metal grains in lunar rocks as indicators of igneous and impact processes. *Meteoritics and Planetary Science*, **55**(8), pp.1793-1807.
- Day, J. M. D., and Taylor, L. A. (2007). On the structure of mare basalt lava flows from textural analysis of the LaPaz Icefield and Northwest Africa 032 lunar meteorites. *Meteoritics and Planetary Science*, **42**(1), 3-17.
- Day, J.M.D. and Paquet, M. (2021). Temporally limited late accretion after core formation in the Moon. *Meteoritics and Planetary Science*, **56**(4), 683-699.
- Delano J. W. (1980) Apollo 15 Yellow Glasses: Chemistry and Possible Origins. In *Lunar and Planetary Science Conference Lunar and Planetary Science Conference*. pp. 213–215.
- Delano J. W. (1986). Pristine lunar glasses: Criteria, data, and implications. *Journal of Geophysical Research: Solid Earth* **91**:201–213.
- Dickinson T., Taylor G. J., Keil K., Schmitt R. A., Hughes S. S. and Smith M. R. (1985) Apollo 14 aluminous mare basalts and their possible relationship to KREEP. *Journal of Geophysical Research: Solid Earth* **90**, C365–C374.

- Dygert N., Liang Y., Sun C. and Hess P. (2014) An experimental study of trace element partitioning between augite and Fe-rich basalts. *Geochimica et Cosmochimica Acta* **132**, 170–186.
- Ebihara M., Wolf R., Warren P. H. and Anders E. (1992) Trace elements in 59 mostly highland moon rocks. In *Lunar and Planetary Science Conference Proceedings* pp. 417–426.
- Elardo S. (2016) Lunar Magma Ocean Theory, Origins, and Rationale. In *Encyclopedia of Lunar Science* (ed. B. Cudnik). Springer International Publishing, Cham. pp. 1–8.
- Elardo S. M. and Astudillo Manoslava D. F. (2021) Ancient Igneous Differentiation Trends in the Moon's Crust Can Be Produced by Secondary Magmatism from a Common Source. In *52nd Lunar and Planetary Science Conference* p. 2313.
- Elardo S. M., Draper D. S. and Shearer C. K. (2011) Lunar Magma Ocean crystallization revisited: Bulk composition, early cumulate mineralogy, and the source regions of the highlands Mg-suite. *Geochimica et Cosmochimica Acta* **75**, 3024–3045.
- Elardo S. M., Shearer C. K., Fagan A. L., Borg L. E., Gaffney A. M., Burger P. V., Neal C. R., Fernandes V. A. and McCubbin F. M. (2014) The origin of young mare basalts inferred from lunar meteorites Northwest Africa 4734, 032, and LaPaz Icefield 02205. *Meteoritics and Planetary Science* **49**, 261–291.
- Elardo S. M., Shearer C. K., Kaaden K. E. V., McCubbin F. M. and Bell A. S. (2015) Petrogenesis of primitive and evolved basalts in a cooling Moon: Experimental constraints from the youngest known lunar magmas. *Earth and Planetary Science Letters* **422**, 126–137.
- Elkins-Tanton L. T., Burgess S. and Yin Q.-Z. (2011) The lunar magma ocean: Reconciling the solidification process with lunar petrology and geochronology. *Earth and Planetary Science Letters* **304**, 326–336.
- Elkins-Tanton L. T., Hager B. H. and Grove T. L. (2004) Magmatic effects of the lunar late heavy bombardment. *Earth and Planetary Science Letters* **222**, 17–27.
- Elkins-Tanton L. T., Van Orman J. A., Hager B. H. and Grove T. L. (2002) Re-examination of the lunar magma ocean cumulate overturn hypothesis: melting or mixing is required. *Earth and Planetary Science Letters* **196**, 239–249.
- Eugster O. (1989) History of meteorites from the Moon collected in Antarctica. *Science* **245**, 1197–1202.
- Eugster O. and Niedermann S. (1988) Noble gases in lunar meteorites Yamato-82192 and-82193 and history of the meteorites from the moon. *Earth and Planetary Science Letters* **89**, 15–27.

- Evans B. W. and Moore J. G. (1968) Mineralogy as a function of depth in the prehistoric Makaopuhi tholeiitic lava lake, Hawaii. *Contributions to Mineralogy and Petrology* **17**, 85–115.
- Fagan T. J., Kashima D., Wakabayashi Y. and Suginothara A. (2014) Case study of magmatic differentiation trends on the Moon based on lunar meteorite Northwest Africa 773 and comparison with Apollo 15 quartz monzodiorite. *Geochimica et Cosmochimica Acta* **133**, 97–127.
- Fagan T. J., Taylor G. J., Keil K., Bunch T. E., Wittke J. H., Korotev R. L., Jolliff B. L., Gillis J. J., Haskin L. A., Jarosewich E., Clayton R. N., Mayeda T. K., Fernandes V. A., Burgess R., Turner G., Eugster O. and Lorenzetti S. (2002) Northwest Africa 032: Product of lunar volcanism. *Meteoritics and Planetary Science* **37**, 371–394.
- Filiberto J. and Dasgupta R. (2011) Fe²⁺-Mg partitioning between olivine and basaltic melts: Applications to genesis of olivine-phyrlic shergottites and conditions of melting in the Martian interior. *Earth and Planetary Science Letters* **304**, 527–537.
- Filiberto J. and Dasgupta R. (2015) Constraints on the depth and thermal vigor of melting in the Martian mantle. *Journal of Geophysical Research (Planets)* **175**, 238.
- Fischer-Gödde M. and Becker H. (2012) Osmium isotope and highly siderophile element constraints on ages and nature of meteoritic components in ancient lunar impact rocks. *Geochimica et Cosmochimica Acta* **77**, 135–156.
- Floss, C., and Crozaz, G. (1991). Ce anomalies in the LEW85300 eucrite: evidence for REE mobilization during Antarctic weathering. *Earth and Planetary Science Letters*, *107*(1), 13-24.
- Fritz J., Greshake A. and Fernandes V. A. (2017) Revising the shock classification of meteorites. *Meteoritics and Planetary Science* **52**, 1216–1232.
- Gaetani G. A. and Grove T. L. (1995) Partitioning of rare earth elements between clinopyroxene and silicate melt Crystal-chemical controls. *Geochimica et Cosmochimica Acta* **59**, 1951–1962.
- Ghiorso M. S. and Sack R. O. (1995) Chemical mass transfer in magmatic processes IV. A revised and internally consistent thermodynamic model for the interpolation and extrapolation of liquid-solid equilibria in magmatic systems at elevated temperatures and pressures. *Contr. Mineral. and Petrol.* **119**, 197–212.
- Ghiorso M. S., Hirschmann M. M., Reiners P. W. and Kress V. C. (2002) The pMELTS: A revision of MELTS for improved calculation of phase relations and major element partitioning related to partial melting of the mantle to 3 GPa. *Geochemistry, Geophysics, Geosystems* **3**, 1030.
- Giguere, T.A., Hawke, B.R., Blewett, D.T., Bussey, D.B.J., Lucey, P.G., Smith, G.A., Spudis, P.D. and Taylor, G.J. (2003). Remote sensing studies of the Lomonosov-Fleming region of the Moon. *Journal of Geophysical Research: Planets*, **108**(E11).

- Gleißner P. and Becker H. (2017) Formation of Apollo 16 impactites and the composition of late accreted material: Constraints from Os isotopes, highly siderophile elements and sulfur abundances. *Geochimica et Cosmochimica Acta* **200**, 1–24.
- Gleißner P. and Becker H. (2019) Origin of lunar fragmental matrix breccias—Highly siderophile element constraints. *Meteorit Planet Sci* **54**, 2006–2026.
- Gleißner P., & Becker H. (2020). New constraints on the formation of lunar mafic impact melt breccias from S-Se-Te and highly siderophile elements. *Meteoritics & Planetary Science*, **55**, 2044-2065.
- Green D., Ringwood A., Ware N., Hibberson W., Major A. and Kiss E. (1971) Experimental petrology and petrogenesis of Apollo 12 basalts. In Lunar and Planetary Science Conference Proceedings. p. 601.
- Griffiths A. A., Barnes J. J., Tartèse R., Potts N. J. and Anand M. (2014) Characterization of Mesostasis Areas in Mare Basalts: Petrography and Mineral Chemistry. In 45th Lunar and Planetary Science Conference Proceedings. 1905.
- Gross J. and Treiman A. H. (2011) Unique spinel-rich lithology in lunar meteorite ALHA 81005: Origin and possible connection to M3 observations of the farside highlands. *Journal of Geophysical Research: Planets* **116**.
- Gross, J., and Joy, K. H. (2016). Evolution, lunar: from magma ocean to crust formation. *Encyclopedia of lunar science*, 1-20.
- Gross, J., Treiman, A.H. and Mercer, C.N., (2014). Lunar feldspathic meteorites: Constraints on the geology of the lunar highlands, and the origin of the lunar crust. *Earth and Planetary Science Letters*, **388**, pp.318-328.
- Grove T. L. (1978) Cooling histories of Luna 24 low-Ti ferrobasalts and ferrogabbros. In *Lunar and Planetary Science Conference* pp. 424–426.
- Grove T. L. and Krawczynski M. J. (2009) Lunar Mare Volcanism: Where Did the Magmas Come From? *Elements* **5**, 29–34.
- Grove T. L. and Vaniman D. T. (1978) Experimental petrology of very low Ti (VLT) basalts. In *Mare Crisium: The view from Luna 24* (eds. R. B. Merrill and J. J. Papike). pp. 445–471.
- Grove T. L. and Walker D. (1977) Cooling histories of Apollo 15 quartz-normative basalts. In *Lunar and Planetary Science Conference Proceedings* pp. 1501–1520.
- Grove T.L. and Vaniman D. T. (1977) Experimental Petrology of Very Low Ti Basalts and Origin of Luna 24 Ferrobasalt. In *LPI Contributions* (eds. R. B. Merrill and J. J. Papike). LPI Contributions. p. 68.
- Gyollai I., Nagy S., Gucsik A., Bérczi S. and Veres M. (2009) Raman and infrared spectroscopy of feldspars in lunar meteorites (Asuka-881757 and Yamato-86032).

- Hallis L. J., Anand M. and Strekopytov S. (2014) Trace-element modelling of mare basalt parental melts: Implications for a heterogeneous lunar mantle. *Geochimica et Cosmochimica Acta* **134**, 289–316.
- Hargraves R. B., Hollister L. S. and Otalora G. (1970) Zoning Significance. , 631–634.
- Hartmann W. K. and Davis D. R. (1975) Satellite-sized planetesimals and lunar origin. *Icarus* **24**, 504–515.
- Hartmann W. K., Phillips R. J. and Taylor G. J. (1986) Origin of the Moon. In *Origin of the Moon*
- Haskin L. A., Gillis J. J., Korotev R. L. and Jolliff B. L. (2000) The materials of the lunar Procellarum KREEP Terrane: A synthesis of data from geomorphological mapping, remote sensing, and sample analyses. *Journal of Geophysical Research: Planets* **105**, 20403–20415.
- Hawke B. and Bell J. (1982) Remote sensing studies of lunar dark-halo impact craters- Preliminary results and implications for early volcanism. In *Lunar and Planetary Science Conference Proceedings*. pp. 665–678.
- Hawke B. R., Gillis J., Giguere T., Blewett D., Lawrence D., Lucey P., Smith G., Spudis P. and Taylor G. J. (2005) Remote sensing and geologic studies of the Balmer-Kapteyn region of the Moon. *Journal of Geophysical Research: Planets* **110**.
- He Q., Li Y., Baziotis I., Qian Y., Xiao L., Wang Z., Zhang W., Luo B., Neal C. R., Day J. M. D., Pan F., She Z., Wu X., Hu Z., Zong K. and Wang L. (2022) Detailed petrogenesis of the unsampled Oceanus Procellarum: The case of the Chang’e-5 mare basalts. *Icarus* **383**, 115082.
- Head J. W. (1976) Lunar volcanism in space and time. *Reviews of Geophysics* **14**, 265–300.
- Head J. W. and Wilson L. (1992) Lunar mare volcanism: Stratigraphy, eruption conditions, and the evolution of secondary crusts. *Geochimica et Cosmochimica Acta* **56**, 2155–2175.
- Hertogen J., Janssens M.-J., Takahashi H., Palme H. and Anders E. (1977) Lunar basins and craters-Evidence for systematic compositional changes of bombarding population. In *Lunar and Planetary Science Conference Proceedings* pp. 17–45.
- Hess P. C. (2000) On the source regions for mare picrite glasses. *Journal of Geophysical Research: Planets* **105**, 4347–4360.
- Hiesinger H., Head III J. W., Wolf U., Jaumann R. and Neukum G. (2010) Ages and stratigraphy of lunar mare basalts in Mare Frigoris and other nearside maria based on crater size-frequency distribution measurements. *Journal of Geophysical Research: Planets* **115**.

- Hiesinger H., Head III J. W., Wolf U., Jaumann R. and Neukum G. (2003) Ages and stratigraphy of mare basalts in Oceanus Procellarum, Mare Nubium, Mare Cognitum, and Mare Insularum. *Journal of Geophysical Research: Planets* **108**.
- Higuchi H. and Morgan J. W. (1975) Ancient meteoritic component in Apollo 17 boulders. In *Lunar and Planetary Science Conference Proceedings* pp. 1625–1651.
- Hill D. H. and Boynton W. V. (2003). Chemistry of the Calcalong Creek lunar meteorite and its relationship to lunar terranes. *Meteoritics and Planetary Science*. **38**:595–626.
- Hoashi, M., Brooks, R.R. and Reeves, R.D. (1993). Palladium, platinum and ruthenium in iron meteorites and their taxonomic significance. *Chemical Geology*, **106**(3-4), pp.207-218.
- Hollister L. S. and Hargraves R. B. (1970) Compositional zoning and its significance in pyroxenes from two coarse grained Apollo 11 samples. *Geochimica et Cosmochimica Acta Supplement* **1**, 541.
- Horan, M. F., Walker, R. J., Morgan, J. W., Grossman, J. N., and Rubin, A. E. (2003). Highly siderophile elements in chondrites. *Chemical Geology*, **196**(1-4), 27-42.
- Houston, G.L. (2022). History of Lunar Science I. In: Cudnik, B. (eds) *Encyclopedia of Lunar Science*. Springer, Cham.
- Howarth G. H., Day J. M. D., Pernet-Fisher J. F., Goodrich C. A., Pearson D. G., Lou Y., Ryabov V. V., and Taylor L. A. (2017). Precious metal enrichment at low-redox in terrestrial native Fe-bearing basalts investigated using laser-ablation ICP-MS. *Geochimica et Cosmochimica Acta*. **203**: 343–363.
- Hu S., He H., Ji J., Lin Y., Hui H., Anand M., Tartèse R., Yan Y., Hao J. and Li R. (2021) A dry lunar mantle reservoir for young mare basalts of Chang'E-5. *Nature* **600**, 49–53.
- Hughes S. S., Delano J. W. and Schmitt R. A. (1989) Petrogenetic modeling of 74220 high-Ti orange volcanic glasses and the Apollo 11 and 17 high-Ti mare basalts. *Lunar and Planetary Science Conference Proceedings* **19**, 175–188.
- Hui H., Oshrin J. G. and Neal C. R. (2011) Investigation into the petrogenesis of Apollo 14 high-Al basaltic melts through crystal stratigraphy of plagioclase. *Geochimica et Cosmochimica Acta* **75**, 6439–6460.
- Ida S., Canup R. M. and Stewart G. R. (1997) Lunar accretion from an impact-generated disk. *Nature* **389**, 353–357.
- Ishikawa A., Senda R., Suzuki K., Dale C. W. and Meisel T. (2014) Re-evaluating digestion methods for highly siderophile element and 187Os isotope analysis: Evidence from geological reference materials. *Chemical Geology* **384**, 27–46.
- Ito K., Huyskens M. H., Yin Q.-Z. and Iizuka T. Pb–Pb dating of Yamato 86032. (2022) 13th Symposium on Polar Science.

- James, O. B., Lindstrom, M. M., and Flohr, M. K. (1989). Ferroan anorthosite from lunar breccia 64435-Implications for the origin and history of lunar ferroan anorthosites. In : *Lunar and Planetary Science Conference, 19th, Houston, TX, Mar. 14-18, 1988, Proceedings (A89-36486 15-91)*. Lunar and Planetary Institute, 1989, p. 219-243. (Vol. **19**, pp. 219-243).
- Jaupart C. and Mareschal J. C. (2015) Heat Flow and Thermal Structure of the Lithosphere. In *Treatise on Geophysics* (ed. G. Schubert). Elsevier, Oxford. pp. 217–253.
- Jochum K. P., Weis U., Stoll B., Kuzmin D., Yang Q., Raczek I., Jacob D. E., Stracke A., Birbaum K., Frick D. A., Günther D. and Enzweiler J. (2011) Determination of Reference Values for NIST SRM 610–617 Glasses Following ISO Guidelines. *Geostandards and Geoanalytical Research* **35**, 397–429.
- Johnson T. E., Morrissey L. J., Nemchin A. A., Gardiner N. J. and Snape J. F. (2021) The phases of the Moon: Modelling crystallisation of the lunar magma ocean through equilibrium thermodynamics. *Earth and Planetary Science Letters* **556**, 116721.
- Jolliff B. L., Gillis J. J., Haskin L. A., Korotev R. L. and Wieczorek M. A. (2000) Major lunar crustal terranes: Surface expressions and crust-mantle origins. *Journal of Geophysical Research: Planets* **105**, 4197–4216.
- Jolliff, B.L. (1998). Large-scale separation of K-frac and REEP-frac in the source regions of Apollo impact-melt breccias, and a revised estimate of the KREEP composition. *International Geology Review*, **40**(10), pp.916-935.
- Jones J. H. and Delano J. W. (1989) A three-component model for the bulk composition of the Moon. *Geochimica et Cosmochimica Acta* **53**, 513–527.
- Jones M. J., Evans A. J., Johnson B. C., Weller M. B., Andrews-Hanna J. C., Tikoo S. M. and Keane J. T. (2022) A South Pole–Aitken impact origin of the lunar compositional asymmetry. *Science Advances* **8**, eabm8475.
- Joy K. H. and Arai T. (2013) Lunar meteorites: new insights into the geological history of the Moon. *Astronomy and Geophysics* **54**, 4.28-4.32.
- Joy K. H., Crawford I. A., Anand M., Greenwood R. C., Franchi I. A. and Russell S. S. (2008) The petrology and geochemistry of Miller Range 05035: A new lunar gabbroic meteorite. *Geochimica et Cosmochimica Acta* **72**, 3822–3844.
- Joy K. H., Crawford I. A., Russell S. S. and Kearsley A. T. (2005) LAP 02205, LAP 02224 and LAP 02226 -- Lunar Mare Basaltic Meteorites. Part 1: Petrography and Mineral Chemistry. In *36th Annual Lunar and Planetary Science Conference* (eds. S. Mackwell and E. Stansbery). Lunar and Planetary Science Conference. p. 1697.
- Joy K. H., Crawford I. A., Russell S. S. and Kearsley A. T. (2010a) Lunar meteorite regolith breccias: An in situ study of impact melt composition using LA-ICP-MS

- with implications for the composition of the lunar crust: Lunar meteorite regolith breccias. *Meteoritics and Planetary Science* **45**, 917–946.
- Joy K.H., Crawford I.A., and Snape J.F. (2010b) Lunar Meteorite Miller Range 07006: Petrography and VLT Basalt Clast Inventory. Lunar Planet. Sci. XLI. Lunar Planet. Inst., Houston. #1793 (abstr.).
- Joy K. H., Nemchin A., Grange M., Lapen T. J., Peslier A. H., Ross D. K., Zolensky M. E. and Kring D. A. (2014) Petrography, geochronology and source terrain characteristics of lunar meteorites Dhofar 925, 961 and Sayh al Uhaymir 449. *Geochimica et Cosmochimica Acta* **144**, 299–325.
- Joy, K. H., Crawford, I. A., Downes, H., Russell, S. S., and Kearsley, A. T. (2006). A petrological, mineralogical, and chemical analysis of the lunar mare basalt meteorite LaPaz Icefield 02205, 02224, and 02226. *Meteoritics and Planetary Science*, **41**(7), 1003-1025.
- Kaiden, H., and Kojima, H. (2002). Yamato 983885: A second lunar meteorite from the Yamato 98 collection. *Antarctic Meteorites XXVII*, 27, 49-51.
- Karouji Y., Arai T. and Ebihara M. (2006) Chemical Composition of Another KREEP-rich Lunar Regolith Breccia Yamato 983885. In *37th Annual Lunar and Planetary Science Conference* p. 1919.
- Karouji, Y., Oura, Y., and Ebihara, M. (2002). Chemical composition of lunar meteorites including Yamato 981031. *Antarctic Meteorites XXVII*, 27, 52-54.
- Kesson S. E. (1975) Mare basalts: melting experiments and petrogenetic interpretations. *Lunar and Planetary Science Conference Proceedings* **1**, 921–944.
- Koeberl C., Kurat G., and Brandstätter F. (1991). Lunarmeteorite Yamato-793274: Mixture of mare and highland components, and barringerite from the Moon. *Proceedings of the NIPR Symposium on Antarctic Meteorites* 4:33–55.
- Kokubo E., Ida S. and Makino J. (2000) Evolution of a circumterrestrial disk and formation of a single Moon. *Icarus* **148**, 419–436.
- Korotev R. L. (2005) Lunar geochemistry as told by lunar meteorites. *Chemie der Erde* **65**, 297–346.
- Korotev R. L., Jolliff B. L., Zeigler R. A., Gillis J. J. and Haskin L. A. (2003) Feldspathic lunar meteorites and their implications for compositional remote sensing of the lunar surface and the composition of the lunar crust. *Geochimica et Cosmochimica Acta* **67**, 4895–4923.
- Korotev R. L., Zeigler R. A., Jolliff B. L., Irving A. J. and Bunch T. E. (2009) Compositional and lithological diversity among brecciated lunar meteorites of intermediate iron concentration. *Meteoritics and Planetary Science* **44**, 1287–1322.
- Korotev, R. L., and Irving, A. J. (2021). Lunar meteorites from northern Africa. *Meteoritics and Planetary Science*, 56(2), 206-240.

- Korotev, R.L. (2012). Lunar meteorites from Oman. *Meteoritics and Planetary Science*, 47(8), pp.1365-1402.
- Korotev, R.L., (1994). Compositional variation in Apollo 16 impact-melt breccias and inferences for the geology and bombardment history of the Central Highlands of the Moon. *Geochimica et Cosmochimica Acta*, 58(18), pp.3931-3969.
- Kouchi A., Sugawara Y., Kashima K. and Sunagawa I. (1983) Laboratory growth of sector zones clinopyroxenes in the system $\text{CaMgSi}_2\text{O}_6 - \text{CaTiAl}_2\text{O}_6$. *Contributions to Mineralogy and Petrology* 83, 177–184.
- Laneuville M., Wieczorek M. A., Breuer D. and Tosi N. (2013) Asymmetric thermal evolution of the Moon. *Journal of Geophysical Research (Planets)* 118, 1435–1452.
- Li Q. L., Zhou Q., Liu Y., Xiao Z., Lin Y., Li J. H., Ma H. X., Tang G. Q., Guo S., Tang X., Yuan J. Y., Li J., Wu F. Y., Ouyang Z., Li C. and Li X. H. (2021) Two-billion-year-old volcanism on the Moon from Chang'e-5 basalts. *Nature* 600, 54–58.
- Lin Y., Shen W., Liu Y., Xu L., Hofmann B. A., Mao Q., Tang G. Q., Wu F. and Li X. H. (2012) Very high-K KREEP-rich clasts in the impact melt breccia of the lunar meteorite SaU 169: New constraints on the last residue of the Lunar Magma Ocean. *Geochimica et Cosmochimica Acta* 85, 19–40.
- Lindsley D. H. (1983) Pyroxene thermometry. *American mineralogist* 68, 477–493.
- Lindsley D. H. and Burnham C. W. (1970) Pyroxferroite: Stability and X-ray crystallography of synthetic $\text{Ca}_{0.15}\text{Fe}_{0.85}\text{SiO}_3$ pyroxenoid. *Science* 168, 364–367.
- Lindsley D. H., Papike J. J. and Bence A. E. (1972) Pyroxferroite: Breakdown at low pressure and high temperature. In *Lunar and Planetary Science Conference* p. 483.
- Litzow, M.R. and Spalding, T.R. (1973) Mass Spectrometry of Inorganic and Organometallic Compounds, *Elsevier*, Amsterdam.
- Liu J., Sharp M., Ash R. D., Kring D. A. and Walker R. J. (2015) Diverse impactors in Apollo 15 and 16 impact melt rocks: Evidence from osmium isotopes and highly siderophile elements. *Geochimica et Cosmochimica Acta* 155, 122–153.
- Liu Y., Balta J. B., Goodrich C. A., McSween H. Y. and Taylor L. A. (2013) New constraints on the formation of shergottite Elephant Moraine 79001 lithology A. *Geochimica et Cosmochimica Acta* 108, 1–20.
- Liu Y., Floss C., Day J. M. D., Hill E. and Taylor L. A. (2009) Petrogenesis of lunar mare basalt meteorite Miller Range 05035. *Meteoritics and Planetary Science* 44, 261–284.

- Lofgren G. E., Huss G. R. and Wasserburg G. J. (2006) An experimental study of trace-element partitioning between Ti-Al-clinopyroxene and melt: Equilibrium and kinetic effects including sector zoning. *American Mineralogist* **91**, 1596–1606.
- Lofgren, G. E., Donaldson, C. H., and Usselman, T. M. (1975). Geology, petrology, and crystallization of Apollo 15 quartz-normative basalts. In *Lunar and Planetary Science Conference Proceedings* (Vol. **6**, pp. 79-99).
- Lognonné P., Gagnepain-Beyneix J. and Chenet H. (2003) A new seismic model of the Moon: implications for structure, thermal evolution and formation of the Moon. *Earth and Planetary Science Letters* **211**, 27–44.
- Longhi J. (1992) Experimental petrology and petrogenesis of mare volcanics. *Geochim. Cosmochim. Acta* **56**, 2235–2251.
- Longhi, J. (1993) Liquidus equilibria of lunar analogs at high pressure (abstract, Lunar Planet. Sci., XXIV, 895-896
- Longhi J. (2006) Petrogenesis of picritic mare magmas: constraints on the extent of early lunar differentiation. *Geochimica et Cosmochimica Acta* **70**, 5919–5934.
- Longhi, J., and Pan, V. (1989). The parent magmas of the SNC meteorites. In *Lunar and Planetary Science Conference, 19th, Houston, TX, Mar. 14-18, 1988, Proceedings (A89-36486 15-91)*, p. 451-464. (Vol. **19**, pp. 451-464).
- Lorenzetti S., Busemann H. and Eugster O. (2005) Regolith history of lunar meteorites. *Meteoritics and Planetary Science* **40**, 315–327.
- Lorenzetti S., Lin Y., Wang D. and Eugster O. (2003) Noble gases and mineralogy of meteorites from China and the Grove Mountains, Antarctica: A 0.05 Ma cosmic ray exposure age of GRV 98004. *Meteoritics and Planetary Science* **38**, 1243–1253.
- Lu, F., Taylor, L. A., and Jin, Y. (1989). Basalts and gabbros from Mare Crisium—Evidence for extreme fractional crystallization. In *IN: Lunar and Planetary Science Conference, 19th, Houston, TX, Mar. 14-18, 1988, Proceedings (A89-36486 15-91)*, 1989, p. 199-207. (Vol. **19**, pp. 199-207).
- Lucey P. G., Taylor G. J., Hawke B. R. and Spudis P. D. (1998) FeO and TiO₂ concentrations in the South Pole-Aitken basin: Implications for mantle composition and basin formation. *Journal of Geophysical Research: Planets* **103**, 3701–3708.
- Ma M. S., Schmitt R. A., Taylor G. J., Warner R. D., Lange D. E. and Keil K. (1978) Chemistry and petrology of Luna 24 lithic fragments and <250 μm soils: constraints on the origin of VLT mare basalts. In *Mare Crisium: The view from Luna 24* (eds. R. B. Merrill and J. J. Papike). pp. 569–592.
- MacDonald A., Ubide T., Mollo S., Masotta M. and Pontesilli A. (2022) Trace element partitioning in zoned clinopyroxene as a proxy for undercooling: Experimental constraints from trachybasaltic magmas. *Geochimica et Cosmochimica Acta* **336**, 249–268.

- MacDonald G. J. (1966) Origin of the Moon: dynamical considerations. In *The Earth-Moon System: Proceedings of an international conference, January 20–21, 1964, sponsored by the Institute for Space Studies of the Goddard Space Flight Center, NASA Springer*. pp. 165–209.
- Mann U., Frost D. J., Rubie D. C., Becker H. and Audétat A. (2012) Partitioning of Ru, Rh, Pd, Re, Ir and Pt between liquid metal and silicate at high pressures and high temperatures - Implications for the origin of highly siderophile element concentrations in the Earth's mantle. *Geochimica et Cosmochimica Acta* **84**, 593–613.
- Masotta M., Pontesilli A., Mollo S., Armienti P., Ubide T., Nazzari M. and Scarlato P. (2020) The role of undercooling during clinopyroxene growth in trachybasaltic magmas: Insights on magma decompression and cooling at Mt. Etna volcano. *Geochimica et Cosmochimica Acta* **268**, 258–276.
- Maurice M., Tosi N., Schwinger S., Breuer D. and Kleine T. (2020) A long-lived magma ocean on a young Moon. *Science Advances* **6**, eaba8949.
- Mavrogenes, J.A. and O'Neill, H.S.C., 1999. The relative effects of pressure, temperature and oxygen fugacity on the solubility of sulfide in mafic magmas. *Geochimica et Cosmochimica Acta*, **63**(7-8), pp.1173-1180.
- McCoy, T.J., Walker, R.J., Goldstein, J.I., Yang, J., McDonough, W.F., Rumble, D., Chabot, N.L., Ash, R.D., Corrigan, C.M., Michael, J.R. and Kotula, P.G., (2011). Group IVA irons: New constraints on the crystallization and cooling history of an asteroidal core with a complex history. *Geochimica et Cosmochimica Acta*, **75**(22), pp.6821-6843.
- McDonough, W. F., and Sun, S. S. (1995). The composition of the Earth. *Chemical geology*, **120**(3-4), 223-253.
- McIntosh E. C., Day J. M. D., Liu Y. and Jiskoot C. (2020) Examining the compositions of impactors striking the Moon using Apollo impact melt coats and anorthositic regolith breccia meteorites. *Geochimica et Cosmochimica Acta* **274**, 192–210.
- McKay G., Le L. and Wagstaff J. (1991) Constraints on the Origin of the Mare Basalt Europium Anomaly: REE Partition Coefficients for Pigeonite. In *Lunar and Planetary Science Conference Lunar and Planetary Science Conference*. p. 883.
- McKay G.A. (1986) Crystal/liquid partitioning of REE in basaltic systems: Extreme fractionation of REE in olivine. *Geochimica et Cosmochimica Acta* **50**, 69–79.
- Meisel T., Moser J., Fellner N., Wegscheider W. and Schoenberg R. (2001) Simplified method for the determination of Ru, Pd, Re, Os, Ir and Pt in chromitites and other geological materials by isotope dilution ICP-MS and acid digestion. *Analyst* **126**, 322–328.
- Melosh H. J. (1989) Impact cratering: a geologic process. *New York: Oxford University Press; Oxford: Clarendon Press*.

- Melosh H. J., Kendall J., Horgan B., Johnson B. C., Bowling T., Lucey P. G. and Taylor G. J. (2017) South Pole–Aitken basin ejecta reveal the Moon’s upper mantle. *Geology* **45**, 1063–1066.
- Mercer C. N., Treiman A. H., and Joy K. H. (2013). New lunar meteorite Northwest Africa 2996: A window into farside lithologies and petrogenesis. *Meteoritics and Planetary Science*, 48:289–315.
- Meyer Jr C. and Hubbard N. J. (1970) High potassium, high phosphorus glass as an important rock type in the Apollo 12 soil samples. *Meteoritics*, Vol. 5, p. 210-211 **5**, 210–211.
- Misawa K., Tatsumoto M., Dalrymple G. B. and Yanai K. (1993) An extremely low UPb source in the Moon: U- Th-Pb, Sm-Nd, Rb-Sr, and 40Ar-39Ar isotopic systematics and age of lunar meteorite Asuka 881757. *Geochimica et Cosmochimica Acta* **57**, 4687–4702.
- Mitler H. E. (1975) Formation of an iron-poor moon by partial capture, or: Yet another exotic theory of lunar origin. *Icarus* **24**, 256–268.
- Miura N., Arai, T, Karouji Y., and Ebihara, M. (2006) Noble gases in the lunar meteorite Yamato 983885, a KREEP-rich lunar regolith breccias. *Antarctic Meteorites*, **30**, pp. 67-68
- Mollo S., Blundy J. D., Iezzi G., Scarlato P. and Langone A. (2013) The partitioning of trace elements between clinopyroxene and trachybasaltic melt during rapid cooling and crystal growth. *Contributions to Mineralogy and Petrology* **166**, 1633–1654.
- Mollo S., Blundy J., Scarlato P., De Cristofaro S. P., Tecchiato V., Di Stefano F., Vetere F., Holtz F. and Bachmann O. (2018) An integrated PT-H₂O-lattice strain model to quantify the role of clinopyroxene fractionation on REE+ Y and HFSE patterns of mafic alkaline magmas: Application to eruptions at Mt. Etna. *Earth-Science Reviews* **185**, 32–56.
- Morgan J. W., Hertogen J. and Anders E. (1978) The Moon: Composition determined by nebular processes. *The moon and the planets* **18**, 465–478.
- Moriarty D. P., Dygert N., Valencia S. N., Watkins R. N. and Petro N. E. (2021) The search for lunar mantle rocks exposed on the surface of the Moon. *Nature Communications* **12**, 1–11.
- Morimoto N. (1988) Nomenclature of Pyroxenes. *Mineralogy and Petrology* **39**, 55–76.
- Morishima R. and Watanabe S. (2001) Two types of co-accretion scenarios for the origin of the Moon. *Earth, planets and space* **53**, 213–231.
- Mungall J. E. and Brenan J. M. (2014) Partitioning of platinum-group elements and Au between sulfide liquid and basalt and the origins of mantle-crust fractionation of the chalcophile elements. *Geochimica et Cosmochimica Acta* **125**, 265–289.

- Nagaoka H., Takeda H., Karouji Y., Ohtake M., Yamaguchi A., Yoneda S. and Hasebe N. (2014) Implications for the origins of pure anorthosites found in the feldspathic lunar meteorites, Dhofar 489 group. *Earth, Planets and Space* **66**, 1–14.
- Naldrett A. J. and Duke J. M. (1980) Platinum metals magmatic sulfide ores. *Science* **208**, 1417–1424.
- Naldrett A. J., Hoffman E. L., Green A. H., Chou C.-L., Naldrett S. R. and Alcock R. A. (1979) The composition of Ni-sulfide ores, with particular reference to their content of PGE and Au. *The Canadian Mineralogist* **17**, 403–415.
- Naldrett, A.J., 1999. World-class Ni-Cu-PGE deposits: key factors in their genesis. *Mineralium deposita*, **34**, pp.227-240.
- NASA (2005) Soviet Lunar Missions [Online]. Available at <https://nssdc.gsfc.nasa.gov/planetary/lunar/lunarussr.html>
- NASA (2016) Lunar Rocks and Soils from Apollo Missions [Online]. Available at <https://curator.jsc.nasa.gov/lunar/index.cfm#>
- Neal C. R. (2009) The Moon 35 years after Apollo: What's left to learn? *Chemie der Erde* **69**, 3–43.
- Neal C. R. and Taylor L. A. (1992) Petrogenesis of mare basalts: A record of lunar volcanism. *Geochimica et Cosmochimica Acta* **56**, 2177–2211.
- Neal C. R., Hacker M. D., Snyder G. A., Taylor L. A., Liu Y. and Schmitt R. A. (1994) Basalt generation at the Apollo 12 site, Part 1: New data, classification, and re-evaluation. *Meteoritics* **29**, 334–348.
- Neal, C. R., Valenciano, J. L., Che, X., Shi, Y., Liu, D., Tao, L., Joy, K. H., Snape, J. F., Tartèse, R., Head, J. and Jolliff, B., (2022) Crystal Size Distribution of Ilmenite in Chang'e 5 Basalt Clasts. In *53rd Lunar and Planetary Science Conference* (Vol. 2678, p. 2353).
- Neave, D.A., Bali, E., Guðfinnsson, G.H., Halldórsson, S.A., Kahl, M., Schmidt, A.S. and Holtz, F., (2019). Clinopyroxene–liquid equilibria and geothermobarometry in natural and experimental tholeiites: the 2014–2015 Holuhraun eruption, Iceland. *Journal of Petrology*, **60**(8), pp.1653-1680.
- Needham D. H. and Kring D. A. (2017) Lunar volcanism produced a transient atmosphere around the ancient Moon. *Earth and Planetary Science Letters* **478**, 175–178.
- Nekvasil, H. The Origin and Evolution of Silica-saturated Alkalic Suites: an Experimental Study. *Journal of Petrology* **45**, 693–721 (2004).
- Nishiizumi K., Arnold J. R., Kohl C. P., Caffee M. W., Masarik J. and Reedy R. C. (2009) Solar cosmic ray records in lunar rock 64455. *Geochimica et Cosmochimica Acta* **73**, 2163–2176.

- Norman M. and Ryder G. (1980) Luna 24 ferrobalt as a low-Mg primary melt. *The moon and the planets* **23**, 271–292.
- Norman M. D., Bennett V. C. and Ryder G. (2002) Targeting the impactors: siderophile element signatures of lunar impact melts from Serenitatis. *Earth and Planetary Science Letters* **202**, 217–228.
- Norman M. D., Borg L. E., Nyquist L. E. and Bogard D. D. (2003) Chronology, geochemistry, and petrology of a ferroan noritic anorthosite clast from Descartes breccia 67215: Clues to the age, origin, structure, and impact history of the lunar crust. *Meteoritics and Planetary Science* **38**, 645–661.
- Nyquist L. E. (1977) Lunar Rb-Sr chronology. *Physics and Chemistry of the Earth* **10**, 103–142.
- Nyquist L. E. and Shih C. Y. (1992) The isotopic record of lunar volcanism. *Geochimica et Cosmochimica Acta* **56**, 2213–2234.
- Nyquist L. E., Shih C. Y. and Reese Y. D. (2007) Sm-Nd and Rb-Sr Ages for MIL 05035: Implications for Surface and Mantle Sources. In *38th Annual Lunar and Planetary Science Conference* Lunar and Planetary Science Conference. p. 1702.
- Nyquist L. E., Wiesmann H., Bansal B., Shih C. Y., Keith J. E. and Harper C. L. (1995) ^{146}Sm - ^{142}Nd formation interval for the lunar mantle. *Geochimica et Cosmochimica Acta* **59**, 2817–2837.
- Nyquist L., Bogard D., Yamaguchi A., Shih C. Y., Karouji Y., Ebihara M., Reese Y., Garrison D., McKay G. and Takeda H. (2006) Feldspathic clasts in Yamato-86032: Remnants of the lunar crust with implications for its formation and impact history. *Geochimica et Cosmochimica Acta* **70**, 5990–6015.
- Nyquist, L. E., Hubbard, N. J., Gast, P. W., Bansal, B. M., Weismann, H., and Jahn, B. (1973). Rb-Sr systematics for chemically defined Apollo 15 and 16 materials. In *Proceedings of the Lunar Science Conference*, vol. **4**, p. 1823
- O'Neill H. St. C. (1991) The origin of the moon and the early history of the earth-A chemical model. Part 1: The moon. *Geochimica et Cosmochimica Acta* **55**, 1135–1157.
- O'Neill H. St. C. and Palme H (1998) Composition of the silicate Earth: Implications for accretion and core formation. In: Jackson I (ed) *The Earth's mantle: structure, composition and evolution – the Ringwood volume*. Cambridge University Press, pp. 3–126
- Oba T. and Kobayashi Y. (2001) The mineral assemblage of symplectites in lunar meteorite Asuka-881757. *Antarctic Meteorite Research* **14**, 21.
- Ohtake M., Matsunaga T., Haruyama J., Yokota Y., Morota T., Honda C., Ogawa Y., Torii M., Miyamoto H. and Arai T. (2009) The global distribution of pure anorthosite on the Moon. *Nature* **461**, 236–240.

- Ohtani E., Ozawa S., Miyahara M., Ito Y., Mikouchi T., Kimura M., Arai T., Sato K. and Hiraga K. (2011) Coesite and stishovite in a shocked lunar meteorite, Asuka-881757, and impact events in lunar surface. *Proceedings of the National Academy of Sciences* **108**, 463–466.
- Opik E. J. (1972) Comments on lunar origin. *Irish Astronomical Journal*, vol. 10 (5/6), p. 190 **10**, 190.
- Palme H., Spettel B., Jochum K. P., Dreibus G., Weber H., Weckwerth G., Wänke H., Bischoff A. and Stöckler D. (1991) Lunar highland meteorites and the composition of the lunar crust. *Geochimica et Cosmochimica Acta* **55**, 3105–3122.
- Palme, Herbert, and H. St C. O'Neill. "Cosmochemical estimates of mantle composition." *Treatise on geochemistry*, 2 (2003): 568.
- Papike J. J., Karner J. M. and Shearer C. K. (2003) Determination of planetary basalt parentage: A simple technique using the electron microprobe. *American Mineralogist* **88**, 469–472.
- Papike J., Taylor L. and Simon S. (1991) Lunar minerals. *Lunar Sourcebook*, 121–181.
- Papike JJ, Ryder G, Shearer CK (1998) Lunar samples. In: Papike JJ (ed) *Planetary materials: Reviews in Mineralogy*. Mineralogical Society of America, Washington, DC
- Pearson D. G. and Woodland S. J. (2000) Solvent extraction/anion exchange separation and determination of PGEs (Os, Ir, Pt, Pd, Ru) and Re–Os isotopes in geological samples by isotope dilution ICP-MS. *Chemical Geology* **165**, 87–107.
- Pernet-Fisher J. F., Howarth G. H., Liu Y., Chen Y. and Taylor L. A. (2014) Estimating the lunar mantle water budget from phosphates: Complications associated with silicate-liquid-immiscibility. *Geochimica et Cosmochimica Acta* **144**, 326–341.
- Pernicka, E. and Wasson, J.T. (1987). Ru, Re, OS, Pt and Au in iron meteorites. *Geochimica et Cosmochimica Acta*, **51**(6), pp.1717-1726.
- Petaev, M.I. and Jacobsen, S.B., 2004. Differentiation of metal-rich meteoritic parent bodies: I. Measurements of PGEs, Re, Mo, W, and Au in meteoritic Fe-Ni metal. *Meteoritics and Planetary Science*, **39**(10), pp.1685-1697.
- Petaev, M.I., Huang, S., Jacobsen, S.B. and Zindler, A., 2013. Large Pt anomaly in the Greenland ice core points to a cataclysm at the onset of Younger Dryas. *Proceedings of the National Academy of Sciences*, **110**(32), pp.12917-12920.
- Phinney W.C. and Morrison D. A. (1990) Partition coefficients for calcic plagioclase: Implications for Archean anorthosites. *Geochimica et Cosmochimica Acta* **54**, 1639–1654.
- Pieters C. M., Adams J. B., Mougini-Mark P. J., Zisk S. H., Smith M. O., Head J. W. and McCord T. B. (1985) The nature of crater rays: The Copernicus example. *Journal of Geophysical Research: Solid Earth* **90**, 12393–12413.

- Potts N. J., Tartèse R., Anand M., van Westrenen W., Griffiths A. A., Barrett T. J. and Franchi I. A. (2016) Characterization of mesostasis regions in lunar basalts: Understanding late-stage melt evolution and its influence on apatite formation. *Meteoritics and Planetary Science* **51**, 1555–1575.
- Potts, P. J. (1992). *A handbook of silicate rock analysis*. Springer Science and Business Media.
- Pritchard M. E. and Stevenson D. J. (2000) Thermal constraints on the origin of the Moon.
- Puchtel I. S., Walker R. J., James O. B. and Kring D. A. (2008) Osmium isotope and highly siderophile element systematics of lunar impact melt breccias: Implications for the late accretion history of the Moon and Earth. *Geochimica et Cosmochimica Acta* **72**, 3022–3042.
- Pumfrey S. (2011) The Selenographia of William Gilbert: His pre-telescopic map of the moon and his discovery of lunar libration. *Journal for the History of Astronomy* **42**, 193–203.
- Putirka K. (2016) Rates and styles of planetary cooling on Earth, Moon, Mars, and Vesta, using new models for oxygen fugacity, ferric-ferrous ratios, olivine-liquid Fe-Mg exchange, and mantle potential temperature. *American Mineralogist* **101**, 819–840.
- Putirka K. D. (2008) Thermometers and Barometers for Volcanic Systems. *Reviews in Mineralogy and Geochemistry* **69**, 61–120.
- Qian Y., Xiao L., Head J. W., van der Bogert C. H., Hiesinger H. and Wilson L. (2021) Young lunar mare basalts in the Chang'e-5 sample return region, northern Oceanus Procellarum. *Earth and Planetary Science Letters* **555**, 116702.
- Rapp J. F. and Draper D. S. (2018) Fractional crystallization of the lunar magma ocean: Updating the dominant paradigm. *Meteoritics and Planetary Science* **53**, 1432–1455.
- Rehkämper M., Halliday A. N., Fitton J. G., Lee D.-C., Wieneke M. and Arndt N. T. (1999) Ir, Ru, Pt, and Pd in basalts and komatiites: new constraints for the geochemical behavior of the platinum-group elements in the mantle. *Geochimica et Cosmochimica Acta* **63**, 3915–3934.
- Righter K., Danielson L. R., Pando K. M., Williams J., Humayun M., Hervig R. L. and Sharp T. G. (2015) Highly siderophile element (HSE) abundances in the mantle of Mars are due to core formation at high pressure and temperature. *Meteoritics and Planetary Science* **50**, 604–631.
- Ringwood A. E. (1992) Volatile and siderophile element geochemistry of the Moon: a reappraisal. *Earth and Planetary Science Letters* **111**, 537–555.

- Ringwood A. E. and Essene E. (1970) Petrogenesis of Apollo 11 basalts, internal constitution and origin of the moon. *Geochimica et Cosmochimica Acta Supplement* **1**, 769.
- Ringwood A. E., Seifert S. and Wänke H. (1987) A komatiite component in Apollo 16 highland breccias: Implications for the nickel-cobalt systematics and bulk composition of the Moon. *Earth and Planetary Science Letters* **81**, 105–117.
- Ripley, E.M. and Li, C., (2013). Sulfide saturation in mafic magmas: Is external sulfur required for magmatic Ni-Cu-(PGE) ore genesis?. *Economic Geology*, **108**(1), pp.45-58.
- Robinson, K. L., Treiman, A. H., and Joy, K. H. (2012). Basaltic fragments in lunar feldspathic meteorites: Connecting sample analyses to orbital remote sensing. *Meteoritics and Planetary Science*, **47**(3), 387-399.
- Rufu R., Aharonson O. and Perets H. B. (2017) A multiple-impact origin for the Moon. *Nature Geoscience* **10**, 89–94.
- Ryder G. and Marvin U. B. (1978) On the origin of Luna 24 basalts and soils. In *Mare Crisium: The view from Luna 24* (eds. R. B. Merrill and J. J. Papike). pp. 339–355.
- Schnare D. W., Day J. M. D., Norman M. D., Liu Y. and Taylor L. A. (2008) A laser-ablation ICP-MS study of Apollo 15 low-titanium olivine-normative and quartz-normative mare basalts. *Geochimica et Cosmochimica Acta* **72**, 2556–2572.
- Schultz, P. H., and Spudis, P. D. (1979). Evidence for ancient mare volcanism. In *In: Lunar and Planetary Science Conference, 10th, Houston, Tex., March 19-23, 1979, Proceedings. Volume 3.(A80-23677 08-91) New York, Pergamon Press, Inc., 1979, p. 2899-2918. (Vol. 10, pp. 2899-2918).*
- Schwandt C. S. and McKay G. A. (2006) Minor- and trace-element sector zoning in synthetic enstatite. *American Mineralogist* **91**, 1607–1615.
- Shannon, R., (1976). Revised Effective Ionic Radii and Systematic Studies of Interatomic Distances in Halides and Chalcogenides. *Acta Cryst*, **32**, p.751.
- Sharp M., Gerasimenko I., Loudin L. C., Liu J., James O. B., Puchtel I. S. and Walker R. J. (2014) Characterization of the dominant impactor signature for Apollo 17 impact melt rocks. *Geochimica et Cosmochimica Acta* **131**, 62–80.
- Shearer C. K. and Borg L. E. (2006) Big returns on small samples: Lessons learned from the analysis of small lunar samples and implications for the future scientific exploration of the Moon. *Chemie der Erde* **66**, 163–185.
- Shearer C. K. and Papike J. J. (1999) Magmatic evolution of the Moon. *American Mineralogist* **84**, 1469–1494.
- Shearer C. K. and Papike J. J. (2005) Early crustal building processes on the moon: Models for the petrogenesis of the magnesian suite. *Geochimica et Cosmochimica Acta* **69**, 3445–3461.

- Shearer C. K., Elardo S. M., Petro N. E., Borg L. E. and McCubbin F. M. (2015) Origin Of The Lunar Highlands Mg-Suite: An Integrated Petrology, Geochemistry, Chronology, And Remote Sensing Perspective. *American Mineralogist* **100**, 294–325.
- Shearer C. K., Hess P. C., Wiczorek M. A., Pritchard M. E., Parmentier E. M., Borg L. E., Longhi J., Elkins-Tanton L. T., Neal C. R., Antonenko I., Canup R. M., Halliday A. N., Grove T. L., Hager B. H., Lee D. C. and Wiechert U. (2006) Thermal and magmatic evolution of the Moon. *Reviews in Mineralogy and Geochemistry* **60**, 365–518.
- Shih C.-Y., Nyquist L. E., Dasch E. J., Bogard D. D., Bansal B. M. and Wiesmann H. (1993) Ages of pristine noritic clasts from lunar breccias 15445 and 15455. *Geochimica et Cosmochimica Acta* **57**, 915–931.
- Shimizu, N., (1981). Trace element incorporation into growing augite phenocryst. *Nature*, 289(5798), pp.575-577.
- Shirey, S.B. and Walker, R.J., (1998). The Re-Os isotope system in cosmochemistry and high-temperature geochemistry. *Annual Review of Earth and Planetary Sciences*, 26(1), pp.423-500.
- Shirley, D., and J.T. Wasson (1981), Mechanism for the extrusion of KREEP, *Proc. Lunar Planet. Sci. Conf.* 12th, 965-978
- Smith J. V., Anderson A. T., Newton R. C., Olsen E. J., Crewe A. V., Isaacson M. S., Johnson D. and Wyllie P. J. (1970) Petrologic history of the moon inferred from petrography, mineralogy and petrogenesis of Apollo 11 rocks. In *Geochimica et Cosmochimica Acta Supplement, Volume 1. Proceedings of the Apollo 11 Lunar Science Conference held 5-8 January, 1970 in Houston, TX. Volume 1: Mineralogy and Petrology. Edited by AA Levinson. New York: Pergamon Press, 1970., p. 897*
- Smith P. M. and Asimow P. D. (2005) Adibat_1ph: A new public front-end to the MELTS, pMELTS, and pHMELTS models. *Geochemistry, Geophysics, Geosystems* **6**, Q02004.
- Smoliar, M.I., Walker, R.J. and Morgan, J.W., (1996). Re-Os ages of group IIA, IIIA, IVA, and IVB iron meteorites. *Science*, 271(5252), pp.1099-1102.
- Snyder G. A., Taylor L. A. and Neal C. R. (1991) The sources of mare basalts: A model involving lunar magma ocean crystallization, plagioclase flotation, and trapped instantaneous residual liquid. In *Mare Volcanism and Basalt Petrogenesis: Astounding Fundamental Concepts* p. 53.
- Snyder G. A., Taylor L. A. and Neal C. R. (1992) A chemical model for generating the sources of mare basalts: Combined equilibrium and fractional crystallization of the lunar magmasphere. *Geochimica et Cosmochimica Acta* **56**, 3809–3823.
- Snyder, G.A., Neal, C.R., Taylor, L.A. and Halliday, A.N., (1997). Anatexis of lunar cumulate mantle in time and space: Clues from trace-element, strontium, and

- neodymium isotopic chemistry of parental Apollo 12 basalts. *Geochimica et Cosmochimica Acta*, **61**(13), pp.2731-2747.
- Sokol A. K., Fernandes V. A., Schulz T., Bischoff A., Burgess R., Clayton R. N., Münker C., Nishiizumi K., Palme H., Schultz L., Weckwerth G., Mezger K. and Horstmann M. (2008) Geochemistry, petrology and ages of the lunar meteorites Kalahari 008 and 009: New constraints on early lunar evolution. *Geochimica et Cosmochimica Acta* **72**, 4845–4873.
- Solomon S. C. and Head J. W. (1980) Lunar mascon basin: lava filling, tectonics, and evolution of the lithosphere. *Reviews of Geophysics and Space Physics* **18**, 107–141.
- Solomon S. C. and Longhi J. (1977) Magma oceanography: 1. Thermal evolution. *Lunar and Planetary Science Conference Proceedings* **1**, 583–599.
- Spudis P. D., Gillis J. J. and Reisse R. A. (1994) Ancient Multiring Basins on the Moon Revealed by Clementine Laser Altimetry. *Science* **266**, 1848–1851.
- Srivastava Y. and Basu Sarbadhikari A. (2020) Silica, Silicate. In *Encyclopedia of Lunar Science* (ed. B. Cudnik). Springer International Publishing, Cham. pp. 1–8.
- Srivastava Y., Basu Sarbadhikari A., Day J. M.D., Yamaguchi A. and Takenouchi A. (2022) A changing thermal regime revealed from shallow to deep basalt source melting in the Moon. *Nature Communications* **13**, 7594.
- Steenstra, E.S., Lin, Y., Dankers, D., Rai, N., Berndt, J., Matveev, S. and van Westrenen, W. (2017). The lunar core can be a major reservoir for volatile elements S, Se, Te and Sb. *Scientific reports*, **7**(1), p.14552.
- Steenstra, E.S., Seegers, A.X., Eising, J., Tomassen, B.G.J., Webers, F.P.F., Berndt, J., Klemme, S., Matveev, S. and van Westrenen, W. (2018). Evidence for a sulfur-undersaturated lunar interior from the solubility of sulfur in lunar melts and sulfide-silicate partitioning of siderophile elements. *Geochimica et Cosmochimica Acta*, **231**, pp.130-156.
- Steenstra, E.S., Berndt, J., Klemme, S., Snape, J.F., Bullock, E.S. and van Westrenen, W. (2020). The fate of sulfur and chalcophile elements during crystallization of the lunar magma ocean. *Journal of Geophysical Research: Planets*, **125**(11), p.e2019JE006328.
- Stöffler D. and Keil K. (1991) Shock metamorphism of ordinary chondrites. *Geochimica et Cosmochimica Acta* **55**, 3845–3867.
- Sugihara T., Ohtake M., Owada A., Ishii T., Otsuki M. and Takeda H. (2004) Petrology and reflectance spectroscopy of lunar meteorite Yamato 981031: Implications for the source region of the meteorite and remote-sensing spectroscopy. *Antarctic Meteorite Research, Vol. 17*, p. 209 **17**, 209.

- Sun C. and Liang Y. (2012) Distribution of REE between clinopyroxene and basaltic melt along a mantle adiabat: effects of major element composition, water, and temperature. *Contributions to Mineralogy and Petrology* **163**, 807–823.
- Takeda H., Arai T. and Saiki K. (1993) Mineralogical studies of lunar meteorite Yamato-793169, a mare basalt. *Antarctic Meteorite Research* **6**, 3.
- Takeda H., Kojima H., Nishio F., Yanai K. and Lindstrom M. M. (1989) Preliminary report on the Yamato-86032 lunar meteorite I: Recovery, sample descriptions, mineralogy, and petrography. In *Proc. NIPR Symp. Antarct. Meteorites* pp. 3–14.
- Takeda H., Miyamoto M., Ishii T. and Lofgren G. E. (1975) Relative cooling rates of mare basalts at the Apollo 12 and 15 sites as estimated from pyroxene exsolution data. *Lunar and Planetary Science Conference Proceedings* **1**, 987–996.
- Taylor G. J. (2009) Ancient lunar crust: Origin, composition, and implications. *Elements* **5**, 17–22.
- Taylor G. J. and Wieczorek M. A. (2014) Lunar bulk chemical composition: a post-Gravity Recovery and Interior Laboratory reassessment. *Philosophical Transactions of the Royal Society A: Mathematical, Physical and Engineering Sciences* **372**, 20130242.
- Taylor G. J., Warner R. D., Wentworth S., Keil K. and Sayeed U. (1978) Luna 24 lithologies-Petrochemical relationships among lithic fragments, mineral fragments, and glasses. In *Mare crisium: The view from Luna 24* pp. 303–320.
- Taylor L. A., Kullerud G. and Bryan W. B. (1971) Opaque mineralogy and textural features of Apollo 12 samples and a comparison with Apollo 11 rocks. In *Lunar and Planetary Science Conference Proceedings* p. 855.
- Taylor L. A., Shervais J. W., Hunter R. H., Shih C.-Y., Bansal B. M., Wooden J., Nyquist L. E. and Laul L. C. (1983) Pre-4.2 AE mare-basalt volcanism in the lunar highlands. *Earth and Planetary Science Letters* **66**, 33–47.
- Taylor S. R. (1982) *Planetary science: A lunar perspective.*, Lunar and Planetary Institute Houston.
- Taylor S. R., Taylor G. J. and Taylor L. A. (2006) The moon: a Taylor perspective. *Geochimica et Cosmochimica Acta* **70**, 5904–5918.
- Taylor, S. R., and Jakes, P. (1974). Geochemical zoning in the Moon. In Abstracts of the Lunar and Planetary Science Conference, volume **5**, page 786,(1974).
- Terada K., Anand M., Sokol A. K., Bischoff A. and Sano Y. (2007) Cryptomare magmatism 4.35 Gyr ago recorded in lunar meteorite Kalahari 009. *Nature* **450**, 849–852.
- Terada K., Sasaki Y. and Sano Y. (2006) In-Situ U-Pb Dating of Phosphates in Lunar Basaltic Breccia Yamato 981031. In *37th Annual Lunar and Planetary Science*

- Conference* (eds. S. Mackwell and E. Stansbery). Lunar and Planetary Science Conference. p. 1665.
- Tian H. C., Wang H., Chen Y., Yang W., Zhou Q., Zhang C., Lin H. L., Huang C., Wu S. T., Jia L. H., Xu L., Zhang D., Li X. G., Chang R., Yang Y. H., Xie L. W., Zhang D. P., Zhang G. L., Yang S. H. and Wu F. Y. (2021) Non-KREEP origin for Chang'e-5 basalts in the Procellarum KREEP Terrane. *Nature* **600**, 59–63.
- Tomoko A., Hiroshi T. and Masamichi M. (2006) Experimental petrology of ancient lunar mare basalt Asuka-881757: spinel crystallization as a petrologic indicator. *Antarctic meteorite research* **19**, 1–19.
- Torigoye-Kita N., Misawa K., Dalrymple G. B. and Tatsumoto M. (1995) Further evidence for a low U/Pb source in the moon: U-Th-Pb, Sm-Nd, and Ar-Ar isotopic systematics of lunar meteorite Yamato-793169. *Geochimica et Cosmochimica Acta* **59**, 2621–2632.
- Tormey D. R., Grove T. L. and Bryan W. B. (1987) Experimental petrology of normal MORB near the Kane Fracture Zone: 22°–25°N, mid-Atlantic ridge. *Contributions to Mineralogy and Petrology* **96**, 121–139.
- Turcotte D. L. and Ahern J. L. (1978) Magma production and migration within the moon. *Lunar and Planetary Science Conference Proceedings* **1**, 307–318.
- Ubide T., Caulfield J., Brandt C., Bussweiler Y., Mollo S., Stefano F. D., Nazzari M. and Scarlato P. (2019a) Deep Magma Storage Revealed by Multi-Method Elemental Mapping of Clinopyroxene Megacrysts at Stromboli Volcano. *Frontiers in Earth Science* **7**.
- Ubide T., Mollo S., Zhao J. xin, Nazzari M. and Scarlato P. (2019b) Sector-zoned clinopyroxene as a recorder of magma history, eruption triggers, and ascent rates. *Geochimica et Cosmochimica Acta* **251**, 265–283.
- Ubide T., Neave D. A., Petrelli M. and Longpré M.-A. (2021) Editorial: Crystal Archives of Magmatic Processes. *Frontiers in Earth Science* **9**.
- Urey H. C. and Korff S. A. (1952) The planets: their origin and development. *Physics Today* **5**, 12–12.
- Valencia, S. N., Jolliff, B. L., and Korotev, R. L. (2019). Petrography, relationships, and petrogenesis of the gabbroic lithologies in Northwest Africa 773 clan members Northwest Africa 773, 2727, 3160, 3170, 7007, and 10656. *Meteoritics and Planetary Science*, **54**(9), 2083–2115.
- Vaniman D. T. and Papike J. J. (1977) Ferrobasalts from Mare Crisium: Luna 24. *Geophysical Research Letters* **4**, 497–500.
- Walker R. J. (2009) Highly siderophile elements in the Earth, Moon and Mars: Update and implications for planetary accretion and differentiation. *Chemie der Erde* **69**, 101–125.

- Walker R. J., Horan M. F., Shearer C. K. and Papike J. J. (2004) Low abundances of highly siderophile elements in the lunar mantle: evidence for prolonged late accretion. *Earth and Planetary Science Letters* **224**, 399–413.
- Walker, D., Longhi, J., Lasaga, A. C., Stolper, E. M., Grove, T. L., and Hays, J. F. (1977). Slowly cooled microgabbros 15555 and 15065. In *Lunar Science Conference, 8th, Houston, Tex., March 14-18, 1977, Proceedings. Volume 2.(A78-41551 18-91)* New York, Pergamon Press, Inc., 1977, p. 1521-1547. (Vol. **8**, pp. 1521-1547).
- Wang X. and Pedrycz W. (2015) Petrologic Characteristics of the Lunar Surface. *Sci Rep* **5**, 17075.
- Wang X., Hou T., Wang M., Zhang C., Zhang Z., Pan R., Marxer F. and Zhang H. (2021) A new clinopyroxene thermobarometer for mafic to intermediate magmatic systems. *European Journal of Mineralogy* **33**, 621–637.
- Wanke H. (1981) Constitution of Terrestrial Planets. *Philosophical Transactions of the Royal Society of London Series A* **303**, 287–301.
- Warren P. H. (1985) The magma ocean concept and lunar evolution. *Annual Review of Earth and Planetary Sciences* **13**, 201–240.
- Warren P. H. (1988) The origin of pristine KREEP: effects of mixing between urKREEP and the magmas parental to the Mg-rich cumulates. *Lunar and Planetary Science Conference Proceedings* **18**, 233–241.
- Warren, P. H. (1989). KREEP: major-element diversity, trace-element uniformity (almost). In *Moon in transition: Apollo 14, KREEP, and evolved lunar rocks* (pp. 149-153).
- Warren P. H. (1993) A concise compilation of petrologic information on possibly pristine nonmare Moon rocks. *American Mineralogist* **78**, 360–376.
- Warren P. H. and Bridges J. C. (2004) Lunar meteorite Yamato-983885: A relatively KREEPy regolith breccia not paired with Y-791197. *Meteoritics and Planetary Science Supplement* **39**, 5095.
- Warren P. H. and Humphrys T. L. (2003) Bulk composition of the moon as constrained by thorium data: Comparison of Lunar Prospector versus Apollo GRS results. *Lunar Planet Sci XXXIV* **2034**.
- Warren P. H. and Wasson J. T. (1978) Compositional-petrographic investigation of pristine nonmare rocks. In *Lunar and Planetary Science Conference Proceedings* pp. 185–217.
- Warren P. H. and Wasson J. T. (1979) The origin of KREEP. *Reviews of Geophysics* **17**, 73–88.

- Warren P. H. and Wasson J. T. (1980) Further foraging for pristine nonmare rocks—correlations between geochemistry and longitude. In *Lunar and Planetary Science Conference Proceedings* pp. 431–470.
- Warren P. H., Jerde E. A. and Kallemeyn G. W. (1991) Pristine moon rocks—Apollo 17 anorthosites. In *Lunar and Planetary Science Conference Proceedings* pp. 51–61.
- Warren P. H., Ulff-Møller F. and Kallemeyn G. W. (2005) “New” lunar meteorites: Impact melt and regolith breccias and large-scale heterogeneities of the upper lunar crust. *Meteoritics and Planetary Science* **40**, 989–1014.
- Warren P.H., and Taylor G.J. (2014) The Moon. In: Holland H.D. and Turekian K.K. (eds.) *Treatise on Geochemistry*, Second Edition, vol. **2**, pp. 213-250.
- Warren, P. H., and Kallemeyn, G. W. (1993). Geochemical investigation of two lunar mare meteorites: Yamato-793169 and Asuka-881757. In *Seventeenth Symposium on Antarctic Meteorites. Proceedings of the NIPR Symposium, No. 6, held August 19-21, 1992, at the National Institute of Polar Research, Tokyo. Editor in Chief, Keizo Yanai, with Hideyasu Kojima, Keiji Misawa, Nobuo Takaoka, and Yoshio Yoshida. Published by the National Institute of Polar Research, 1993, p. 35 (Vol. 6, p. 35).*
- Webb, S., Neal, C.R., Che, X., Shi, Y., Liu, D., Tao, L., Joy, K.H., Snape, J.F., Tartèse, R., Head, J. and Jolliff, B., (2022). Crystal Size Distribution of Plagioclase in Basalt Fragments from Oceanus Procellarum Recovered by Chang'e-5. *LPI Contributions*, 2678, p.2896.
- Webster RK (1960) Mass spectrometric isotope dilution analysis. In: Smales AA, Wager LR (eds) *Methods in geochemistry*. Interscience Publishers, New York, pp 202–246
- Wentworth S. J., McKay D. S., Lindstrom D. J., Basu A., Martinez R. R., Bogard D. D. and Garrison D. H. (1994) Apollo 12 ropy glasses revisited. *Meteoritics* **29**, 323–333.
- White, F.A. (1968) *Mass Spectrometry in Science and Technology*. John Wiley and Sons, New York
- Whitten J. L. and Head J. W. (2015a) Lunar cryptomaria: Physical characteristics, distribution, and implications for ancient volcanism. *Icarus* **247**, 150–171.
- Whitten J. L. and Head J. W. (2015b) Lunar cryptomaria: Mineralogy and composition of ancient volcanic deposits. *Planetary and Space Science* **106**, 67–81.
- Wieczorek M. A. and Phillips R. J. (2000) The “Procellarum KREEP Terrane”: Implications for mare volcanism and lunar evolution. *Journal of Geophysical Research: Planets* **105**, 20417–20430.
- Wieczorek, M.A., Jolliff, B.L., Khan, A., Pritchard, M.E., Weiss, B.P., Williams, J.G., Hood, L.L., Righter, K., Neal, C.R., Shearer, C.K. and McCallum, I.S., (2006). The constitution and structure of the lunar interior. *Reviews in Mineralogy and*

- Geochemistry*, 60(1), pp.221-364. Wilhelms D.E., McCauley J.F., and Trask N.J. (1987) The geological history of the Moon. US Geological Survey Professional Paper 1348. United States Geological Survey, Dept. of the Interior, Washington D.C., 1987.
- Wieczorek, M.A., Neumann, G.A., Nimmo, F., Kiefer, W.S., Taylor, G.J., Melosh, H.J., Phillips, R.J., Solomon, S.C., Andrews-Hanna, J.C., Asmar, S.W. and Konopliv, A.S., (2013). The crust of the Moon as seen by GRAIL. *Science*, **339** (6120), pp.671-675.
- Wilhelms, D. E. (1987), The geologic history of the Moon, *U.S. Geol. Surv. Prof. Pap.*, **1348**, 302 pp.
- Wise D. U. (1963) An origin of the moon by rotational fission during formation of the earth's core. *Journal of Geophysical Research* **68**, 1547–1554.
- Włodarczyk J. (2019) The pre-telescopic observations of the Moon in early seventeenth-century London: The case of Edward Gresham (1565–1613). *Notes and Records: the Royal Society Journal of the History of Science* **74**, 35–53.
- Wolf R., Woodrow A. and Anders E. (1979) Lunar basalts and pristine highland rocks- Comparison of siderophile and volatile elements. In *Lunar and Planetary Science Conference Proceedings* pp. 2107–2130.
- Wood J. A. (1986) Moon over Mauna Loa-A review of hypotheses of formation of earth's moon. *Origin of the Moon*, 17–55.
- Wood J. A., Dickey Jr J. S., Marvin U. B. and Powell B. N. (1970) Lunar anorthosites and a geophysical model of the moon. In *Geochimica et Cosmochimica Acta Supplement, Volume 1. Proceedings of the Apollo 11 Lunar Science Conference held 5-8 January, 1970 in Houston, TX. Volume 1: Mineralogy and Petrology. Edited by AA Levinson. New York: Pergamon Press, 1970., p. 965 p. 965.*
- Wu Y. and Hsu W. (2020) Mineral chemistry and in situ UPb geochronology of the mare basalt Northwest Africa 10597: Implications for low-Ti mare volcanism around 3.0 Ga. *Icarus* **338**, 113531.
- Xu Z., Guo D. and Liu J. (2021) Maria basalts chronology of the Chang'E-5 sampling site. *Remote Sensing* **13**, 1515.
- Xue, Z., Xiao, L., Neal, C. R., and Xu, Y. (2019). Oldest high-Ti basalt and magnesian crustal materials in feldspathic lunar meteorite Dhofar 1428. *Geochimica et Cosmochimica Acta*, **266**, 74-108.
- Yamaguchi A., Karouji Y., Takeda H., Nyquist L., Bogard D., Ebihara M., Shih C. Y., Reese Y., Garrison D., Park J. and McKay G. (2010) The variety of lithologies in the Yamato-86032 lunar meteorite: Implications for formation processes of the lunar crust. *Geochimica et Cosmochimica Acta* **74**, 4507–4530.
- Yamaguchi A., Takeda H., Nyquist L. E., Bogard D. D., Ebihara M. and Karouji Y. (2004) Lunar and Planetary Science XXXV (2004) the origin and impact history of

- lunar meteorite Yamato 86032 . Institute of Technology , Narashino 257-0016 , Japan , 3 NASA Johnson Space Center , Houston , TX77058 , Lunar and Planetary Science XXXV (2004) . , 3–4.
- Yamamoto, T., 1985. Formation history and environment of cometary nuclei. *Ices in the Solar System*, **156**, pp.205-219.
- Yanai K. (1991) Gabbroic meteorite Asuka-31-Preliminary examination of a new type of lunar meteorite in the Japanese collection of Antarctic meteorites. *Proceedings of Lunar and Planetary Science* **21**, 317–324.
- Yao L., Sun C. and Liang Y. (2012) A parameterized model for REE distribution between low-Ca pyroxene and basaltic melts with applications to REE partitioning in low-Ca pyroxene along a mantle adiabat and during pyroxenite-derived melt and peridotite interaction. *Contributions to Mineralogy and Petrology* **164**, 261–280.
- Zeigler R. A., Korotev R. L., Jolliff B. L. and Haskin L. A. (2005) Petrography and geochemistry of the LaPaz Icefield basaltic lunar meteorite and source crater pairing with Northwest Africa 032. *Meteoritics and Planetary Science* **40**, 1073–1101.
- Zeigler R. A., Korotev R. L., Jolliff B. L., Haskin L. A., and Floss C. (2006). The geochemistry and provenance of Apollo 16 mafic glasses. *Geochimica et Cosmochimica Acta* **70**:6050–6067.
- Zeng X., Joy K. H., Li S., Pernet-Fisher J. F., Li X., Martin D. J. P., Li Y. and Wang S. (2018) Multiple lithic clasts in lunar breccia Northwest Africa 7948 and implication for the lithologic components of lunar crust. *Meteorit Planet Sci* **53**, 1030–1050.
- Zeng X., Li X. and Liu J. (2023) Exotic clasts in Chang’e-5 regolith indicative of unexplored terrane on the Moon. *Nat Astron* **7**, 152–159.
- Zhang A. and Hsu W. (2009). Petrography, mineralogy, and trace element geochemistry of lunar meteorite Dhofar 1180. *Meteoritics and Planetary Science*. **44**:1265–1286.
- Zhang N., Ding M., Zhu M.-H., Li Huacheng, Li Haoyuan and Yue Z. (2022) Lunar compositional asymmetry explained by mantle overturn following the South Pole–Aitken impact. *Nat. Geosci.* **15**, 37–41.

List of Publications

Related to Thesis

Srivastava, Y., Basu Sarbadhikari, A., Day, J., Yamaguchi, A. and Takenouchi, A., 2022. A changing thermal regime revealed from shallow to deep basalt source melting in the Moon. *Nature Communications*, 13(1), pp.1-9. <https://doi.org/10.1038/s41467-022-35260-y>

Srivastava Y., and Basu Sarbadhikari A. (2022) Silica, Silicate. In: Cudnik B. (eds) *Encyclopedia of Lunar Science*. Springer, Cham. https://doi.org/10.1007/978-3-319-05546-6_215-1

Under Review

Srivastava, Y., et al., 2023. Magmatic evolution of KREEP-free lunar meteorite Asuka-881757 inferred from sector-zoned clinopyroxene, symplectites and model crystallization calculations.

In preparation

Srivastava, Y., et al., 2022. Petrogenesis of Antarctic lunar regolith breccia meteorites Y-981031, 983885 and Y-86032: Insight into crustal diversity of the Moon.

Srivastava Y., et al., 2023. Understanding highly siderophile abundance of lunar mantle and crust outside the Procellarum KREEP Terrane (PKT) from Lunar regolith breccia meteorites: Implication to nature and composition of impactor striking the Moon

Conference Abstracts

Related to Thesis

Srivastava, Y., Basu Sarbadhikari, A., Day, J.M.D., and Yamaguchi, A., 2023. Insights into KREEP-free volcanism on the Moon from Lunar Meteorites. *Goldschmidt 2023*.

Srivastava, Y., Basu Sarbadhikari, A., Day, J.M.D., and Yamaguchi, A., 2023. A 187Re-187Os and Highly Siderophile Element Study of the KREEP-Free YAMM Basalts. *LPI Contributions*, 2806, p. 2806.

Srivastava, Y., Basu Sarbadhikari, A., Day, J.M.D., and Yamaguchi, A., 2023. Mineralogical and Petrological Investigation of Lunar Meteorite Regolith Breccia: Y-981031, Y-983885 and Y-86032. *LPI Contributions*, 2806, p. 2111.

Srivastava, Y., Basu Sarbadhikari, Day, J.M.D., A., Yamaguchi, A., and Takenouchi, A., 2022. Understanding Mare Basalt Generation From Ancient KREEP-Free Meteorites: Evidence For Possible Shallow Melting On The Moon. American Geophysical Union (AGU) Fall Meeting 2022.

Basu Sarbadhikari, A. and **Srivastava, Y.** Evaluation of thermal condition as stated by KREEP-free meteorites from the lunar surface. 44th COSPAR Scientific Assembly. Held 16-24 July, 2022. Online at <https://www.cosparathens2022.org/>. Abstract C3.2-0036-22.

Srivastava, Y., Basu Sarbadhikari, A., Yamaguchi, A., Takenouchi, A. and Day, J.M.D., 2022. Petrogenesis of Lunar Ferroan Gabbro Meteorite Asuka 881757. LPI Contributions, 2678, p.1903.

Srivastava, Y., Basu Sarbadhikari, A., Day, J.M.D., 2021. Highly Siderophile Element Conundrum of the Moon. In LunGradCon2020, 12th annual Lunar and Small Bodies Graduate Forum.

Recognition/awards

LPI Career Development Award.	— 2023
Young Researcher Award, MetMeSS 2022 Conference	— 2022
Invitation to contribute a chapter in Encyclopedia of Lunar Science	— 2020

Research in news

- Research highlighted in ISRO Story of the Week.
 - *Group of lunar meteorites suggest a new scenario for the origin of lunar basalts. Feb, 16, 2023: <https://www.isro.gov.in/lunarbasalts.html>*
- NIPR confirms changes in lunar volcanic activity from lunar meteorites collected in Antarctica. **Mycom:** <https://news.mynavi.jp/techplus/article/20230214-2591559/>
- Indian scientists reveal unique detail about how our Moon evolved. **India Today:** <https://www.indiatoday.in/science/story/isro-moon-evolution-prl-apollo-mission-chandrayaan-2335938-2023-02-17>
- A changing thermal regime revealed from shallow to deep basalt source melting in the Moon. **Karmaka Meteorites:** <https://karmaka.de/?p=31680>
- Group of lunar meteorites throw light on origin of basalts on Moon: ISRO. **The Times of India:** <https://timesofindia.indiatimes.com/home/science/group-of->

[lunar-meteorites-throw-light-on-origin-of-basalts-on-moon-isro/articleshow/97986595.cms](https://www.isro.gov.in/press-releases/2023-02-14-lunar-meteorites-throw-light-on-origin-of-basalts-on-moon-isro-2/1376595)

- A group of ancient lunar basaltic meteorites discovered. **JournalsOfIndia:** <https://journalsofindia.com/a-group-of-ancient-lunar-basaltic-meteorites-discovered/>
- ISRO Proposes Different Scenario for the Origin of ‘Lunar Basalt’. **Transcontinental Times:** <https://www.transcontinentaltimes.com/isro-the-origin-of-lunar-basalt/>
- Group of lunar meteorites throw light on origin of basalts on Moon: ISRO. **ThePrint:** <https://theprint.in/india/group-of-lunar-meteorites-throw-light-on-origin-of-basalts-on-moon-isro-2/1376595/>
- Scientists From Physical Research Laboratory, US And Japan Find Unique Lunar Meteorites. **ABP Live:** <https://news.abplive.com/science/scientists-from-physical-research-laboratory-us-and-japan-find-unique-lunar-meteorites-know-everything-1582696>

- ‘Rare, unique’: Diyodar meteorite in 2022 was India’s first aubrite in 170 years. **The Hindu:** <https://www.thehindu.com/sci-tech/science/rare-unique-diyodar-meteorite-in-2022-was-indias-first-aubrite-in-170-years/article66496695.ece>
- Rare meteorite that crashed in India may reveal secrets of other planets. **WION:** <https://www.wionews.com/science/rare-meteorite-that-crashed-in-india-may-reveal-secrets-of-other-planets-562405>
- Diyodar meteorite was India’s first aubrite in 170 years. **JournalsOfIndia:** <https://journalsofindia.com/diyodar-meteorite-was-indias-first-aubrite-in-170-years/>
- Rare aubrite meteor that crashed in Gujarat could shed light on evolution of planets. **IndiaToday:** <https://www.indiatoday.in/science/story/aubrite-meteor-diyodar-gujarat-crash-planet-evolution-2334988-2023-02-15>
- Rare Aubrite Meteor That Crashed In Gujarat May Uncover Secrets Of Other Planets. **IndiaTimes:** <https://www.indiatimes.com/news/india/rare-aubrite-meteor-may-uncover-secrets-of-other-planets-593394.html>
- Diyodar Meteorite That Crashed In Gujarat Last Year Is a Rare ‘Aubrite’ With Possible Mercurian Origins. **The Weather Channel:** <https://weather.com/en-IN/india/space/news/2023-02-14-diyodar-meteorite-that-struck-gujarat-could-be-from-mercury>

